Nadir Sounding of Clouds and Aerosols in the O_2 A-Band

By
Andrew K. Heidinger and Graeme L. Stephens

Department of Atmospheric Science
Colorado State University
Fort Collins, Colorado

NASA NAGI-1849 and NAGI-1702

Colorado State University

Department of Atmospheric Science

Paper No. 650

NADIR SOUNDING OF CLOUDS AND AEROSOLS IN THE O_2 A-BAND

Andrew K. Heidinger and Graeme L. Stephens

Research Supported by NASA grants NAG1-1849 and NAG1-1702

Principal Investigator: Graeme L. Stephens

Department of Atmospheric Science
Colorado State University
Fort Collins, CO 80523

April 1998

Atmospheric Science Paper No. 650

ABSTRACT

This paper explores the feasibility of using O_2 A-band reflectance spectra in the retrieval of cloud and aerosol optical properties. Analyses demonstrate that these reflection spectra are sensitive to optical properties of clouds and aerosol such as optical depth and phase function, vertical profile information including cloud top pressure, pressure thickness and the surface albedo. An estimation method is developed to demonstrate how well this information might be retrieved assuming realistic instrument parameters (spectral resolution, calibration accuracy and signal-to-noise properties). The quality of the retrievals are expressed in terms of two indices, one relating to total error and another that quantifies the extent of reliance of the retrieval on the measurement, or conversely on other *a priori* information. Sources of total error include instrument related errors, forward model errors include phase function errors and errors due to spatial variability.

The results show that: (i) the optical depth, surface albedo, cloud top pressure and cloud layer pressure thickness can be retrieved with an accuracy of approximately 5% for most cases of low cloud. The pressure thickness of the low-level can be retrieved with an expected accuracy of less than 10 % and with little reliance on any prior data. (ii) Phase function uncertainties are known to cause large errors in cirrus retrievals. Estimation of a limited amount of information about the phase function is possible and reduces the errors in optical depth to less than 20 % more most cirrus conditions. (iv) A-band spectra are shown to provide a limited amount of vertical profiling capability (4-5 layers of information at the most) provided the measurements are obtained with a spectral resolution of about $0.5cm^{-1}$ and obtained with an accuracy of 2% or better. A specific example demonstrates the capability of estimating the optical depths of multi-layered clouds. (v) Additional information provided by active profilers (radar and lidar) can significantly improve the

estimation of properties in each layer. (vi) In addition, a novel technique for diagnosing the effects of cloud structure in the retrieval is demonstrated using satellite derived cloud fields.

ACKNOWLEDGEMENTS

We would like to thank Dr. Stephen Cox, Dr. Thomas Vonder Haar and Dr Patrick Burns for their technical advice and generous assistance in performing this research and evaluating the manuscript. A great debt is owed to Mrs. Susan Lini for her assistance in this manuscript's production. In addition, we would like to acknowledge the assistance on various aspects of this work by our colleagues at Colorado State University including Dr. Philip Gabriel, Dr. Richard Engelen, Mr. Ian Wittmeyer, Mr. Charles Drummond, Mr. Arlie Huffman, Mr. Steve Miller, Mr. Philip Partain, Dr. Renata Rybka and Mr. Robert McCoy. Much appreciation is extended to Dr. Denis O'Brien for his insight at the onset of this research and for assistance in the development and validation of the three dimensional radiative transfer code. In addition, Dr. David Winker and Dr. Chris Hostetler of NASA Langley Research Center generously provided equipment and support for ground-based measurements. The advice offered by Dr. David Crisp of JPL concerning the line-by-line radiative transfer modelling was invaluable. This research was supported under NASA Grants NAG1-1702 and NAG1-1849 under contract # PNO 34402.

Contents

List of Figures

Chapter 1

Introduction

In the spectral region between 0.760 - 0.770 μm resides a molecular oxygen absorption band that occurs as a result of rotational transitions produced by the strong magnetic dipole moment of oxygen (O_2). The absorption that results ranges in strength over several orders of magnitude. This paper explores the feasibility of retrieving the properties of cloud and aerosol layers in the atmosphere from nadir reflectance spectra in this absorption band. A schematic illustration of the physical processes involved in A-band remote sensing is shown in Fig 1.1. At A-band wavelengths (0.760 - 0.770 μm), emission at terrestrial temperatures is negligible and the radiance measured by a nadir viewing space-borne A-band radiometer arises from the scatter of solar radiation by constituents in the atmosphere.

Since the vertical profile of oxygen is known, the growth of the absorption lines in reflectance spectra provides information about the properties and distribution of scatters in the atmosphere. This conceptual application differs from the more traditional use of scattering as a way of deducing gaseous concentrations on planets. The ability to measure at many frequencies in the A-band allows for a retrieval to selectively tune out contributions from photons which travel extended paths through the atmosphere. For example, using the schematic as a guide, measurements of reflectance at different wavelengths provides a way of separating those photons scattered from cirrus from those photons scattered lower in the atmosphere from clouds, aerosols or the underlying surface.

The goals of this paper are to demonstrate which properties of the atmosphere can be retrieved from nadir A-band spectra, to develop a method for retrieving these properties and to provide an assessment of the uncertainty associated with such retrievals.

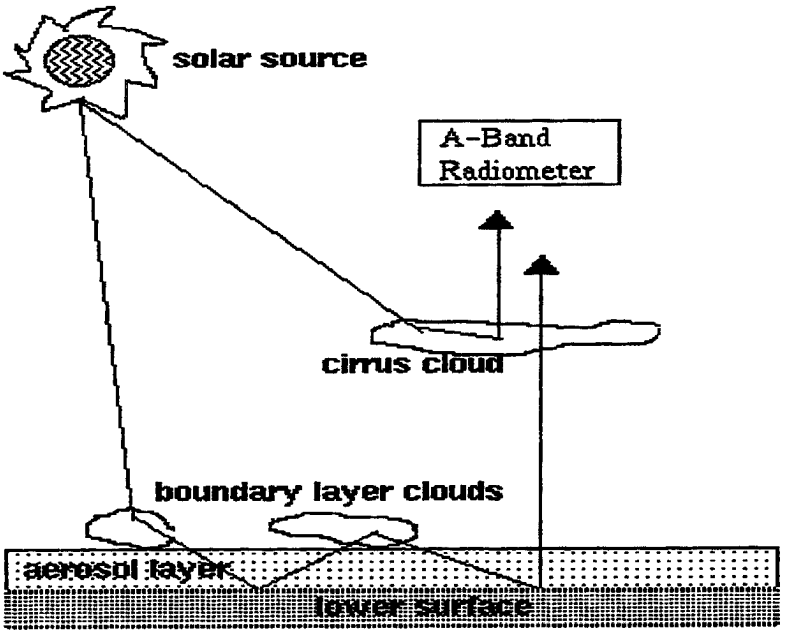

Figure 1.1: Schematic diagram illustrating transfer of radiation involved with nadir sounding the the O_2 A-band.

Detailed sensitivity analyses will be given in Chapters 6,7 and 8 to identify these properties. The list of parameters that will be retrieved can be divided into three groups. The first group pertains to the optical properties of the scattering layer such as the optical depth, the single scatter albedo and some information of the phase function, such as the asymmetry parameter. The second group contains properties that define how the scatters are distributed in the atmosphere such as the top pressure and pressure thickness of the scattering layer. The last group of parameters to be retrieved deal with the reflecting properties of the underlying surface.

1.1 The Necessity of Remotely Sensing Cloud Optical Properties

The influence of clouds on the energy budgets at the surface and at the top of the atmosphere has been well documented (Ardanuy *et al*, 1989, Harrison *et al*, 1990). In addition, clouds affect the magnitude and the distribution of radiative heating in the atmosphere. It is the radiative heating in the atmosphere which links the radiative properties of clouds to other atmospheric processes and it is the accurate estimate of radiative heating that is most desired by climate modellers. To illustrate the importance of accurately knowing the properties of clouds in the atmosphere, several simulations of the effect of clouds on the radiative heating profiles are shown. Fig 1.2 compares the infrared heating profile between a clear tropical atmosphere to one containing a cirrus cloud with an optical depth of 0.1 placed between 300 and 400 mb. This simulation represents a scenario where an A-band retrieval is superior to current retrieval methods. As will be discussed in Chapter 8, current cirrus remote sensing techniques have difficulty both detecting thin cirrus over bright surfaces and accurately placing them correctly in the atmosphere. This paper will show that A-band retrievals can overcome a number of existing weakness of current observing systems. As Fig 1.2 shows, the presence of the thin cirrus has a significant effect on the radiative heating profile. Climate models need to be validated against measurements and a systematic misrepresentation of cirrus clouds in observations could lead to systematic errors in the radiative heating in climate models.

Another strength of A-band retrievals, which will be demonstrated later is the ability to distinguish between clouds high and low in the atmosphere. Fig 1.3 shows the infrared heating profiles for a tropical atmosphere with a low cloud with an optical depth of 10 placed between 850 and 900 mb and the heating profile for the same scenario except the cirrus cloud from Fig 1.2 is added. Current passive remote sensing techniques have difficulty in detecting thin cirrus over lower clouds or bright surface, due to the lack of contrast. As Fig 1.3 shows, the presence of thin cirrus significantly affects the heating profile of atmosphere. The multi-layer retrievals shown in Chapter 10 demonstrate the utility of A-band retrievals in discerning the presence of cirrus over lower clouds.

Chapter 7 demonstrates the ability of A-band retrievals to position cloud in the atmosphere as well as estimate their pressure thickness. Fig 1.4 shows the effect of cloud pressure thickness on the heating profiles. The figure compares the heating profiles for the same low cloud as in Fig 1.3 and the heating for the same cloud except now that cloud extends from 850 to 950 mb. The effect of the doubling of the cloud pressure thickness is to change both the magnitude and distribution of the cloud heating. The distribution of heating in the cloud is also important since it influences both the microphysical and dynamical evolution of the cloud layer (Roach, 1976). The ability of the A-band retrieval to estimate pressure thickness stems from the sensitivity of the growth of absorption lines from the photon pathlength.

1.2 Brief Comparison of A-band and Current Cloud Observing Systems

The remote sensing of clouds from space began with the advent of the weather satellite in the mid 1960's. At first, only cloud imagery was studied and later estimates of cloud fraction were produced(Rossow, 1991; Stowe *et al*, 1991). Within the last 15 years, attempts have been made to deduce cloud properties from satellite radiometric data (Arking and Childs, 1985; . Current operational cloud property retrievals are performed using the Advanced Very High Resolution Radiometer (AVHRR) instruments on the NOAA polar orbiting satellites and using radiances obtained from the imager on the Geostationary Environmental Satellites (GOES). The spectral location of channels currently used for cloud

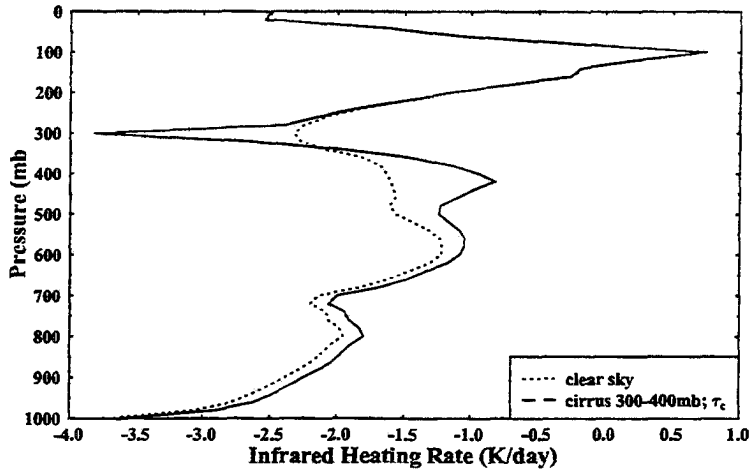

Figure 1.2: Infrared heating profile in a McClatchey Tropical atmosphere with and without a thin cirrus cloud

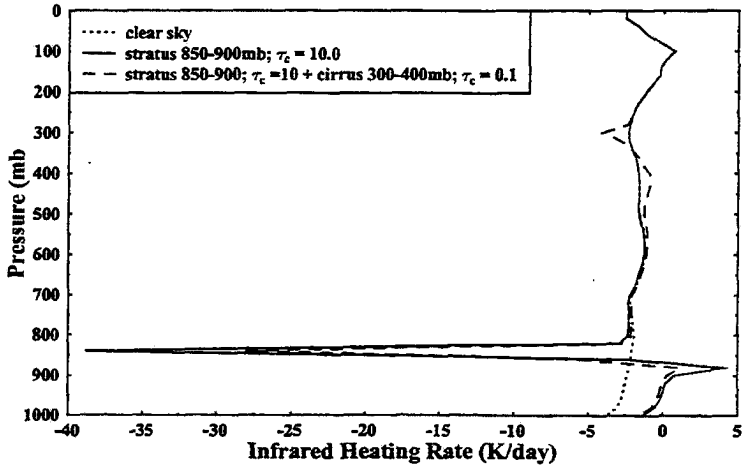

Figure 1.3: Infrared heating profile in a McClatchey Tropical atmosphere for a stratus, stratus + cirrus and clear skies

property retrieval from satellites are shown in Fig 1.5 and referenced to a spectrum of nadir radiance at the top of the atmosphere simulated using MODTRAN (Rothman *et al*, 1990). The spectrum was simulated assuming a single layer of cumulus cloud in a tropical atmosphere. Channel numbers 1,2,5,6 and 7 are the five channels of AVHRR. Channel number 4 is the 6.7 μm channel of GOES. Also shown in Fig 1.5 is the 1.4 μm channel of

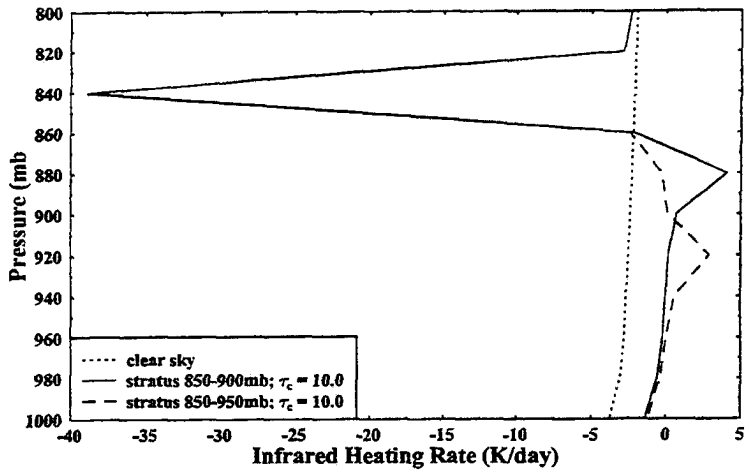

Figure 1.4: Infrared heating profile in a McClatchey Tropical atmosphere for two stratus with identical optical thicknesses but different pressure thickness, Δp

the MODerate resolution Imager and Spectrometer (MODIS) which will be launched in 1998 as part of the Earth Observing System (EOS). The main use of this channel will be cirrus remote sensing. (Gao *et al*, 1993).

To illustrate the information content contained in selected channels of the current and near future cloud observing systems, Fig 1.6 was produced. The plots in Fig 1.6 show the unit change in the nadir radiance with a unit change for several parameters that influence the reflection and may possibly be retrieved. Results are shown for the 5 AVHRR channels, the 6.7 μm GOES channel and the 1.4 μm channel of MODIS. The results in Fig 1.6 pertain to a cirrus cloud with placed in a mid-latitude summer atmosphere over a dark surface. The results are shown for cirrus optical depths of 0.1 and 1.0. The upper-left panel of this figure shows the sensitivity of the channel radiances to changes in the cloud optical depth τ_c, the center-left panel shows the sensitivity to the effective radius, r_e of the particle size distribution, and the lower-left panel shows the sensitivity to the cloud top pressure, p_t. The previous three parameters are those most often estimated from satellite measurements. The right-hand panel shows the sensitivity of the channel radiances to the slope of the extinction in the cloud layer (in this case taken to be linear). The center-right panel illustrates the sensitivity to particle scattering phase function which is characterized

by the parameter b, which controls the shape of the phase function described in more detail in Chapter 7. The sensitivity of the channel radiances to the pressure thickness of the cirrus layer is given in the lower-right panel. The bottom panel shows This slope characterizes the vertical profile within the cloud and the ice water content.

Current cloud retrieval schemes use radiance in the visible (channel 1) and at 3.7 μm (channel 6) to retrieve both optical depth and effective radius (Nakajima and King, 1989, Nakajima and Nakajima, 1995, Platnick and Valero, 1995, Han *et al*, 1994). The physical basis for this retrieval approach can be seen in the sensitivities in Fig 1.6 where the visible radiance is sensitive to both optical depth and effective radius while the 3.7 μm channel is much more sensitive to effective radius than optical depth. In addition, infrared channels (AVHRR channels 4 & 5) are used to estimate cloud optical depth in the infrared and to place the cloud vertically by matching the observed brightness temperature to an atmospheric level. The combination of visible and infrared channel for cloud retrievals has been explored by Minnis(1993) and others. It is evident from Fig 1.6 that infrared techniques have difficulty in detecting cirrus due to their channel sensitivity to both optical depth and effective radius. From Fig 1.6, it appears only th 1.4 μm channel offers information about the cloud top pressure and pressure thickness of the cloud. Since the absorbing gas is water vapor at 1.4 μm, the exploitation of this signal into actual retrieved quantities requires knowledge the distribution of water vapor in the upper troposphere, a quantity which is not well known and difficult to retrieve accurately (Engelen and Stephens, 1997). The 1.4 μm channel of MODIS is also highly sensitive to the distribution on extinction the cloud layer, given here by the slope of the ice water content. One last conclusion from Fig 1.6, is the large sensitivity in any reflectance measurement (channels 1,2 and 7) to the particle phase function. This error source is ubiquitous in all retrievals which use reflectance and is large in cirrus retrievals due to the uncertainty in the phase function. The retrievals shown later will attempt to accurately estimate this error and show how A-band retrievals can minimize its effect.

In summary, current approaches to passive remote sensing of cloud properties are to use multiple broad-band channels. These methods are subject to significant uncertainties

and require specification of information not generally available (such as phase function, water vapor profiles and others). The A-band retrieval approach developed in this thesis is fundamentally different to the current methods. An A-band observing system uses many measurements in a narrow spectral region were the only variation in the measurements is due to the variation in oxygen absorption. The sensitivity analysis of Chapters 6,7,8 will show measurements of this type to contain information about parameters that current observing systems with the above channels can not retrieve.

1.3 Organization of Paper

To attempt to address the feasibility of remotely sensing cloud and aerosol properties from nadir A-band reflectance measurements, the following paper was written. Following the introduction, . Chapter 3 briefly overviews the previous research concerning the use of A-band measurements in cloud remote sensing.Chapter 3 discuss the spectral variation of oxygen absorption in the A-band as well the spectral variation of cloud optical properties in the A-band. The method of retrieval of the optical properties is developed in Chapter 4. This method has not previously been applied to cloud and aerosol retrievals and has several advantages over current approaches including a clear treatment of errors and an assessment of the information content of the observations. The appropriate forward model of A-band radiance required for retrievals is developed in Chapter 5. Chapters 6-8 will show retrieval results for representative atmospheric scenarios. The ability of A-band retrievals to estimate properties in multiple layers is explored in Chapter 9. The benefits of combining A-band measurements with those from active sensors such as LIDAR and RADAR is discussed in Chapter 10 and this combination provides a new paradigm for observing atmospheric particulates which has demonstrable advantages over existing methods. Lastly, the application of A-band retrievals to clouds with spatial variability is explored in Chapter 11. While the importance of 3D effects is widely recognized, these effects are ignored in all existing retrieval methods.

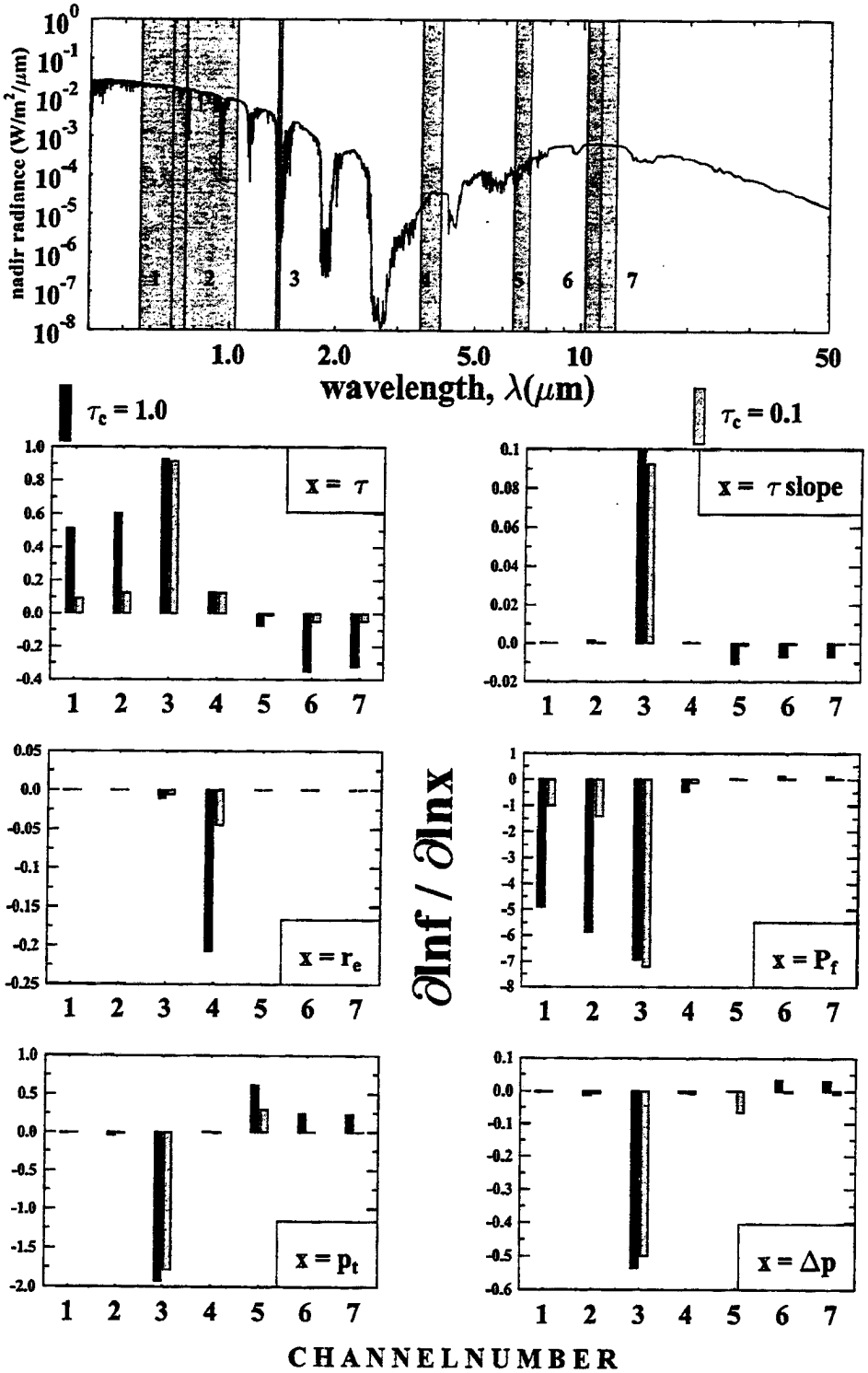

Figure 1.5: The sensitivity of nadir radiance in selected channels to several cloud properties. The simulation is for a cirrus placed 300-400 mb in a mid-latitude summer atmosphere. Results are shown for cirrus optical depths of 0.1 and 1.0.

Chapter 2

Previous Research concerning the O_2 A-band

In this chapter, the previous research on the use of A-band measurements for remote sensing is discussed. Interest in the use of the A-band for remote sensing began with the works of Yamamoto and Wark(1961) and Chapman(1962) which proposed that A-band measurements from space-borne satellites could be used to determine cloud top pressure. The physical rationale is that knowing the vertical and spectral variation of oxygen absorption, the observed absorption along a path could be translated directly to an estimate of cloud top pressure. However early attempts to deduce cloud top pressures from A-band spectra using the direct inversion of the oxygen transmission to a corresponding pressure consistently overestimated the cloud top pressure. It became apparent that multiple scattering in clouds caused these pressure biases. Most of the research in A-band remote sensing has continued to be concerned with cloud top pressure retrieval and taking into account the in-cloud absorption by oxygen. The remainder of this chapter provides a brief discussion of selected research on A-band remote sensing.

2.1 Hanel (1961), Yamato and Wark(1961) and Chapman(1962)

The short paper of Hanel(1960) appears to be the first work advocating the use of reflection spectra to determine cloud top pressures from space. He proposed using absorption lines of CO_2 whose vertical concentration is well known. The idea of using the A-band of oxygen to retrieve cloud top pressures was first put forth by Yamamoto and Wark(1961)

and Chapman(1962). The absorption lines of O_2 were preferable to CO_2 since water vapor lines do not contaminate the absorption in the A-band to the extent that CO_2 absorption is contaminated by water vapor lines in the near-infrared region of the spectrum.

2.2 Saiedy, Jacobowitz and Wark (1966)

Using A-band measurements from a hand-held spectrograph flown on the Gemini-5 manned spacecraft, this work was the first to test the ability of cloud top pressure measurement from space-borne A-band measurements. The spectrograph had a spectral resolution of .5 nm centered on .7631 μm for low and medium clouds and at 0.7607 μ m for high clouds. The spectra were recorded on high speed infrared film which also coincidently recorded images of the observed cloud field. Knowing the density versus. intensity properties of the film allowed for the retrieval of radiometric values of the spectrum. Saiedy derived a correction factor for the in-cloud oxygen absorption from two-stream theory. For cases where cloud observations were present, the uncorrected observations reported cloud top pressures that were 50 to 120 mb too large. The application of the correction term improved the agreement but only for observations at high zenith angles.

2.3 Russian A-band Research

As the measurements of Saiedy *et al* showed, the problem of photon penetration in cloud layers significantly affected the reflected spectra and therefore the estimates of cloud top pressure. The use of direct measurements of the extension of photon path-lengths due to multiple scattering in clouds was explored by Dianov-Klokov *et al* (1970), Dianov-Klokov and Krasnokutskaya (1972), Grechko *et al* (1973) and Grechko *et al* (1975) and others. The measurements were based on matching the observed ratios of radiances in an absorbing region of the A-band, I_ν to the radiance measured in the continuum where oxygen absorption is minimal, I_c. Measurements were taken in clear skies to where scattering is negligible to tabulate the variation of the directly transmitted solar radiance, $I_c^\odot$ and $I_\nu^\odot$ versus the air mass, m, defined as the inverse of the solar zenith angle cosine. By matching

the radiance ratios measured in cloudy conditions for a given value of m,

$$\frac{I_\nu}{I_c}(m) = \frac{I_\nu^\odot}{I_c^\odot}(m^*)$$

the apparent airmass, m^*, traveled by the photons in the cloudy atmosphere could be deduced. The ratio $\frac{m^*}{m}$ therefore represented the extension of the path-length due to multiple scattering. From aircraft measurements, they measured maximum mean path-lengths to be 1.5 times the layer thickness. Cloud top pressure biases due to the observed path-length extensions were as large as 7 km for multi-layer cloud systems.

2.4 Wu (1985)

Using data from the Multispectral Cloud Radiometer (MCR), this study also attempted to reconcile observed and measured cloud top pressures. The MCR consisted of three channels in the A-band (0.754 μm, 0.7609 μmm, 0.7634 μm). The first channel is a near transparent region and is used for the continuum radiance values. The other channels are situated at the most opaque regions of the P and R branches of the A-band. The resolution of these channels was approximately $10cm^{-1}$. Unlike the work above, which assumed cloud properties to apply a correction for multiple scattering, this work tried to retrieve cloud properties with the goal of increasing the accuracy of the cloud top pressure estimation. Using the scaling relationships of van de Hulst and Grossman (1968), the optical properties of the cloud could be condensed into two properties. These properties are the scaled optical depth

$$\tau^* = (1-g)\tau$$

and the similarity parameter

$$s = \left(\frac{1-\omega_o}{1-g\omega_o}\right)^2$$

Wu studied the effect of these properties on the reflection properties of clouds and compared them to mirror clouds which have no in-cloud oxygen absorption. Therefore, with the three measurements from the MCR, Wu was able to retrieve the cloud top pressure and two scaled optical properties of the cloud. In actuality, Wu assumed a volume scattering coefficient and estimated only one scaled optical parameter, the scaled

optical depth. In 1981, the MCR was flown during the CCOPE project on a high altitude aircraft which also contained a LIDAR. Wu was able to show significantly better agreement between the LIDAR and MCR cloud top estimates for the retrieval which used all three channels to estimate the scaled optical depth.

2.5 Fischer and Grassl (1991), Fischer, Cordes, Schmitz-Peiffer, Renger and Mörl (1991)

The theoretical study of Fischer and Grassl(1991), presented simulations of A-band reflectance spectra to show the dependence of cloud-top pressure on properties of the cloud layer. From these simulations, Fischer and Grassl(1991) showed that accurate cloud top estimation required information both on the optical thickness and the vertical distribution of the cloud. Using simulated spectra with a resolution of $1nm$, they were able to reduce the cloud top errors to within 100 meters with a 1% level of noise imposed on the measurements. In the follow-up work of Fischer *et al*(1991), LIDAR measurements of cloud-top height were compared with A-band spectra measurements with a resolution of 10 cm^{-1}. Using data from a wide range of cloud models, simulations indicated that errors on the order of 150 meters were obtained. These errors errors were reduced to below 50 meters when the spectra were averaged together to reduce the level of noise.

2.6 O'Brien and Mitchell (1991)

A theoretical study of cloud top pressure retrieval from space-borne A-band measurements was also undertaken by O'Brien and Mitchell (1991). Assuming semi-infinite clouds, O'Brien and Mitchell developed a model for A-band reflectance based on the cloud top pressure and the photon path-length distribution within the cloud. In addition, their model also included the effects of Rayleigh and aerosol scatter above the cloud which were modeled using single scatter theory. The photon path-length distribution was assumed to be represented by a gamma distribution whose parameters were determined solely by the mean path-length and the path-length variance. The authors argued that the mean and at least the variance should be able to be estimated from A-band spectra. Using a linear

least squares type of retrieval, the cloud top pressure errors were determined as a function of the instrumental and modeling errors. From these results, O'Brien and Mitchell claim an accuracy of 5 mb in cloud top pressure is possible. This level of accuracy assumed a spectral resolution of $1cm^{-1}$ could be measured with a 1% level of noise - a noise level that was described as conservative based on the experience of O'Brien in the design of A-band spectrometers. In addition, the 5 mb accuracy also assumed a temperature profile known to within 1K and an aerosol profile known to within 100 %. O'Brien and Mitchell also discuss the effect of instrument resolution on the retrievals, noting that with decreased resolution, the sensitivity to instrumental errors increases.

2.7 Barton and Scott(1986), Mitchell and O'Brien(1987)

Using the same basic principle for the cloud top pressure estimation, Barton and Scott(1986) and Mitchell and O'Brien (1987) studied the problem of retrieving the surface pressure from A-band reflectance spectra. As pointed out by both studies, to be useful to the scientific and forecasting community, surface pressure estimates have to be accurate to within 2 mb or at a 0.2% accuracy level. In Mitchell and O'Brien, simulations using single scatter theory treatment of molecular and aerosol absorption and simulated oceanic reflecting surface, different sets of channel resolutions and channel spectral locations were used to optimize the retrieval of surface pressure. The results indicated that measurements at multiple frequencies with a high spectral resolution of 2 cm^{-1} or better were necessary. To retrieve the surface pressure to within 2 mb, the simulations indicated that errors in the temperature profile had to be known to better than 1 K rms and uncertainties in the aerosol profile needed to be less than 10%. In addition, the instrumental noise had to be less than 0.1%. The work of Mitchell and O'Brien concluded that current technology (circa 1987) makes this a viable proposition.

2.8 O'Brien (1997)

In the recent work of O'Brien (1997), the utility of space-based A-band measurements to the retrieval of aerosols was explored. Performing radiative transfer simulations using

single scatter theory, O'Brien was able to demonstrate how measurements associated with varying degrees of oxygen absorption could distinguish the effects of aerosol and surface scatter. For example, Fig 2.1 shows the components of the radiance received by a nadir viewing A-band spectrometer. The radiance, I is composed of a component from surface scatter, I_s, aerosol scatter, I_1 and Rayleigh scatter, I_0. The ordinate is this figure is the total column optical depth due to oxygen. As this figure illustrates, the surface term dominates in the region with little oxygen absorption. As the amount of oxygen absorption increases however, the relative contribution of the aerosol scatter increases allowing for the detection of the effects of aerosol. As this figure highlights, the relative effects of aerosol scatter compared to the surface increase with increasing oxygen optical depth. As will be discussed later, this, in effect, drives the need for higher spectral resolution. The results of this work indicate that low values of aerosol optical depths can be retrieved for high spectral resolution measurements. The signal to noise ratio used in the simulations was 1000:1. The results also indicate the ambiguity of A-band retrievals in the presence of multiple layer of aerosols. The effect of upper aerosol layers is to mask the lower layers.

2.9 Conclusions

Having briefly summarized the last 30 years of research on the use of space-borne A-band measurements for remote sensing, those areas in which this work will attempt to contribute are summarized below. The areas include

- Which optical properties can be theoretically retrieved from A-band reflectance spectra?
- Under what conditions can these properties be retrieved and with what accuracy?
- What is the effect of cloud spatial variability on the A-band retrievals of cloud properties?
- Can A-band retrievals be used to diagnose cloud heterogeneity?
- How do A-band measurements compliment active sensors?

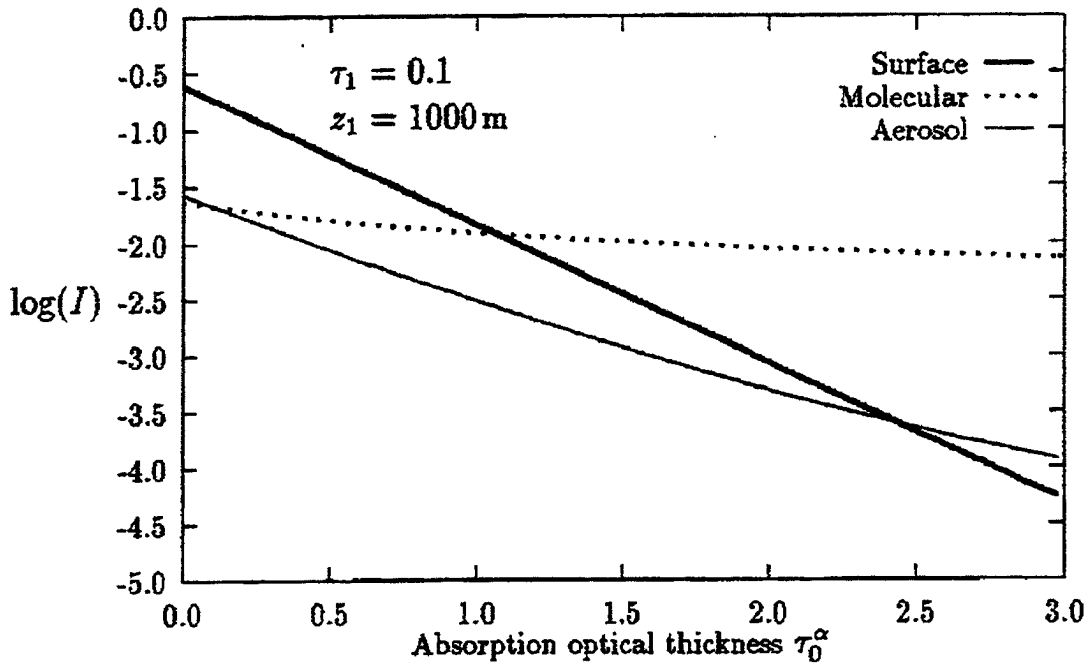

Figure 2.1: Figure 15 from O'Brien 1997 illustrating change in relative contributions to the nadir radiance with increasing column optical depth of oxygen, τ_O^α

Chapter 3

The O_2 A-band

In this chapter, the physical characteristics of oxygen absorption in the A-band will be described. Results from line-by-line (lbl) simulations will be used to discuss the effects of instrument resolution on the A-band spectra. In addition, the spectral variation in the optical properties in the A-band and the entire visible to near-infrared spectrum will be shown to address the utility of retrieving optical parameters in the A-band spectral region. Lastly, an approximation will made to simplify the treatment of the vertical variation of the oxygen absorption with height. This approximation is validated by comparison with results computed using the actual vertical variation in oxygen absorption computed from the full lbl model.

3.1 The O_2 A-band

The A-band of oxygen spans the spectral region from 12900 to 13200 cm^{-1}. Molecular oxygen is a stable homo-nuclear molecule with a large magnetic dipole moment. As a consequence, forbidden magnetic dipole transitions occur in the rotation band of oxygen. Fig 3.1 illustrates the role of oxygen in the context of other atmospheric absorbers. The upper panel of Fig 3.1 shows the total column atmospheric transmission due to every gas in the HITRAN 96 database except oxygen. In this spectral region, water vapor is the dominant absorbing gas with CO_2 being the the other significant contributor.

The location of the bands of oxygen absorption in the near-infrared visible regions of spectrum is indicated in the second panel. The region surrounded by the dotted lines encompasses the A-band. To the right of the A-band, is the B-band of oxygen which

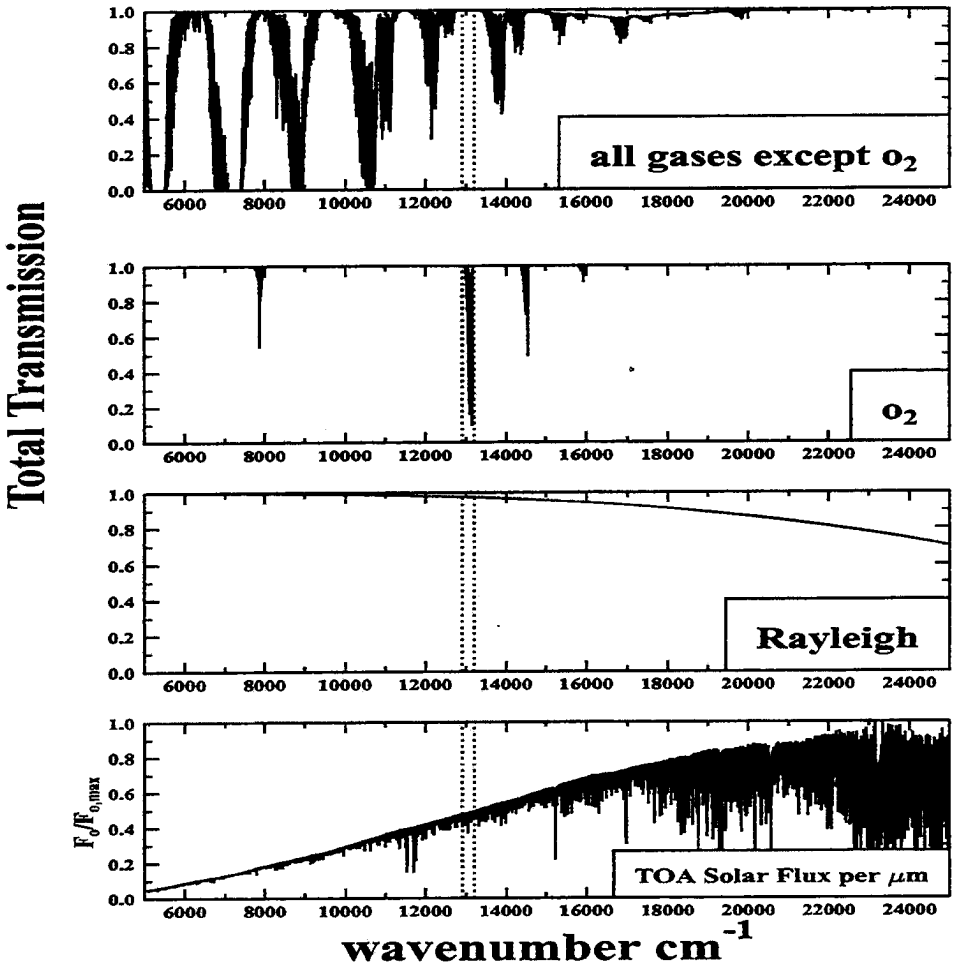

Figure 3.1: Spectral variation of the total column transmission due to atmosphere gases and Rayleigh scatter. The bottom panel shows the spectral variation of the solar flux at the top of the atmosphere.

involves a different vibrational transition than the A-band. Barely seen at 15902 cm^{-1} is the γ band of oxygen which involves a higher energy vibrational transition. At 7882 cm^{-1} (1.26 μm) is one of the infrared bands of oxygen which involves a different electronic transition the the A,B and γ bands of oxygen. In comparing the upper two panels of Fig 3.1, one sees that in the spectral region of the A-band, oxygen is only the gaseous absorber. As a consequence, the retrievals discussed later are free for any errors concerning assumed water vapor distributions. Note that both the B-band and γ-band of oxygen occur in spectral regions where some significant effect of other atmospheric absorber is occurring.

It is interesting to note, though the B-band of oxygen has never been suggested for remote sensing applications, it may be very useful for cirrus cloud studies. Besides oxygen, the other absorber gas is water vapor. An ideal situation would be for a strong oxygen band to occur simultaneously with a strong water vapor band. The water vapor absorption would be confined to the lower few kilometers of the atmosphere. As a consequence, the effects of the surface and lower clouds would be eliminated leaving only the cirrus clouds exposed to the effects of O_2 absorption. The cirrus retrieval based on the oxygen absorption would then be carried out in manner similar to the retrievals described later in Chapters 5-8. At the very least, dual A-band and B-band retrievals could be used to retrieve water vapor information which would be relatively insensitive to assumed temperature profiles.

The spectral variation of molecular or Rayleigh scattering total transmission is shown in the third panel of Fig 3.1. The total transmission due the Rayleigh Scattering in the A-band in 0.975 for a standard mid-latitude summer atmosphere. The strength of Rayleigh scatter is significant enough to produce an observable clear sky signal but not strong enough to reduce the sensitivity of the retrievals to thin cloud or aerosol layers. The bottom panel is the spectral variation of top of atmosphere (TOA) solar flux normalized by its maximum. Even though the A-band of oxygen is classified as being in the near infrared spectra, the TOA solar flux is still 20% of its maximum value. This number can be compared the infrared band of oxygen where the TOA solar flux is only 3 % of its maximum. Consequently, the large incoming solar energy in the A-band allows for accurate measurements that are little affected by instrument noise

3.2 Line by Line simulations of the A-band

Line by line simulations were performed to study the effect of instrument resolution on the A-band spectra. The mass absorption coefficient, k, for a a given frequency, ν, is defined as

$$k_{\nu_o} = \sum_{\nu'=0}^{\nu'=\infty} S(T)_{\nu_o} f_{\nu_o - \nu'} \tag{3.1}$$

where S(T) is the line strength and f_ν is the line shape. In order to include the effects of distant lines, the above summation is performed beginning at the desired frequency, ν, and all lines which contribute some threshold percentage to the value of k are included in the computation. For the results shown here a threshold of 0.001% was used. In order to estimate the line strength and line shape, line parameters for the A-band were taken from the HITRAN 96 database (Rothman *et al* , 1994). The line parameters compiled in the HITRAN96 database include $S(T_o)$, the line strength at a standard temperature, T_o, the line energy (E), the line half-width (α_o) at a specified standard pressure (P_o) and T_o, and the temperature exponent (n). For the computations performed in this work, values of $T_o = 296$ K and $P_o = 1000$ mb were used. For any temperature, T, the line strength can be expressed in terms of the reference temperature T_o by the following relation.

$$S(T) = S(T_o)\left(\frac{T_o}{T}\right)^n \left(\exp\frac{-hc}{k}E(\frac{1}{T}-\frac{1}{T_o})\frac{1-\exp\frac{-hc}{k}\frac{E}{T}}{1-\exp\frac{-hc}{k}\frac{E}{T_o}}\right) \tag{3.2}$$

The first term in the above equation represent an approximation to the partition function while the second term represents the Boltzmann factor.

Throughout this study, the Voigt line shape is assumed to apply the A-band absorption lines. The Voigt line shape is derived by applying the Doppler shift to the Lorentzian line shape and averaged over the Maxwell distribution (Goody, 1989). This assumes that Lorentzian, and Doppler broadening are independent of each other. Laboratory measurements confirm the accuracy of the Voigt line shape which has the following form given by (Liou, 1992)

$$f_{voigt} = \sqrt{\frac{\ln 2}{\pi}}\frac{1}{\alpha_{voigt}} 1-\zeta \exp -\ln 2\eta^2 + \frac{1}{\pi\alpha_{voigt}}\zeta$$
$$\frac{1}{1+\eta^2} - \frac{1}{\pi\alpha_{voigt}}\zeta(1-\zeta)(\frac{1.5}{\ln 2}+1+\zeta)(0.066\exp -0.4\eta^2 - \frac{1}{40-5.5*\eta^2+\eta^4}$$

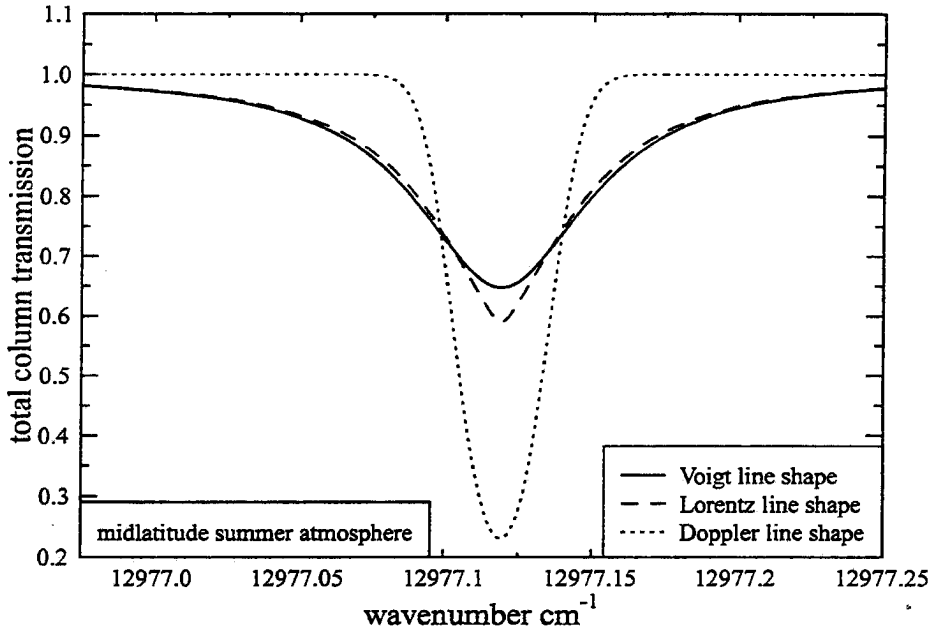

Figure 3.2: Comparison of the spectral variation of the total transmission for a single A-band line for various models of the line shape.

where $\zeta = \frac{\alpha_{lor}}{\alpha_{dop}}$ and $\eta = \frac{\nu}{\alpha_{voigt}}$. In the equation, α_{lor} is the standard Lorenz half-width given by

$$\alpha_{lorenz}(P,T) = \alpha_o \frac{P}{P_o}\left(\frac{T_o}{T}\right)^n$$

and α_{dop} is the Doppler half-width.

$$\alpha_{doppler}(T) = \frac{\nu_o}{c}\sqrt{\frac{2RT}{M}}$$

As the expression for the line shape, f, given above shows, under high pressure the Voigt shape becomes the Lorenz shape and under low pressures the Voigt profile is identical to the Doppler shape, which is strictly a function of temperature. Fig 3.2 shows a comparison of the total column transmission for an A-band line centered at 12977.0 cm^{-1} computed using the Voigt, Lorentz and Doppler line shapes. As this example shows, the Voigt and Lorentz line shapes are significantly different for moderately strong A-band lines.

Fig 3.3 shows a comparison between line by line computations for two isolated lines in the A-band. The small circles represent rigorous line by line simulations computed by Dr.

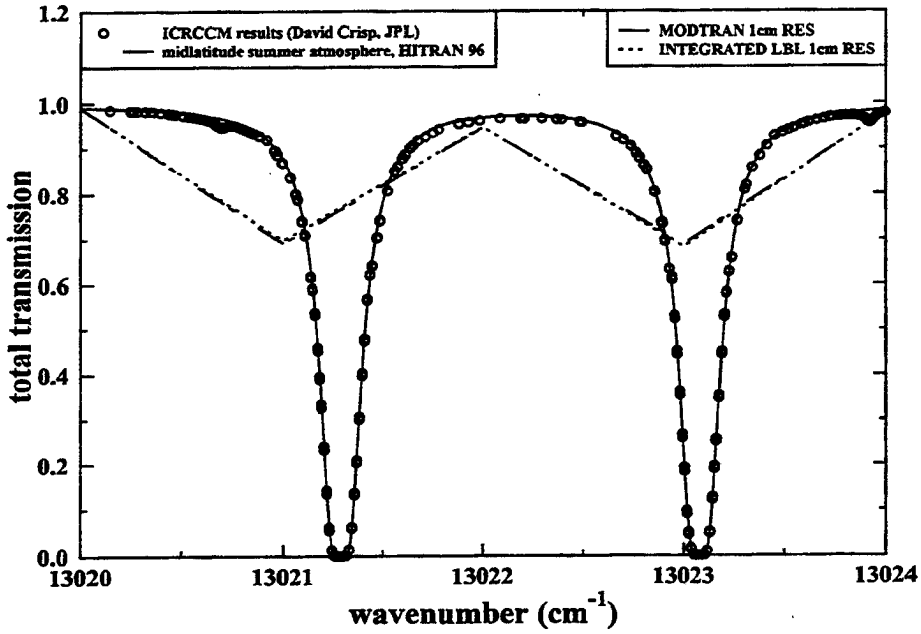

Figure 3.3: Comparison of the total transmission computed from the model used here and the results from Dr. David Crisp of JPL and MODTRAN.

David Crisp of the Jet Propulsion Laboratory for the standard mid-latitude summer atmosphere. The solid line in Fig 3.3 was derived from results of the model described above. The agreement between the two results indicates that the line by line spectra computed in this work are as accurate as the knowledge of the line parameters of the HITRAN database will allow. Also shown in Fig 3.3 is a comparison of the line by line data averaged to a resolution of $1cm^{-1}$ and of the results from MODTRAN, a atmospheric radiative transfer code with a spectral resolution of $1cm^{-1}$. (Rothman, 1994). The $1cm^{-1}$ comparison was shown since it is the ability to simulate accurately the radiances in instrument channels, whose spectral width can be on the order of $1cm^{-1}$, which is needed to perform accurate A-band retrievals.

3.3 Effect of Instrument Resolution on A-band Spectra

The retrieval results shown in later chapters illustrate the need for measurements taken over a wide range of channel opacities. If an instrument had infinite spectral resolution, the channel opacities are limited only by the strength of individual absorption line. For realistic instruments, however, the available range of channel opacities is strongly affected by the instrument spectral resolution. The upper-left panel of Fig 3.4 shows the line by line spectral variation of the total column transmission due to O_2 absorption in the A-band. As this figure shows, an A-band spectrometer of infinite resolution could view the atmosphere at virtually any level of column oxygen optical depth, $\tau^*_{o_2}$. To compute the actual transmission in a channel with a central frequency, ν_o and spectral width of $\delta\nu$, the line by line transmittance are averaged over the spectral width of the channel as

$$\mathcal{T}_{chan}(\nu_o) = \frac{1}{\delta\nu}\int_{\nu_o+\delta\nu}^{\nu_o-\delta\nu} f(\nu,\nu')\mathcal{T}(\nu')d\nu' \tag{3.3}$$

where $f(\nu_o,\nu')$ is the spectral response function of the instrument channel. Unless stated otherwise, the spectral response channel of each channel will assumed to be a triangular slit function whose half power points are located at $\nu_o \pm \frac{\delta\nu}{2}$ and the resolution of each channel will be defined by the value of $\delta\nu$.

Fig. 3.4 shows the effect of the instrument resolution on the spectra of total column transmission. The assumed atmospheric profiles are again taken from the McClatchey

mid-latitude summer atmosphere and the effects of Rayleigh scatter are omitted from these calculations. The instrument resolutions shown in Fig. 3.4 range from the line by line results to a resolution of 24 cm^{-1}; these resolutions represent current and past A-band spectrometers. For example, the Multi-Channel Radiometer (MCR) instrument, described by Curran *et al* (1981), contained three channels in the A-band with resolution of approximately 20 cm^{-1} (1-1.4 nm) and the hand-held A-band spectrometer described by Saiedy *et al*(1966) had a resolution of 10 cm^{-1} (0.5 nm) and measured the entire A-band spectra. In addition, the A-band spectrometer used by Fischer *et al* (1991) also had a resolution of approximately 1 nm. In the recently proposed NASA missions of CloudSat and Picasso, A-band grating spectrometers were proposed with resolutions of 0.5 cm^{-1}. For proposed validation studies of the third phase of the Stratospheric Gas and Aerosol Experiment (SAGE III), an A-band grating spectrometer width a resolution of $0.05cm^{-1}$ is being proposed. The currently flying Global Ozone Monitoring Experiment (GOME) has an A-band interferometer with a resolution of 5 cm^{-1}.

As Fig 3.4 shows, the instrument resolution has a profound effect on the structure of the observed spectra. As the instrument spectral resolution decreases, the maximum channel opacity also decreases. Fig 3.5 shows the variation of the maximum channel oxygen optical depth $\tau^*_{o_2}$ as a function of the spectral resolution of the channels in the A-band. As Fig 3.5 shows, the maximum value of $\tau^*_{o_2}$ of an instrument rapidly decreases with decreasing spectral resolution. To attenuate the effects of the underlying surface, a channel must have a value of τ^*_{o2} of at least 2 which occurs for instruments with spectral resolutions greater than approximately $1cm^{-1}$. As Fig 3.5 shows, the resolutions of past A-band instruments are unable to eliminate the effects of reflecting surfaces and would difficulty in separating the effects of atmospheric from surface scatter - a capability crucial to retrieval of optical properties from clouds and aerosol from A-band reflectance spectra.

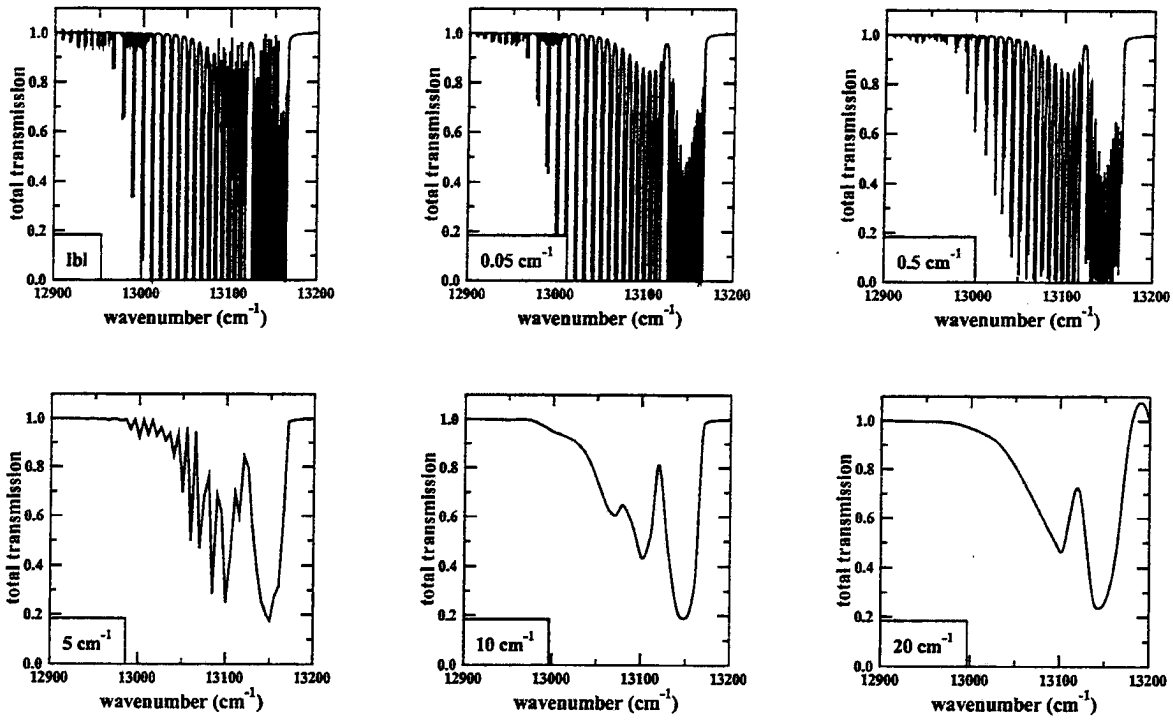

Figure 3.4: Variation of total column transmission for various channel resolutions.

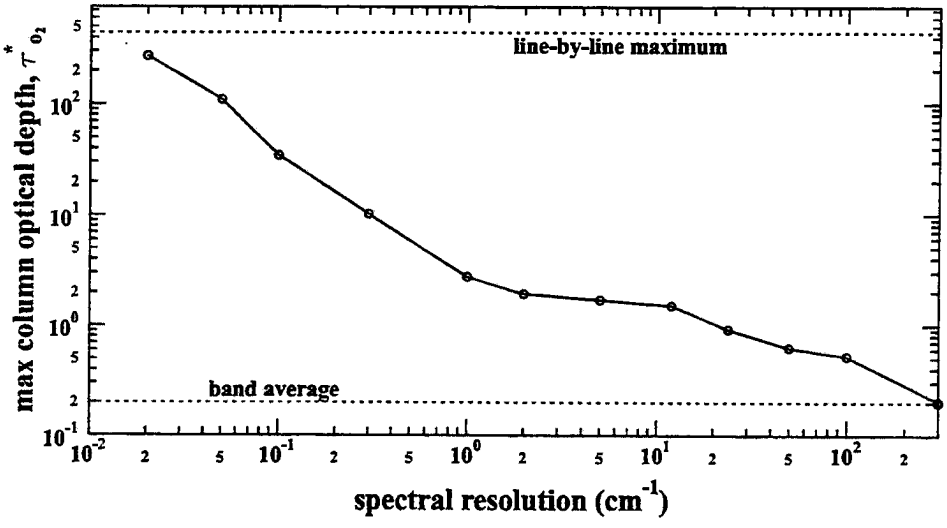

Figure 3.5: Variation of maximum channel oxygen optical depth as a function of channel spectral resolution

3.4 Approximation of Gaseous Absorption within the O_2 A-band

As described above, a line by line (lbl) radiative transfer model was written to explore the absorption properties of the A-band. The computational effort in generating the lbl radiance values is intensive. Retrievals require a much more computational efficient means of accounting for the spectral variation of the gaseous absorption. Currently, the most popular method of accounting for the variation of gaseous absorption in an instrument channel is the correlated-k method (Lacis and Oinas, 1989). The method involves reordering the k values in an instrument channel to replace the frequency integration with an integration over k or some function of k. While this method would most likely be used in an operational retrieval, the generation of the correlated-k data from lbl calculations is also computationally intensive and is specific to the channel resolution and response function. Since this study is theoretical in nature study and no applicable space-borne A-band radiometer exists, a simple approximation to model the gaseous absorption in the A-band is employed at this time.

The approximation starts with the assumption of a Lorentz line shape. The mass absorption coefficient thus becomes

$$k(p,\nu) = \frac{S}{\pi} \frac{\alpha_o \frac{p}{p_o}}{(\nu - \nu_o)^2 + (\alpha_o \frac{p}{p_o})^2} \tag{3.4}$$

where α_o is the line half-width at the reference pressure, p_o. In this formulation, we have ignored the effect of temperate on the half-width. If the absorption in the line wings is assumed to be dominant relative to the absorption in the line centers, the expression for k can be simplified to

$$k(p,\nu) = \frac{S}{\pi} \frac{\alpha_o \frac{p}{p_o}}{(\nu - \nu_o)^2} \tag{3.5}$$

While this assumption of the dominance of line wing absorption seems severe, the largest contribution to reflected radiance will be greatest from the radiance in the weaker parts of the spectrum since the radiance in the line centers is effectively extinguished.

In general, the optical depth measured from the top of the atmosphere,($p = 0$, to the pressure level p is given by

$$\tau_{o_2}(0,p) = \int_p^0 \frac{\tau k(p,\nu) dp}{g}$$

where r is the gas mixing ratio. In the case of a uniformally mixed gas such as oxygen, the value of τ_{o_2} can be expressed as

$$\tau_{o_2}(0,p) = \frac{Sr\alpha_o}{2\pi g(\nu-\nu_o)^2 p_o} p^2 = \tau^*_{o_2} p^2 \tag{3.6}$$

Therefore, the optical depth for any layer in the atmosphere is a function solely of the column oxygen optical depth, $\tau^*_{o_2}$ and the pressure levels which surround the layer.

The above line wing approximation will be used to represent the gaseous A-band absorption. As was shown, by Fig 3.5, the maximum value of $\tau^*_{o_2}$ is a function of the instrument resolution. To simplify the analysis of the A-band spectra, the spectra will be reordered with respect to $\tau^*_{o_2}$. For example, Fig 3.6 shows an A-band nadir radiance simulation for a cloud with an optical depth of 10 placed between 800 and 900 mb in a mid-latitude summer atmosphere over a surface with an albedo of 0.15. The spectra was generated from rigorous lbl calculations and integrated spectrally to give a resolution of 0.5 cm^{-1}. When the spectra are reordered with respect to $\tau^*_{o_2}$, Fig 2.7b results. Note that the spectra shown this way are analogous to the growth of a single absorption line. Also shown in Fig 3.6b is the resulting spectrum using the line wing approximation given above. As this figure illustrates, the line wing approximation very accurately reproduces the variation of the lbl data with $\tau^*_{o_2}$. Differences exist with the lbl points straddling the smooth curve predicted by (3.6). These differences occur because any given values of $\tau^* o_2$ may be comprised of different numbers and strengths of lines which will results in differing vertical distribution of the gaseous absorption.

3.5 Variation of Optical Properties within the A-band

Throughout this paper, optical properties of clouds and aerosol and surface properties will be retrieved from simulated A-band spectra. These retrieved values however will only be strictly valid for the spectral region containing the A-band. For example, cloud parameterizations in numerical weather models often desire properties referenced to 0.55μm. In this section, we explore the variation of both optical and surface properties in the entire spectral region from 0.2 to 1.0 μm to demonstrate that properties measured in the A-band do in fact represent properties at visible and near-infrared wavelengths.

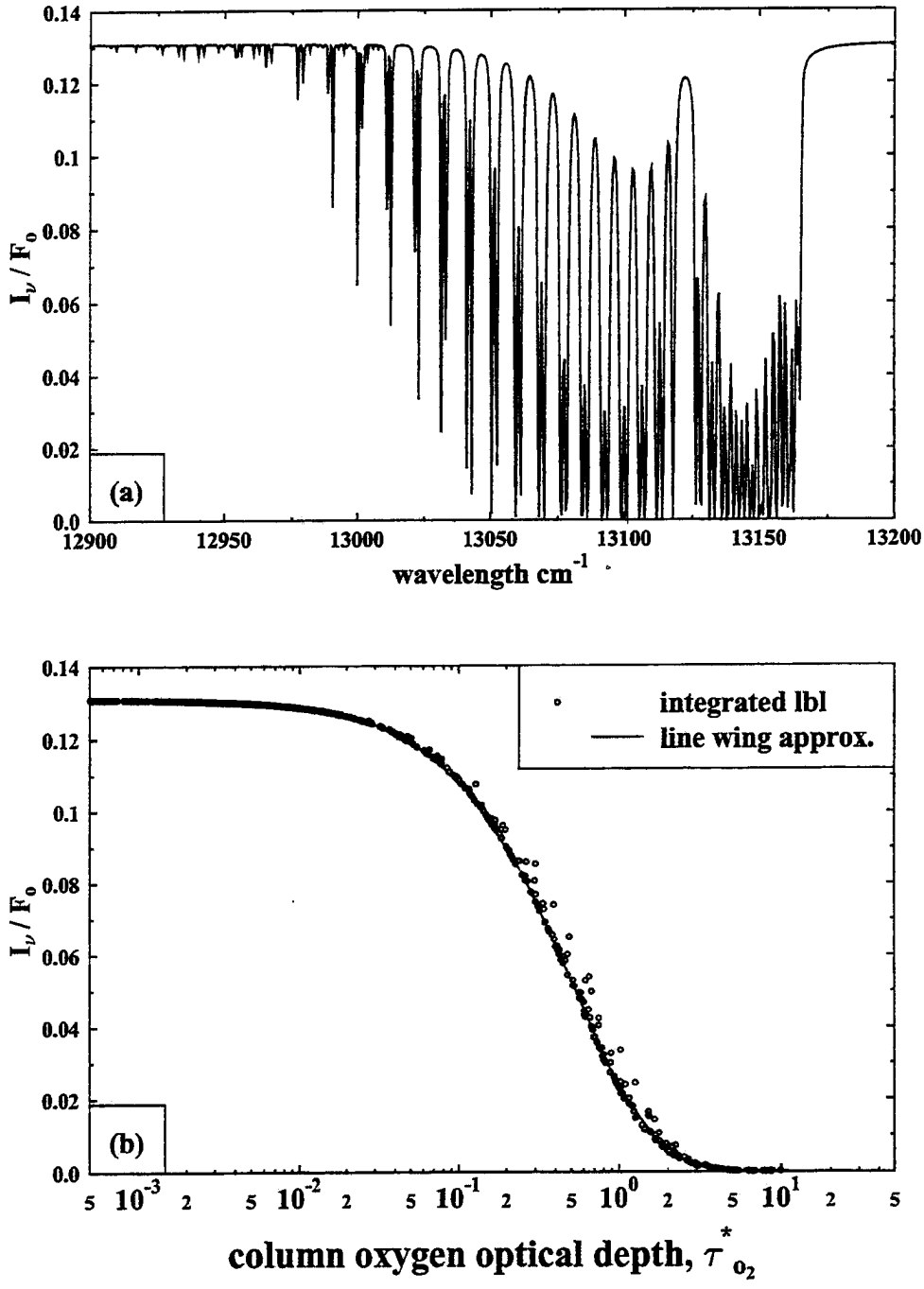

Figure 3.6: Top figure shows a simulated A-band reflectance spectrum for a scene with a thick low cloud. Bottom figure shows same results reorder with respect to $\tau^*_{o_2}$. The dots are the values using (3.6).

To explore the variation in cloud optical properties, the Mie scattering code from Bohren and Huffman(1983) was used. Using the index of refraction data from Wiscombe and Warren(1980), the Mie code was used to generate the variation with wavelength, λ and with particle radius, r, of Q_{ext} and Q_{sca} which represent the extinction and scattering efficiency factors. To compute the actual spectral variation of optical properties of clouds requires the integration of efficiency factors over the particle size distribution. To model the size distribution, we chose a modified gamma distribution of the form

$$n(r) = \frac{N_o}{r_n \Gamma(a)} \left(\frac{r}{r_n}\right)^{a-1} e^{-\frac{r}{r_n}} \tag{3.7}$$

were N_o is the total number concentration, r_n is a radius which characterizes the distribution and α is related to the variance of the distribution. Having assumed a size distribution, the volume extinction, σ_{ext} and volume scattering coefficients can be computed by

$$\sigma_{ext} = \int_0^\infty \pi r^2 n(r) Q_{ext}(r) dr$$

$$\sigma_{sca} = \int_0^\infty \pi r^2 n(r) Q_{sca}(r) dr$$

. The particle single scattering phase function is also computed by integrating over the size distribution as

$$P(\theta) = \frac{\pi}{\sigma_{sca}} \int_0^{infty} Q_{sca}(r) P(r,\theta) n(r) r^2 dr \tag{3.8}$$

. The desired single scatter albedo, ω_o and the asymmetry parameter follow from these quantities

$$\omega_o = \frac{\sigma_{sca}}{\sigma_{ext}} \tag{3.9}$$

$$g = \frac{1}{2} \int_0^\pi P(\theta) \cos(\theta) d\theta \tag{3.10}$$

.

Fig 3.7c-d shows the spectral variation of th optical properties ($\sigma_{ext}, \omega_o, g$) for three representative size distribution shown in Fig 3.7a. The parameters of the gamma distribution (r_n, α) used in (3.1) were computed from published values of the liquid or ice water path, total concentration, and mode radius. Three distributions were chosen to roughly

represent typical boundary layer clouds, cirrus clouds and boundary layer aerosol layers. The controlling parameters of the distribution are given in Table 1. The stratocumulus cloud was mad to approximate the stratocumulus I cloud given by Stephens (1979) and the cirrus cloud parameters approximate cirrus measurements presented in Stackhouse and Stephens(1991). The cirrus properties were computed using equivalent area ice spheres. The realistic treatment of non-spherical ice particles is a current area of research and is beyond the scope of this paper.

cloud type	N_o	lwc	r_d	r_n	α
stratocumulus	350	0.14	3.5	0.55	7.4
cirrus	0.1	0.012	6.0	13.75	1.4

Two points relevant to remote sensing of cloud properties in the A-band can be deduced from Fig 3.7. First, if the simulated clouds can be considered representative of all clouds, then properties retrieved using A-band measurements are roughly valid for the entire visible spectrum. In Figs 3.7b-d, the the spectral region of the A-band is highlighted. For each type of distribution, both σ_{ext} and g are relatively spectrally flat from 0.2 to 0.8 μm. In addition, since the A-band is not influenced by the water absorption features, the value of ω_o in this region is virtually unity as it is for the entire visible spectrum. Another point made by Fig 3.7 is that properties in the A-band can be assumed to be constant across the entire band. This assumption will be made throughout the course of this thesis.

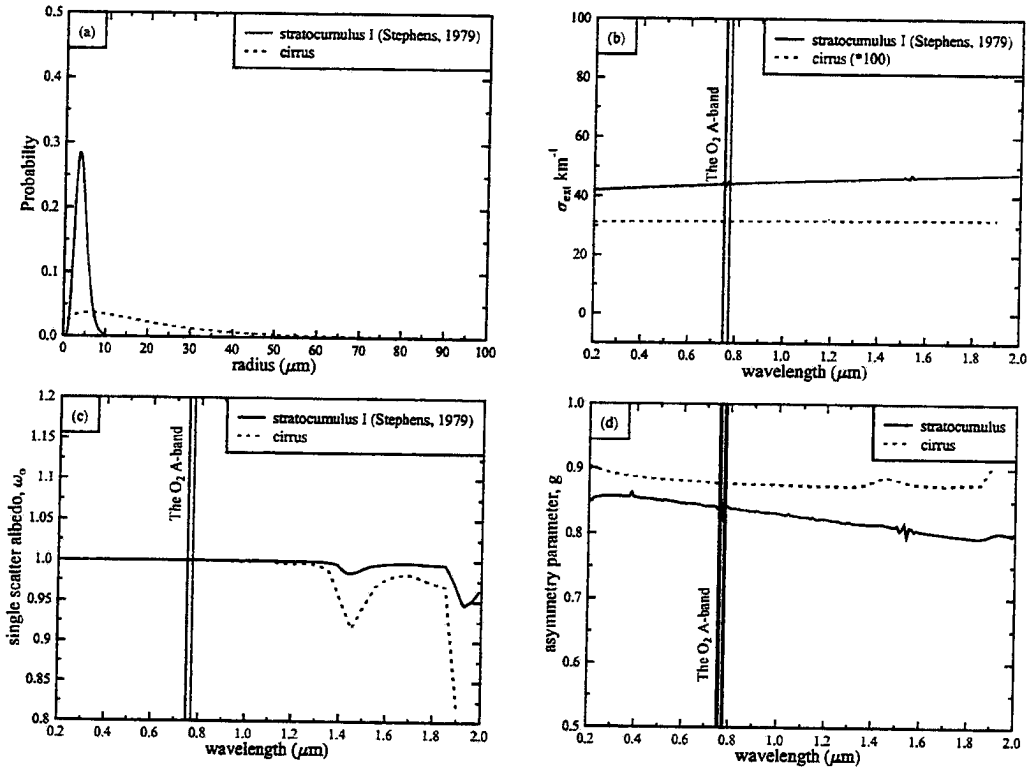

Figure 3.7: Spectral variation of optical properties for modelled stratocumulus and cirrus simulations.

Chapter 4

Retrieval Theory

In this chapter, the retrieval theory to be used throughout the remainder of this paper is reviewed. The retrieval approach, based on the optimal estimation approach of Rodgers (1976), was originally developed for use in the retrieval of profiles of temperature, water vapor and other gaseous concentration profiles. (Marks and Rodgers, (1993), Fishbein *et al* (1995), Rodgers(1990). This retrieval approach was chosen due its ability to self-diagnose the validity of the retrieval by inherently estimating the retrieval errors and the contribution to the errors of the *a priori* constraints. This was deemed to be important owing to the general lack of error analysis or quality assessment of existing cloud and aerosol retrieval methods.

4.1 The Optimal Estimation Approach

This retrieval approach begins by introducing a scalar cost function, Φ, of the form

$$\Phi = (\tilde{x} - x_a)^T S_a^{-1} (\tilde{x} - x_a) + (y - f(\tilde{x}))^T S_y^{-1} (y - f(\tilde{x})).$$

As with traditional retrieval methods, the cost function above contains a term involving the difference between the vector of measurements, y, and the vector of modeled measurements, f. Using the technique of Rodgers, the cost function also has a contribution from the difference in the retrieved parameter vector, $\tilde{x}$ and the *a priori* parameter vector, x_a. Each term in the cost function is weighted by its corresponding error covariance matrix. The matrix S_a corresponds to the errors associated with x_a and the matrix S_y contains the error estimates of both the measurements and the ability to model those measurements.

As will be shown later, the addition of the *a priori* constraint on the retrieval greatly stabilizes the retrieval of cloud and aerosol optical properties.

From the above cost function, we can define the value of $\tilde{x}$ which produces the minimum cost as

$$\tilde{x} = x_a + S_a K^T S_y^{-1}(y - f(\tilde{x})) \tag{4.1}$$

where K is the kernel matrix defined as

$$K = \frac{\partial f}{\partial x}$$

An iterative approach must be used to solve (4.1) for $\tilde{x}$, the optimal vector of parameters. As done in Marks and Rodgers(1993), for the $i+1$ iteration, we can use a Newtonian iteration approach and estimate the next value of f by assuming a linear variation from the previous value and that K remains constant from x^i to x^{i+1}. Thus

$$f(x^{i+1}) = f(x^i) + K^i(x^{i+1} - x^i) \tag{4.2}$$

With this assumption, the incremental change in the parameter vector, $\delta x^{i+1} = x^{i+1} - x^i$, can be expressed as

$$\delta x = \frac{K^T S_y^{-1}(y - f^i) + S_a^{-1}(x_a - x^i)}{S_x^{-1}} \tag{4.3}$$

where the covariance matrix of the estimated parameter vector is given by

$$S_x^{-1} = S_a^{-1} + K^T S_y^{-1} K \tag{4.4}$$

The diagonal elements of S_x give the estimated errors of the retrieved parameters while the off-diagonal elements give the correlations between parameter errors. From (4.4), it can be seen that S_x is only meaningful if the error estimates used in forming S_a andS_y physically represent the actual values for the particular retrieval scenario. In addition, by introducing the matrix

$$A = \frac{K^{i,T} S_y^{-1} K^i}{S_x^{-1}} \tag{4.5}$$

(4.3) can be written as

$$\delta x^{i+1} = \mathcal{A} K^{-1}(y - f^i) + (I - \mathcal{A})(x_a - x^i). \tag{4.6}$$

The matrix $\mathcal{A}$ is termed the model resolution matrix, (e.g. Menke,1994) or the averaging kernel matrix (Rodgers, 1990). The elements of $\mathcal{A}$ represent the response of the retrieval to perturbation in each parameter. An ideal observing system would be characterized by an identity matrix for $\mathcal{A}$.

In the retrieval of gaseous profiles, the elements of of $\mathcal{A}$ represent the changes in retrieval values at a level due to changes in the values at other atmospheric levels. In this scenario, $\mathcal{A}$ defines the vertical resolution of the retrieval. In the cloud/aerosol retrievals performed here, $\mathcal{A}$ defines the parameter resolution of the observing system. For example, Fig 5.1 shows $\mathcal{A}$ matrices computed for cirrus retrievals performed in Chapter 7. The cirrus had an optical depth of 1.0 and the surface had an albedo of 0.15. The $\mathcal{A}$ matrix shown on the left side was computed using a retrieval using only radiance. The values of $\mathcal{A}$ show that the retrieval is very sensitive to changes in the perturbation in p_t and α_{sfc} while this retrieval configuration has difficulty in recognizing perturbations in τ_c and to a lesser extent perturbation in g. The right panel shows the $\mathcal{A}$ matrix computed for the same retrieval scenario except that both radiances and radiance ratios were used. Comparison of the two $\mathcal{A}$ matrices shows how the inclusion of the radiance ratio information greatly increase the ability to detect changes in τ_c and changes in g.

According to (4.6), the physical effect of the matrix $\mathcal{A}$ on the actual retrievals can be seen. It represents an effective weighting of the contribution of the *a priori* estimate of the parameter vector, x_a to the next estimate of the parameter vector, x^{i+1}. For example, a value of 1.0 for $\mathcal{A}(i,j)$ signifies that the value of $x_a(i)$ had no contribution to value of $x(j)$ and the observing system in this sense is considered to be ideal. The deviation of values of $\mathcal{A}$ from 1.0 represent the contribution of the *a priori* estimates. From (5.4) it can be seen the values of A are governed by the relative confidences in the *a priori* estimates given by S_a and the measurements given by S_y. If the sensitivity of measurement to a certain parameter is low or errors in the measurements or forward model are high, elements of $\mathcal{A}$ will reflect these retrieval weaknesses and fall below unity.

The contributions to the total error covariance matrix, S_x can be decomposed in the contributions for the *a priori* constraints and the measurements and forward model. As

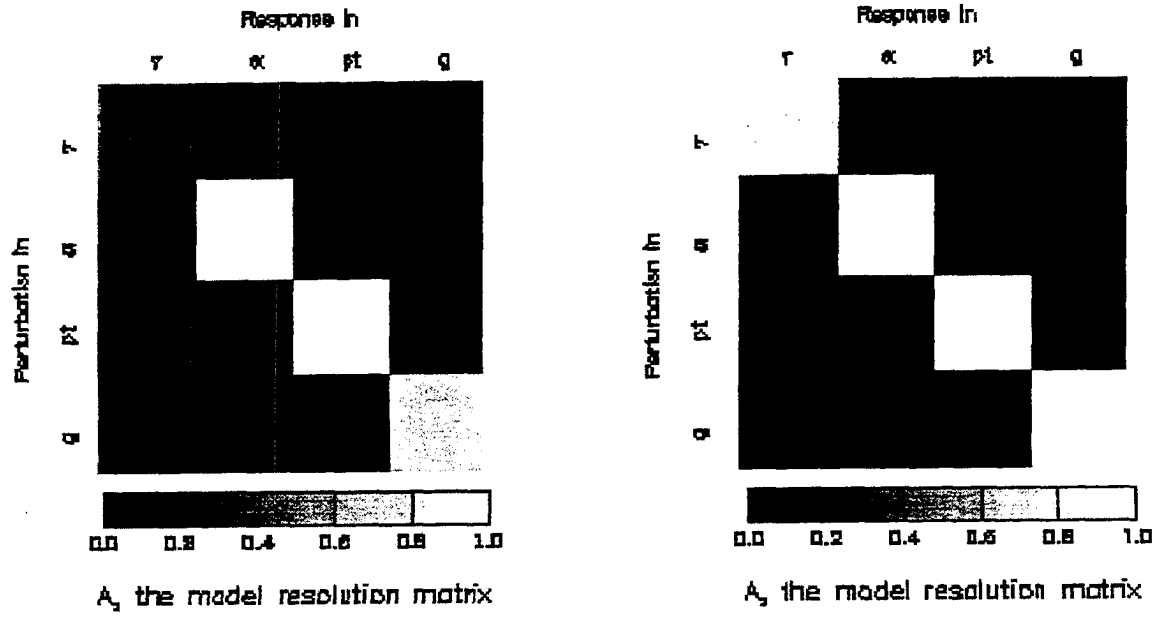

Figure 4.1: The model resolution, A, matrix for two retrieval scenarios. The left panel is for a cirrus retrieval using radiance and the right panel is the same retrieval using both radiance and radiance ratios

done in Marks and Rodgers(1993), the matrix S_x can be written as

$$S_x = D_y S_y D_y^T + D_a S_a D_a^T \tag{4.7}$$

where the first term represents the combined errors due the measurements and the forward model and the second term represents the errors due to the *a priori* constraints. The matrix D_y is called the matrix of contribution functions and can be expressed as

$$D_y = \frac{K^T S_y^{-1}}{S_x^{-1}}$$

Physically, D_y represents the response of the inverse model to changes in the retrieved parameters while D_a is the response of the inverse model to changes in the *a priori* parameters. The matrix D_a follows as $D_a = E - \mathcal{A}$ where E is the identity matrix (Marks and Rodgers, 1993).

The above iteration is continued until some level of convergence has been achieved. The level of convergence can be defined by the scalar ϵ which can be represented as

$$\epsilon = (\delta x)^T S_x^{-1} \delta x. \tag{4.8}$$

As suggested by Marks and Rodgers(1993), an appropriate convergence criterion is given by

$$\epsilon << n_x$$

where n_x is the number elements in the parameter vector. For this study, we will assume convergence when $\epsilon < \frac{n_x}{10}$.

An estimate of the errors of the retrieved parameters, ϵ_x, can be obtained by

$$\epsilon_x = \frac{\sqrt{S_x}}{x}. \tag{4.9}$$

In summary, the two diagnostic products that provide a measure of the goodness of any retrieval are the estimated errors in the retrieved parameters, ϵ_x, and the matrix $\mathcal{A}$, which represents the relative contribution of the measurements compared to the *a priori* constraints. Quality of the retrieval results shown in Chapters 6-8 will therefore be measured by these two quantities. As mentioned earlier, the error estimates produced by the retrieval are only meaningful if the error estimates used in constructing S_y and S_a are themselves meaningful. The remainder of this chapter deals with the estimation of the various errors sources required by the retrievals introduced in chapters 6-8.

4.2 Error Sources

As we have seen in the above description of the retrieval method, the ability to estimate the sources of errors accurately is crucial since these errors ultimately drive the retrieval. For instance, if the errors in the *a priori* estimates are too small, the retrieval may be over-constrained by the values of the *a priori* guesses. If the estimated measurement or forward models are incorrect, the retrieval may place inappropriate weight on either the measurements or the *a priori* estimates and retrieve physically impossible parameters. In addition, a fundamental product of this retrieval is estimate of the errors as defined by (4.9) and this estimate is meaningful only if the error covariance matrices S_a and S_y can be determined to some level of accuracy(so that that are at least physically reasonable). In this section, we describe the estimation of the individual sources or error which can be grouped in three categories, measurement, forward model and *a priori* parameter errors.

As will be described later, the forward model error is comprised of several components and assigning magnitudes to these errors presents a challenge.

4.2.1 Measurement Error

In this section we describe how an estimation of the measurement error is made. Any measurement, y can be expressed as

$$y = cv + \delta cv + c\delta v = y_{true} + \epsilon_{cal} + \epsilon_{shot}$$

where v is the raw measurement from the instrument, ie a voltage, and c is the true calibration coefficient. The noise value of y is given by the first term in the above expression the next two terms comprise the sources of error in the measurements. The first error term is the error due to calibration, ϵ_{cal} and the second is the error due to the absolute or shot noise, ϵ_{shot}.

The calibration error is typically defined in terms of a % uncertainty in the calibration coefficient, c. For example, the MODIS instrument is designed to have an absolute calibration error of 1 %. (Guenther *et al*, 1996) To account for realistic calibration errors, retrievals will be performed for a calibration error of 2% unless stated otherwise. In addition, the calibration error is assumed to be constant for all channels which is reasonable for an instrument with a single detector. Thus calibration errors cancel for radiance ratio quantities. We show below that calibration error is not a main source of error and that it could be doubled from 2 % to 4 % without any significant consequence on the retrieval of cloud properties.

As is typically done, the shot noise or absolute error in a measurement is usually quoted as a percentage of some reference value. As was done in the development of the space-borne A-band spectrometer for CloudSat, this reference signal will be the radiance reflected from a Lambertian reflecting surface with an albedo of 5%. A shot noise amount specified by a signal to noise (SNR) would signify an absolute radiance error, ϵ_y of

$$\epsilon_y = \tau \frac{0.05}{\pi} \frac{F_o}{SNR}$$

where r is a random number which varies uniformly from -1.0 to 1.0 and F_o is the solar intensity in A-band region.

In the calculation of the error covariance matrices, S_y, we will make the reasonable assumption that the errors in a particular channel are uncorrelated with the errors in surrounding channels. With this assumption, the off-diagonal terms of S_y are set to zero. As described earlier, the two measurements from A-band spectra are the spectral radiances, I_ν and the spectral radiance ratios, s_ν. The values of S_y, the measurement error covariance matrices will have different forms for each type of measurement. For I_ν, the diagonal terms of measurement error covariance matrix is given by

$$S_y(i,i) = (\epsilon^2_{cal}(i) + \epsilon^2_{shot})$$

For s_ν, the calibration errors disappear if we assume that $I_c >> \epsilon_{shot}$, where I_c is the continuum A-band radiance, the measurement covariance matrix for s_ν is given by

$$S_y(i,i) = \left(\frac{\epsilon_{shot}}{I_c}\right)^2.$$

Note the diagonal term of S_y for s_ν are independent of the frequency or the the value of $\tau^*_{o_2}$.

4.2.2 Forward Model Error

In this section, we describe the error source associated with the forward model used to perform the retrievals. As will be shown later, these errors are typically the largest of any errors and therefore have the largest effect upon the retrieval. As done in Marks and Rodgers(1994), the forward model error can be included with the instrument as

$$S_{\bar{y}} = S_y + S_f$$

where S_y is the error covariance matrix for the measurement error described above and S_f is the error covariance matrix for the forward model errors. We can consider the forward model error to be comprised of the following components:

1. errors due to the discretization of the radiance field into a finite number of angles

2. errors of the discretization of vertical variation of the cloud and gas extinction profiles

3. the deviation of the actual particle single scattering phase function from the form used in the forward model

4. the inability of the forward model to account for horizontal variability

5. uncertainties in the line parameters used to simulate A-band spectra

6. errors in model parameters that are not retrieved

We now discuss the estimation of magnitude of each of the above error sources.

The most easily identifiable error sources in the above list are the first two since the forward model itself can be used to estimate them. Both of these error sources can be eliminated by increasing the resolution, angular or vertical, of the forward model. This might not be practical for an operational application of the retrieval method. These errors can be computed by comparing the forward model results for some set number of angular streams and vertical layers to forward model runs with a sufficient number of angular streams and vertical layers to make these error sources negligible. As described in the last chapter, the standard forward model used in this paper is a three layer model, with scattering properties being retrieved in only the second or third layers and the first and topmost layer being comprised solely of oxygen absorption. To resolve the vertical variation of the O_2 absorption with pressure, each of these main layers is divided into sub-layers. The number of streams used in the forward model refers to the number of quadrature points used to represent the total upward and downward radiance fields. Fig. 5.2 shows the effect of the number of sub-layers and the number of streams on the nadir reflected radiance for a simulation consisting a cirrus cloud positioned from 300-400 mb over a surface with an albedo of 5%. A low surface albedo was chosen since the effect of a bright surface generally reduces the errors due to angular approximations. The two panels in Fig 5.2 correspond to simulations performed for a double Henyey-Greenstein (dHG) phase function and for a phase function computed from ray-tracing for hexagonal crystals. The results for the dHG phase function show that the angular errors dominate

for low numbers of streams but at high numbers of streams, the vertical discretization error becomes the dominant error source. From this result, a simulation using 32 streams and 4 sub-layers in each model layer should give radiances accurate to within 1 %. The results for the hexagonal crystal phase function show a much more marked dependence on the number of streams. Unlike the smooth HG phase functions, the angular structure of the hexagonal crystal phase function requires more terms for accurate simulation. From these simulations, it appears using 32 streams gives only a 2-5% accuracy level. This phase function represents a worse case scenario since clouds are typically comprised of a broad distribution of particles which tends to smooth out the structure of the phase function (Macke *et al*, 1997). From simulations such as this, we propose that a forward model which simulates 16 streams and divides each layer into 4 sub-layers should reduce the first two errors listed above to within 2%. Of course, greater numerical accuracy could be achieved at the expense of additional computational time, but such accuracy is unwarranted considering the magnitudes of the other errors sources to be described.

The next error source, the error due to modeling single scattering phase functions, can also be estimated from forward model simulations directly. The precise nature of this error depends on the retrieval scenario. For example, the error due to phase function uncertainties is largest for cirrus clouds due to the variation in ice crystal shapes and sizes. For clouds composed of water droplets or aerosol layers, the phase functions are better known. For optically thick clouds, the actual shape of the phase functions becomes less important since the radiative transfer is governed mainly by the asymmetry parameter of the phase function, g. Quantification of this error will therefore left until later when different retrieval scenarios are explored in Chapters 6-8. These results will show that this error source can dominate the retrieval of cloud and aerosol properties.

4.2.3 Errors due to uncertainties in the line parameters used in A-band retrievals

This error is comprised of two components. The first component being the actual uncertainty in the molecular database used to compute the A-band transmission for the individual channels. With the recent release the HITRAN96 database, we propose these

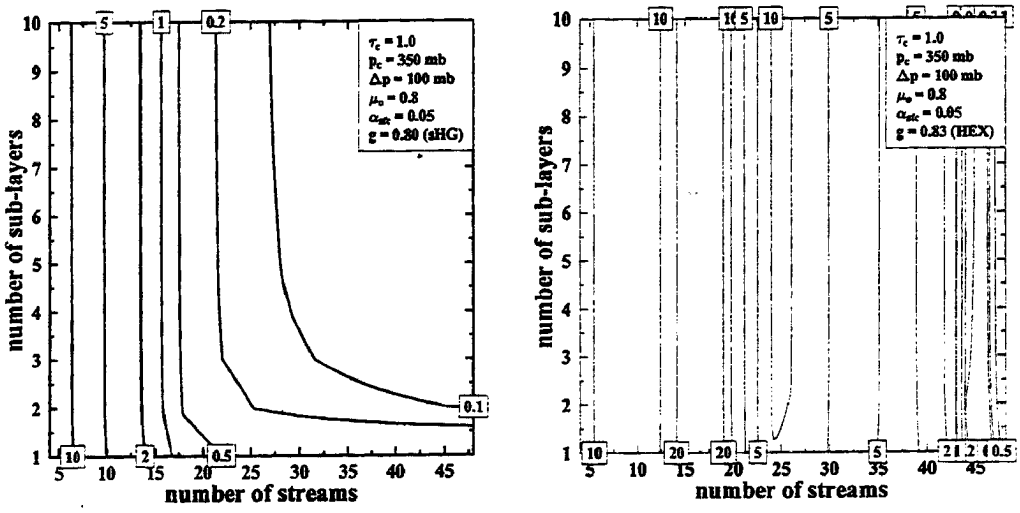

Figure 4.2: Map of radiance errors of a low cloud simulation with $\tau^*_{o_2} = 1.0$. The left panel is for a double HG phase function and the left panel is for hexagonal ice crystal phase function

errors are probably well below 1 % and will be ignored in this study. Another component of this error is the error in the A-band transmission due to method of integrated the line-by-line values to the particular channel resolution. For example, the work of Kratz(1996) quotes errors of 0.2 % in channel radiance using the correlated-k method. For this study we will conservatively assume that the errors in the A-band spectra are below to with 0.5 % due the uncertainties in the line parameters and due to the spectral integration.

4.2.4 Errors due to model parameters not retrieved

In addition to the retrieved parameters, other parameters also effect the forward model but can not or are chosen not to be retrieved. Following Rodgers(1990) we will call these model parameters and denote them by the vector b. For A-band and any visible - near ir retrieval, the largest components of this error are due to the phase function and three dimensional effects. As will be shown later, A-band retrievals allows inferences to be made both about the phase function and the degree of spatial heterogeneity. Using the A-band for retrievals offers benefits to the reduction of both of these error components.

4.2.5 *A Priori* Error Estimation

In temperature or water vapor profile remote sensing, the ability to make meaningful *a priori* estimates is possible due to both the continuous nature of the profiles and the existence of climatological and numerical model sources of data. Such data sources for cloud properties do not exist. While the International Satellite Cloud Climatology Project (ISCCP) provides monthly estimates of cloud amount for three different atmospheric layer (Rossow nd Schiffer 1982), no climatology on cloud position and optical depth is available. Clearly, of the list of desired optical properties to be retrieved, the bounds of possible values can be deduced from physical reasoning or other data sources. For example, the single scatter albedo of clouds at A-band wavelengths is known to be very close to unity while for aerosol, it varies with aerosol composition. Similarly, the asymmetry parameter is known to vary generally between 0.7 and 0.9 for most all cloud particles at visible and near-ir wavelengths. Though the surface albedo can vary from as low as 2% for calm oceans to as high as 80% for freshly fallen snow, a meaningful *a priori* guess of its value can be

made from the seasonal and geographic variation. The most difficult parameters to assign *a priori* values to are the cloud pressure and cloud optical depth. As will be shown in the next chapter, the sensitivity of A-band spectra to cloud top pressure is so strong, that the influence of the *a priori* guess is negligible for almost all retrieval scenarios. In the following paragraphs, we will use physical arguments to select *a priori* parameters and their uncertainties.

Estimation of *a priori* optical depth

The most difficult *a priori* parameter to estimate is the optical depth. Unlike the temperature or water vapor content of a layer, the cloud or aerosol optical depth can vary greatly over small temporal and spatial scales. For example, the horizontal optical depth often follow a log normal distribution spanning several decades (Barker, 1996). To make a meaningful estimate of the *a priori* value of optical depth a simple one channel type retrieval is used. Similar to the commonly used technique of matching a visible reflectance to an equivalent plane parallel optical depth, the continuum radiance value of the A-band could be used to make an estimate of optical depth that could suffice for the *a priori* value. As will be discussed in the next chapter, the continuum radiance is sensitive to the optical depth of the entire atmosphere as well as the surface properties for clouds of thin or moderate optical depths. Fig.4.3 shows a variation of the continuum radiance as functions of both cloud optical depth and surface albedo. Due to the lack of any gaseous absorption in the continuum, the vertical placement or geometric depth of the cloud has no influence on the radiance. Using the measured continuum radiance and the *a priori* estimate of surface albedo, the a priori value of optical depth could be obtained. To explore the errors of such an approach the simulations shown in Fig 4.3 were performed.

Fig 4.3 shows the retrieved errors in τ_c as a function of the *a priori* surface albedo assuming a true surface albedo of 0.15. As Fig 4.3 shows, the errors increase as α_{sfc} deviates from 0.15. As would be expected, the errors decrease as the τ_c increases, becoming less than 10 % for all values of $\tau_c > 10$. The largest errors, approaching 1000%, occur for $\tau_c < 0.1$ and values of $\alpha_{sfc} < 0.05$. In addition, a large region of 100 % errors occur for values of $\alpha_{sfc} > 0.15$. The errors of 100 % occur when the clear sky radiance exceeds the

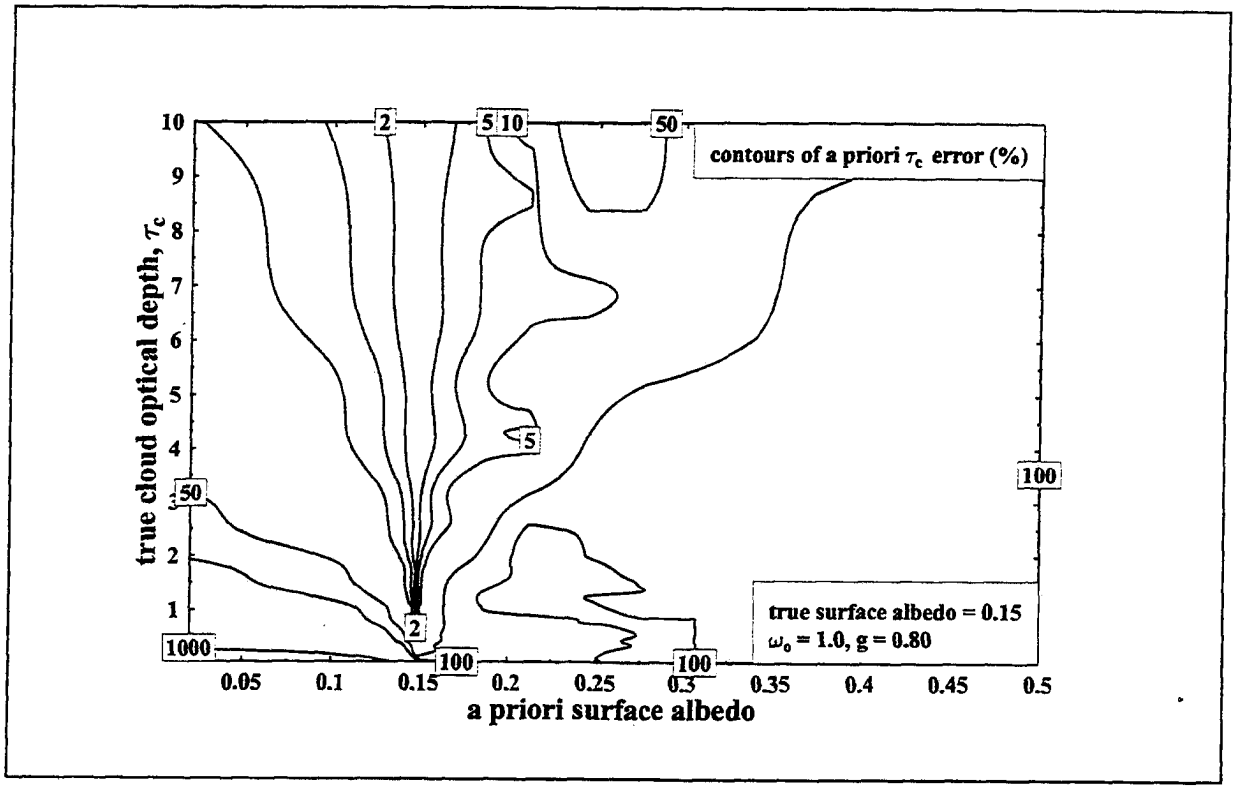

Figure 4.3: Contours of error in *a priori* estimate tau computed assuming a surface albedo of 0.15

measured radiance and the retrieval returns a value of $\tau_c = 0$. A conservative estimate of the uncertainty in the *a priori* value of τ_c produced by such a procedure is 100 %. Clearly, any meaningful *a priori* estimate of α_{sfc} would be able to greatly reduce the true uncertainty of the *a priori* value of τ_c to be below 100 %.

Estimation of *a priori* cloud top pressure

Since the growth of absorption lines to the first order is governed by the pressure of the scatters, cloud top pressure is probably the most easily retrieved quantity from A-band spectra. Due to the high sensitivity of A-band measurements to the cloud top pressure, the need for an accurate *a priori* estimation of pressure is not required. This qualitative assessment can be confirmed by the magnitude of $\mathcal{A}$, the *a priori* contribution matrix. Having computed the *a priori* estimate of τ_c using the procedure described above, this information could conceivably be used as a basis for the initial guess of p_c. However this approach is unnecessary for the reason described above and a constant value of 500 mb will

be assumed for the *a priori* value of p_c unless stated otherwise. Since cloud top pressure generally range from 200 to 900 mb, we will roughly assume an uncertainty of 100 % for the *a priori* estimate of p_c.

Estimation of *a priori* single scatter albedo and asymmetry parameter

Unlike the variation of τ_c and p_c, the range of possible values of the scattering properties clouds are known to fall within specific limits. For example, the single scatter albedo at A-band wavelengths is known to very close to unity (conservative scatter). We will therefore assume an *a priori* value of 1.0 for $\omega_{o,c}$ for all cloud retrievals and not even attempt to retrieve the value. For aerosol layers, the values of $\omega_{o,c}$ range from 0.7 to 1.0 depending on aerosol composition. We will therefore assume a value of 0.9 in the aerosol retrievals and assume an uncertainty of 10 %.

As described above, the variation of the phase function is one of the major sources of uncertainty in cirrus clouds retrievals. Previous work has shown that for thick water clouds, composed of spherical water droplets, the asymmetry parameter, g, which does not vary significantly from 0.85. In fact for water clouds, we will choose to not even retrieve the asymmetry parameter. From numerical simulation and laboratory measurements, the value of g for cirrus clouds is known to range from 0.7 to 0.9 depending on the sizes and shapes of the ice crystals. For cirrus retrievals, we will assume an *a priori* value of g to be 0.8 with an uncertainty of 10 %. Due to the smaller size of aerosol particle, the scattering is more isotropic and the values of g range from 0.5 to 0.7(?). For aerosol retrievals, we will therefore assume a value of 0.6 and an uncertainty of 10 %.

The Estimation of the *a priori* surface albedo

Like the *a priori* estimation of cloud top pressure, the sensitivity analysis in the next chapter will show that A-band reflectance spectra are very sensitive to surface albedo. Accordingly, an accurate estimation of the uncertainty of the *a priori* estimate of α_{sfc} is as critical. The global range of surface albedoes ranges from 2 % for a calm ocean to over 50 % for a snow covered surface. Since the ocean covers the majority of the surface of the globe, a value of α_{sfc} of 5 % will be assumed. The uncertainty of this value depends on

the *a priori* knowledge of geographical position and time of year. For example, a retrieval carried out over a region known to be oceanic can prescribe α_{sfc} to within 50%. However in this study, we will assume an uncertainty of 100 % in the *a priori* estimate of α_{sfc}. This uncertainty is probably conservative due to the known variation of α_{sfc} geographically and seasonally.

4.2.6 Effect of *A Priori* Data on Retrievals

Having just described the process of making estimates *a priori* values and uncertainties of the properties to be retrieved, we now illustrate the benefits of using *a priori* data in the retrieval. As a simple illustration, imagine a retrieval of optical depth using one channel which has little gaseous absorption such as the continuum channels in the A-band. In this example, the true optical depth is 1.0 and the *a priori* estimate of the optical depth was taken to be 2.0. Figure 4.5 shows simulated retrievals of τ_c as a function of the signal to noise ratio. As described above, the signal to noise ratio represents the level of absolute uncertainty of the measurements. The errors arising from improper *a priori* estimates of other properties are ignored in this simple example. The filled circles in Fig 4.5 show the results for values of 100% uncertainty in the *a priori* estimate of τ_c, which will be assumed for most of the retrievals in this study. Also shown, in Fig.4.5, as the open circles, are the results for assuming a 1000% uncertainty in the *a priori* values of τ_c. The results in Fig 4.5 clearly show the effect of the *a priori* estimate in the retrieval. For the 100 % uncertainty case, low values of SNR result in the retrieval returning the *a priori* value as the retrieved value. The physical explanation for this is that the error in the measurements does not justify a deviation from the *a priori* measurements. This lack of influence of the measurements in the retrieval is shown in the values of $\mathcal{A}$ which are significantly below 1.0 for low values of SNR. These results can be contrasted to the 1000 % uncertainty case. Due the higher uncertainty in the *a priori* estimates, the retrieval places more weight on the measurements. Consequently, at low values of SNR, the retrieved values of τ_c are determined mainly by the instrumental noise. In addition, the values of $\mathcal{A}$ for the 1000 % case are greater due to relative greater contribution from the measurements. While a wild fluctuation in optical depth may not appear to be unphysical, a similar noise driven

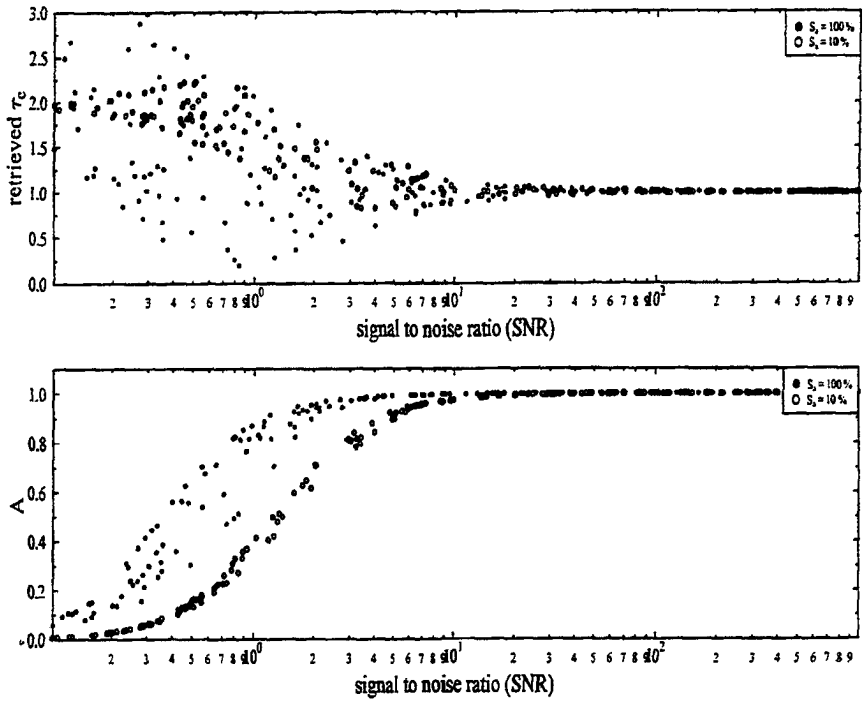

Figure 4.4: Effect of signal to noise on one channel optical depth retrievals as a function of the signal to noise.

fluctuation in other optical properties such as the asymmetry parameter would result in unreasonable solutions. The role of *a priori* data in the retrieval is therefore to act to fix a parameter to a value deemed reasonable unless the measurements are of high enough accuracy to warrant a departure.

4.3 Summary

In this chapter, the optimal estimation approach of Rodgers(1976) was set up for use as a retrieval method of cloud properties. In addition to the retrieved parameters, this technique also provides an estimate of the error of the parameters and an estimate of the reliance on the *a priori* values. These diagnostic products are only meaningful if the individual error estimates of the retrieval component have meaning. The rest of the chapter was therefore an attempt to diagnose the uncertainties in A-band measurements, in the forward model and in the *a priori* estimates. The above estimates of the errors in the measurements and *a priori* parameter estimates will be used throughout the remainder of

this thesis to attempt to make meaningful assessment of the ability of an A-band observing system to remotely sense cloud and aerosol layers.

Chapter 5

The Forward Model

In this chapter, a forward model is developed for computing radiances in the A-band at the top of the atmosphere. The forward model will then be used in later chapters in the retrieval of cloud properties from A-band measurements. In the development of the forward model, we will assume plane parallel theory is valid. A three dimensional radiative transfer was also developed and is used to study the effects of spatial variability on A-band retrievals in a later chapter. While the forward model developed here is not meant to be used in an operational mode, the model developed here does account for all the relevant physics effecting A-band spectra in a computationally efficient manner.

Current forward modeling of cloud remote sensing typically involves running a forward model and generating look-up tables which allow for the conversion of observed radiances to estimated parameters. This approach is feasible if the number of parameters is small as is the case for the optical depth and effective radiance retrieval method of Nakajima and King(1989). In this paper, A-band retrievals are being used to estimate 3-5 parameters and ability of constructing look-up tables for all scenarios becomes intractable. The use of a true forward model also allows for the computation of kernel matrices, described in the last chapter, which are required for proper error estimation. In this chapter, the development of a standard adding/doubling radiative transfer model is reviewed. The treatment of vertical variation in the adding/doubling technique is accomplished through treating continuous variation as series of homogeneous layers.

5.1 The Radiative Transfer Equation

As stated above, we have chosen to ignore the effects of horizontal heterogeneity in the forward model of A-band radiances. With this assumption, the development of a plane parallel radiative transfer model is reviewed here. In its most general sense, the change in the spectral intensity, I_ν along the path s can be written as

$$\frac{dI_\nu}{ds} = -\sigma_{ext} I_\nu + \sigma_{sca} \mathcal{J}_\nu - \sigma_{abs} \mathcal{B}_\nu$$

where σ_{ext}, σ_{sca} and σ_{abs} are the volume extinction, scattering and absorption coefficients whose units are the inverse units of the path, s. The above equation is merely an expression of an energy balance with change of intensity being the sum of the loss due to extinction and the gain due to sources. For atmospheric radiative transfer, only the source due to thermal emission, $\mathcal{B}$, and the source due to scattering of radiance into the direction defined by s, $\mathcal{J}$. Thermal emission is not relevant to A-band radiative transfer and will be ignored in the development of the model. The inclusion of the thermal source for all three modeling methods is described in Appendix D. The scattering source can be expressed as:

$$J_\nu = \int_0^{4\pi} I_{\nu,s'} \frac{P(s,s')}{4\pi} d\Omega + F_o \frac{P(s,s_\odot)}{4\pi} \tag{5.1}$$

where P is the single scattering phase function for intensity, P_{11}, and is normalized to 4π. In the above expression, the scattering source has been divided into a diffuse component and a component due to the scattering of the solar radiance, assumed to be a collimated beam pointed in the direction $s_\odot$ and with a strength F_o. With the scattering source defined by (4.1), the monochromatic radiative transfer equation can now be written as

$$\frac{dI(\tau,\xi,\phi)}{d\tau} = I(\tau,\xi,\phi) - \omega_o(\tau) \int P(\tau,\xi,\phi,\xi',\phi') I(\tau,\xi',\phi') \frac{d\Omega}{4\pi} - \sigma(\tau,\xi,\phi) \tag{5.2}$$

where ω_o is the single scattering albedo and the the vertical coordinate has been changed from geometrical distance, s, to optical distance, τ and the direction is now defined in terms of the zenith angle cosine, ξ, and the azimuth angle, ϕ. As is traditionally done in radiative transfer models, the scattering source term in (4.2) has been divided into two terms. The integral term in (4.2) represents the scattering source due to the diffuse

radiation field and the term involving σ represents to source due to the scattering of the direct solar beam.

The forward model developed here, like virtually all plane parallel radiative transfer models, employs discrete ordinates to treat the continuous radiance fields as a finite number of streams along fixed ordinates or angles. As will shown here, the treatment of the radiance field as finite number of streams allows for derivation of a set of un-coupled integrodifferential equations which are easily solved. This section briefly reviews the development of plane parallel radiative transfer models since details of this problem can be found in numerous references(Goody and Yung (1994), Hansen(1974), Twomey *et al* (1966) and others). The derivation of discrete ordinates model begins with approximating the phase function as a expansion of Legendre polynomials.

$$P(\cos\Theta) = \sum_{n=0}^{N} \chi_l P_l(\cos\Theta)$$

where χ_l is the expansion coefficient for the l^{th} Legend-re polynomial, P_l. Using the addition theorem of spherical harmonics, the Legendre Polynomials can be expanded in terms of Fourier series.

$$P(\tau,\xi,\phi,\xi',\phi') = \sum_{m=0}^{N} P^m(\tau,\xi,\phi,\xi',\phi')\cos m(\phi-\phi')$$

where

$$P^m(\tau,\xi,\phi,\xi',\phi') = \sum_{l=m}^{N}(2-\delta_{0,m})\chi_l\frac{(l-m)!}{(l+m)!}P_l^m(\xi)P_l^m(\xi')$$

In addition, for a plane parallel medium, the radiance and the source can also be represented by a Fourier series in cosines.

$$I(\tau,\xi,\phi) = \sum_{m=0}^{N} I^m(\tau,\xi)\cos m(\phi-\phi_o)$$

$$\sigma(\tau,\xi,\phi) = \sum_{m=0}^{N} \sigma^m(\tau,\xi)\cos m(\phi-\phi_o)$$

As described by Stephens(1988), the simulation of spatial variability necessitates the inclusion of both cosine and sine terms in the Fourier expansion. Exploiting the orthogonality

of Fourier series, allows (4.2) to written as n+1 independent equation where n is the number of azimuthal modes being simulated.

$$\xi \frac{dI^m(\tau,\xi)}{d\tau} = -I^m(\tau,\xi) + \frac{\omega_o(\tau)}{4}(1+\delta(0,m)) \int_{-1}^{1} P^m(\tau,\xi,\xi')I^m(\tau,\xi')d\xi' - \sigma(\tau,\xi) \quad (5.3)$$

The above steps have produced an equation in which the various azimuthal modes are decoupled from one another. Applying the notion of the discrete ordinates, the continuous radiance fields can be written as discrete vectors as

$$I^+ = \begin{pmatrix} I(+\xi_1) \\ \vdots \\ I(+\xi_n) \end{pmatrix} \quad I^- = \begin{pmatrix} I(-\xi_1) \\ \vdots \\ I(-\xi_n) \end{pmatrix}$$

where $\pm\xi$ are the chosen zenith directions of the radiance streams and I^+ is radiance vector for directions in the upwelling hemisphere ($0 > \xi > 1$) and I^- is the radiance vector for the downwelling hemisphere ($0 < \xi < -1$). The source terms in (4.3) can also be transformed into a discrete vector in a similar manner. Using discrete ordinates, phase matrix in (4.3) can be represented by two square matrices representing the scatter of radiation into the same hemisphere, P^{++} and representing the scatter of radiation into the opposing hemisphere, P^{+-}. By assuming that the phase function is dependent only on the scattering angle, the phase matrices for for forward and back scattering are identical for each hemisphere. With the simplification offered by a discrete ordinates representation, (4.3) can be expressed as

$$\begin{aligned} \frac{dI^+(\tau)}{d\tau} &= -M^{-1}I^{+,m} + \frac{\omega_o(\tau)}{4}(1+\delta_{0,m})M^{-1}C\left(P^{++,m}I^{+,m} + P^{+-,m}I^{-,m}\right) + M^{-1}\sigma^{+,m} \\ \frac{dI^-(\tau)}{d\tau} &= M^{-1}I^{-,m} - \frac{\omega_o(\tau)}{4}(1+\delta_{0,m})M^{-1}C\left(P^{++,m}I^{-,m} + P^{+-,m}I^{+,m}\right) - M^{-1}\sigma^{-,m} \end{aligned} \quad (5.4)$$

where M is a diagnol matrix whose elements are the values of ξ representing the direction of each stream. The matrix C is a diagnol matrix whose elements are the quadrature weights associated with each element of M. For the results in this paper, the Lobatto quadrature is used since it gives an abscissa at nadir, the desired viewing direction. Energy conservation requires the degree of expansion used in the Legendre polynomial representation of the phase function to be less than $2n-3$ where n is the total number of streams,

including both upwelling and downwelling, used in the discrete ordinates representation of the radiance (Michaels, 1962). For Gaussian quadrature, the maximum degree of the Legendre expansion is $2n-1$ (Chandrasekhar, 1960).

Using matrix notation, the discrete ordinates radiative transfer equation can be written as

$$\frac{d}{d\tau}\begin{pmatrix} I^{+,m} \\ I^{-,m} \end{pmatrix} = A^m \begin{pmatrix} I^{+,m} \\ I^{-,m} \end{pmatrix} + \begin{pmatrix} \sigma^{+,m} \\ \sigma^{-,m} \end{pmatrix} \tag{5.5}$$

where the matrix $\mathcal{A}$ is defined by

$$\mathcal{A}^m = \begin{pmatrix} -t^m & r^m \\ -r^m & t^m \end{pmatrix}$$

where the r^m and t^m are the local reflection and transmission matrices for the m^{th} azimuthal mode and can identified from (4.4) to be

$$r^m = \frac{\omega_o}{4}(1+\delta_{0,m})M^{-1}P^{+-,m}C \tag{5.6}$$

$$t^m = M^{-1}\left(I_d - (1+\delta_{0,m})\frac{\omega_o}{4}P^{++,m}C\right). \tag{5.7}$$

Since this paper deals primarily with nadir radiances, only the azimuthally symmetric terms (m=0) will be kept. In addition, Lobatto quadrature will be used since it allows for a quadrature point to be located directly at nadir, the desired viewing location.

5.2 The Adding of Multiple Layers

In the previous section, a brief derivation of the discrete ordinates radiative transfer equation was given. This expression simulates the local or microscopic interaction of matter and radiation. In this section, the large-scale or macroscopic interaction between radiation and matter is used in the form of the Interaction principle to describe how multiple layers may be added together to allow for the computation of emerging radiance field from atmospheres with multiple layers. The emerging radiance field will then serve as the product of the forward model, f, to be used in the retrieval scheme.

To begin the description of the adding method, imagine a layer bounded by on top by level $\dashv$ and on bottom by layer g. Assuming the radiances incident on each boundary (I_a^-

and I_g^+) are known, the emergent radiances can be written as

$$I_a^+ = R_{ag} I_a^- + T_{ga} I_g^+ + \Sigma_{ag}^+ \tag{5.8}$$

$$I_g^- = R_{ag} I_g^+ + T_{ag} I_a^- + \Sigma_{ag}^- \tag{5.9}$$

where $R_{ag}, R_g a, T_{ag}, T_{ga}$ are the global reflection and transmission matrices for the layer between levels a and g. The above equations are known as the interaction principle (Chandrasekhar, 1960) which states that the photons emerging from layer either originated in the layer due a source function or where reflected or transmitted photon incident on the layer boundaries. Note that in the presence of any vertical inhomogeneity, the elements of R_{ag} and T_{ag} are not equal to R_{ga} and T_{ga}. The matrices $\Sigma^{\pm}$ are the global sources for the entire layer. In general, the lowest layer will be a reflecting surface and or a emitting surface. Under these condition, the incident radiance on the lower boundary can be expressed as

$$I_g^+ = R_g I_g^- + I_{g,o}^+$$

To demonstrate the process of adding, imagine a level b placed in between levels a and g. The interaction principle can now be applied to each layer separately. To give

$$I_a^+ = R_{ab} I_a^- + T_{ba} I_b^+ + \Sigma_{ab}^+ \tag{5.10}$$

$$I_b^- = R_{ba} I_b^+ + T_{ab} I_a^- + \Sigma_{ab}^- \tag{5.11}$$

$$I_b^+ = R_{bg} I_b^- + T_{gb} I_g^+ + \Sigma_{bg}^+ \tag{5.12}$$

$$I_g^- = R_{gb} I_g^+ + T_{bg} I_b^- + \Sigma_{bg}^- \tag{5.13}$$

The radiance on the interior level b can be solved for by substituting (4.7)-(4.8) into (4.9)-(4.12) to give

$$I_b^+ = (I_d - R_{bg} R_{ba})^{-1} (R_{bg} T_{ab} I_a^- + T_{gb} I_g^+ + R_{bg} \Sigma_{ab}^- + \Sigma_{bg}^+) \tag{5.14}$$

$$I_b^- = (I_d - R_{ba} R_{bg})^{-1} (R_{ba} T_{gb} I_g^+ + T_{ab} I_a^- + R_{ba} \Sigma_{bg}^- + \Sigma_{ab}^-) \tag{5.15}$$

where I_d is the identity matrix. The above expressions for $I_b^{\pm}$ can be substituted in (4.10)-(4.11) to allow the emergent radiances from the atmosphere to expressed solely in terms

of the known incident boundary radiances and the global matrices of the two layers.

$$I_a^+ = (T_{ba}\Gamma_{bgba}T_{gb})I_b^+ + (T_{ba}\Gamma_{bgba}R_{bg}T_{ab} + R_{ab})I_a^- + T_{ba}\Gamma_{bgba}R_{bg}\Sigma_{ab}^- + \quad (5.16)$$

$$T_{ba}\Gamma_{bgba}\Sigma_{bg}^+ + \Sigma^+ ab \quad (5.17)$$

$$I_g^- = (T_{bg}\Gamma_{babg}T_{ab})I_a^+ + (T_{ab}\Gamma_{babg}R_{ba}T_{gb} + R_{gb})I_g^+ + T_{bg}\Gamma_{babg}R_{ba}\Sigma_{bg}^+ + \quad (5.18)$$

$$T_{bg}\Gamma_{babg}\Sigma_{ab}^- + \Sigma^- bg \quad (5.19)$$

where

$$\Gamma_{babg} = (I_d - R_{ba}R_{bg})^{-1} \quad (5.20)$$

$$\Gamma_{bgba} = (I_d - R_{bg}R_{ba})^{-1} \quad (5.21)$$

Each term in (4.16)-(4.17) represents the contribution to the emergent radiances from the source terms and the incident radiance vectors. The coefficient of each term account for the reflections and transmission as the photons move through the layers. Comparing (4.16)-(4.17) with the interaction principle written for the entire system, (4.7)-(4.8), reveals the following expressions for the global reflection, transmission and source terms expressed in terms of the global values for the individual layers.

$$R_{ag} = T_{ba}\Gamma_{bgba}R_{bg}T_{ab} + R_{ab} \quad (5.22)$$

$$R_{ga} = T_{bg}\Gamma_{babg}R_{ba}T_{gb} + R_{gb} \quad (5.23)$$

$$T_{ag} = T_{bg}\Gamma_{babg}T_{ab} \quad (5.24)$$

$$T_{ga} = T_{ba}\Gamma_{bgba}T_{gb} \quad (5.25)$$

$$\Sigma_{ag}^+ = T_{ba}\Gamma_{bgba}(R_{bg}\Sigma_{ab}^- + \Sigma_{bg}^+) + \Sigma_{ab}^+ \quad (5.26)$$

$$\Sigma_{ag}^- = T_{bg}\Gamma_{babg}(R_{ba}\Sigma_{bg}^+ + \Sigma_{ab}^-) + \Sigma_{bg}^- \quad (5.27)$$

5.3 The Doubling Method for the Computation of Global Reflection, Transmission and Source Matrices

The previous sections of this chapter discussed the calculation of the local transfer quantities (4.4),(4.5) and discussed means of combining the global the radiative properties of layers to generate properties of the entire atmosphere. This section describes the doubling

method which allows for the computation of the global properties of a layer knowing its local properties. Computationally, this procedure would occur before the adding procedure developed in the last section. Since doubling is just a specialized form of doubling, the adding process was described first.

The doubling method for the computation of the global matrices follows directly from the adding method. Instead of adding layers of arbitrary optical thickness the process of doubling involves the addition of layers of identical thickness until the desired optical thickness is obtained. The process of doubling begins with a layer sufficiently optically thin so that its global properties can be deduced directly from its local properties. The work of Wiscombe (1976a) explores several techniques used in initializing the doubling scheme. In this study we shall use the infinitesimal generator scheme where the global matrices for a layer of optical thickness $\Delta\tau$ can be written as

$$R_o = \frac{\omega_o}{4}(1+\delta_{0,m})I_d M^{-1} P^{+-} c\Delta\tau \tag{5.28}$$

$$T_o = I_d - M^{-1}(I_d - (1+\delta_{0,m})\frac{\omega_o}{4})P^{++}c\Delta\tau \tag{5.29}$$

$$\Sigma_o^+ = = \frac{\omega_o}{4\pi}P_\odot^- F_o(1-e^{-\Delta\tau/\mu_o})\mu_o M^{-1} \tag{5.30}$$

$$\Sigma_o^- = = \frac{\omega_o}{4\pi}P_\odot^+ F_o(1-e^{-\Delta\tau/\mu_o})\mu_o M^{-1}. \tag{5.31}$$

where the phase matrices for backward and forward scattering have be expressed as $P^{\pm}$ and P^{++}. The matrix M denotes a diagonal matrix containing the quadrature abscissa and the matrix c is a diagonal matrix containing the quadrature weights. The doubling rules for the reflection and transmission matrices are simply an extension of the adding method where the two layer being added are identical. After n doubling steps, the optical thickness of the layer will be $\tau = 2^n\Delta\tau$. The next doubling step will involve adding two layer with $\tau = 2^n\Delta\tau$ to give a new optical thickness of the layer to be $\tau = 2^{n+1}\Delta\tau$. The doubling rules for R and T are then merely specialized versions of (4.10) and can be expressed as

$$R_{n+1} = T_n\Gamma_n R_n T_n + R_n$$

$$T_{n+1} = T_n\Gamma_n T_n$$

The doubling rules for the solar source also follow from the adding rules When two identical layers are added, the solar sources in two layers are identical except that the lower layer's source terms are attenuated by the direct transmission through the top layer. With this attenuation, the doubling rules for the solar source term are

$$\begin{aligned}\Sigma^+_{n+1} &= T_n\Gamma_n(R_n\Sigma^-_n + \Sigma^+_n) + e_n\Sigma^+_n \\ \Sigma^-_{n+1} &= T_n\Gamma_n(R_n\Sigma^+_n + e_n\Sigma^-_n) + \Sigma^-_n\end{aligned}$$

where

$$e_n = e^{-\frac{2^n\Delta\tau}{\mu_o}}$$

The traditional treatment of vertical inhomogeneity in the doubling and adding approach is to break up the atmosphere into homogeneous layers and use doubling on each of the individual layers. As will be shown later, when the errors of the forward model are estimated, the strong vertical variation of A-band absorption typically requires even homogeneous cloud layers to be broken up into several sub-layers.

5.3.1 Validation of Model

The purpose of this model is simulate the radiances at the top of the atmosphere measured by a satellite. Fig. 5.1 shows a comparison of the upwelling radiance at the top of an atmosphere consisting of a cirrus cloud placed between 300 - 400 mb. The optical depth of the cloud is 1.0 and the asymmetry of its phase function is 0.85. The solar zenith angle was set to 45^o for these simulations. The upper panel shows the equivalent radiance field computed using the discrete ordinates radiative model described above. The contours of Fig 5.1 are of the upwelling radiance normalized by the incoming solar flux The lower panel shows the radiance field computed from a the Monte Carlo model described in Appendix B. The center of each figure represents the nadir view. The solar beam is incident from the right side of the Fig 5.1. Lines of constant azimuth converge at the nadir point and lines of constant zenith angle form concentric circle around the nadir point. Since the Monte Carlo approach invokes none of the approximations employed in the above discrete ordinates radiative transfer model development and the agreement between the two approaches is taken as validation of them both.

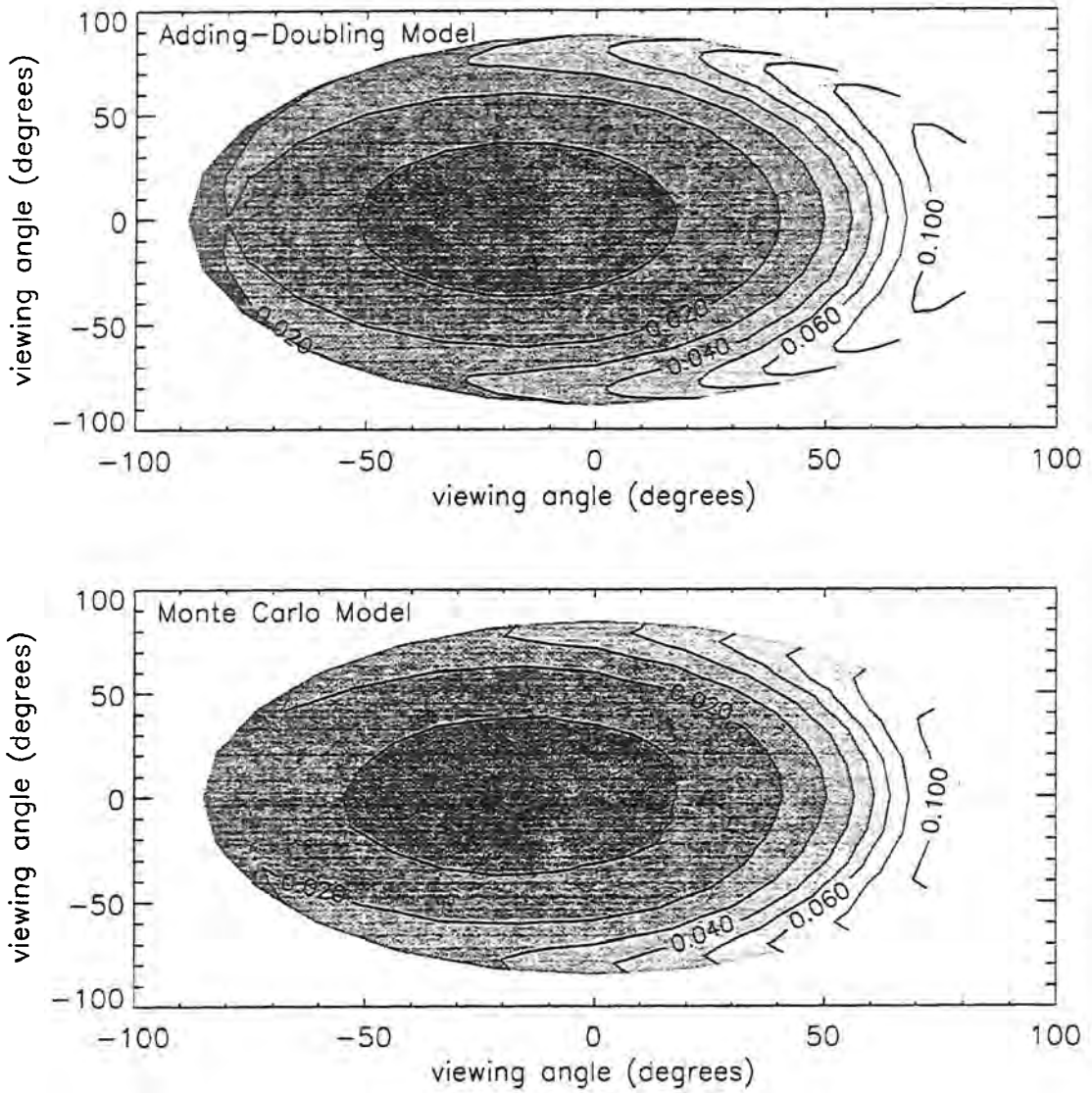

Figure 5.1: Comparison of the distribution with viewing angle of the nadir radiance at the top of an atmosphere for simulated cirrus scene.

5.4 Conclusions

This chapter discussed the development of a discrete ordinates plane parallel radiative transfer model. This model will be used in the coming chapters as the forward model for A-band radiances at the top of the atmosphere. The retrieval of optical parameters showed in Chapters 6-8 rely on this model to accurately predict the sensitivity of A-band radiances to each of the retrieved optical parameters. While the modeling approach used here is too slow to be used in an operational context, the future development of operational retrieval models should not change the results based on the forward model developed here.

Chapter 6

Retrieval of Optical Properties from Low Clouds

In the previous chapter, a retrieval methodology was discussed which, when grouped with a suitable forward model (developed in Chapter 3) and accurate measurements, should allow for the retrieval of optical properties from cloud and aerosol layers. In the next three chapters, we will apply the retrieval scheme to simulated A-band measurements to determine which optical properties can be retrieved and under which conditions. Each of the next chapters will deal with three of the most common potential applications of A-band retrievals. These retrieval scenarios are the retrieval of properties from low clouds, from high-level cirrus clouds and from boundary layer aerosol layers. The format of these chapters will all be similar. Each chapter will begin with a brief discussion of strengths and weakness of the currently used methods to remotely sense optical properties for each retrieval scenario. A sensitivity analysis will be used to explore which of the possible set of properties can be retrieved from A-band reflectance spectra. Lastly, sample retrievals will be performed to address the potential accuracy of A-band retrievals in the context of each retrieval scenario.

6.1 Description of Optical Properties to be retrieved from A-band Measurements

In this section, we will explore through a theoretical analysis which optical properties affect the magnitude and shape of A-band spectra. This analysis is applicable to any retrieval scenario and will not be repeated in the next two chapters. The parameters which affect the

radiance and are deemed retrievable will be placed in the retrieval vector $\tilde{x}$ as described in the Chapter 4. To show which parameters affect A-band reflectance spectra, we will evoke single scatter theory. Even though these retrievals will be applied to conditions where single scattered radiance is only a small component of the total radiance, the insight this theory offers on which parameters control A-band measurements remains valid. In general, we can model a single layer of scatters as having a uniform distribution of extinction due to scattering. Imposed upon this vertically uniform scattering extinction is the vertically varying oxygen absorption. The total scattering optical depth is given by τ_c and the total column optical depth of O_2 is given by $\tau^*_{o_2}$. Including the effects of surface scattering, we can write the single scattered reflected radiance measured along some direction defined by μ at the top of the atmosphere where pressure, $p = 0$ as

$$I_{ss}(\mu, 0) = \int_{p=p_b}^{p=p_t} \omega_o(p) \frac{P(\mu, \mu_o)}{4\pi} e^{-m\tau^p} \frac{\partial \tau}{\partial p} dp + \frac{\alpha_{sfc}}{\pi} F_o e^{-m\tau(p_{sfc})} \tag{6.1}$$

where μ_o is the solar zenith angle and m is the airmass factor $(\frac{1}{\mu} + \frac{1}{\mu_o})$. In the above expression for the single scattered radiance, the contributions from photons which both scatter in the atmosphere and reflect off the surface have been ignored. The inclusion of these terms would introduce no new parameters and would therefore not change the results of this theoretical investigation. To evaluate the pressure integrals in the above equation, the scatters were assumed to vary uniformly between the top of the layer defined by $p = p_t$ and the bottom of the layer defined by $p = p_b$. With this assumption, the optical depth integrated from the top of the atmosphere to some level p can be written as

$$\tau(p) = \tau_c \left(\frac{p - p_t}{\Delta p} \right) u_{p_t}(p) + \tau^*_{o_2} p^2$$

where Δp is the pressure thickness of the scattering layer and $u_{p_t}(p)$ is the unit step function. In the above expression we have utilized the gaseous absorption approximation discussed in Chapter 2 where the optical depth due to o_2 above a layer was assumed to be proportional to p^2. Due the varying gaseous absorption, the single scatter albedo also varies vertically in the cloud and can be written as

$$\omega_o(p) = \frac{\omega_{o,c} \partial \tau_c(p)}{\partial \tau(p)} = \frac{\omega_{o,c} \tau_c}{\tau_c + 2p\Delta p \tau^*_{o_2}} \left(u_{p_t}(p) - u_{p_b}(p) \right).$$

With these simplifications, the single scattered radiance at the top of the atmosphere becomes

$$I_{ss}(\mu,0) = \omega_{o,c}F_o\frac{P(\mu,\mu_o)}{4\pi}\frac{\tau_c}{\Delta p}\left(\frac{1}{2}\sqrt{\frac{\pi}{m\tau^*_{o_2}}}\exp\frac{\left(\frac{m\tau_c}{\Delta p}\right)^2 4m^2\tau^*_{o_2}p_t}{4m\tau^*_{o_2}}\right.$$
$$\left. erf\left(p\sqrt{m\tau^*_{o_2}}+\frac{m\tau_c}{2\sqrt{m\tau^*_{o_2}}}\right)\right)\Bigg|_{p_t}^{p_b}+\frac{\alpha_{sfc}}{\pi}F_o e^{-m\tau(p_{sfc})} \quad (6.2)$$

this can be compared to the expression assuming a uniform distribution of both scattering and absorption optical depth through the layer

$$I_{ss}(\mu,0)=\frac{F_o}{m\mu}\frac{P(\mu,\mu_o)}{4\pi}\frac{\omega_{o,c}\tau_c}{\tau_c+\tau_{c,o_2}}\left(e^{-m\tau_{o_2}(p_t)}-e^{-m\left(\tau_c+\tau_{c,o_2}\right)}\right)+\frac{\alpha_{sfc}}{\pi}F_o e^{-m(\tau_c+\tau^*_{o_2})} \quad (6.3)$$

where $\tau_{c,o_2}=\tau^*_{o_2}(2p_t\Delta p+(\Delta p)^2)$ is the amount oxygen optical depth in the scattering layer. Using the simpler expression for the single scattered radiance, an approximation for the radiance ratio, $s_{\tau^*_{o_2}}$ can be written as

$$s_{ss}(\mu,0)=\frac{\frac{1}{m\mu}\frac{P(\mu,\mu_o)}{4\pi}\frac{\omega_{o,c}\tau_c}{\tau_c+\tau_{c,o_2}}\left(e^{-m\tau_{o_2}(p_t)}-e^{-m\left(\tau_c+\tau_{c,o_2}\right)}\right)+\frac{\alpha_{sfc}}{\pi}e^{-m(\tau_c+\tau^*_{o_2})}}{\frac{\omega_{o,c}}{m\mu}\frac{P(\mu,\mu_o)}{4\pi}(1-e^{-m\tau_c})+\frac{\alpha_{sfc}}{\pi}e^{-m\tau_c}}. \quad (6.4)$$

The above expression identifies the following list of parameters which control the A-band radiance measured from a satellite:

- τ_c - the cloud optical depth,
- $\omega_{o,c}$ - the cloud single scatter albedo,
- $P(\mu,\mu_o)$ - the cloud phase function,
- p_t - the cloud top pressure,
- Δp - pressure thickness of cloud layer, and
- α_{sfc} - surface albedo

The first three parameters listed above are concerned with the optical properties of the scatters (cloud and aerosol particles). The next two parameters deal with the spatial arrangement of the scatters. The last item characterizes the radiative properties of the

underlying surface. While the above equation, derived from single scatter theory, shows a dependence on the each of the listed parameters exists to some extent, the following chapter will explore which of parameters from this list can be meaningfully retrieved from A-band reflectance spectra with known uncertainties. As described in Chapter 2, the variation with $\tau^*_{o_2}$ will be used as surrogate for the true spectral variation in A-band spectra. Furthermore, the inherent profiling ability of A-band retrievals allows for the retrieval of parameters in multiple layers of the atmosphere. The retrieval of properties from more the one layer is described in Chapters 9 and 10.

6.2 Current Methodologies used to retrieve properties of Low Clouds

The retrieval of the properties of low clouds present some difficulties to the current techniques of existing and soon to be deployed satellite instruments. Low clouds offer little temperature contrast to infrared low cloud detection and retrieval techniques. For example, low stratus overlying cold oceans regions, such as the marine stratus off the coast of California, can can present little thermal contrast relative to the underlying ocean, making it difficult to extract information from infrared radiances. In addition, optically thin low clouds like those observed during ASTEX (Heidinger and Cox, 1995), also exacerbate the lack of thermal contrast. The use an infrared-only techniques to detect low clouds requires the use of high spectral resolution measurements and some *a priori* knowledge of the temperature and water vapor distribution (Hofstadter and Heidinger, 1997).

Retrieval of optical depth using data from AVHRR, GOES and MODIS, all rely on an broad-band visible channels to retrieve cloud optical thickness. This requires some knowledge of the surface albedo in order to obtain that part of the radiance due to scattering from clouds. Retrievals using only broad-band visible channels have little ability to vertically position the cloud layer and must rely on *a priori* estimates of surface reflection. As will be shown later, A-band measurements with sufficient spectral resolution can effectively separate the effects of low clouds from reflection from the underlying surface. To illustrate these difficulties, Fig 6.1 shows the difference between a nadir A-band

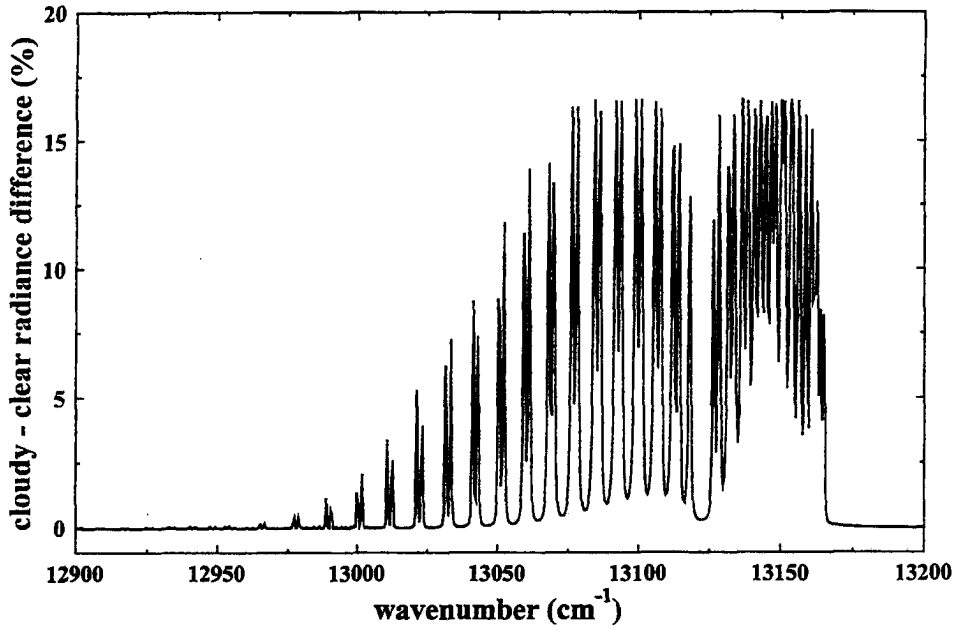

Figure 6.1: Percentage difference in simulated nadir reflectance spectra for cloudy scene over a snow surface and the corresponding clear sky scene.

reflectance spectra for a simulated low cloud over a snow surface and the corresponding clear sky spectra. It is clear from this figure that virtually no information about the presence or properties of the cloud is contained in the continuum radiances which most represent the types of measurements available from the above-mentioned radiometers. Only in the O_2 absorption lines does the radiance contain information about the cloud. Clearly this a worst-case scenario for current low cloud retrieval schemes but illustrates the potential benefits of A-band retrievals. Combined visible and infrared techniques have been explored (e.g. Reynolds and Vonder Haar, 1986) but these techniques suffer from the ambiguities in each of the methods described above. The CO_2 slicing technique first described by Smith *et al.* (1970) uses coarse resolution 14 μm CO_2 radiance ratios to determine the effective level of emission of the cloud layer. As shown by (Wielicki and Coakley, 1981), this technique has difficulty with clouds with cloud top pressures greater than 850 mb. Bias errors of up to 100 mb were reported using CO_2 slicing techniques

applied to the HIR-2 instrument for the cloud top pressures for low boundary layer clouds. The results will show that O_2 A-band retrievals can potentially retrieve low cloud heights much more accurately. In addition, CO_2 slicing provides no information on the optical properties of low cloud layers. As the following sensitivity analysis and sample retrievals will show, A-band retrievals offer several benefits not available from the current methods of remote sensing of low clouds.

6.3 Sensitivity Analysis of A-band Spectra from Low Clouds

In this section, we conduct a sensitivity analysis on simulated A-band spectra to determine which of the above listed parameters can be retrieved from spectra measured during low cloud conditions. To show the sensitivity of the A-band spectra, we have computed the quantity $\frac{\partial f}{\partial \ln x}$ which represents the absolute change in f with a unit change the parameter x. In the case of A-band retrievals, the quantity f is either the reflected radiance, I_ν, or the radiance ratio, s_ν, and the parameter x is any one of the parameters listed above. The figures which follow will show the variation of the sensitivities so defined as a function of $\tau^*_{o_2}$.

Simulating A-band reflection spectra of low cloud were carried out assuming p_t of 800 mb and $\Delta p = 100$ mb. Scatter by cloud particles is assumed to conservative, $\omega_{o,c} = 1.0$, and a single Henyey Greenstein phase function with $g = 0.85$ and the lower surface is Lambertian with an albedo, $\alpha_{sfc} = 0.15$. The phase function characteristics of cloud droplets will be assumed to be known. This is reasonable for low clouds composed of spherical droplets of a size that does not vary substantially from $10\mu m$(eg. Han and Rossow, 1994) except in the case of drizzle. Thus we consider for this problem

$$x = (\tau_c, p_t, \Delta p, \alpha_{sfc})$$

6.3.1 Sensitivity variation as a function of τ_c

Figs 6.2-6.4 show the the sensitivity of both I_ν and s_ν to each of the above parameters for the above set of conditions for three different value of cloud optical depth, τ_c. The left panel in each figure shows the sensitivity of I and the right panel shows the sensitivity

of s_ν. In Fig 6.2, the cloud optical depth, τ_c, is 1.0. Looking at the I_ν sensitivity, we see the largest sensitivity to τ_c and α_{sfc} occurs in weakly absorbing (small $\tau^*_{o_2}$) regions of the spectrum. The decrease of sensitivity of I with increasing values of $\tau^*_{o_2}$ is due to the decrease in reflection due to gaseous absorption. The sensitivity to p_t is low in the weakly absorbing regions since without gaseous absorption the only effect of increasing p_t is to increase the amount of Rayleigh scatter above the cloud layer which is a small effect. The sensitivity of I to p_t reaches a maximum where the gaseous optical depth from the top of the atmosphere to the cloud top equals $\frac{1}{m}$. For the simulations shown in Figs 6.2-6.4, this occurs for $\tau^*_{o_2} = 0.7$ which roughly corresponds to the maximum magnitude of $\frac{\partial I}{\partial \ln p_t}$. There appears to be little sensitivity of I to Δp for all values of $\tau^*_{o_2}$ in Fig 6.1. The negative values of $\frac{dI}{d\ln \Delta p}$ and $\frac{dI}{d\ln p_t}$ are caused by the increase in τ_{c,o_2}, the amount of oxygen contained in the cloud layer, which as (6.2) shows, decreases the reflected radiance. In addition, an increase in p_t also causes the transmission from cloud top to the sensor at the top of the atmosphere to decrease.

The values of $\frac{\partial I}{\partial \ln x}$ can be compared to the values of $\frac{\partial s}{\partial \ln x}$ shown in the left panel. Since s_ν is formed as a ratio relative to I_c, there is no sensitivity to any of the parameters in the continuum part of the spectrum. As seen from (6.4), in the optically thin limit, $s = e^{-m\tau^*_{o_2}}$ which states that the effective level of scatter is coincident with the lower surface. In general, the addition of scatters or turbidity to an atmosphere raises the effective level of scatter and decreases the mean pathlength for reflection and therefore increases s. This physical argument is consistent with Fig 6.2, where $\frac{ds}{d\ln \tau_c}$ is positive and $\frac{ds}{d\ln \alpha_{sfc}}$ is negative. An increase in τ_c would tend to raise the effective level of scatter away from the surface while an increase in α_{sfc} would tend to pull the effective level of scatter down. The negative values of $\frac{ds}{d\ln p_t}$ can also be explained by a decrease in the level of scatter since an increase in p_t means a lowering of the scattering layer into a more strongly absorbing region of the atmosphere. In addition, the positive values of $\frac{ds}{d\ln \Delta p}$ can also be explained by a lowering of the effective level of scattering. These qualitative arguments can be verified by Eq (4). For example, an increase in either p_t or Δp will clearly decrease the numerator will leaving the denominator, the continuum radiance, unchanged.

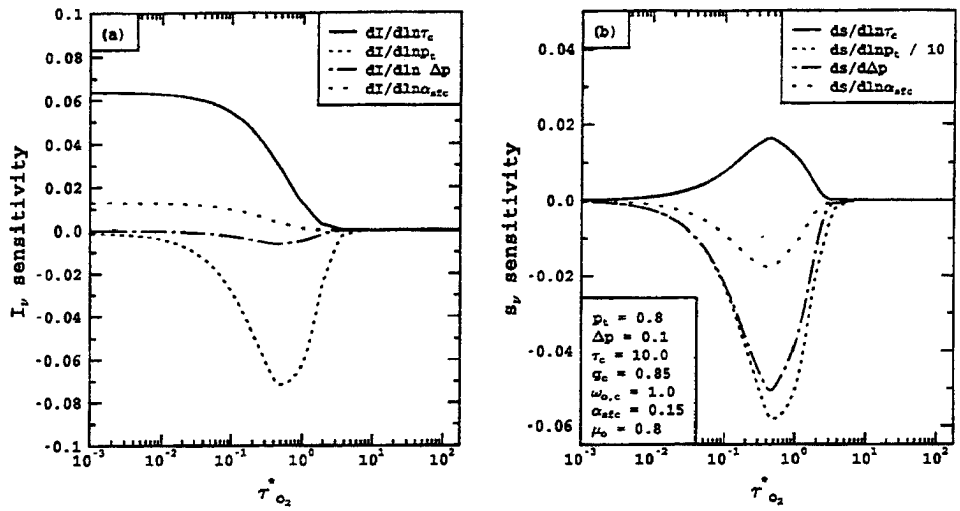

Figure 6.2: Variation of sensitivity of I and s to changes in optical properties as a function of $\tau^*_{o_2}$. The results are for a simulated low cloud with $\tau_c = 10.0$, $g = 0.85$, $\omega_{o,c} = 1.0$, $p_t = 0.8$, $\Delta p = 0.1$, and $\alpha_{sfc} = 0.15$

Figs 6.3 and 6.4 are identical to Fig 6.2 except that results in Fig 6.3 were computed for $\tau_c = 10.0$ and in Fig 6.4 were computed for $\tau_c = 100.0$. The results in Figs 6.3-6.4 are qualitatively similar to those explained above for Fig 6.2. Due to the increased attenuation of solar radiance in the scatter layer as τ_c increases, the values of $\frac{dI}{d\ln \alpha_{sfc}}$ and $\frac{ds}{d\ln \alpha_{sfc}}$ are smaller. In Fig 6.4, $\tau_c = 100$, there is virtually no sensitivity to α_{sfc}. Another trend obvious from these results is the increase in sensitivity of I and s to changes in Δp as τ_c increases. This increase in sensitivity is due to the increase in multiple scattering associated with optically thicker clouds. As Δp increases, the geometric pathlength of the photons increases and therefore the amount of gaseous extinction on the photon pathlengths increases and the value of s decreases. As a cloud becomes semi-infinite, the scattering is contained within the top most region of the cloud layer and as Fig 6.6 shows, an increase in Δp has little effect on either I or s for the $\tau_c = 1000$ simulation. In addition, the sensitivity to p_t for both observables increases with increasing τ_c. In the optically thin limit, there is no sensitivity to p_t since the reflection dominates the reflected radiance. In the semi-infinite limit the sensitivity to p_t is governed solely by the change in transmission

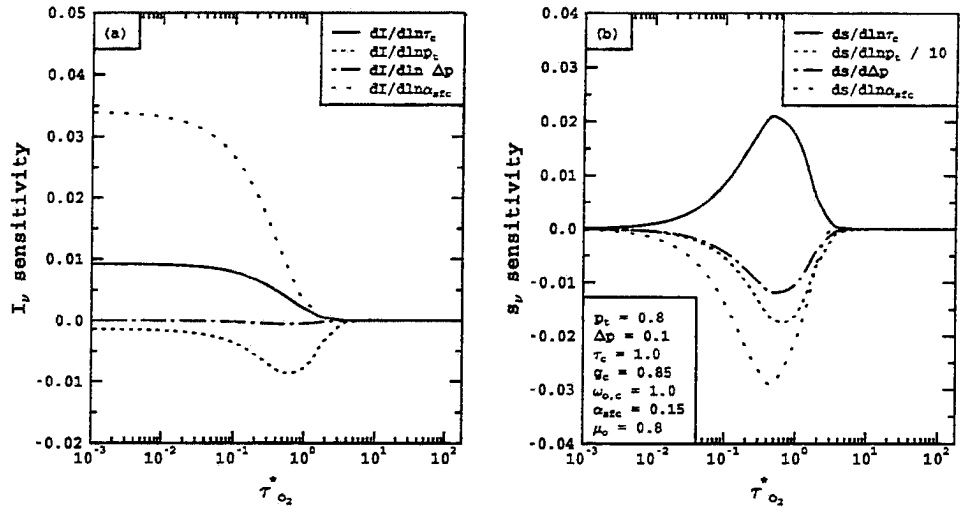

Figure 6.3: Same as Fig. 6.2 except $\tau_c = 1.0$.

due to gaseous absorption from the cloud top, p_t and the top of of the atmosphere.

6.3.2 Sensitivity variation as a function of Δp

The above sensitivity analysis showed the potential to retrieve the pressure thickness , Δp, for a cloud layer. This type of measurement is not available from any type of passive remote sensing platform except for where stereo-graphic analysis can be performed. As mentioned earlier, this parameter is useful for a number of reasons, including proper assignment of the vertical distribution of the heating. The sensitivity of the radiances to Δp can be demonstrated by using the equivalence theorem of Irvine which states that s can be written as:

$$s_\nu = \frac{I_\nu}{I_c} = \int_0^\infty p(l) e^{-\sigma_{o_2} l} dl$$

where $p(l)$ is the photon pathlength distribution. As Δp increases, the geometric thickness of the layer increases and therefore $p(l)$ shifts to longer pathlengths. For a given value of σ_{o_2}, the oxygen absorption coefficient, the absorption along the paths will increase as l increases causing s_ν to decrease. In the limiting case of a cloud layer with a geometrical thickness of 0, increasing Δp should have no effect on the s_ν since the pathlengths have

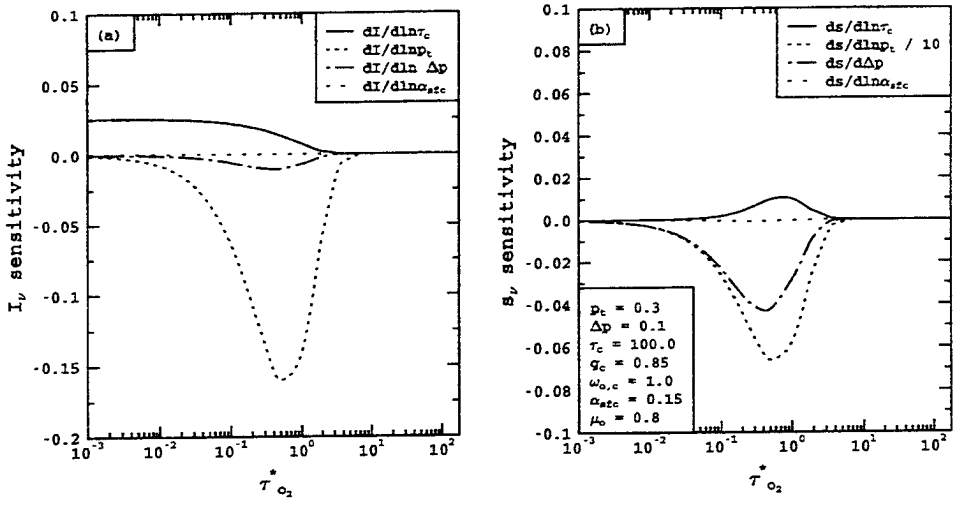

Figure 6.4: Same as Fig. 6.2 except $\tau_c = 100.0$.

no geometrical length. As we have seen in Figs 6.2-6.5, decreasing τ_c for a given Δp also decreases the sensitivity to I_ν and s_ν to Δp. The results presented in Figs 6.6 and 6,7 further illustrate the sensitivity of I_ν and s_ν to changes in Δp. These figures are identical to Fig 6.2 except that the values of Δp was 0.05 (50mb) in Fig 6.6 and 0.01(10mb) in Fig 6.7. As Fig 6.6-6.7 shows decreasing Δp has virtually eliminated the sensitivity of I to Δp for these simulations. However, the sensitivity of s to Δp is still relatively large for $Deltap = 0.05$ but becomes small for the $\Delta p = 0.01$ simulation of Fig 6.6. From these results, it appears that the reflection of solar radiation in the O_2 absorption lines from low cloud with $\Delta p > 20mb$ exhibits a significant sensitivity to changes in Δp.

6.3.3 Sensitivity variation as a function of α_{sfc}

In addition to τ_c and Δp, the surface albedo, α_{sfc} also plays a significant role in controlling the sensitivities of the A-band observables. Figs 6.8-6.9 are identical to Fig 6.2 except that in Fig 6.8 $\alpha_{sfc} = 0.0$ and in Fig 6.9 $\alpha_{sfc} = 0.60$. The former conditions represent low cloud over a dark surface like the ocean and the latter corresponds to low cloud over a bright like snow or ice. The results of Fig 6.8 are similar qualitatively to Fig 6.2 except that the sensitivity of I_ν to τ_c is even larger in the $\alpha_{sfc} = 0$ case. Fig 6.8 shows the

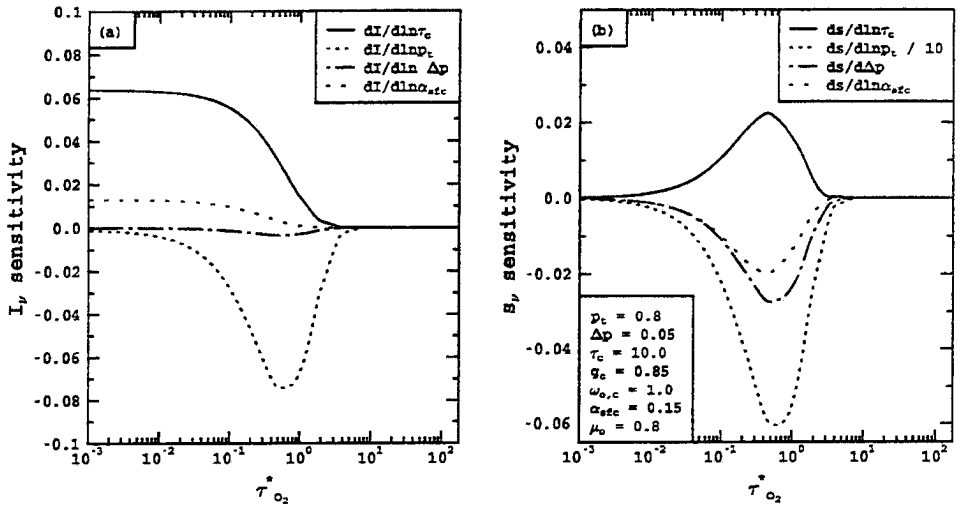

Figure 6.5: Same as Fig. 6.2 except $\Delta p = 0.05$.

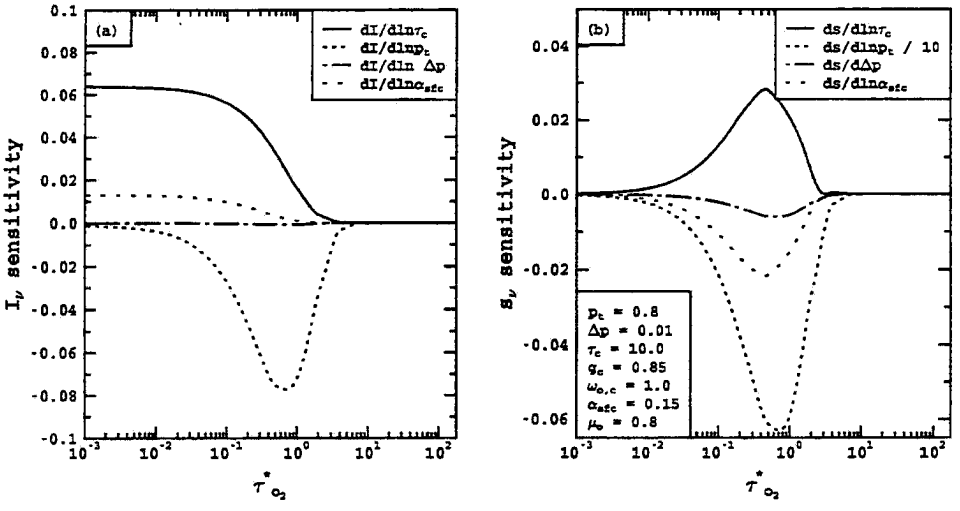

Figure 6.6: Same as Fig. 6.2 except $\Delta p = 0.01$.

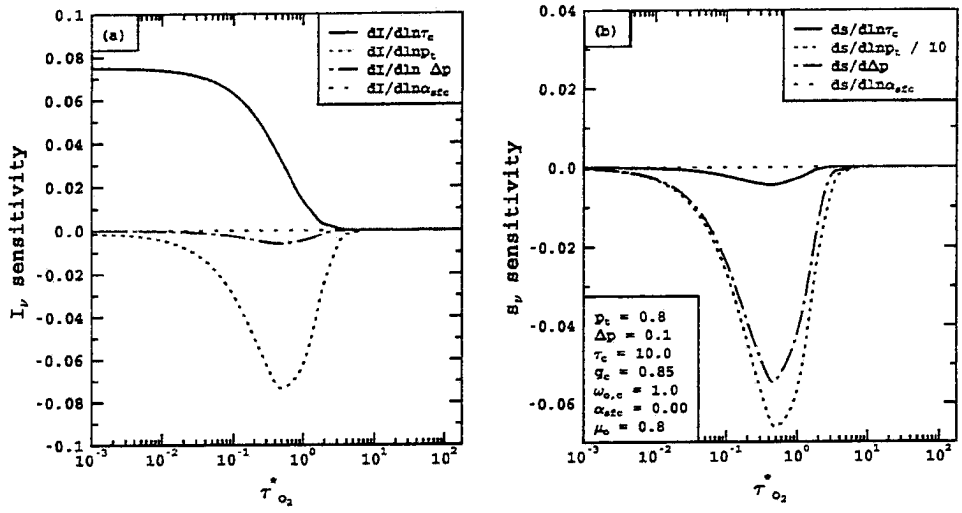

Figure 6.7: Same as Fig. 1 except $\alpha_{sfc} = 0.00$.

sensitivity of s to τ_c becomes negative since an increase in τ_c lowers the effective level of scatter since the only other scattering component is Rayleigh scattering and this occurs predominantly above the cloud layer. Fig 6.9 is also qualitatively similar to Fig 6.2 except for the increase in sensitivity the α_{sfc}. In addition, the sensitivity to Δp and p_t is reduced for the high surface albedo. This reduction in sensitivity can be explained by looking the terms of (6.3) where the increasing α_{sfc} increases the surface component which has no sensitivity to p_t or Δp_t. As will be shown in the next sections, the case of a low cloud over a bright surface offers a challenge to A-band retrievals that can be overcome by increasing the instrument resolution and signal to noise characteristics.

6.4 Sample Retrievals

In the previous section, the sensitivity of the optical parameters listed earlier in the chapter were explored for representative low cloud scenarios. In this section, we apply the retrieval method developed in the last chapter and the forward model developed in chapter 3 to perform sample retrievals. These retrievals presented provide an indication of the ability of A-band retrievals to exploit the above sensitivities to extract estimates of the optical

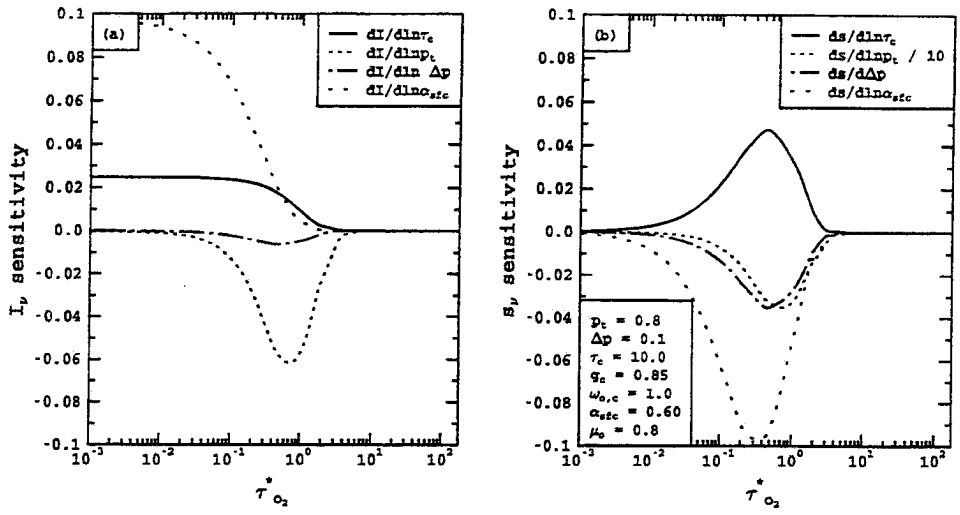

Figure 6.8: Same as Fig. 1 except $\alpha_{sfc} = 0.60$.

properties of low cloud layers. This section will be comprised of three parts - one will focus on retrievals using only spectral radiances, a second will focus on retrievals that use only the radiance ratios, s_ν and the third will consider a retrieval using combinations of I_ν and s_ν. The merits of each retrieval scheme will be compared and discussed. This is important since instrument requirements (e.g. calibration) differ according to whether I_ν or s_ν is the primary observation. Using the forward model developed in Chapter 4 and the optimal estimation retrieval methodology discussed in Chapter 5, the feasibility of performing nadir A-band retrievals of cloud properties can be explored. As mentioned in Chapter 5, in addition to actual retrieved parameters, the products from the retrieval include estimates of the errors of the retrieved parameters and an estimate of the reliance of the retrieval on the *a priori* constraints. In the following section, these quantities will be given to judge the validity of the retrieval under various scenarios. The actual errors of the retrievals will not be shown. Even though the actual errors could be computed directly for these simulations, since the true values are known, the actual errors in the retrieved parameters are not as meaningful as the error estimates produced by the retrieval. Since a plane parallel forward model, as used in this study, can never hope to adequately simulate

all aspects of the retrieval problem, the actual errors in simulated retrievals are always less than those predicted by the retrieval method. In the following sections, results for simulated retrievals will be shown for both of the A-band observables, the spectral radiance (I_ν) and radiance ratio (s_ν), and for a retrieved base of the observables. Throughout the discussion, the retrieval results will be compared with sensitivity analysis performed above in order to explain the observed strengths and weakness of the retrievals.

All the simulations here will be based on the following scenario. The cloud layer is situated between 800 and 900 mb in a mid-latitude summer atmosphere. The underlying surface is assumed to behave as a Lambertian reflector. In addition, the solar zenith angle cosine is set to 0.8. Since the sensitivity analysis above shows that the cloud optical depth and surface albedo were the most significant parameters in affecting radiances and radiance ratios, the retrieval results will shown for a range of low cloud optical depths for three different values of the surface albedo. As done previously, the values of the surface albedo used were 0.0(dark ocean), 0.15(land) and 0.60(snow or ice).

6.4.1 Phase Function Errors in the Forward Model

Before sample retrievals are shown, the error in the forward model due uncertainties in the phase function needs to be quantified so that the error estimates presented next are meaningful. A section similar to this one will appear in each of the next three chapters since the phase function error depends on the retrieval scenario and is therefore different for boundary layer water clouds, cirrus cloud and aerosol layers.

To explore the sensitivity of the A-band low cloud retrievals to errors in the phase function, A-band spectra were computed using a variety of representative phase functions for water droplets characteristic of those observed in low clouds.. Fig 6.9 shows the variation in the phase function for several different droplet size distribution found in low clouds. The C1 phase function, taken from Diemierjian (1969), corresponds to typical droplet size distribution found in cumulus clouds. Also shown in Fig 6.9 are phase functions for other size distribution referenced to the work of Stephens(1979) computed using standard Mie scattering procedures. Fig 6.9 also contained a double Henyey Greenstein phase function

constructed using the parameters $g_1 = 0.90, g_2 = -0.6$ with $g_{eff} = 0.84$, which is the same value of the C1 phase function asymmetry parameter.

To quantify the errors in A-band spectra due the phase function uncertainty the phase functions shown in Fig 6.9 were expanded into 64 term Legendre polynomials and included simulated using the forward model described in Chapter 4. The forward peaks of phase functions were truncated and replaced by a δ-function peak to allow for an accurate representation in the model. To estimate the uncertainties in A-band spectra due to phase function uncertainties, spectra were computed using the phase functions computed from the size distributions with $r_e = 8\mu m$ and $r_e = 20\mu m$. This range in r_e spans the range seen in non-precipitating low clouds, which tend to have values of r_e around $10\mu m$ (Han and Rossow, 1989). The differences caused by these phase function differences should give a meaningful estimates of the true effect of phase function uncertainty in low cloud retrievals. Fig 6.10 shows the errors due the phase function differences for a low cloud with $\tau_c = 10$ for a range of surface albedoes, α_{sfc}. The left column shows the errors in the radiance, I_ν and the right column shows the errors in s_ν, the radiance ratio. As these results show, the phase function errors generally decrease for both observables as the cloud becomes thicker. This can be explained by noting that the details of the phase function are more important in thin media while in thick media, the multiple scattering reduces the sensitivity to phase function details. The general increase in the errors with increasing $\tau^*_{o_2}$ is due to the reduction of multiple scattering due to gaseous absorption and an increased sensitivity again to the details of the phase function. For the radiances, the effect of surface albedo acts to reduce the errors since the surface contribution is affected by phase function errors to much lesser extent than the cloud contribution. This effect is opposite in the phase errors for s_ν. In the ratio of radiances, the phase function errors tend to cancel. This effect can be seen the upper right panel where the errors for s_ν are lowest for the dark surface and increase with surface albedo. In general we can deduce that the phase function errors for the radiance ratios, s_ν are half as large as the errors in the radiances. Phase function uncertainties for low clouds (water-droplet clouds) are incorporated into S_y as follows. A constant 1 % radiance error is assumed for phase

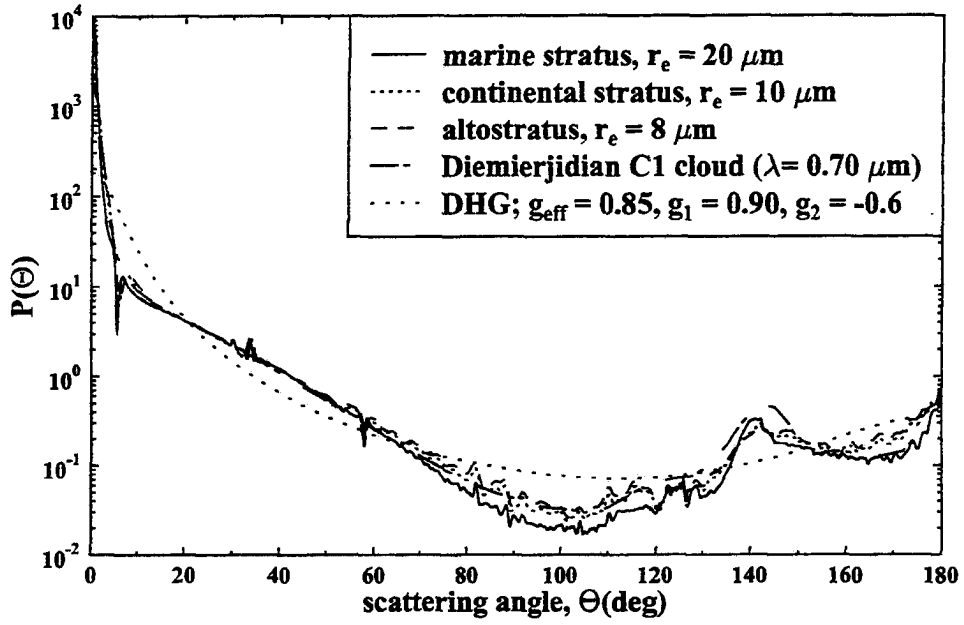

Figure 6.9: Comparison of the C1 phase function and Mie phase functions for representative low cloud droplet distributions

function error on I_ν consistent with the results of Fig. 6.10. The s_ν error associated with phase function uncertainty was approximated by

$$\epsilon_{P_f,s_\nu} = \epsilon_{max}(1 - e^{-0.15*(\tau^*_{o_2})}) \tag{6.5}$$

where $\epsilon_{max} = 0.5$ based again based on the results of Fig. 5. In a rigorous sense, these errors should be tabulated as a function of solar zenith angle and cloud properties. In an actual retrieval, these properties are not known *a priori* and the above errors values are assumed for all low cloud scenarios.

6.4.2 Sample Retrieval Results

Using the forward model developed in Chapter 4 and the optimal estimation retrieval methodology discussed in Chapter 5, the feasibility of performing nadir A-band retrievals of cloud properties can be explored. As mentioned in Chapter 5, in addition to actual retrieved parameters, the products from the retrieval include estimates of the errors of

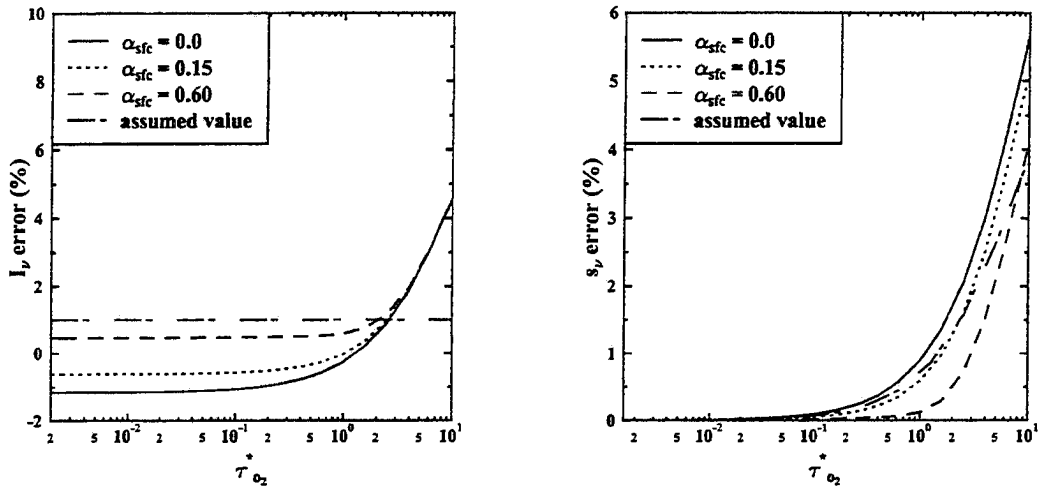

Figure 6.10: Errors due to the difference in phase functions shown in Fig. 6.9. The left column are errors in radiance, I_ν and the right column shows errors in the radiance ratio, s_ν. All computations were for a cloud with $\tau_c = 10$ from 800 to 900 mb.

the retrieved parameters and an estimate of the reliance of the retrieval on the *a priori* constraints. In the following section, these values will be shown to judge the validity of the retrieval under various scenarios. The actual errors of the retrievals will not be shown. Even though the actual could be computed directly for these simulation where the true values are known, the actual errors in the retrieved parameters are not as meaningful as the error estimates produced by the retrieval. Since a plane parallel forward model, as used in this study, can never hope to adequately simulate all aspects of the retrieval problem, the actual errors in simulated retrievals are ways less than those predicted by the retrieval method. In the following sections, results for simulated retrievals will be shown for both of the A-band observables, the spectral radiance (I_ν) and radiance ratio (s_ν), and for a retrieved base of the observables. Throughout the discussion, the retrieval results will be compared with sensitivity analysis performed above in order to explain the observed strengths and weakness of the retrievals.

All the simulations here will be based on the following scenario. The cloud layer is situated between 800 and 900 mb in a mid-latitude summer atmosphere. The underlying surface is assumed to behave as a Lambertian reflector. In addition, the solar zenith angle

cosine is set to 0.8. Since the sensitivity analysis above shows that the cloud optical depth and surface albedo were the most significant parameters in controlling the sensitivity of the observables to the parameters, the retrieval results will shown for representative low optical depths for three different values of the surface albedo. As done previously, the values of the surface albedo used were 0.0(dark ocean), 0.15(land) and 0.60(snow or ice).

6.4.3 Radiance Based Retrievals

This section explores the use of the spectral radiance, I_ν, alone in the retrieval of the optical parameters of the interest for low cloud. Fig. 6.11 shows the simulated retrieval results for the low cloud scenario described above using only the radiance data. In the computation of the error covariance matrix, S_x, the calibration error on the radiance was assumed to be 2% and the signal to noise ratio was assumed to be 400:1. The structure of Fig 6.11 is as follows. The left column shows the estimated retrieval errors as a percentage from Eq (5.9) and the right column shows the values of the diagonal elements of the matrix A Eq(5.5).

The variation of the retrieval errors and the *a priori* parameter, A, for each parameters can be understood by using the sensitivity analysis performed earlier in the chapter, since these sensitivities define the kernel matrix, K introduced in Chapter 5. For example, the increase in the optical depths errors for small values of τ_c are due to decreases in the sensitivity of I_ν to τ_c seen by comparing Figs. 6.2-6.4. The increase in errors with the surface albedo can also predicted by comparing Figs 6.2, 6.7, and 6.8 where for $\tau_c = 10.0$, $\frac{\partial I_\nu}{\partial \ln \tau_c}$ decreases with increasing albedo. The general increase in the τ_c errors with increasing τ_c can be explained by the asymptotic nature of reflected radiance with increasing τ_c. Analysis of the corresponds values of $\mathcal{A}$ indicate the reliance of the retrieval on the *a priori* constraint due to either as a result of a lack of sensitivity or a result of uncertainty in the measurements. As described in chapter 5, the *a priori* error of optical depth was assumed to be 100 % which puts a limit on the range of the retrieval errors. This is consistent with Fig. 6.11 where the value of A drops down to 0.8 and the errors in τ_c approach 40 % for the very thin low clouds over a land surface. In this case, the retrieval relies significantly on the *a priori* estimate of τ_c.

Using the same reasoning, the values of the errors and the *a priori* reliance for the other parameters can be deduced. Figs 6.2, 6.7 and 6.8 illustrate, $\frac{\partial I}{\partial \ln \alpha_{sfc}}$ increases with increasing α_{sfc} and which can explain why the retrieval errors in α_{sfc} are less than 5% for the bright surface case and over 10 % in the $\alpha_{sfc} = 0.15$ case. The increase in the errors in the retrieved α_{sfc} with τ_c can be seen from Figs. 6.2,6.3 and 6.4 were retrieval of α_{sfc} becomes difficult due to the reduction of surface contributions by the overlying clouds. Again, these errors are consistent with the values of A which are largest for small values of τ_c.

It was apparent from the sensitivity analysis that the sensitivity of I_ν to the cloud top pressure , p_t is large. As Fig. 6.11 shows, the errors for most values of τ_c and α_{sfc} are less then 5 %. The low errors for the dark surface case can be explained by the fact the high sensitivity to τ_c and lack of any contributing surface effects allows the retrieval to very accurately place the cloud in the atmospheric column. This accurate ability of A-band retrievals to determine p_t is again reflected in the high values of A.

The last parameter results shown in Fig. 6.11 are for the pressure thickness of the layer, Δp. As Figs. 6.2, 6.3 and 6.4 show, the sensitivity of the radiance to Δp increases with τ_c so that the largest errors occur for optically thin clouds. In addition, the decrease in the values of $\frac{\partial I}{\partial \ln \Delta p}$ with α_{sfc} are consistent with the increase in errors of Δp with increasing α_{sfc}. It appears from these simulations that Δp can be estimated with an uncertainty of 10 %.

6.4.4 Radiance Ratio Retrievals

In this section, the same reasoning used in the above section is applied to retrievals performed with other A-band observable, the spectral radiance ratio, s_ν. Fig. 6.12 is identical to Fig. 6.11 except that results pertain to retrievals using only s_ν. Fig 6.12 shows that retrievals of low cloud based on radiance ratios do not perform as well as the retrievals based on spectral radiances. As described earlier, to the first order, the value of s_ν is governed by the effective level of scatter in the atmosphere. For a cloud over a reflecting surface, this level will vary from the surface to the top of the cloud depending on the

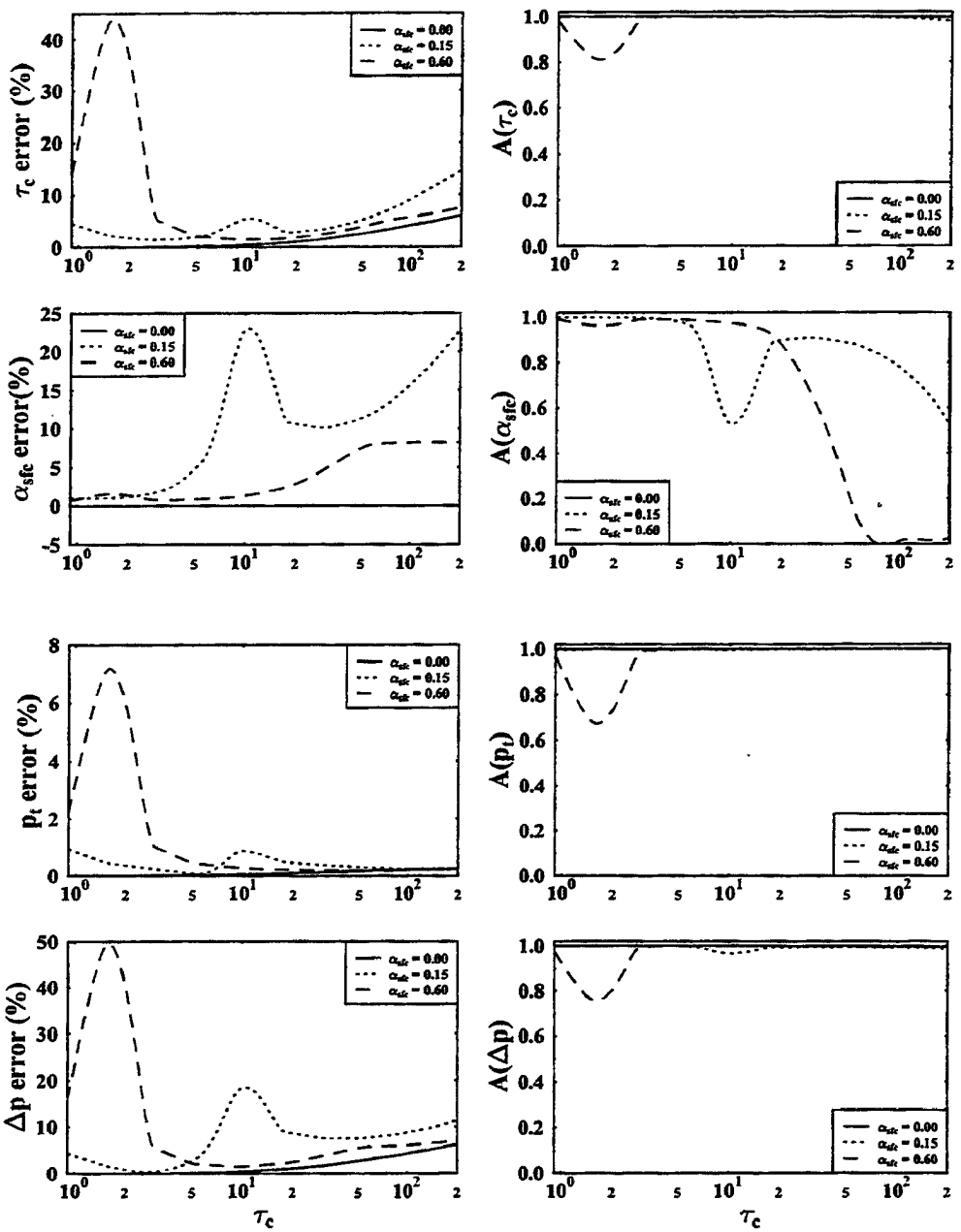

Figure 6.11: Simulated retrieval results for a low cloud scene. The left column shows the estimated errors in the retrieval and the right column shows the estimated reliance on the *a priori* constraints. The retrieval was based only on the spectral radiance, I_ν.

optical thickness of the cloud compared to the albedo of the surface. The dynamic range of s_ν therefore depends on the vertical separation of the cloud layer form the surface. For clouds close to the surface, a low sensitivity of s_ν to τ_c and to α_{sfc} is therefore expected. This conclusion is consistent with Figs. 6.2,6.3,6.4 where the sensitivity of s_ν to τ_c decreases as τ_c increases since the effective level of scatter is fixed to the cloud top. This explains the larger errors in τ_c compared to those seen in the retrievals using radiances.

As the sensitivity analysis showed above, however, s_ν exhibits a large sensitivity to changes in p_t, the cloud top pressure. The errors in the s_ν retrievals of p_t are lower than the values for the radiance retrievals. Both methods seem able to estimate p_t to within 5 % (50 mb) with the assumed uncertainties in the measurements and the forward model. In addition, the radiance ratio retrieval is unable to estimate accurately Δp for these simulations as evidenced by the large errors in Fig 6.12.

6.4.5 Combined Radiance and Radiance ratio Retrievals

As the two sections described above, with realistic errors sources, the radiance retrievals generally out performed the radiance ratio retrievals. Fig 6.13 shows the combined retrieval using both radiance and radiance ratios. The resulting error estimates show a significant benefit from combining both measurements into one simultaneously retrieval. Even though the radiance ratio retrieval was inferior by itself, it still offers offers additional information to the retrieval. Theoretically, the inclusion of additional information can never increase the errors in a retrieval unless the additional information conflicts with the original measurements such as would be the case for measurements taken at differing times or spatial scales. For example, the errors in optical depth using the combined retrieval are typically below 10 % compared to 20 % for the separate retrievals. This behavior can explained the sensitivity analysis performed earlier in this chapter. This analysis showed that the sensitivity of I_ν and s_ν to τ_c peaked in different spectral regions and could even be of opposite sign. The information of these two observables is different and the ability to base a retrieval on both produces an observing system superior to that based on any one data source. In addition, the errors of Δp are greatly reduced in the combined retrieval.

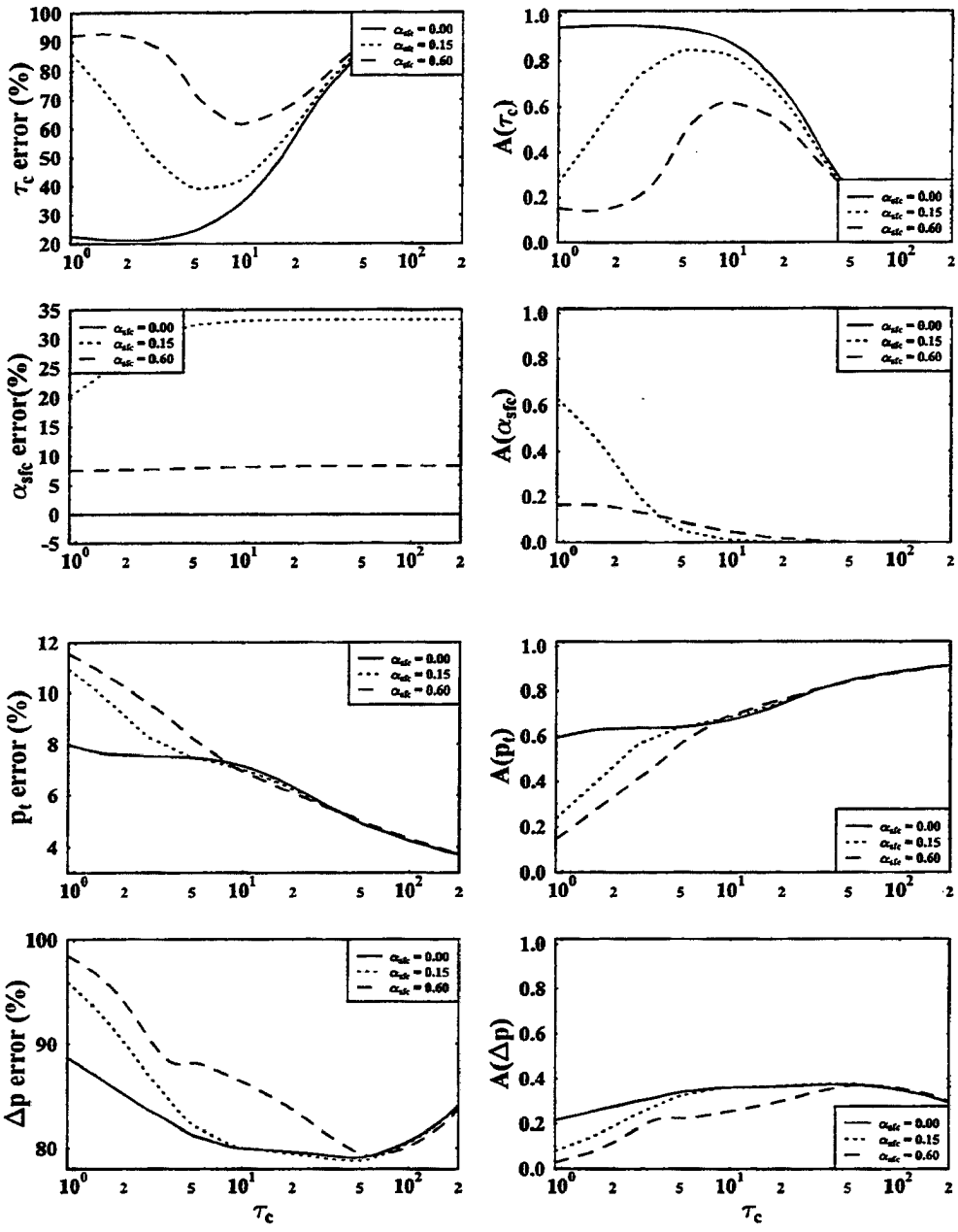

Figure 6.12: Same as Fig. 6.11 except for retrievals based on the spectral radiance ratio, s_ν.

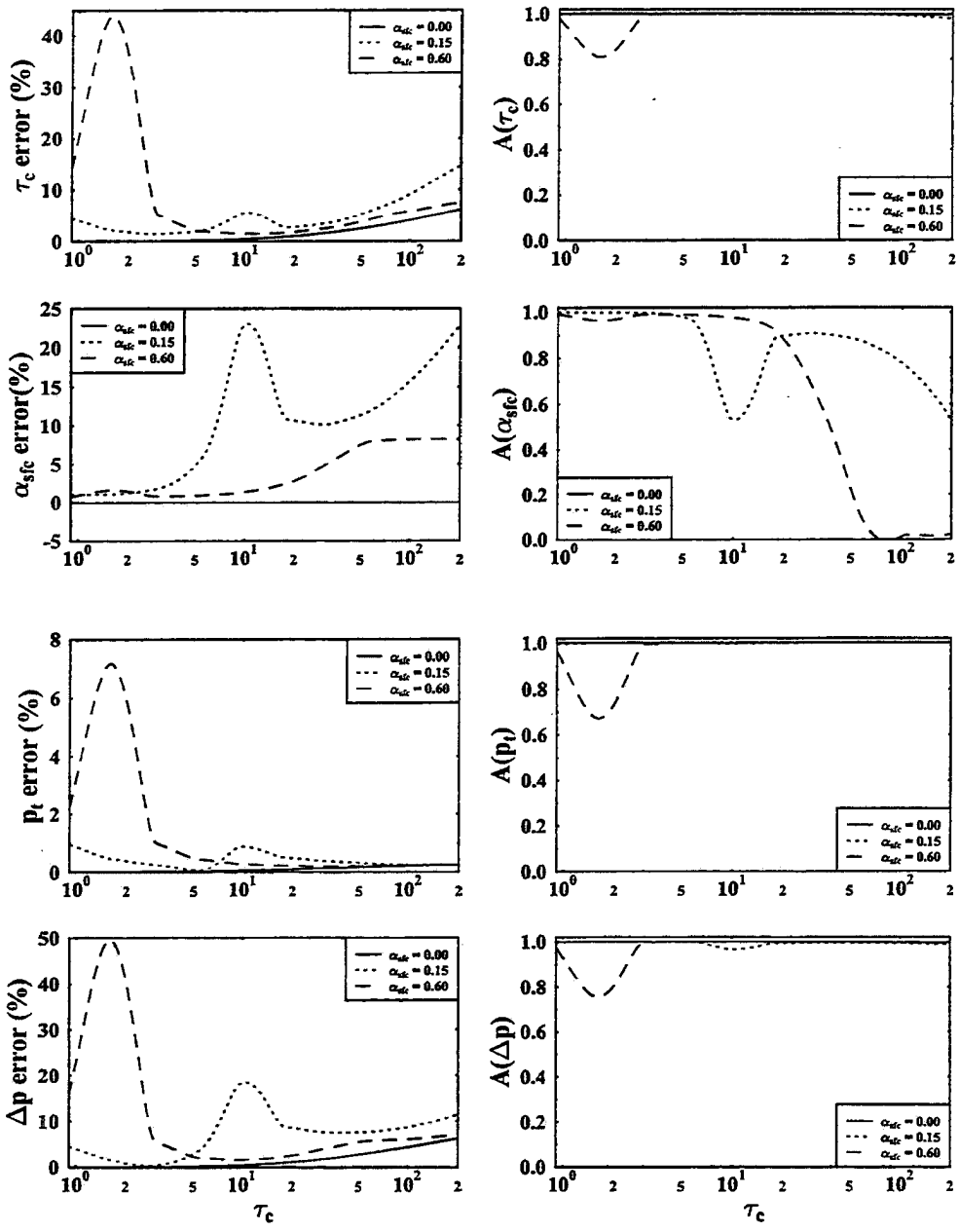

Figure 6.13: Same as Fig. 6.11 except for retrievals based on both the the spectral radiance, I_ν, and the spectral radiance ratio, s_ν.

6.4.6 Effect of Cloud Heterogeneity on Retrievals

In Chapter 12, a three dimensional radiative transfer model is used to quantify the effect of cloud spatial heterogeneity on A-band spectra. The results of Chapter 10, based on two spatially heterogeneous clouds fields, showed errors that ranged from 2 % to over 20 % depending on the magnitude of the heterogeneity. To include the effects of heterogeneity, the low cloud retrievals presented above are repeated with an additional 5 % error added to the forward model error to account for cloud spatial variability. This error identical to the phase function error already included in the retrieval results. Fig 6.14 shows the results of a retrieval using both observables with the inclusion of the error due to cloud heterogeneity. As the results indicate, the effect of the heterogeneity error is slightly increase the errors in all retrieved parameters. For example, for $\tau_c = 10$ and $\alpha_{sfc} = 0.15$, the error in τ_c increased from 6 % to 7%. While this amount of heterogeneity error may seem conservative, the results of Chapter 11 will show that A-band retrievals can diagnose when the errors due to spatial heterogeneity become large.

6.5 Conclusions

This chapter describes the first of three retrieval scenarios, the retrieval of optical properties of low clouds. Using realistic error estimates for the forward model and measurement errors, some measure of confidence of the retrievals is given. For these results, it appears A-band measurements from currently available or planned instruments could produce errors in τ_c from 5-15%, errors in α_{sfc} from 2 - 10%, errors in p_t from 3-45% and errors in Δp from 5 - 20%. These estimates include a level of spatial variability. In summary, it appears that an A-band observing applied to low cloud retrievals is able to make meaningful estimates of the four retrieved parameters ($\tau_c, \alpha_{sfc}, p_t and \Delta p$) which represents a significant advancement over current passive cloud retrieval methods.

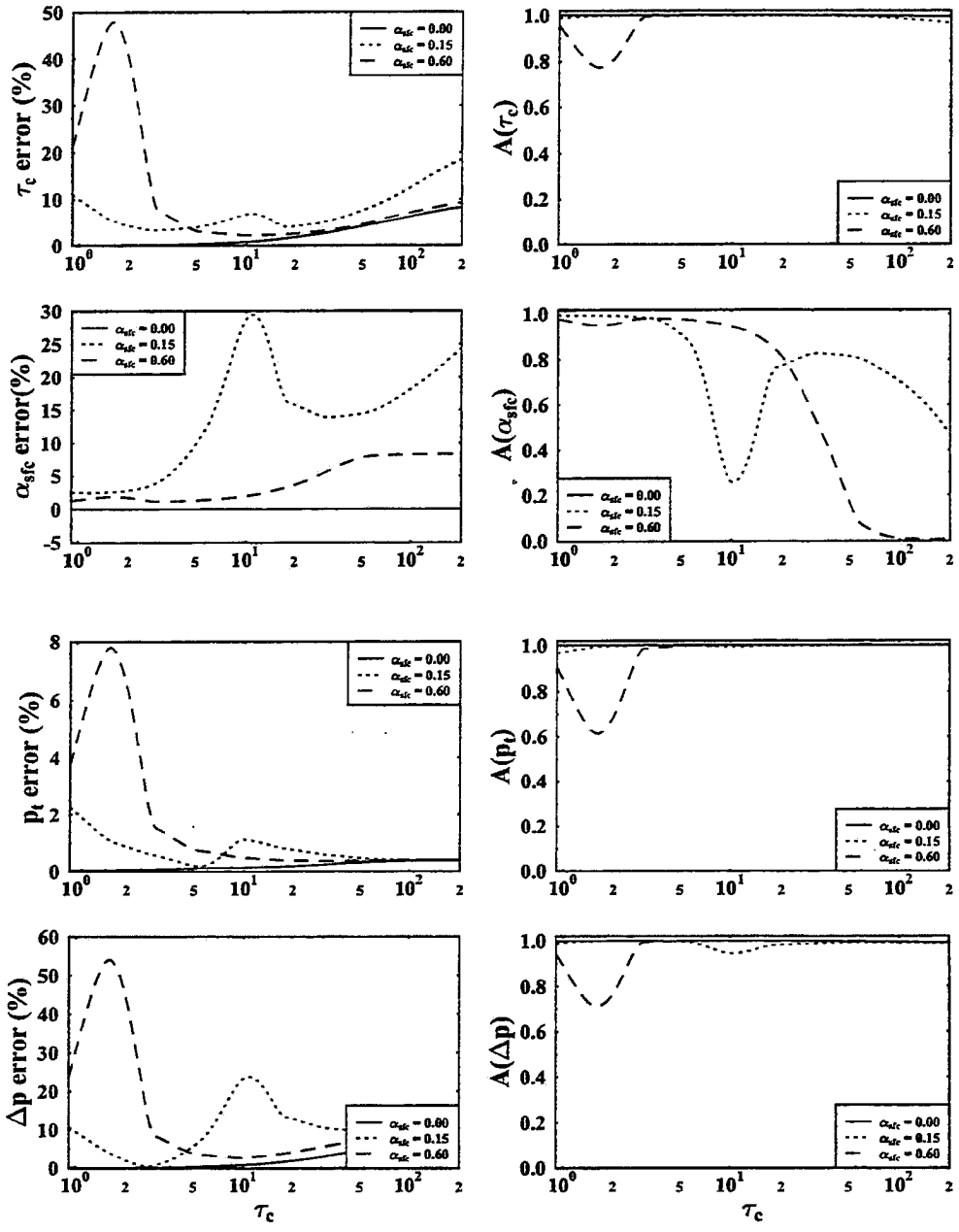

Figure 6.14: Same as Fig. 6.13 except errors accounting for cloud spatially variability were included

Chapter 7

Retrieval of Optical Properties from Cirrus Clouds

This chapter is the second of the three chapters which deals with the retrievals of optical properties from individual layers. While the last chapter considered low level water clouds, this chapter deals with the retrieval of properties from a distinctly different scenario, cirrus clouds. In contrast to low clouds, cirrus clouds are located high in the atmosphere with most of the O_2 absorption occurring below the cloud. In addition, cirrus clouds tend to be optically thinner than low clouds which, as shown in the sensitivity analysis of the last chapter, strongly affects the magnitudes of the sensitivity of the observed radiances to each optical property. Another distinct difference between cirrus and low clouds is the uncertainty of the cirrus phase functions. As shown in Chapter 3, the sensitivity of I_ν and s_ν to the phase function is large and uncertainties in the latter lead to significant uncertainties in any retrieval. Unlike low cloud, ice crystal phase functions are likely to be more variable, being affected by the shape, size and orientation of the crystals. The phase function of ice crystals cannot therefore be assumed known and information about the phase will be retrieved.

7.1 Current methodologies used to retrieve properties of cirrus clouds

As mentioned earlier, any visible reflectance retrieval of cirrus properties can easily be 100 % in error due to the phase function uncertainty. The current suite of satellite sensors on-board the geostationary and polar orbiting satellite are all sensitive to phase function

errors. In addition, the optical thickness of cirrus clouds is often small enough that the surface reflection is a significant component of the detected radiance. Current retrieval methods thus also suffer from uncertainties in the surface albedo. As a consequence, all current visible techniques have difficulty in detecting thin cirrus above a bright surface, a shortcoming which A-band retrievals circumvents. Using emission techniques, such as CO_2, slicing provides some information on cirrus heights. However retrievals of cirrus properties from broad band channels are sensitive to errors in the temperature profile and the profile of extinction in the cloud itself. The high spectral resolution from the HIRS (High Infrared Resolution Spectrometer) is able to deduce cirrus infrared optical depth through the slope of the spectra through the infrared window (8-12 μm) (Smith and Frey, 1990) and particle size information may be provided from such data for very thin clouds (Prabhakara *et al*, 1988).

7.2 Sensitivity Analysis of A-band Spectra from cirrus clouds

As in the previous chapter,a sensitivity analysis will be presented to explore the sensitivity of the A-band radiances to changes in the parameters listed in Section 5.1. In the same manner as the previous chapter, the sensitivities are computed in the from of the quantity $\frac{\partial f}{\partial \ln x}$ which represents the absolute change in f with a unit change the parameter x. In the case of A-band retrievals, the quantity f is either the reflected radiance, I_ν or the radiance ratio s_ν and the parameter x is any one of the retrieved parameters. The sensitivities were calculated for a cirrus cloud with a cloud top pressure, $p_t = 300mb$ and $\Delta p = 100mb$. The cloud is conservative scattering, $\omega_{o,c} = 1.0$, and the lower surface is Lambertian with $\alpha_{sfc} = 0.15$. The asymmetry parameter of the phase function, g, is 0.80. A double Henyey-Greenstein representation of the phase function with $g_1 = 0.90, g_2 = -0.6$ will be used in this sensitivity analysis. This approximation to the ice crystal phase function roughly simulates the shape of the hexagonal ice crystal phase function from Takano and Liou (1989).

Unlike water cloud droplets whose scattering phase functions are well well represented by Mie theory, cirrus cloud crystal phase functions are highly variable and not well known.

Therefore, in the sensitivity analysis for cirrus clouds, the sensitivity to the phase function will also be explored. To show the sensitivity of the observables to the phase function, we will compute the expression $\frac{df}{d\ln Pf}$. In order to theoretically justify the choice of this expression over another, we revisit the single scatter equation of the previous chapter. Expanding the exponential term $(e^{-m(\tau_c+\tau^*_{o_2})})$ allows us to write

$$I_{ss}(\mu,0)=\frac{\omega_{o,c}\tau_c}{\mu}\frac{P(\mu,\mu_o)}{4\pi}F_o e^{-m\tau_{o_2}(p_t)}+\frac{\alpha_{sfc}}{\pi}F_o e^{-m\tau^*_{o_2}}(1-m\tau_c)=I_{atm,\tau^*_{o_2}}+I_{sfc,\tau^*_{o_2}} \quad (7.1)$$

where we have identified the radiance scattered once in the atmosphere as I_{atm} and reflected once of the surface as I_{sfc}. Using the above expression for the radiance, we can express the sensitivity $\frac{\partial I}{\partial \ln P_f(\mu,\mu_o)}$ as

$$\frac{\partial I_{\tau^*_{o_2}}}{\partial \ln P_f(\mu,\mu_o)}=I_{atm,\tau^*_{o_2}} \quad (7.2)$$

and the sensitivity $\frac{\partial I}{\partial \ln \tau_c}$

$$\frac{\partial I}{\partial \ln \tau_c}=\frac{\partial I}{\partial \ln P_f(\mu,\mu_o)}+I_{sfc}-I^{\tau_c=0}_{sfc} \quad (7.3)$$

Since $I_{sfc,\tau^*_{o_2}}<I_{sfc,\tau^*_{o_2},\tau_c=0}$, single scatter theory predicts that $\frac{\partial I_{\tau^*_{o_2}}}{\partial \ln P_f(\mu,\mu_o)}>\frac{\partial I}{\partial \ln \tau_c}$ whenever the underlying surface is reflecting. If the underlying surface is bright enough such that $I_{sfc}>>I_{atm}$, negative values of $\frac{\partial I}{\partial \ln \tau_c}$ can result. In the case of a non-reflective surface, single scatter theory predicts $\frac{\partial I_{\tau^*_{o_2}}}{\partial \ln P_f(\mu,\mu_o)}=\frac{\partial I}{\partial \ln \tau_c}$. Using the same approach, we can approximate the radiance ratio at a frequency , $s_{\tau^*_{o_2}}$ as

$$s_{ss}(\mu,0)=\frac{I_{atm,\tau^*_{o_2}}+I_{sfc,\tau^*_{o_2}}}{I_{atm,c}+I_{sfc,c}} \quad (7.4)$$

Using the same approximation above to compute the radiance sensitivities allows

$$\frac{\partial s_{\tau^*_{o_2}}}{\partial \ln P_f(\mu_o,\mu)}=\frac{I_{atm,\tau^*_{o_2}}-(I_{sfc,\tau^*_{o_2}}-I^{\tau_c=0}_{sfc,\tau^*_{o_2}})}{I_c} \quad (7.5)$$

and the sensitivity to τ_c can be expressed as

$$\frac{\partial s_{\tau^*_{o_2}}}{\partial \ln \tau_c}=\frac{I_{atm,\tau^*_{o_2}}-(I_{sfc,\tau^*_{o_2}}-I^{\tau_c=0}_{sfc,\tau^*_{o_2}})}{I_c}-s_{\tau^*_{o_2}}\frac{I_{atm,c}-(I_{sfc,c}-I^{\tau_c=0}_{sfc,c}}{I_c} \quad (7.6)$$

which can be simplified to

$$\frac{\partial s_{\tau^*_{o_2}}}{\partial \ln \tau_c}=\frac{\partial s_{\tau^*_{o_2}}}{\partial \ln P_f(\mu_o,\mu)}-\frac{s_{\tau^*_{o_2}}}{I_c}\left((I^{\tau_c=0}_{sfc,c}-I^{\tau_c=0}_{sfc})-(I_{sfc,c}-I_{sfc})\right). \quad (7.7)$$

Since the left hand term tends to be negative, single scatter theory predicts $\frac{\partial s_{\tau^*_{o_2}}}{\partial \ln \tau_c} < \frac{\partial s_{\tau^*_{o_2}}}{\partial \ln P_f(\mu,\mu_o)}$.

In the case of a non-reflecting underlying surface, $\alpha_{sfc} = 0.0$, the expression for $s_{\tau^*_{o_2}}$ becomes

$$s_{ss}(\mu, 0) = e^{-m\tau_{o_2}(p_t)} \tag{7.8}$$

and $\frac{\partial s_{\tau^*_{o_2}}}{\partial \ln \tau_c} = \frac{\partial s_{\tau^*_{o_2}}}{\partial \ln P_f(\mu,\mu_o)} = 0$. To numerically validate the qualitative arguments made above, a single scatter radiance transfer model was used to explore these sensitivities. As in the sensitivity plots in the previous chapter, Fig 7.1 shows the radiance sensitivity in the left panel and the radiance ratio sensitivity in the right panel. Only the sensitivities to τ_c and $P_f(\mu_o, \mu)$ are shown. As is consistent with the above theoretical discussion, the values of $\frac{\partial I_{\tau^*_{o_2}}}{\partial \ln P_f(\mu,\mu_o)}$ exceed those of $\frac{\partial I_{\tau^*_{o_2}}}{\partial \ln \tau_c}$ in the weaker absorbing regions of the spectrum but become equal once the gaseous absorption becomes strong enough to reduce the surface effect. In addition, the single scatter sensitivities for $s_{\tau^*_{o_2}}$ are greater for P_f than for τ_c and are both positive as predicted by (7.5) and (7.7). As described later, the ability of A-band retrievals to separate the effect of changes in τ_c and P_f is a major advantage over current cirrus observing methods. The guidance offered by the above theoretical study will be useful in interpreting sensitivity analysis results to follow.

7.2.1 Sensitivity variation as a function of τ_c

Figs 7.2-7.4 show the the sensitivity of both $I_{\tau^*_{o_2}}$ and $s_{\tau^*_{o_2}}$ to each of the above parameters for the above set of conditions and for three different value of cloud optical depth, τ_c. The left panel of each figure shows the sensitivity of I_ν and the right panel shows the sensitivity of s_ν. The largest sensitivity of I_ν and s_ν to τ_c and α_{sfc} occur in the weakly absorbing (small $\tau^*_{o_2}$) regions of the spectrum. The decrease of the sensitivity of I_ν with increasing values of $\tau^*_{o_2}$ is due to the decrease in reflected sunlight when gaseous absorption is strong. The sensitivity to p_t is low in the weakly absorbing regions since without gaseous absorption the only effect of increasing p_t is to increase the amount of Rayleigh scatter above the cloud layer which is a small effect. As mentioned in the previous chapter, the sensitivity of I_ν to p_t reaches a maximum where the gaseous optical depth from the top

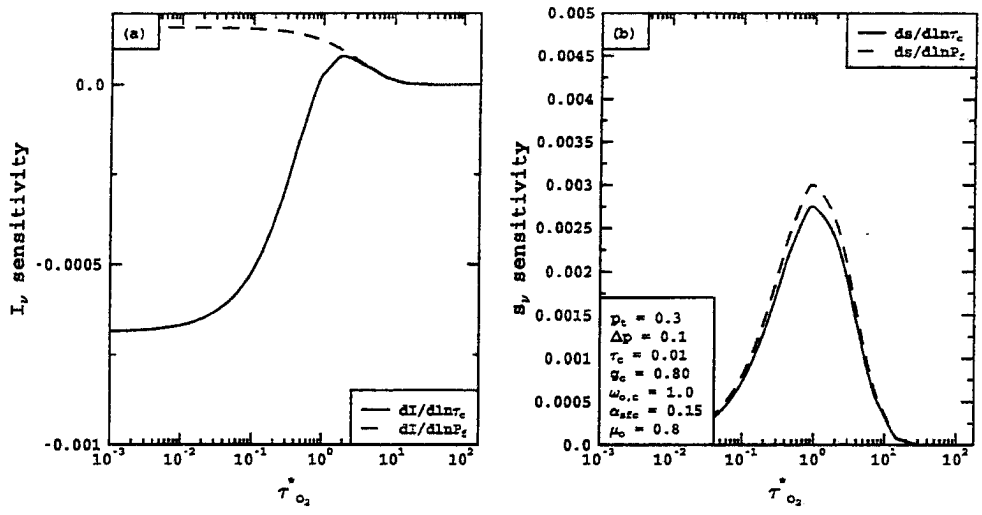

Figure 7.1: Sensitivity of I_ν nd s_ν to cirrus optical depth τ_c, and phase function, P_f.

of the atmosphere to the cloud top equals $\frac{1}{m}$. For the simulations shown in Figs 7.2-7.4, this occurs for $\tau^*_{o_2} = 0.7$ which roughly corresponds to the maximum magnitude of $\frac{\partial I}{\partial \ln p_t}$. There appears to be little sensitivity of I_ν to Δp for all values of $\tau^*_{o_2}$ in Fig 7.2. The negative values of $\frac{\partial I}{\partial \ln \Delta p}$ and $\frac{dI}{d\ln p_t}$ are caused by the increase in τ_{c,o_2}, the amount oxygen optical depth in the cloud layer decreases the reflected radiance.

Values of $\frac{\partial I}{\partial \ln x}$ can be compared to the values of $\frac{\partial s}{\partial \ln x}$ which are shown in the right panels. Since s_ν is formed as a ratio relative to I_c, there is no sensitivity to any of the parameters in the continuum part of the spectrum. As seen from (6.4), in the optically thin limit, $s = e^{-m\tau^*_{o_2}}$ which states that the effective level of scatter is coincident with the lower surface. In general, the addition of scatters or turbidity to an atmosphere raises the effective level of scatter away from the surface and decreases the mean path-length for reflection and therefore increases s. This physical argument is consistent with Fig 7.2, where $\frac{ds}{d\ln\tau_c}$ is positive and $\frac{ds}{d\ln\alpha_{sfc}}$ is negative. An increase in τ_c would tend to raise the effective level of scatter away from the surface while an increase in α_{sfc} would tend to pull the effective level of scatter down. The negative values of $\frac{ds}{d\ln p_t}$ can also be explained by a decrease in the level of scatter since an increase in p_t means a lowering of the scattering

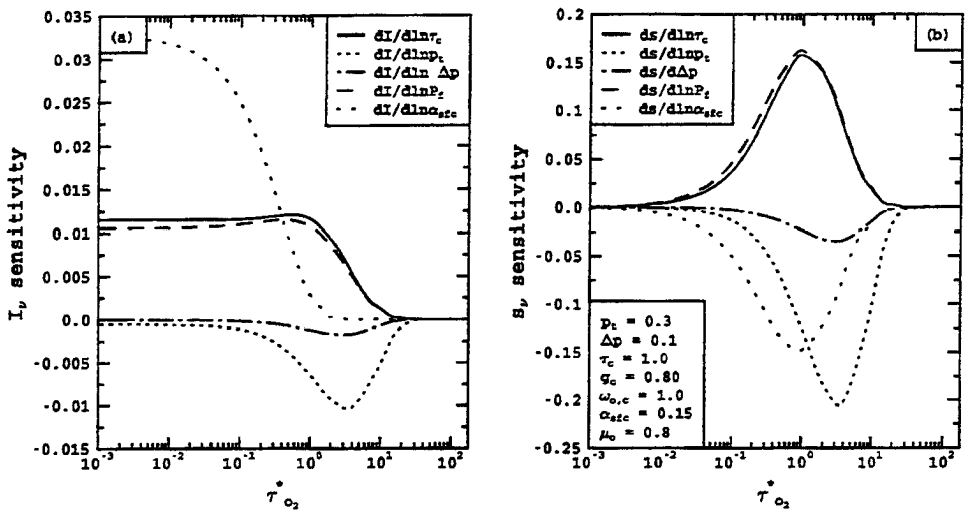

Figure 7.2: Variation of sensitivity of I and s to changes in optical properties as a function of $\tau^*_{o_2}$. The results are for a simulated low cloud with $\tau_c = 1.0$, $g = 0.85$, $\omega_{o,c} = 1.0$, $p_t = 0.3$, $\Delta p = 0.1$, and $\alpha_{sfc} = 0.15$

layer into a more strongly absorbing region of the atmosphere. In addition, the negative values of $\frac{ds}{d\ln \Delta p}$ can also be explained by a lowering of the effective level of scattering. These qualitative arguments can be verified by (4). For example, an increase in either p_t or Δp will clearly decrease the numerator will leaving the denominator, the continuum radiance, unchanged.

7.2.2 Sensitivity variation as a function of Δp

Comparison of the magnitude of the sensitivity of both $I_{\tau^*_{o_2}}$ and $s_{\tau^*_{o_2}}$ in Fig. 7.2 to the corresponding sensitivity for low clouds shown in Fig. 6.2 reveals a sensitivity for cirrus that is much lower than low cloud because for any given Δp, the amount of absorbing gas in the cloud layer is smaller at low pressure (high cloud) than at high pressure (low cloud). Similar to section 6.3.2, the sensitivity of the A-band observables to changes in Δp are explored as function of Δp. As the layer pressure thickness decreases, the amount of gaseous absorption in the cloud decreases. From Figs 7.5 and 7.6, it is clear that accurate retrievals of Δp are not possible from A-band nadir reflectance spectra. As

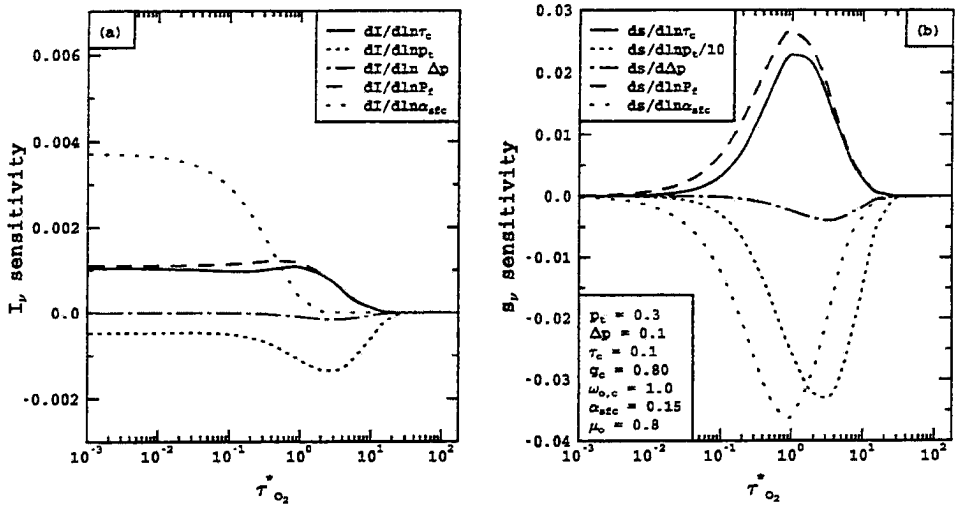

Figure 7.3: Same as Fig 7.2 except $\tau_c = 0.1$

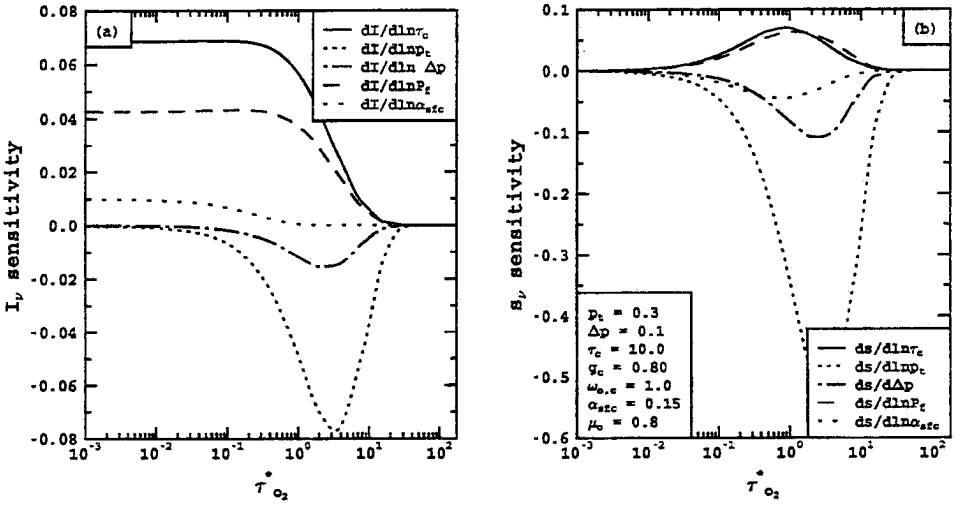

Figure 7.4: Same as Fig 7.3 except $\tau_c = 10.0$

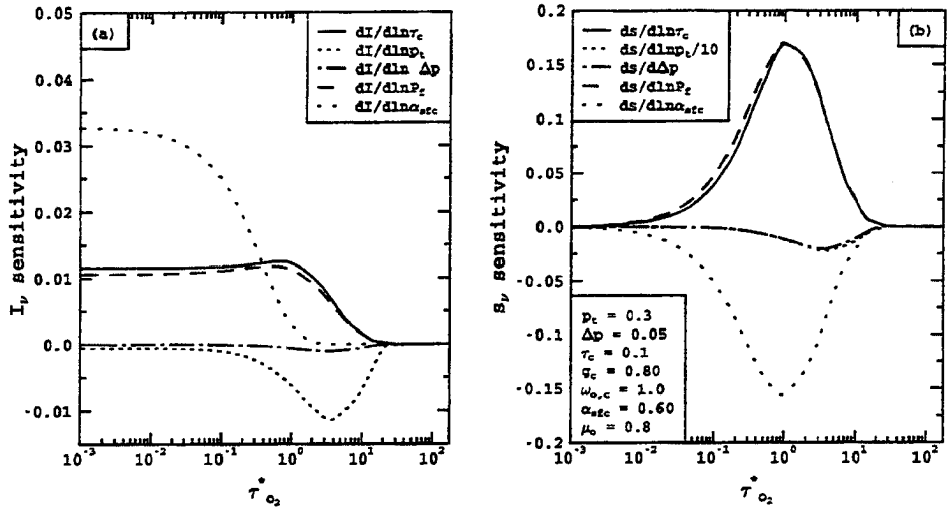

Figure 7.5: Same as Fig 7.2 except $\Delta p = 0.05$ (50 mb)

a consequence, the following retrievals will show little ability of an A-band retrieval to estimate Δp meaningfully. However, because of the low sensitivity of both the radiance and the radiance ratio, error in the assumed value of Δp should have little effect on the errors of the other parameters. This is consistent with comparison of the sensitivity of the other parameters in Figs 7.2, 7.5 and 7.6 which change little for the different values of Δp.

7.2.3 Sensitivity variation as a function of α_{sfc}

The sensitivity of the A-band radiances to α_{sfc} is shown in Figs. 7.2, 7.7 and 7.8. The radiance sensitivity to both τ_c and P_f shows a decrease in magnitude as α_{sfc} increases in the continuum part of the spectrum. Single scatter theory predicts no sensitivity of I_ν to the value of P_f (7.2). For optically thick cirrus clouds, which produce sufficient multiple scatter over a bright surface, the contribution from multiple reflections between the cloud and the surface can be much larger than the contribution by scattering within cloud. Therefore, the sensitivity to $P_f(\mu, \mu_o)$ decreases with increasing surface albedo. Similarly, (7.4) predicts a decrease in the sensitivity in τ_c due to to the decrease in the sensitivity to P_f. In the more strongly absorbing parts of the spectrum, the surface effects

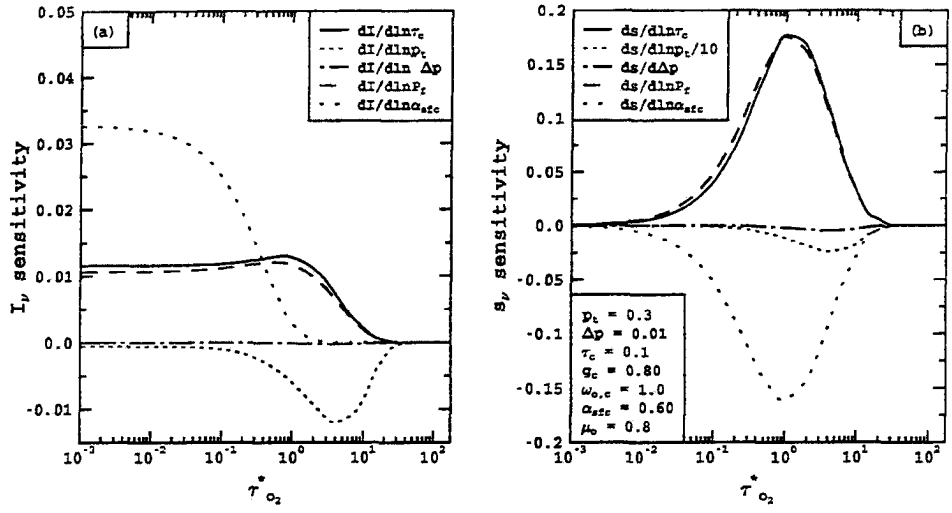

Figure 7.6: Same as Fig 7.3 except $\Delta p = 0.01$ (10mb)

are reduced and the sensitivity to both τ_c and P_f increase. This example clearly illustrates the advantage of having high resolution measurements which allow the cloud scattering to be isolated from scattering at the surface or lower in the atmosphere.

The sensitivity in s_ν to τ_c shows the maximum sensitivity for the moderate surface albedo case, $\alpha_{sfc} = 0.15$. As explained before, the value of s_ν is related to the effective level of scatter in the atmosphere. For a dark surface, there is no significant contribution from the lower atmosphere so that changes in τ_c do not have a large effect of the effective level of scatter. Similarly, for a very bright surface, the effective level of scatter is fixed near the surface unless the cloud becomes optically thick enough to screen the photons from the surface. In the weakly absorbing continuum, the sensitivity of the s to τ_c actually becomes negative which, according to (7.4), is possible for bright surfaces. As an additional consequence, the sensitivity of $s_{\tau^*_{o_2}}$ to p_t also decreases for case of cloud over a bright surface. Like the radiance sensitivities, the ability to look into deep absorption lines allows the A-band retrieval to isolate the cloud form the surface and thus provides a way of retrieving cirrus properties even over a bright surface.

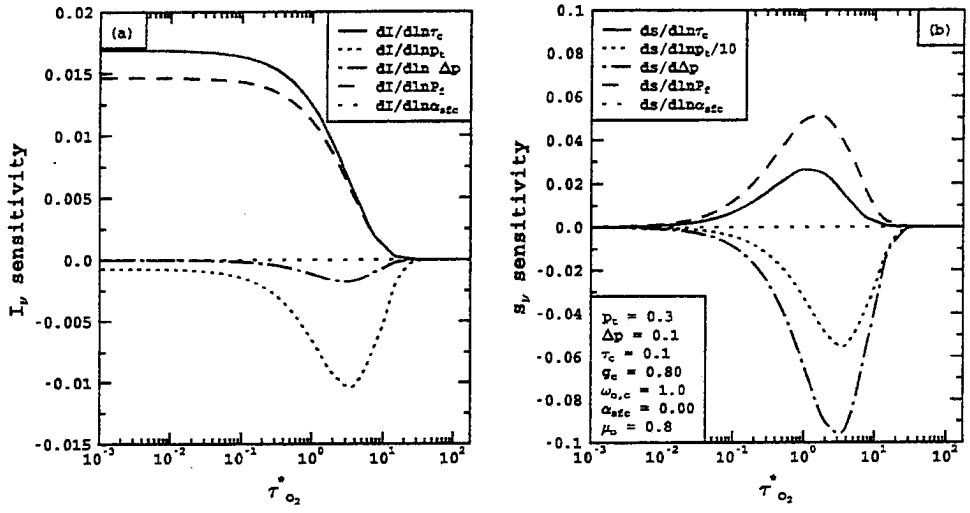

Figure 7.7: Same as Fig. 7.2 except $\alpha_{sfc} = 0.00$.

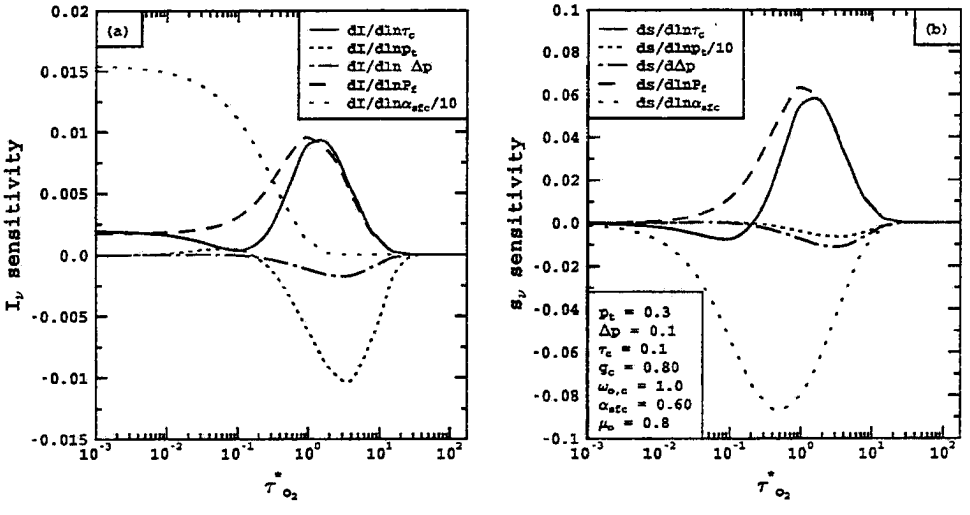

Figure 7.8: Same as Fig. 7.2 except $\alpha_{sfc} = 0.60$

7.3 Sample Retrievals

In the previous section, the sensitivity of the optical parameters listed earlier in the chapter were explored for representative low cloud scenarios. In this section, we apply the retrieval method developed in Chapter 5 and the forward model developed in Chapter 4 to perform sample cirrus retrievals. These retrievals will give an indication of the ability of A-band retrievals to exploit the above sensitivities and extract estimates of the optical properties of cirrus cloud layers. As in the previous chapter, the following discussion considers separately retrievals based on radiances, retrievals based on radiance ratios, and retrievals using the combination of I_ν and s_ν.

7.3.1 Phase Function Errors for Cirrus Retrievals

Due to the large variation in cirrus ice crystal size and shape, the variation in the single scattering phase function is much larger for cirrus than it is for clouds composed of water droplets. Actual measurement of cirrus phase functions are lacking and most studies which attempt to use realistic phase functions resort to scattering models based on specific measurements of ice crystal shapes and size distributions. These scattering models, based on realistic crystal shapes and sizes, produce phase functions with asymmetry parameters between 0.77 and 0.85. For example, the ray-tracing technique applied to hexagonal crystals yields the phase function shown in Fig. 7.9 with a value of $g = 0.83$. Interpretation of aircraft data suggest values for the asymmetry parameters being as low as 0.7 (Stackhouse and Stephens, 1991). Since no current observational evidence points to a preferred phase function, a double Henyey Greenstein (dHG) representation will be used as was done for the low cloud retrievals. The double Henyey Greenstein phase function can be expressed as

$$P(\Theta) = bP_{HG}(g_1, \Theta) + (1-b)P_{HG}(g_2, \Theta) \tag{7.9}$$

where P_{HG} represents the value for the traditional Henyey-Greenstein phase function and g_1,g_2 and b are the parameters which control the shape of the phase function. The effective asymmetry parameter of this phase function is given as

$$g = bg_1 + (1-b)g_2. \tag{7.10}$$

Also shown in Fig. 7.9 are three dHG phase functions with values of g of 0.77, 0.87, and 0.90. The shaded portion of Fig 7.9 therefore represents the range of uncertainty backscattering region of the dHG phase function associated with a given variation in g.

If the true phase function is assumed to be that for the hexagonal crystals, Fig 7.10 shows the errors in the radiance and radiance ratios using the dHG phase function with $g = 0.77$. The errors in Fig. 10 are of the same order of magnitude if the $g = 0.90$ dHG phase function were used. Looking first at the radiance errors, Fig. 7.10 shows the errors are largest for optically thin clouds and decrease with increasing surface albedo. This can be explained by the fact that multiple scattering reduces the sensitivity of the radiance to the detailed shape of the phase function. For optically thick clouds, the sensitivity to the phase function is determined solely by the value of g. Since the difference in the single scatter value of the phase function is much greater than the difference in the values of g, the radiance errors decrease with increasing τ_c. The effect of increasing the surface albedo is to reduce the relative contribution from the cloud scattering and therefore reduces the errors due the cloud phase function. As the amount of gaseous absorption increases, the surface contribution is eliminated and the radiance errors for all values of α_{sfc} become equal. It is clear from Fig. 7.10 that for thin cirrus over a dark ocean, errors of 30 % are possible. The retrievals described in the next sections were performed using a phase function error of 25 % for a dark surface and 5 % when the underlying surface is bright.

The right panel of fig 7.10 shows the errors in the spectral radiance ratio, s_ν. As discussed in Chapter 6, single scatter theory predicts no sensitivity to the phase function for values of s_ν computed over a dark surface. Consistent with this interpretation, the errors in s_ν are lowest for the dark surface case and increase with increasing α_{sfc}. The errors are largest in the strongly absorbing parts of the spectrum since the continuum radiance is affected by the surface while the radiance in an absorbing line is not. Even for the dark surface, in an optically thick case ($\tau_c = 10$), the errors increase in s_ν with increasing $\tau^*_{o_2}$. This increase can be explained by noting that in the continuum multiple scattering reduces the sensitivity to the single scatter phase function. The effect of increasing gaseous absorption is to limit contributions by multiple scattering and to increase the contribution

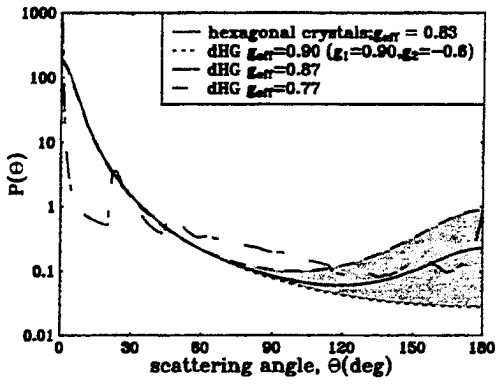

Figure 7.9: Comparison of hexagonal crystal phase function versus a range of double Henyey-Greenstein phase functions

by single scattering, thus increasing the sensitivity to the phase function. Therefore the phase function errors in the continuum and non-continuum radiance no longer cancel even without a surface contribution, leaving s_ν sensitive to the phase function as shown. The error in s_ν is also assumed to take the form given by (6.5) with $\epsilon_{max} = 0.05$ for a dark surface and $\epsilon_{max} = 0.5$ for bright surfaces.

Retrieval of both τ_c and g

As first discussed by van de Hulst(1977), the reflected radiance for an optically thick layer is governed by the scaled optical depth, $\tau' = \tau_c(1-g)$. As a consequence, one is unable to separate the competing effects of changes in τ_c and g from reflectance measurements. In the following cirrus retrievals, the phase function information is assumed to be contained in g so an investigation of the ability of A-band measurements to retrieve both τ_c and g is warranted. Fig. 7.11 shows contours of both the radiance and the radiance ratio for a cirrus cloud as a function of both τ_c and g. The upper left panel shows the contour of radiance for three different values of $\tau^*_{o_2} = 0.0, 1.0, 4.0$, the upper range in $\tau^*_{o_2}$ corresponds to a spectral resolution of $0.5cm^{-1}$. The right panels show the contours in the radiance computed form $\tau_c = 1.0$ but with the three values of α_{sfc} used in the retrieval examples shown later. The lower panels are identical to upper panels except that the radiance ratios are shown. The ability to retrieve τ_c and g is qualitatively related to the difference in the

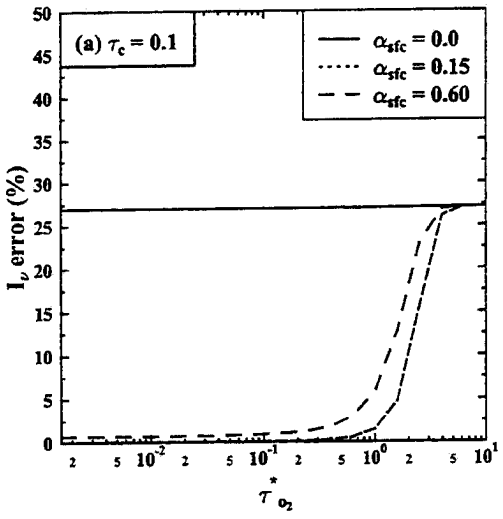
(a) $\tau_c = 0.1$
$\alpha_{sfc} = 0.0$
$\alpha_{sfc} = 0.15$
$\alpha_{sfc} = 0.60$
I_ν error (%)
$\tau^*_{o_2}$

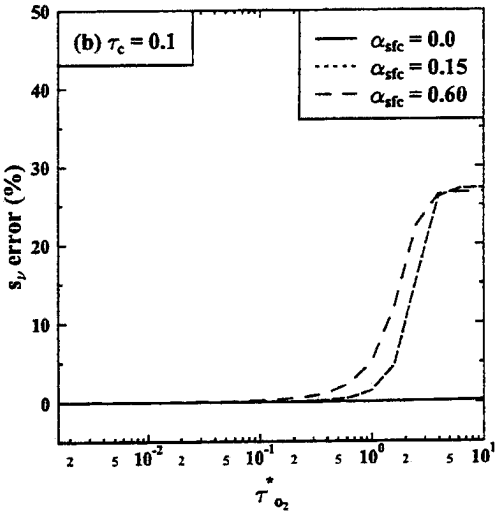
(b) $\tau_c = 0.1$
$\alpha_{sfc} = 0.0$
$\alpha_{sfc} = 0.15$
$\alpha_{sfc} = 0.60$
s_ν error (%)
$\tau^*_{o_2}$

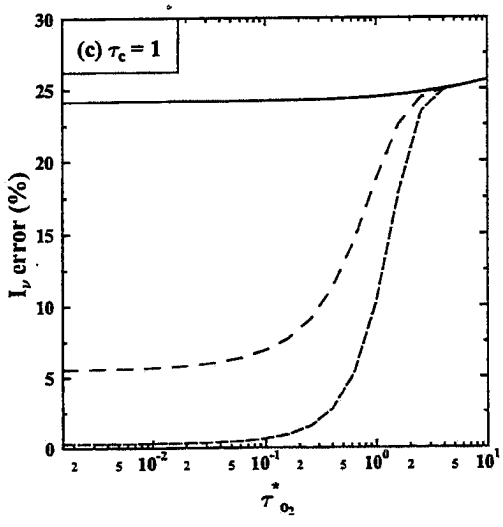
(c) $\tau_c = 1$
I_ν error (%)
$\tau^*_{o_2}$

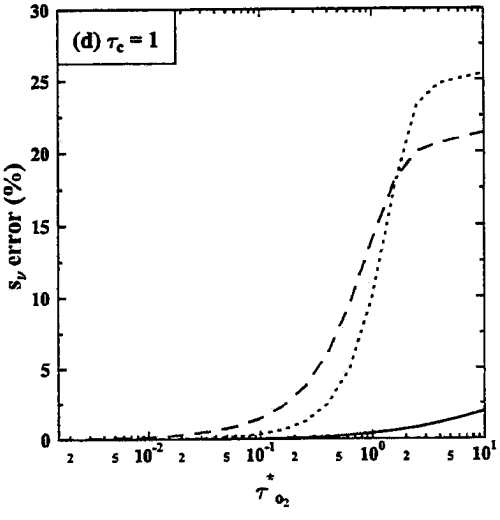
(d) $\tau_c = 1$
s_ν error (%)
$\tau^*_{o_2}$

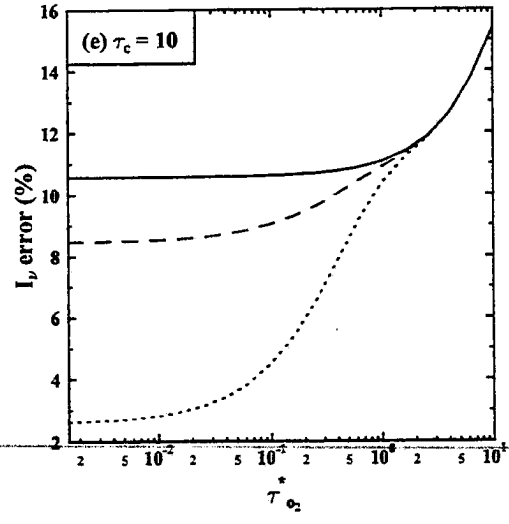
(e) $\tau_c = 10$
I_ν error (%)
$\tau^*_{o_2}$

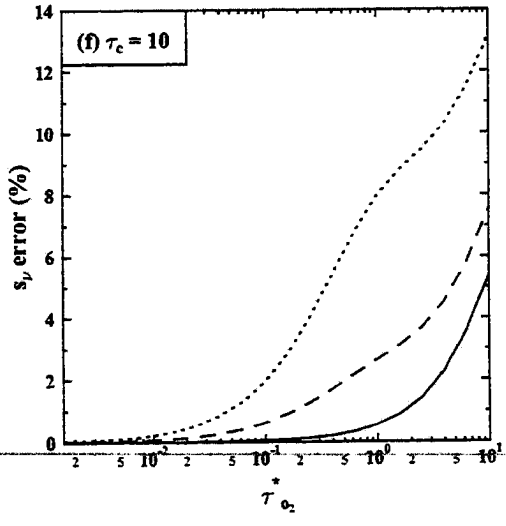
(f) $\tau_c = 10$
s_ν error (%)
$\tau^*_{o_2}$

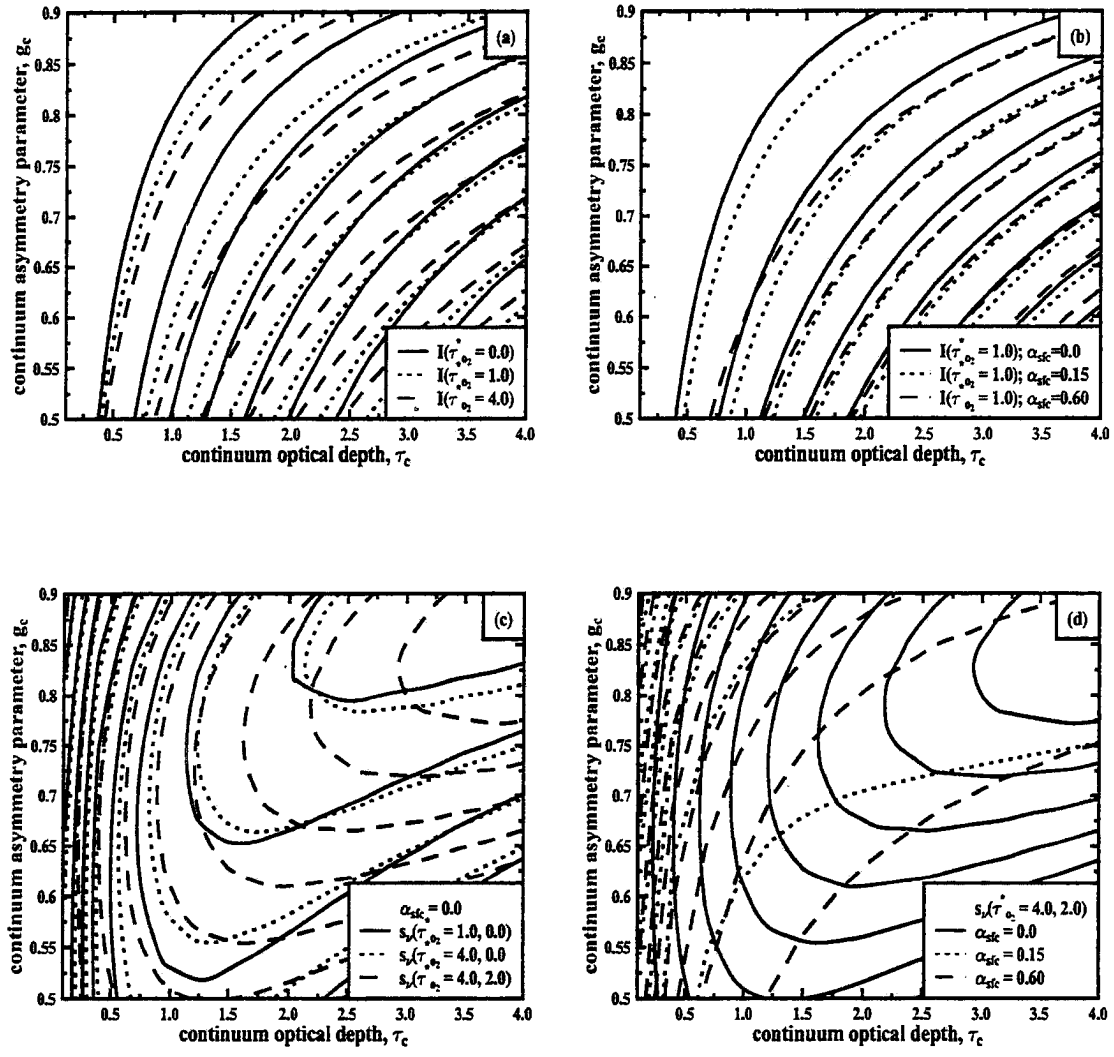

Figure 7.11: Comparison of the contribution of the radiance which has traveled a path l for the domain averaged nadir radiance for cloud field #2 and a plane parallel cloud with the same optical properties.

shapes of the contours. If the contours are parallel to each other, the separation of τ_c and g is impossible. As this figure shows, the ability to look into absorption lines offers little ability to separate the effects of τ_c and g. If the contours of I_ν and s_ν are overlaid however, it evident that performing simultaneous retrievals with both I_ν and s_ν will lead to improved estimates of both τ_c and g. This benefit of combining both observables in the retrieval of cirrus optical properties will be quantitatively verified below.

The previously stated error estimates due to the phase function were based on the assumption that no information about the phase function could be estimated from A-band measurements. As Fig 7.11 shows, A-band spectra clearly do allow for an estimation of phase function information and the previously reported phase function errors are too large. For example, Fig.12 shows the variation in the value of I_ν and s_ν for $\tau^*_{o_2} = 2$ as a function of the phase function asymmetry parameter, g, used in the dHG phase function representation defined above. The true optical properties for this case are a cirrus cloud with $\tau_c = 1.0$ and placed between 300 and 400 mb over a surface with $\alpha_{sfc} = 0.15$. The actual phase function used in simulating the observations was the hexagonal ice crystal phase function shown previously. A dHG phase function, defined above, was assumed for the forward model. The lightly shaded region in Fig. 7.12 expresses the range in both quantities using the true optical depth and the expected range in g of 0.7 to 0.9. A retrieval was performed using the assumed dHG representation for the phase function. The dark shaded region is the difference between the true observations and the forward model computations using the true value of τ_c and the retrieved value of g. The forward model computation using both the retrieved τ_c and g gives a value close to the observed case. Even though the forward model is constrained by an incorrect model of the phase function, it is able to estimate a value of g which reduces the errors in the retrieval of other optical properties, such as τ_c. This ability therefore reduces the sensitivity of A-band retrieval to phase function uncertainties. Using Fig. 7.12 as a guide, when values of g are estimated, the errors due to phase function uncertainties are reduced by a factor of 4.

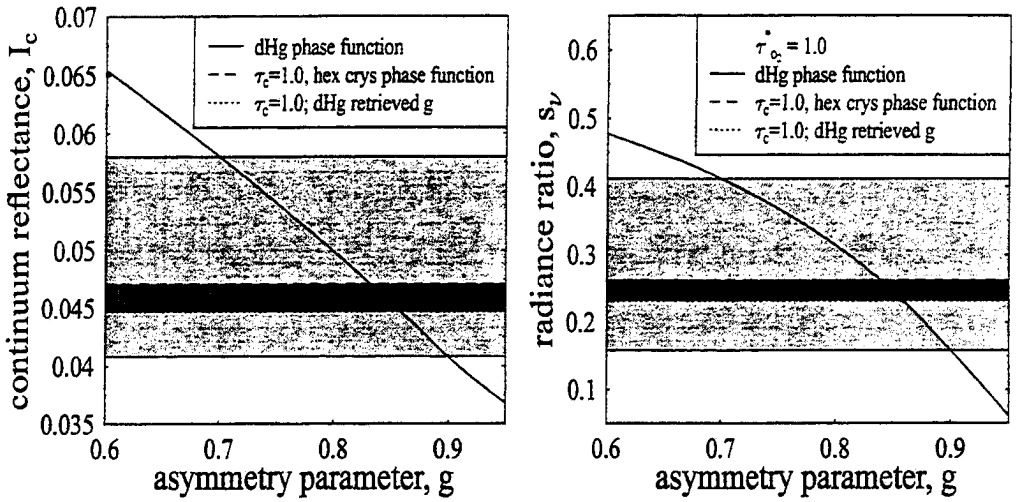

Figure 7.12: Variation of the radiance (left) and radiance ratio(right) with asymmetry parameter for a simulated cirrus scene. Shown are values for the hexagonal crystal phase function and the retrieved dHG phase functions

7.3.2 Radiance Retrievals

Applying the phase function errors described above and the other measurement and forward error estimates described in Chapter 5, the accuracy of A-band retrievals of cirrus properties using only the spectral radiances is now explored. The format for the presentation of the retrieval results is identical to that used in Chapter 6. The right column shows the estimated errors in the retrieved properties and left column shows the value of A for that property. Since the phase function is an unknown and variable quantity in cirrus clouds, an additional property, the phase function asymmetry parameter, g, will also be shown. For cirrus clouds, the list of retrieved parameters, $\tilde{x}$ becomes then

- τ_c - the cloud optical depth,
- g - the cloud phase function asymmetry parameter,
- p_t - the cloud top pressure,
- Δp - pressure thickness of cloud layer, and
- α_{sfc} - surface albedo

Again, as with water droplets, ice crystals at A-band wavelengths are known to be highly conservatively scattering and the single scatter albedo, $\omega_{o,c}$ will be assumed to be 1.0 and not retrieved. The 5 rows in the following figures will relate then to each of the retrieved properties list above. As was done for the low cloud retrieval results, retrieval results will be shown for retrievals based on the spectral radiance, I_ν, on the spectral radiance ratio, s_ν, and for retrievals using both quantities. The retrieval results will be shown as a function of τ_c for three varying values of α_{sfc}.

The following retrievals will assume a base state of a cirrus cloud placed between 300 and 400 mb in a mid-latitude summer atmosphere. The solar zenith is fixed at 36^o and the viewing is fixed at nadir. The underlying surface is assumed to be Lambertian with the given surface albedo. The purpose of these retrievals is not to show results for all possible cirrus conditions but to simulate enough realistic scenarios to identify possible strengths and weakness of cirrus retrievals using A-band spectra.

The retrieval results for the retrievals using only I_ν are shown in Fig. 7.13. As the described above, retrievals of cirrus based on I_ν alone are sensitive to uncertainties in the phase function due to an inability to estimate both τ_c and g meaningfully. This effect is seen in Fig. 7.13 by the errors in τ_c being roughly 50 and the errors in g being near 10uncertainty in g. This weakness of the retrieval is also witnessed by the relatively low values of A for both τ_c and g for all values of τ_c. The retrievals using I_ν can estimate p_t for optically thin cirrus ($\tau_c < 1$) to within 15% (40 mb) for all surfaces. For optically thick cirrus, p_t can be estimated to within 10% (30mb). It appears that the retrieval using I_ν can accurately estimate α_{sfc} with errors less than 3% for $\tau_c < 1$. Errors increase in α_{sfc} for thick cirrus due to a lack of sensitivity of nadir reflectance to surface characteristics. As the last row of Fig 7.13 shows, a retrieval using only I_ν has difficulty estimating the pressure thickness, Δp, of cirrus for any conditions. It is important to note that the errors in any one property are related to the errors and uncertainties in each other property. As will be shown in Chapter 10, the additional constraints provided by active sensors on certain properties (i.e. p_t or Δp) can greatly reduce the errors in all estimated properties.

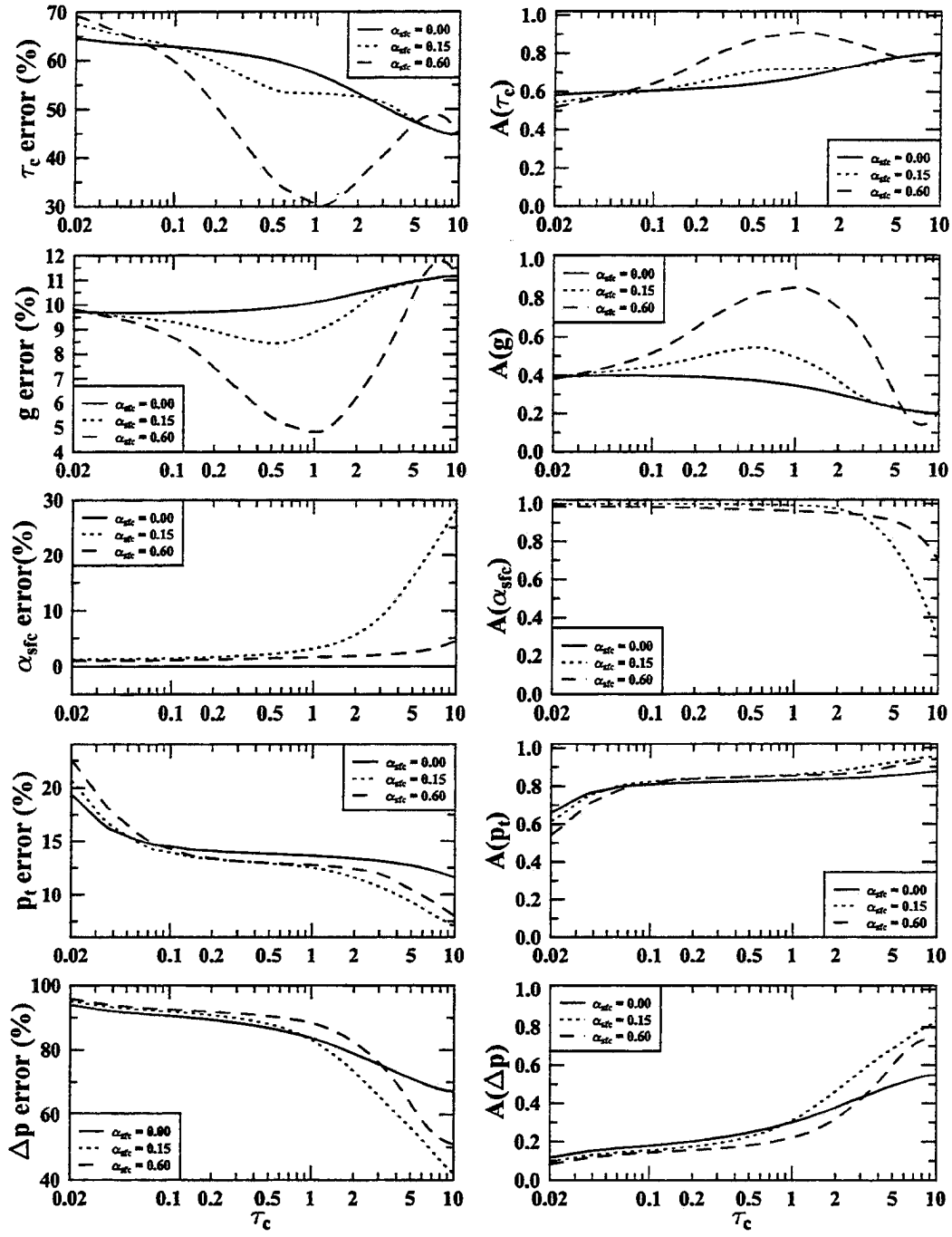

Figure 7.13: Estimated retrieval errors and reliance on *a priori* constraints for retrieval of cirrus properties from nadir reflected radiance

7.3.3 Radiance Ratio Retrievals

In the last chapter concerning low cloud retrievals, the retrievals based on the spectral radiance ratios, s_ν were inferior to those based on I_ν. Theoretical arguments previously have shown the sensitivity of s_ν is sensitive to the effective level of scattering in the atmosphere. For optically thick low clouds, there is relatively less sensivitity of the effective level of scatter on the cloud properties excluding the cloud top pressure, p_t. Due to greater altitude and smaller optical thicknesses of cirrus clouds, the level of scatter is much more influenced by the optical properties of the cirrus layer. As a result, the retrievals based on s_ν alone, shown in Fig. 7.14, for cirrus contain relatively more information than the retrievals based on s_ν alone for the low cloud simualtions. For example, the s_ν retrieval is able to estimate τ_c within 30% for the bright surfaces and roughly 50% for the dark surface. The larger errors for the dark case can be explained by noting that the effective level of scatter for a dark surface is fixed at the cloud layer and has little sensitivity to the optical depth of the cirrus. The general reduction in the errors in τ_c can be attributed to a better ability of the retrieval to estimate g and reduce the sensitivity to phase function errors. Accurate estiamtes of g for thin cirrus ($\tau_c < 0.2$) appear possible for dark surface and this accounts for obsevred relatively low errors in τ_c for thin cirrus over a dark surface. The retrievals using s_ν can estimate p_t for optically thin cirrus ($\tau_c < 1$) to within 15% (40 mb) for the bright surfaces and to within 10% (30mb) for the dark surface. For optically thick cirrus, p_t can be estimated to within 5% (15mb) and to with 10% (30 mb) for the bright surfaces. Unlike the retrieval using I_ν, the retreival based on s_ν is able meaningfully estimate Δp in the case for a dark surface with errors of less than 20 % occuring for $\tau_c > 1$. The retrieval is unable to estimate Δp for cirrus over bright surfaces.

7.4 Combined Radiance and Radiance Ratio Retrievals

The results above showed the retrievals based on I_ν or s_ν alone had differing strengths and weaknesses. For example, α_{sfc} was better estimated using I_ν than using s_ν. Also estimates of τ_c were more accurate using s_ν than using I_ν. Using a retrieval using both quantities simultaneously should lead to a superior than with alone. In addition, previous

results indicate that a combined retrieval should offer a much improved ability to retrieve τ_c and g independently. The results of combined retrieval using I_ν and s_ν in Fig. 7.15 are consistent with this argument. The combined retrieval is now able to estimate τ_c to within 20 % for τ_c between 0.1 and 4 for the dark and very bright surface. The errors are slightly larger for the moderately bright surface but are still much improved for either of the individual retrievals. The reason for this improvement in the estimation of τ_c is due to increase in the ability to estimate g. For the combined retrieval, errors in g are less than 3% for $0.1 < \tau_c < 4$ except for the moderately bright surface where the errors in g are within 5 %. In addition, the increase in the validity of the estimates of τ_c and g in combined retrieval compared to the individual retrievals can be seen in the increase of the values of A for each parameter, showing a decrease in the reliance on the *a priori* in each case. The combined retrieval is clearly able to rely on the I_ν observations to retrieve α_{sfc} with roughly same accuracy as in the retrieval using only I_ν. As expected the errors in p_t and Δp for the combined retrieval are close to those for the s_ν based retrieval since values of I_ν offered little information in these two cases.

7.5 Conclusions

Using the both the radiance and ratios from nadir A-band reflectance spectra, meaningful estimates of cirrus properties are obtainable even accounting for the phase function uncertainty, the largest source of error in cirrus retrievals. The results in this chapter show that values of τ_c can be estimated to within 20 % and values of surface albedo can be estimated to within 5%. For thin cirrus, the errors in cloud top pressure, p_t are approximately 30 mb and for thick cirrus the errors drop to 10 mb. In addition, the asymmetry parameter can be estimated to with in 3% for many conditions. While the meaning of this asymmetry parameter is couched in the assumed dHG phase function, it still represents information about the true phase function that is unavailable from any other passive instrument. The ability of the A-band retrieval to lessen its sensitivity to phase functions uncertainties produces estimates of cirrus properties far superior to those produce by current visible-near infrared techniques which rely on *a priori* phase function information. In Chapter 10, the

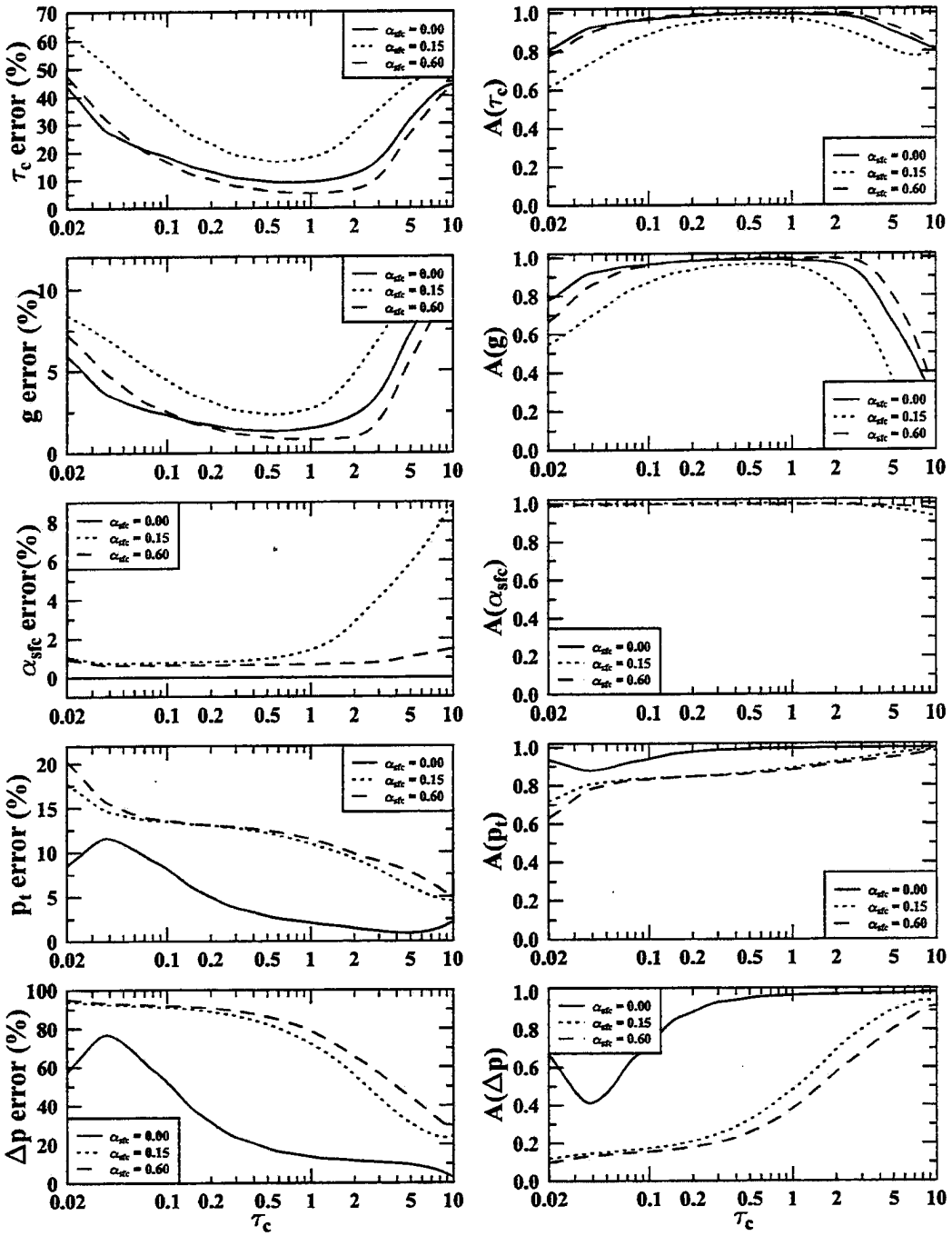

Figure 7.14: Same as Fig 7.12 except for retrievals using both radiance, I_ν and radiance ratio, s_ν.

use of an A-band sensor with a LIDAR will be shown to provide even more information about the phase function than that provided by an A-band sensor.

Chapter 8

Retrieval of Optical Properties from Aerosol Layers

As was pointed out by O'Brien (1995), A-band reflectance spectra of sufficient spectral resolution can be used to detect atmospheric aerosols even over bright surfaces. In his study, O'Brien used single scatter theory and based his retrievals on the differences of measured spectra and computed clear sky spectra. In this chapter, we will also concentrate on the retrieval of aerosol layer optical properties from A-band spectra. As with the previous two chapters, this chapter will begin with a sensitivity analysis of simulated A-band spectra and then performs sample retrievals to attempt to explore how well and under which conditions the properties of aerosol layers can be deduced from A-band spectra.

8.1 Current Methodologies used to retrieve properties of Aerosol Layers

Operational aerosol retrievals are currently based on the visible channels of AVHRR and the GOES instruments. Due to the variation in surface reflectance over land, aerosol retrievals are performed only over the ocean. These methods attempt to retrieve only the total column aerosol optical depth which is dominated by aerosols in the boundary layer, the lowest region in the atmosphere which typically has a height from 1 to 4 km (Stull, 1984). This chapter will also deal mainly with boundary layer aerosols since stratospheric aerosols typically have optical thicknesses of well below 0.01 and are nearly impossible to retrieve from a nadir viewing passive radiometer. In Appendix A, the benefit of limb sounding with an A-band spectrometer is explored and a similar error analysis shows

that accurate profiles of upper tropospheric aerosol profiles are possible. As described in Chapter 6, the visible sensors of AVHRR and GOES have no profiling ability and are unable to distinguish between surface and cloud/aerosol reflectance. The sensitivity results and sample retrievals below show that A-band retrievals are able to separate the effects of aerosol and surface scatter. In addition, these results will show that under certain conditions, additional optical properties over and above the total optical depth can be retrieved.

8.2 Sensitivity Analysis of A-band Spectra from Aerosol Layers

This section will explore the sensitivity of the two A-band observable, $I_{\tau^*_{o_2}}$ and $s_{\tau^*_{o_2}}$, to the vector of optical properties listed in Chapter 6. Since we are dealing with aerosols, whose single scatter albedo $\omega_{o,c}$ is not necessarily known *a priori* and varies with particle composition and size, sensitivities to $\omega_{o,c}$ will be shown. In the previous chapters, which dealt with cloud retrievals, the sensitivities to $\omega_{o,c}$ were ignored since $\omega_{o,c}$ is considered known and to be near unity. In addition, since boundary layer aerosols tend to be well mixed, the aerosols will be assumed to distributed evenly between the lower surface and some the layer-top pressure, p_t. Therefore the sensitivities to p_t and Δp are equivalent. The deviation of the actual profile from this assumed profile is another source of error in the forward model. For these sensitivity studies, values of $\omega_{o,c}$ of 0.90 were used which approximates the value for urban-residential regions quoted by Waggoner *et al* (1981). Values of $\omega_{o,c}$ range from 0.5 for urban-industrial to over 0.95 for remote locations. The total column visible optical depths of boundary layer aerosol range from near 0 to over 0.8. Since aerosols are small than cloud particles, their scattering is more isotropic and a phase function asymmetry parameter of 0.75 will be used in the following sensitivity analysis.

The sensitivity of the optical properties of aerosol are qualitatively similar to the sensitivities shown previously for cloud layers. The use of single scatter theory to qualitatively explain the behavior of the sensitivities was beneficial in the analysis of the cloud parameter sensitivities and is therefore applied again the aerosol retrieval problem. The single

scatter sensitivities to all optical parameters except $\omega_{o,c}$ have been previously shown. Using (7.1), the sensitivity of the A-band observables to changes in $\omega_{o,c}$ can be expressed as

$$\frac{\partial I_{\tau^*_{o_2}}}{\partial \ln \omega_{o,c}} = I_{atm,\tau^*_{o_2}} = \frac{\partial I_{\tau^*_{o_2}}}{\partial \ln P_f(\mu,\mu_\odot)} \tag{8.1}$$

for radiance and for the spectral radiance ratio as

$$\frac{\partial s_{\tau^*_{o_2}}}{\partial \ln \omega_{o,c}} = \frac{I_{atm,\tau^*_{o_2}}}{I_c} - s_{\tau^*_{o_2}} \frac{I_{atm,c}}{I_c} = \frac{\partial s_{\tau^*_{o_2}}}{\partial \ln P_f(\mu,\mu_\odot)}. \tag{8.2}$$

where I_{atm} is the radiance scattered by the atmosphere alone and I_c is the total radiance in the continuum, including both atmospheric and surface scattering. From these equations, it is evident that single scatter theory predicts the the sensitives with respect to phase function and $\omega_{o,c}$ are essentially identical. As the following simulations will show however that multiple scattering causes these sensitivities to differ significantly from each other.

As a basis for the sensitivity studies, an aerosol layer with the properties ($\omega_{o,c} = 0.90, g = 0.75$) was placed between the surface and 900 mb. The optical depth, τ_c was set to 0.1 and the underlying surface was assumed to be a Lambertian reflector with an albedo of 0.15. Fig 8.1 shows the sensitivity of $I_{\tau^*_{o_2}}$ and $s_{\tau^*_{o_2}}$ to changes in the appropriate optical parameters for the scenario described above. The results from Fig 8.1 can be compared to the results for a cirrus cloud of the same optical thickness to indicate the effects of layer height on the sensitivities. From the radiance sensitivities, we note several features unique to these aerosol simulations. For the surface albedo used here, $\alpha_{sfc} = 0.15$, there is very little sensitivity in the radiance the changes in aerosol optical depth,τ_c, for all values of $\tau^*_{o_2}$. This occurs since the increase in aerosol scatter is offset by a decrease in the surface scatter. As will be shown later, the sensitivity of $I_{\tau^*_{o_2}}$ is a strong function of α_{sfc}. Since the phase function and $\omega_{o,c}$ have little effect on the contribution from the surface, the offsetting effects do not occur and the sensitivities of I to both P_f and $\omega_{o,c}$ are positive in all simulations. While single scatter theory predicts an identical sensitivity of the radiance to phase function and $\omega_{o,c}$, multiple scattering acts to increase the value of $\omega_{o,c}$ over the P_f. As described earlier, multiple scattering decreases the sensitivity of the radiance to the details of the phase function leaving a sensitivity only to the asymmetry parameter

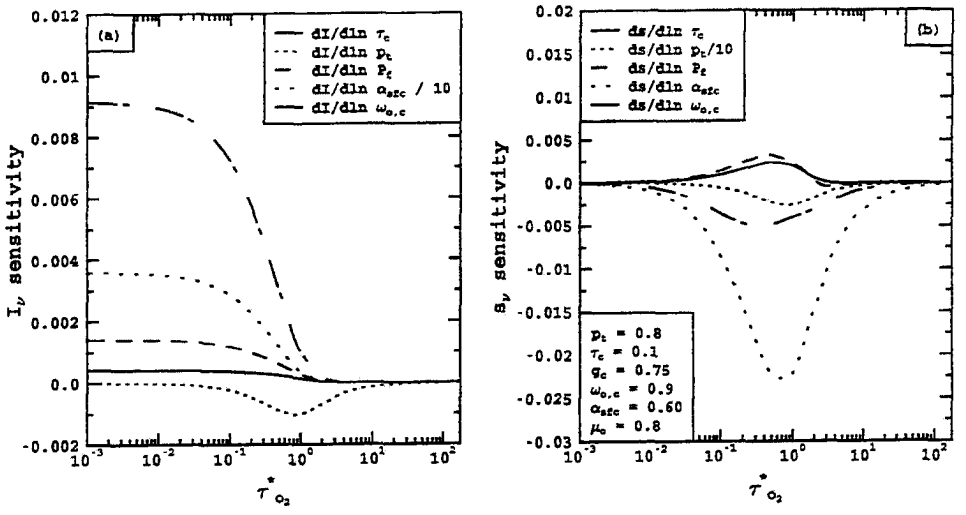

Figure 8.1: Variation of the sensitivity of I_ν and s_ν to changes in optical properties as a function of $\tau^*_{o_2}$. The results are for an aerosol layer with $\tau_c = 0.1, g = 0.75$, $\omega_o = 0.90$, $p_t = 0.8(800mb)$ and $\alpha_{sfc} = 0.15$.

of the phase function, g. The sensitivity of the radiance to $\omega_{o,c}$ increases due to multiple scattering since the radiance scattered n times is proportional to $\omega^n_{o,c}$.

The sensitivities of the radiance ratio, s_ν to the aerosol parameters for the simulation described above is shown in the left panel of Fig 8.10. As (8.2) indicates, single scatter theory predicts a negative value for $\frac{\partial s}{\partial \ln \omega_{o,c}}$ for all values. An increase in $\omega_{o,c}$ will lead to an increase in the contributions from multiple scattering in the aerosol layer which will increase the path-length and absorption due to O_2 and cause a decrease in s_ν. Again the sensitivity to τ_c is low for all values of $\tau^*_{o_2}$. As with the low cloud and cirrus sensitivities, increasing p_t lowers the effective level of scatter in the atmosphere and lowers the value of s_ν.

8.2.1 Variation of Sensitivities with τ_c

Measurements of total column aerosol visible optical depth range from below 0.01 to nearly 1.0. The changes in the parameter sensitivities to the value of τ_c is explored in Figs 8.2 and 8.3. Fig 8.3 shows the same sensitivity analysis in Fig 8.1 except for an optically thinner

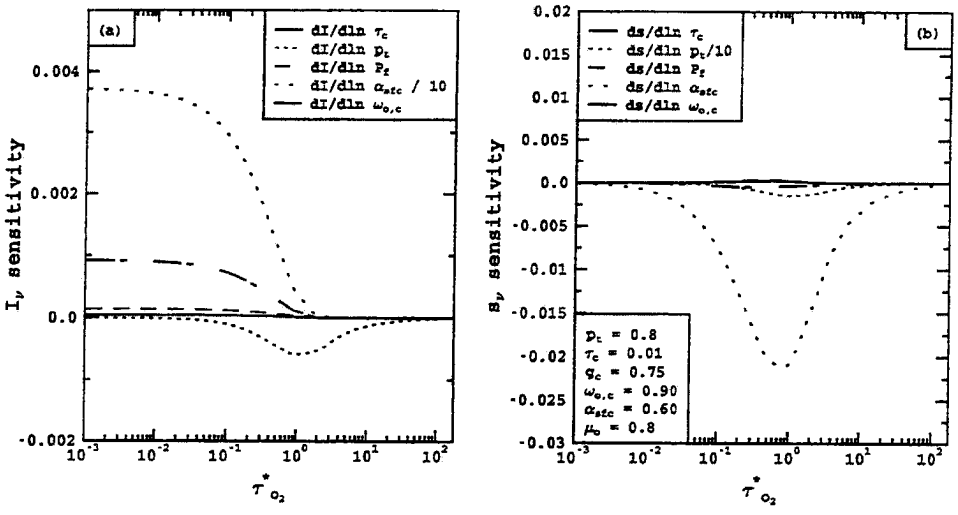

Figure 8.2: Same as Fig 8.1 except $\tau_c = 0.01$

layer of aerosol with $\tau_c = 0.01$. As Fig 8.2 shows, the sensitivity to τ_c is virtually negligible for the optically thin layers of aerosol near the surface over a moderately reflecting surface ($\alpha_{sfc} = 0.15$). In addition the sensitivity to p_t for both observables is greatly reduced for $\tau_c = 0.01$ compared to $\tau_c = 0.1$ shown in Fig 8.1. The sensitivity to P_f is also reduced in the optically thin case due to the dominance of surface reflection. As would be expected, the sensitivity to α_{sfc} is the dominant term of the parameter sensitivities for the optically thin case. Fig 8.3 shows an identical sensitivity analysis performed for a very thick layer of aerosol, $\tau_c = 1.0$. Compared to Fig 8.1, the sensitivities of all parameters increases relative to the sensitivity to α_{sfc} as the τ_c increases. A striking feature of these simulations is the rapid increase in the sensitivity of both observables to $\omega_{o,c}$ as τ_c increases. This increase can be explained by the rapid and non-linear increase in the multiple scattering in the aerosol layer.

8.2.2 Variation of Aerosol Sensitivities with α_{sfc}

The properties of the lower reflecting surface have a large effect on any retrieval attempting to estimate the optical properties of an aerosol layer located low in the atmosphere. Since aerosol layers are located near the surface, A-band measurements have difficulty in

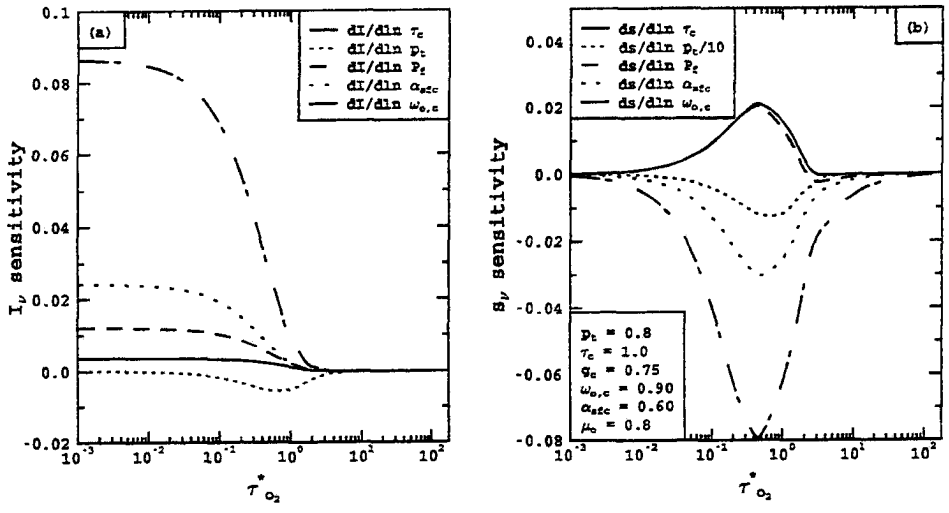

Figure 8.3: Same as Fig 8.1 except $\tau_c = 1.0$

isolating the radiative contributions from the aerosol layer and the surface. The effect of the albedo of the lower surface on the sensitivities of the A-band observables to the optical properties is shown in Figs. 8.4 and 8.5. As predicted by the single scatter analysis performed above, the sensitivities of both observables to τ_c, P_f and $\omega_{o,c}$ are similar. Comparison of the magnitudes of these sensitivities to those for moderately reflecting surface shown in Fig 8.1 shows a dramatic increase for the dark surface case. This is to be expected since the only other contribution to the radiance is that due to Rayleigh scatter. This figure shows why the success of most aerosol retrievals has been limited to retrievals over oceanic surfaces with low surface albedoes (Stowe *et al*, 1994). In addition, both observables are more sensitive to p_t for the dark surface than for a reflecting surface. Fig 8.5 shows the same analysis performed for a bright surface ($\alpha_{sfc} = 0.60$). Like a low cloud over a bright surface, this scenario represents a challenge to current retrieval schemes. As would be expected for an absorbing aerosol over a bright surface, the sensitivity of the radiance is negative to τ_c. In addition, since the main contribution to the observed radiance of τ_c for a scene with an aerosol layer over a very bright surface is the attenuation of radiance reflected off the surface, the radiance shows little sensitivity to either p_t or P_f.

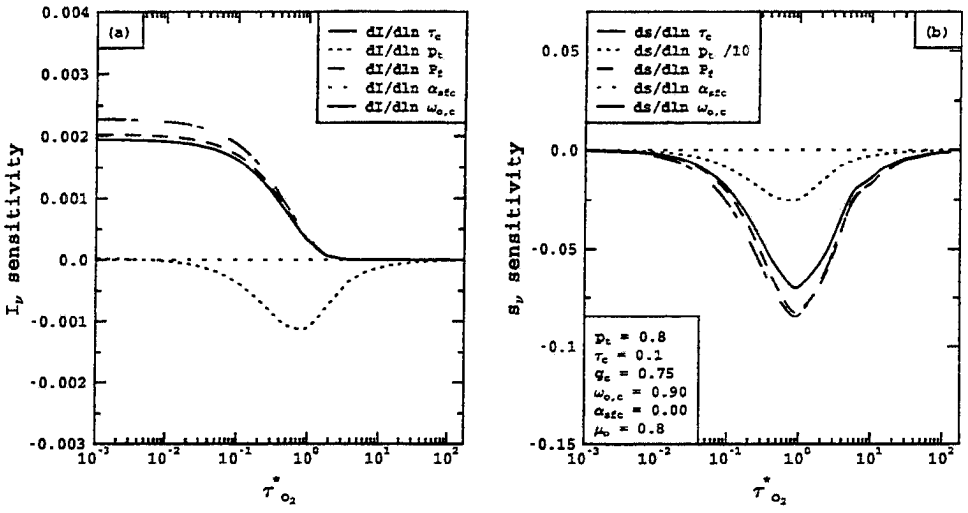

Figure 8.4: Same as Fig 8.1 except $\alpha_{sfc} = 0.0$

One noticeable feature of Fig 8.6 is the high sensitivity of the radiance to changes of $\omega_{o,c}$. Similar to the radiance sensitivity, the radiance ratios show little sensitivity to both P_f, τ_c and p_t. This lack of sensitivity to τ_c and p_t is because most of the scattering occurs near the surface and the effective level of scatter is little effected by τ_c and p_t for the optical thicknesses of aerosol layers. Again, the the radiance ratio shows a significant sensitivity to $\omega_{o,c}$.

8.2.3 Variation of Aerosol Sensitivities with p_t

As mentioned previously this chapter deals with the retrieval of boundary layer aerosols. Since the aerosol tend to be well-mixed, the layers are assumed to occupy the region from the surface to some pressure level, p_t. The value of p_t determines the amount of the oxygen absorption contained within the scattering layer. The higher the layer extends into the atmosphere, the more easily can the retrievals isolate its properties from those of the surface. In Fig 8.1, p_t was set to 0.8 and in Figs 8.6 and 8.7, the value of p_t is varied from 0.7 to 0.9.

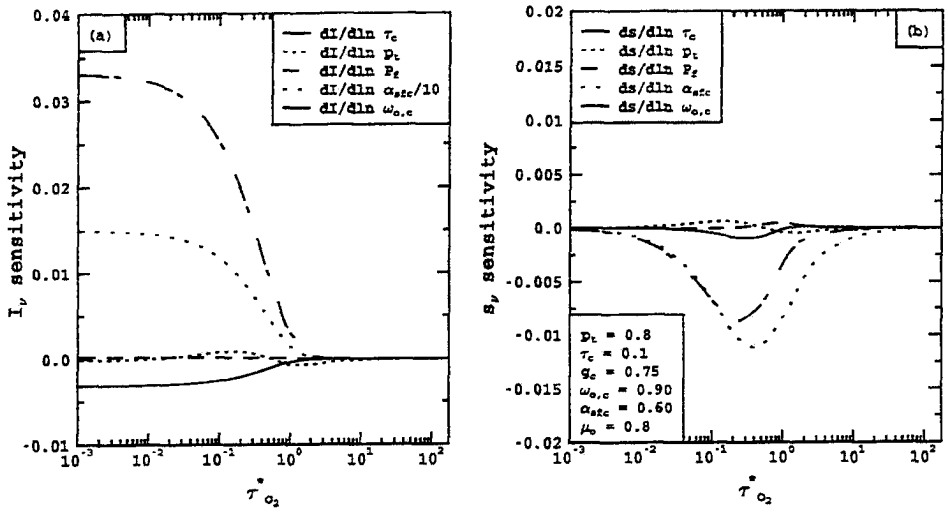

Figure 8.5: Same as Fig 8.1 except $\alpha_{sfc} = 0.60$

8.3 Sample Retrievals

This section explores the retrieval of the above mentioned parameters using nadir reflectance measurements in the A-band. As was done with the previous two chapters, the magnitude of the errors in the forward model due to the phase function uncertainty needs to be addressed specifically for the retrieval of aerosols. Actual aerosol phase functions vary with both particle size and composition. Through the process of deliquescence, the phase functions also vary with relative humidity. The detailed simulation of the aerosol phase function is beyond scope of this work. The work of Koepke and Quenzel(1981) use detailed calculations which showed the back-scattering peak of phase functions was known to within 4 % for a wide range of conditions. This error value will used used a guide in the following sample retrievals.

O'Brien(1996) examined the ability of A-band radiances to provide information on atmospheric turbidity which in his study referred to both aerosol and cirrus clouds. The retrieval put forth in this paper was based on the radiance differences between computed clear sky spectra and observed spectra. O'Brien states that clear sky spectra can be modeled to within 1 % which would therefore imply that the surface albedo is know to the

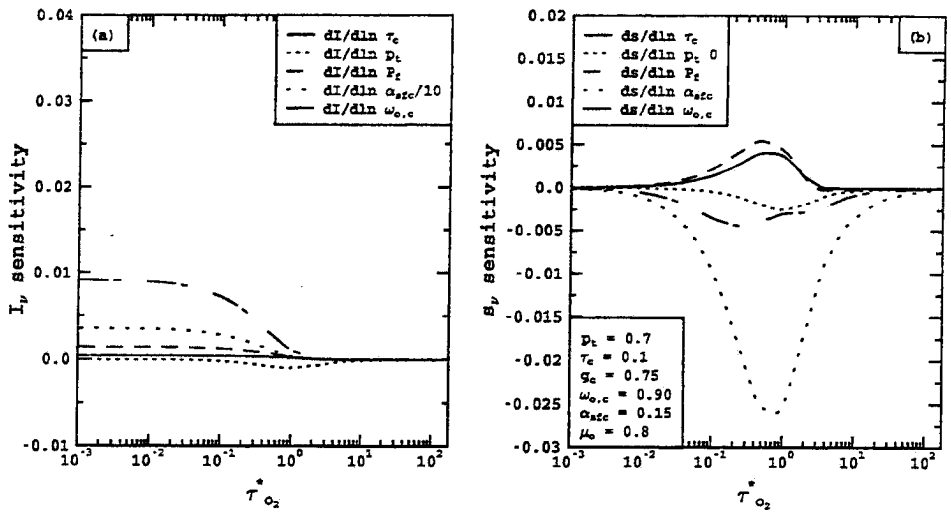

Figure 8.6: Same as Fig 8.1 except $p_t = 0.7(700mb)$

within 1 %. The results of O'Brien demonstrate high levels of accuracy for the retrieval of the layer heights of aerosol, the optical thickness and the surface reflectance. In this work, realistic estimates of errors in both measurements and the ability to model aerosol are used and consequently the errors in this work are greater than the errors proposed by O'Brien(1997). In computing his errors, O'Brien did not include the effects of calibration errors or phase function uncertainties. As the results show, the magnitudes of these errors drive the final error estimates of the retrieval.

The following retrieval results for aerosol retrievals are shown in the same format as used in previous chapters. The left column are the error estimates in the parameters and the right column are the measures of reliance of the retrieval on the *a priori*. The rows will correspond to values for each retrieved parameter, the aerosol optical depth (τ_c), the surface albedo (α_{sfc}), the layer top pressure (p_t) and the single scatter albedo (ω_o). The *a priori* estimates used are similar to those used in the previous chapters. The aerosol optical depth is assumed to be known to within 50 % and the surface albedo is assumed to be known within 10 %. The *a priori* value of p_t is assumed to be within 100 mb of the true value and a 10 % error is assumed in ω_o. When the retrieval is unable to move

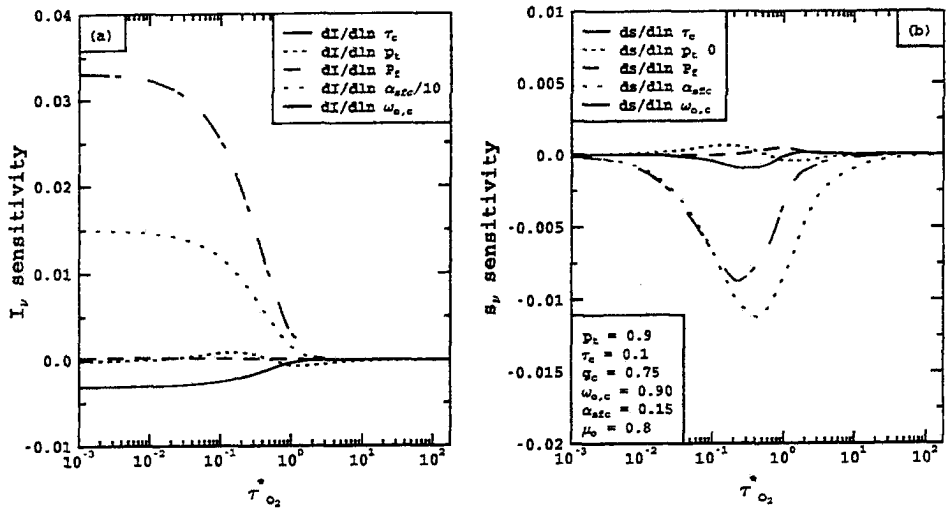

Figure 8.7: Same as Fig 8.1 except $p_t = 0.9(900mb)$

its estimate away from the *a priori* estimates, the retrieved errors will be close to the *a priori* errors and the reliance on the *a priori* will be high ($A \approx 0$). Unlike these previous retrievals which assumed a signal to noise ratio of 400:1, the single to noise ratio in these simulations is assumed to by 4000:1. Current technology allows a space-borne sensor to record spectra over a 400 meter footprint with a snr of 400:1. A snr of 4000:1 would therefore represent an accumulation of pixels representing 4 km by 4 km footprint. The current operational AVHRR aerosol retrievals are also performed on 4 km by 4 km size area (Stowe *et al*, 1997). Since the horizontal distribution aerosol is thought to be much more uniform than clouds, this spatial scale should not cause aerosol heterogeneity to be a problem.

Fig 8.8 shows the retrieval results for a layer of aerosol placed between the surface and 800 mb with solar zenith angle cosine of 0.8. Results were computed for three different surface albedoes roughly approximating a dark ocean, a land surface and snow or ice covered surface. The results in Fig 8.6 were computed assuming no phase function or instrument calibration errors. The only noise in Fig 8.8 is therefore the shot noise defined by an snr of 4000:1. The measurements in Fig 8.8 consist of both radiances and radiance

ratios and have values of $\tau^*_{o_2}$, the total column optical depth in each channel, which corresponds to an instrument with a spectral resolution of $0.5cm^{-1}$.

As the results Fig 8.8 show, the A-band retrievals with only shot noise is able to accurately measure the optical depth of aerosols especially those over oceans ($\alpha_{sfc} = 0.0$). As evidenced by the high values of A, the retrieval is able to estimate both p_t and α_{sfc} accurately. The only difficulty in the retrieval appears to be for estimating τ_c for thin aerosol layers with $\alpha_{sfc} \approx 0.15$. In addition, the retrieval has difficulty in estimate ω_o for values of $\tau_c < 0.1$.

The optimistic results of Fig 8.8 can be compared with the results of Fig 8.7, which contain the effects of phase function and calibration errors. Using the computations of Koepke and Quenzel(1981) as a guide, the phase function errors was assumed to 4 % and consistent with the previous chapters, the calibration error was assumed to 2%. Fig 8.8 shows the results of retrievals using the above errors estimates imposed on the radiances. As Fig 8.7 illustrates, these errors on the radiance have a profound effect on the retrieval. The retrieval has lost the ability to meaningfully estimate the aerosol optical depth over bright surfaces except for very thick layers of aerosol $\tau_c > 0.5$. Also, meaningful estimates of ω_o are now possible only for very thick aerosol layers. Even with these realistic noise estimates, it appears that the retrieval can still meaningfully retrieval p_t and α_{sfc} under all conditions. In addition, the retrieval is still able to provide meaningful estimates of τ_c and p_t over the dark surface. In this case, the A-band retrieval, even with realistic errors, can outperform the operational AVHRR retrieval which can make no estimate of p_t and relies on knowing α_{sfc} accurately.

The dramatic effect of noise on the radiance retrievals as shown in Fig 8.8, suggest that the obvious next step would be be to explore the accuracy of retrievals based solely on the radiance ratio data. As described in Chapter 4, the calibration error disappears in the radiance ratio. In a similar manner, the magnitude of phase functions errors is reduced in the radiance ratio compared to actual errors in the radiance. The small errors in the radiance ratios computed for cloud droplet phase functions are shown in Chapters 6 and 7. Fig 8.10 shows an identical retrieval to the one in Fig 8.8 except that only the

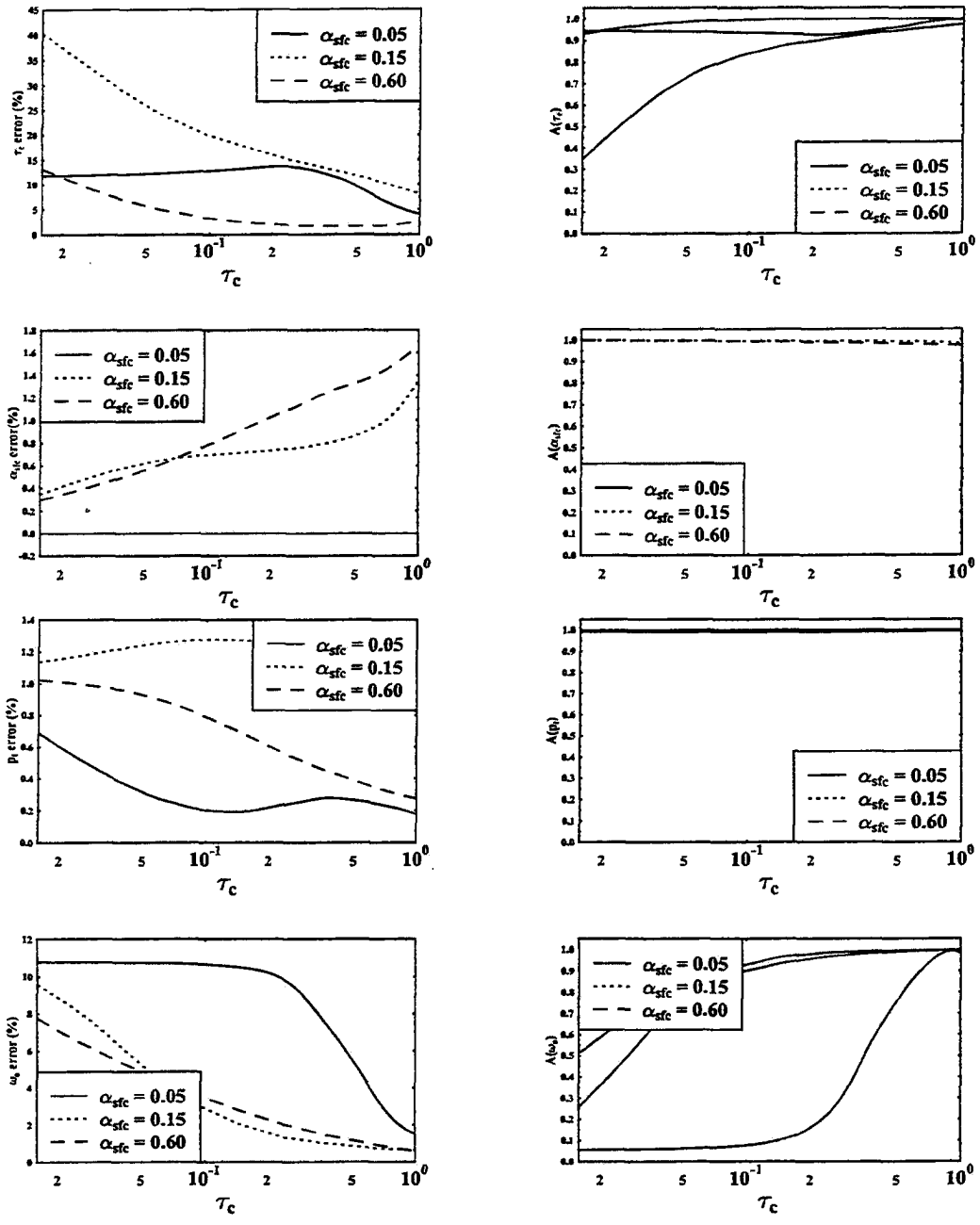

Figure 8.8: A-band retrieval of an aerosol layer place between the surface and 800 mb. The solar zenith angle cosine is 0.8. The signal to noise ratio is 4000:1 and the no calibration or phase function error is assumed.

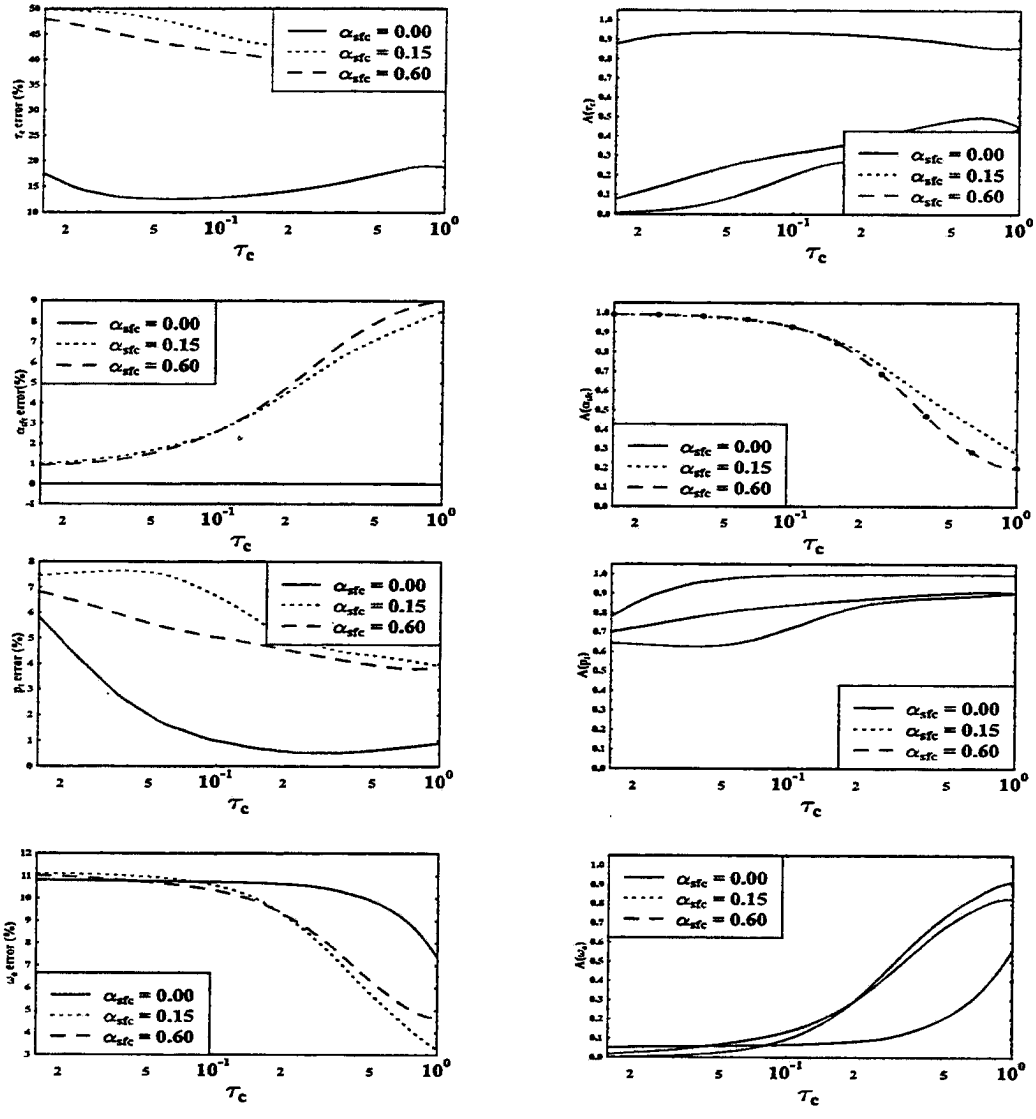

Figure 8.9: Same as Fig 8.8 except that the calibration error is 2% and the phase function error is 4 %.

radiance ratios were used and the phase function errors on the ratios was assumed to 0.5 %. This phase function error is consistent with a phase function error of about 4% on the radiances. As Fig 8.8 shows, even with the low errors on the radiance ratios, the retrieval still has difficulty in providing values of optical depths accurately over land and bright surfaces. This difficulty can be explained by the lack of sensitivity of the radiance ratios to τ_c over both bright and moderately bright surfaces shown earlier in the chapter. The retrieval does well very well at retrieving aerosol optical depths over dark surfaces.

Having shown above that realistic error estimates opposed on the A-band observables greatly limits to ability to remotely sense aerosols over land, the question of what accuracy on the measurements are needed for meaningful aerosol optical depth estimates over land. As indicated above, most the sensitivity to τ_c and ω_o is contained in the radiances and therefore the most benefits to the retrieval would come through a reduction of the errors on the radiances. Fig 8.10 shows the same retrieval performed, above except that only a 1% error is imposed on the radiances. This error can be considered to be due to either calibration or phase function uncertainty since both errors effect the retrieval identically. As Fig 8.10 shows, the radiance retrievals with 1% error now offer meaningful estimates of the aerosol optical depth for all surface albedoes. In addition, errors in ω_o are less than 5 % for values of $\tau_c > 0.2$. This 1% requirement on the ability to match observations and models is consistent with the work of O'Brien(1996), who estimated a 1 % error in the ability of a forward model to simulate radiances relative to an aerosol free atmosphere.

8.4 Conclusions

It is important to place the pessimistic tone of this chapter in context. The results of this chapter clearly show that a space-borne A-band radiometer is clearly capable of outperforming the current visible channel aerosol retrieval methods. With realistic estimates of instrument and forward model noise, the A-band retrievals produce accurate aerosol optical depths over the ocean. In addition, A-band retrievals can accurately estimate both the surface albedo and estimate the layer top pressure, two feats unobtainable by current passive aerosol techniques. For thick layers of aerosol, the A-band retrieval can estimate

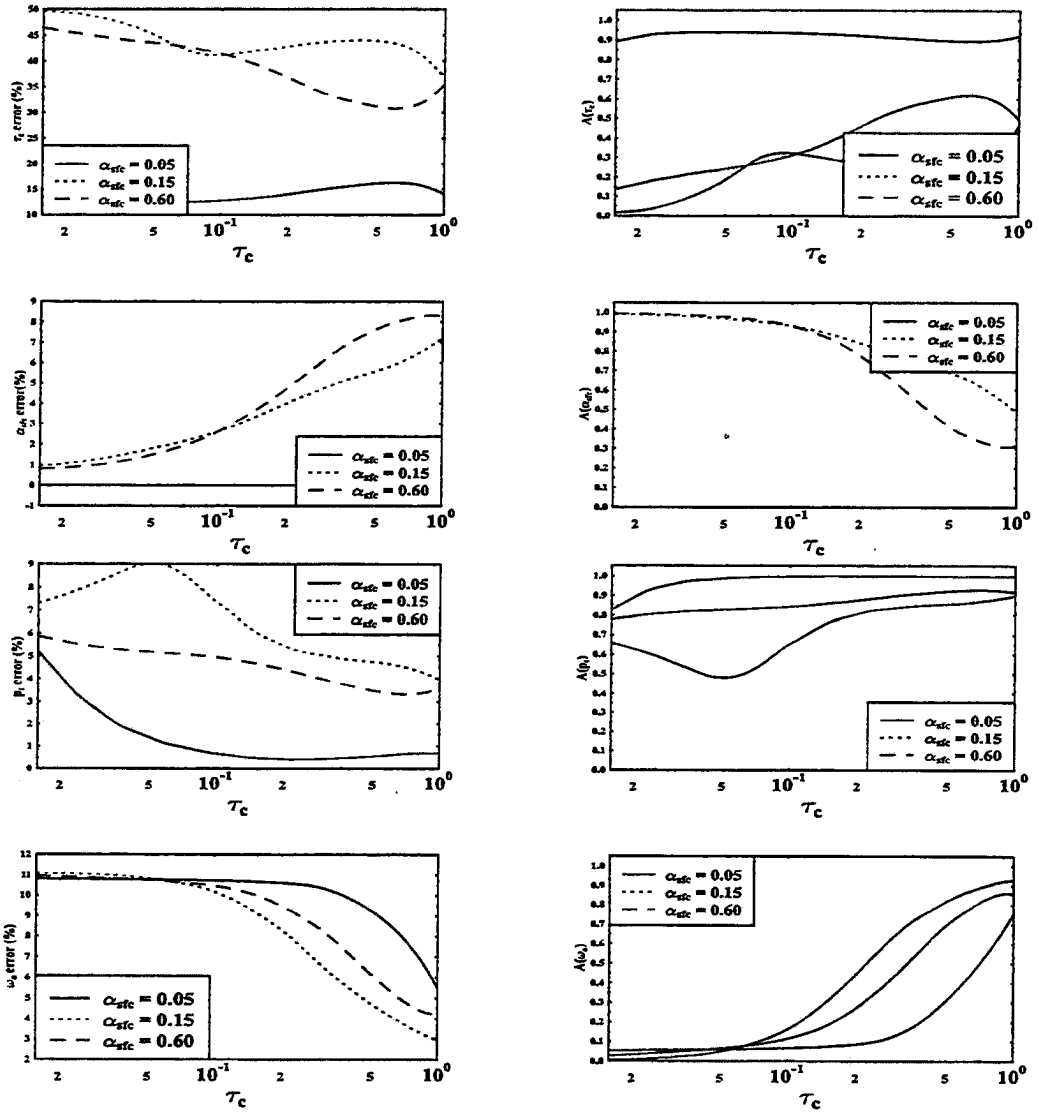

Figure 8.10: Same as Fig 8.8 except only radiance ratios are used and the phase function error is 0.5 %.

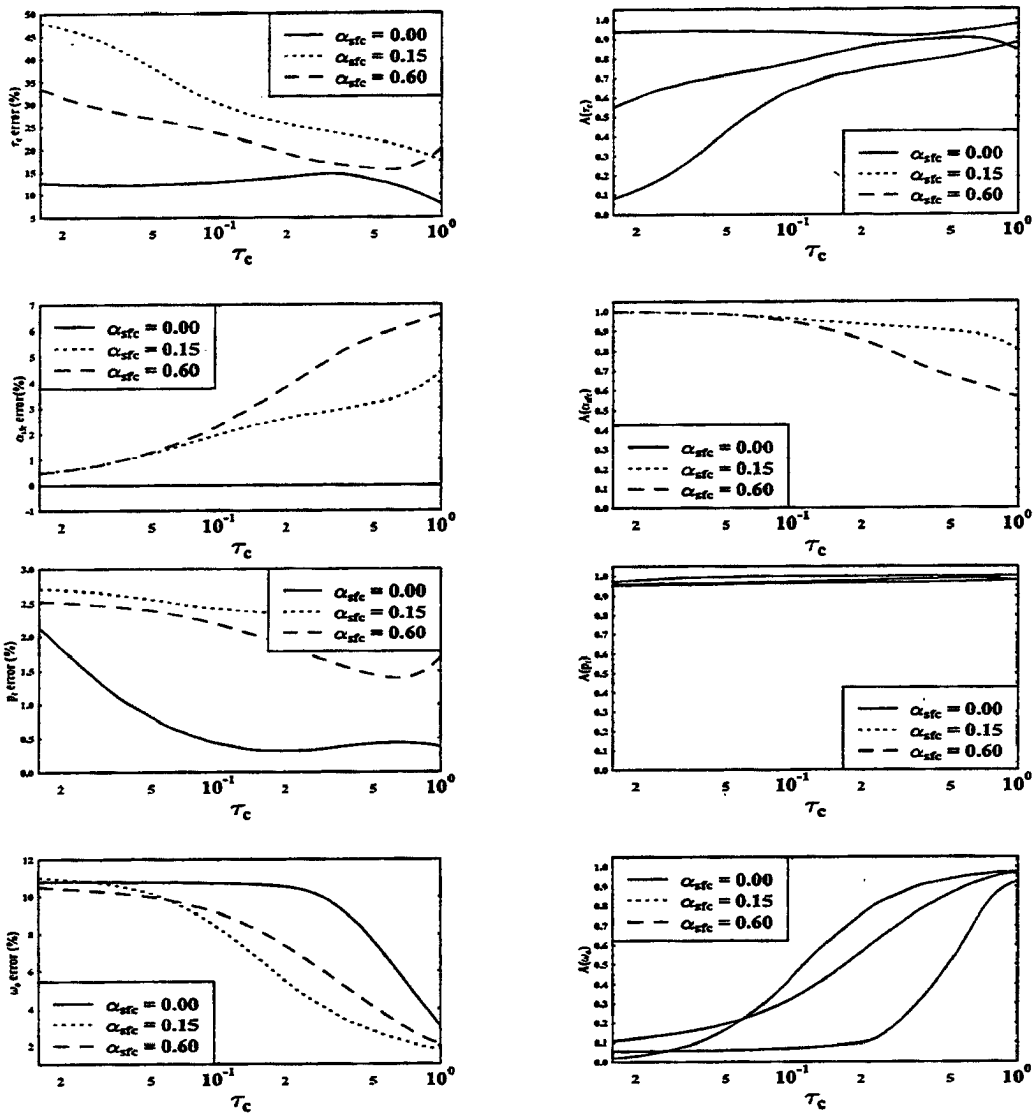

Figure 8.11: Same as Fig 8.8 except that the phase function error is 1 % and no calibration error is assumed

the single scatter albedo, ω_o. This is a significant advance in passive retrieval abilities. The ability to estimate ω_o aids in the diagnosis of aerosol composition as well as decrease in the errors in the optical depth. With realistic estimates of instrument noise and phase uncertainties, the retrieval of aerosol optical depths to within 50 % over bright surfaces is difficult. These errors are not unique to the A-band retrievals shown here. Results indicate that accurate optical depth estimates over reflecting surfaces need radiances accurate to within 1 %.

Chapter 9

Retrieval of Optical Properties from Multiple Layers with Nadir A-band Reflectance Spectra

In this chapter, the retrieval of optical properties from more than one layer in the atmosphere is explored. This chapter will deal exclusively with the retrieval of multiple layers of extinction and does not consider the vertical variation of other properties.

Except for conditions where stereo-graphic analysis can be used, no current passive system offers the ability to differentiate the extinction in multiple layers in the atmosphere from colocated satellite measurements. As discussed in Chapter 1, the visible channels of AVHRR and GOES are sensitive to only the total column cloud optical depth and therefore cannot be used to infer its distribution. In this chapter, the ability of A-band spectra to retrieve multiple layers will be illustrated using realistic retrieval scenarios.

9.1 Vertical Information Content of A-band Spectra

One desired feature of a cloud/aerosol observing system is the ability to distinguish between cloud and aerosol scattering. Fig. 9.1 shows a hypothetical atmospheric extinction profile with a cirrus cloud between 300 and 400 mb and an exponentially decaying boundary layer aerosol profile. The optical depth of the cirrus layer is 0.5 and the optical depth of the aerosol layer is 0.2. To determine the amount information about the vertical structure of extinction, an eigenvector analysis was performed on the kernel matrix, K that was computed using the extinction profile. As described in Chapter 5, the Kernel ma-

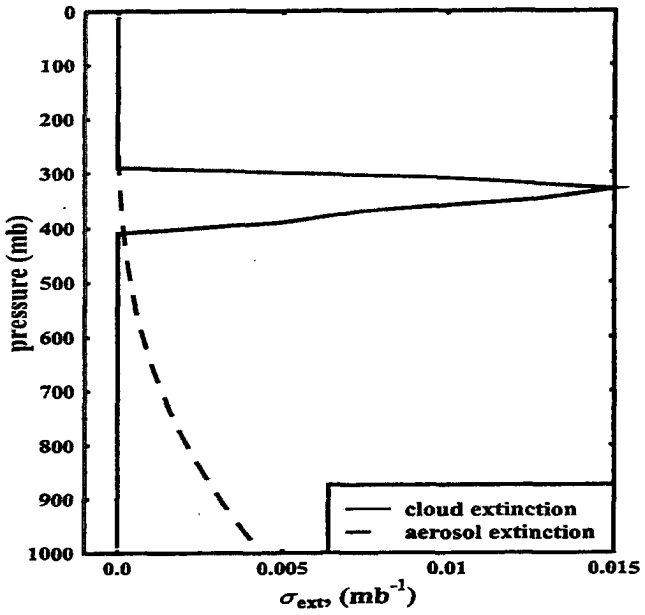

Figure 9.1: A hypothetical atmospheric profile with a cirrus cloud and a exponentially distrusted layer of boundary layer aerosol

trix is the matrix whose elements represent the change in the observables with changes in each element of the vector of retrievables, x. In this example, the vector contains the extinction value of many levels in the atmosphere. The measurements were assumed to consist of 8 values with varying values of $\tau^*_{o_2}$. The range of $\tau^*_{o_2}$ selected is characteristic of an A-band radiometer with a spectral resolution of 0.5 cm^{-1}. Fig. 9.2 and 9.3 show the columns of the kernel matrix (these are weighting functions) for both the radiance and the radiance ratios. As would be expected, the values of the radiance weighting functions are positive since adding extinction (scattering) at any level in the atmosphere will increase the nadir radiance. The negative values in the radiance ratio weighting functions can be explained using the effective level of scatter argument used earlier. The positive values of the weighting functions high the atmosphere are due to the additional extinction there raising the effective level of scatter. Similarly, the negative values lower in the atmosphere arise since additional extinction low in the atmosphere acts to lower the effective level of scatter and therefore acts to decrease the radiance ratio.

As described by Twomey(1977), the eigenvalues of the kernel matrix define the resolution of the retrieved solution, in this case the vertical profile of extinction. Figure 9.4 shows the eigenvectors from the kernel matrix composed of the weighting functions shown in Figure 9.2 and Fig 9.5 shows the eigenvectors for the radiance ratio weighting functions shown in Fig 9.3. The eigenvectors are plotted in order of decreasing eigenvalue. In general, the larger eigenvalues are associated with the smoother eigenvectors. For example, the largest eigenvalue is associated with an eigenvector which corresponds to little vertical resolution in the extinction profile. The ability to retrieve a profile with the resolution given by the eigenvector depends on the magnitude of the eigenvalue and the eigenvectors which drive the retrieval have eigen values much larger than the noise of the measurements, that is

$$\lambda >> \epsilon^2.$$

For example, assuming a 400:1 signal to noise ratio, as was done in the previous chapters, causes the last two eigenvectors in both the radiance and radiance ratio cases to become unretrievable. The structures of the last two eigenvectors correspond to resolutions to small to discern, such as the variation of the extinction within the cirrus cloud layer. From this example, it appears with realistic noise values, A-band retrievals can not retrieve extinction variations with in cloud layers. Analyzing those eigenvectors with eigenvalues much larger than than noise shows A-band retrievals may be able to retrieve 3-5 layers of extinction in the atmosphere. It also appears that radiance and radiance ratio retrievals offer about the same vertical resolution information.

As discussed in chapter 2, an A-band radiometer with high spectral resolution can conceivably take hundreds of measurements within the A-band. The issue of the need for such a high number of measurements needs to be addressed. Using the same approach as before, the radiance weighting functions were computed for the atmospheric profile given in Fig 9.1. The effect of increasing both the number of channels and spectral resolution on the number of significant eigenvectors was explored. The distribution of channel opacities was assumed to vary logarithmically from zero in the continuum to the maximum channel opacity determined by the instrument resolution (See Fig 3.4). Fig 9.6

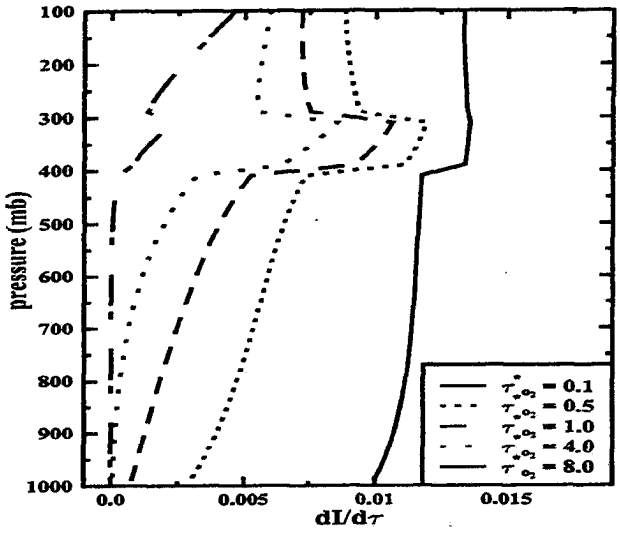

Figure 9.2: Kernel Function for the nadir A-band radiance as a function of the total column oxygen optical depth, $\tau^*_{o_2}$ for the atmospheric profile given Fig. 9.1

shows the variation of the number of significant eigenvalues as a function of the number of channels and maximum channel oxygen optical depth. As this figure shows, for a small number of channels (< 3), the number of significant eigenvalues increases linearly with the number of channels. For instruments with low spectral resolution, the number of significant eigenvalues reaches of maximum of 3-4. To increase the number of significant eigenvalues, and hence information, increased spectral resolution is needed. As Fig. 9.6, shows the number of significant eigen values is increased to 4-5 if the maximum channel oxygen optical depth is increased to 4 which corresponds to a spectral resolution of 0.5 cm^{-1}. More vertical information may be obtained with even further increase in resolution only snr remains significantly low.

Figure 9.6 provides a way of interpreting content of the vertical resolution of previous A-band spectrometers. The MCR, described previously in Chapter 3, has three A-band channels and resolves an effective maximum channel optical depth of 1.2. For this analysis it would appear that the MCR could retrieve 2 layers of extinction which might provide a way of separating the effects of the cirrus and aerosol layers of Fig. 9.1 to some extent. The

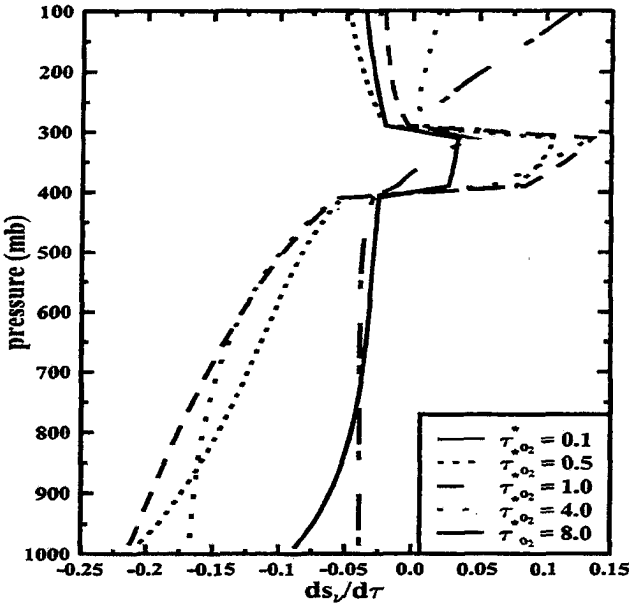

Figure 9.3: Kernel Function for the nadir A-band radiance as a function of the total column oxygen optical depth, $\tau^*_{o_2}$ for the atmospheric profile given Fig. 9.1

GOME A-band radiometer (5 channels, 10 cm^{-1} resolution) has the ability of providing 2-3 layers of extinction in the atmosphere.

9.2 Retrieval of Multiple Cloud Layers from A-band Spectra

The eigenvector analysis demonstrated the ability of A-band spectra to resolve multiple layers of extinction such as layers of cirrus over an aerosol profile as in Fig 9.1. This section now explores the retrieval of multiple layers of extinction in the presence of multiple cloud layers in a quantitative fashion. Unlike the last section, actual retrievals will be shown, which validate the above arguments based on the eigenvector analysis. As discussed in chapter 7, the retrieval of cirrus in the presence of low clouds is a difficulty that plagues current remote sensing techniques and identification of over-lapping cloud layers is critical for a number of applications.

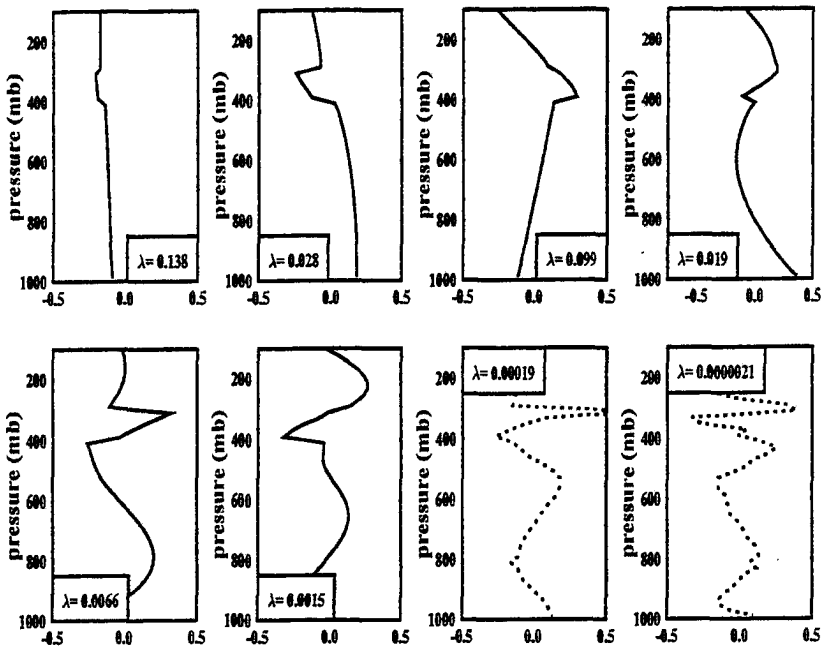

Figure 9.4: Eigen-vectors of the radiance kernel functions shown in Fig. 9.2. Eigen-values of each vector are shown in boxes

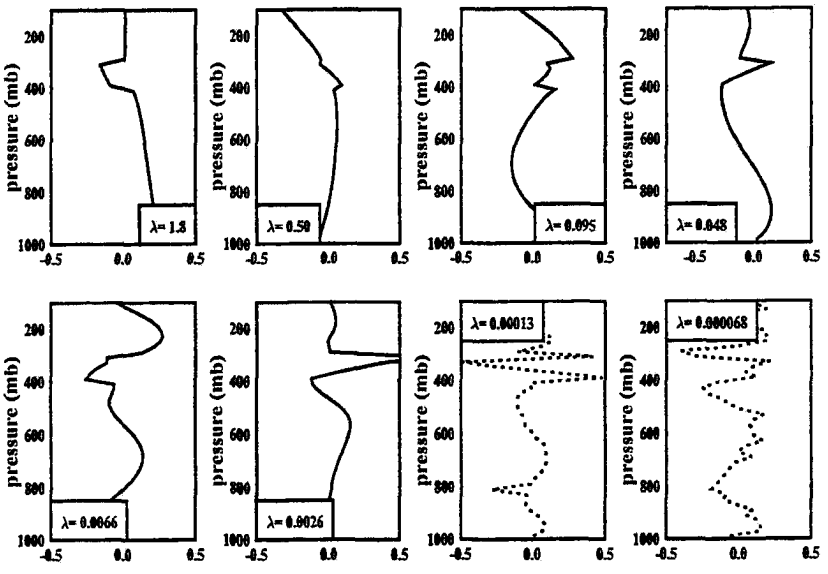

Figure 9.5: Eigen-vectors of the radiance kernel functions shown in Fig. 9.3. Eigen-values of each vector are shown in boxes

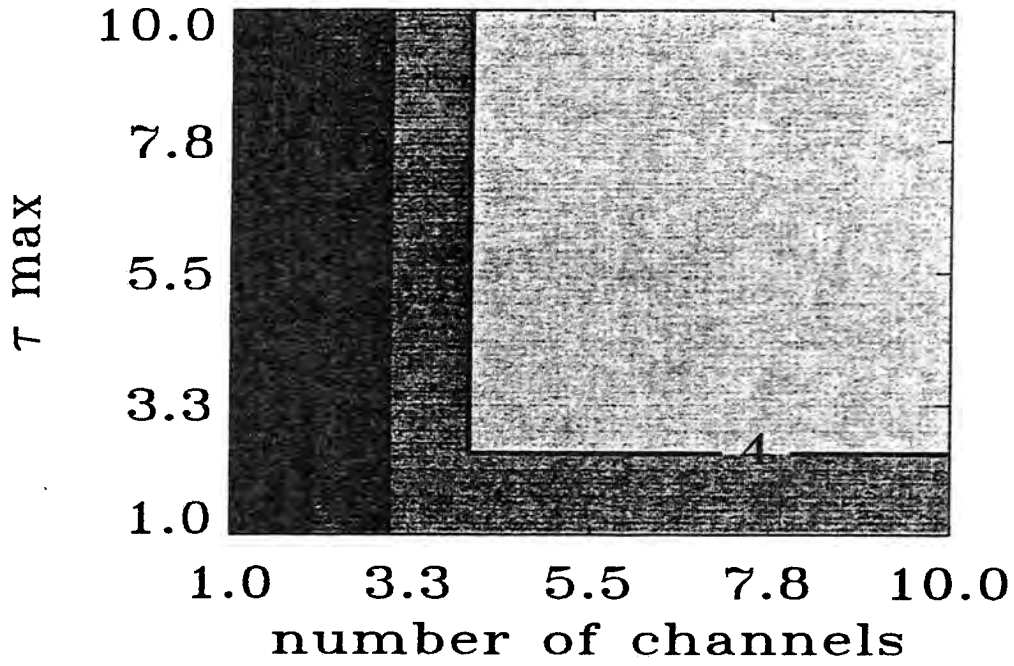

Figure 9.6: Variation of the number of significant eigenvalues with the increasing number of channels and increasing instrument resolution(maximum value of $\tau^*_{o_2}$.

The ability of A-band retrieval methods to give profiles of optical depths of multiple cloud layers is tested via a simulation using the vertical extinction profile shown in the left panel of Fig 9.7. This extinction profile was constructed to represent a cirrus cloud with an optical depth of 0.5 above a boundary layer cloud with an optical depth of 10.0.

Without any *a priori* knowledge of the cloud distribution, the A-band retrieval is forced to retrieve the optical depth in predefined layers. According to the eigenvector analysis above, the A-band spectral measurements at a resolution of 0.5 cm^{-1} are likely to provide the means of retrieving profiles of extinction defined by 4-5 layers. To test this, the A-band retrieval was configured to attempt to obtain the optical depth in 4 200 mb layers. The topmost layer was assumed to have no cloud. The results of this retrieval, shown in the center panel of Fig. 9.7, indicate that within the confines of the preset 200 mb intervals, the A-band retrieval is able to proportion the cirrus and boundary layer optical depths properly into the appropriate layers. Since the noise of the measurements precludes the A-band retrieval from resolving higher resolution structures in the extinction profile, an

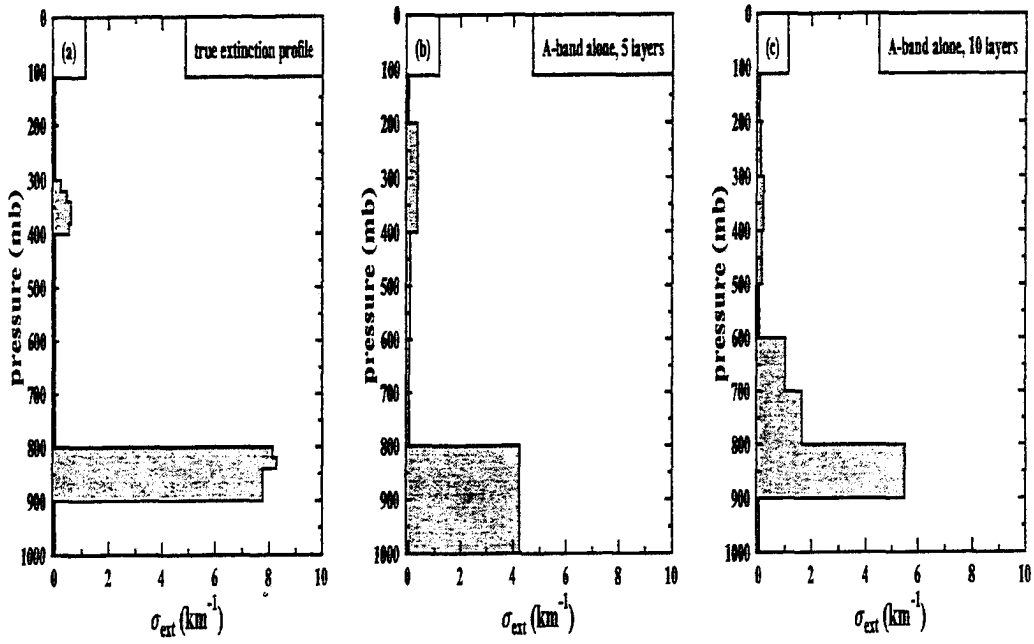

Figure 9.7: Comparison of true extinction profile (left) with retrieved extinction profiles. The center panel shows results for a 5 layer retrieval and the right panel shows the results for a 10 layer retrieval.

attempt to retrieve more than 5 layers results in erroneous profiles. The right-hand panel of Fig 9.7 demonstrates this point showing a retrieval attempted for 10 layers 100 mb thick. As this figure shows, the 10 layer retrieval produced a spurious profile of extinction through the atmosphere. The retrieval attempted to distribute the extinction in the lower cloud higher in the atmosphere and attempted to distribute the cirrus cloud extinction over a wider pressure thickness than actually occupied.

9.3 Conclusions

Through the use of an eigenvector analysis of the kernel functions and simulated retrievals, it is shown that an instrument with a resolution of $0.5cm^{-1}$ can differentiate extinction within 4-5 layers in the atmosphere. This vertical resolution exceeds that of all preceding A-band radiometers and is a substantial improvement over other passive means. Higher spectral resolution will increase the vertical resolution only if the noise on the measurement

can be reduced significantly from currently achievable values.

Chapter 10

Combined Retrievals Using A-band Nadir Radiances and Active Sensors

Thus far all retrievals presented above use only the spectral A-band data. This chapter now explores the benefits of using information from active sensors in conjunction with these spectral measurements. The term active sensor refers to to a remote instrument which radiates and receives it own signals. The active sensors applied most frequently to cloud remote sensing are LIDARs (light detection and ranging) and radars (radio detection and ranging). LIDARs involve the measurements of laser reflections and are typically operated at visible to near-infrared wavelengths for application to cloud and aerosol remote sensing. Radars involve the transmission of much longer wavelength energy (0.3 - 10 cm). The attenuation of radar wavelength radiation by clouds is much less than is the attenuation of radiation transmitted by LIDAR.

The age of active systems in space has already begun.The first space-borne LIDAR, the LIDAR in Space Technology Experiment (LITE) was flown successfully on the space shuttle in 1995. Within days of the completion of this paper, the first space-borne radar for meteorological studies will be launched as part of the Tropical Rainfall Mapping Mission(TRMM). The Clouds and the Earth Radiation Energy System(CERES) and the Visual Infrared Sensor (VIRS) are flying as part of TRMM and will be used for cloud remote sensing. . Currently proposals are being considered by the major space agencies to fly LIDARs and millimetric RADARs on satellites.

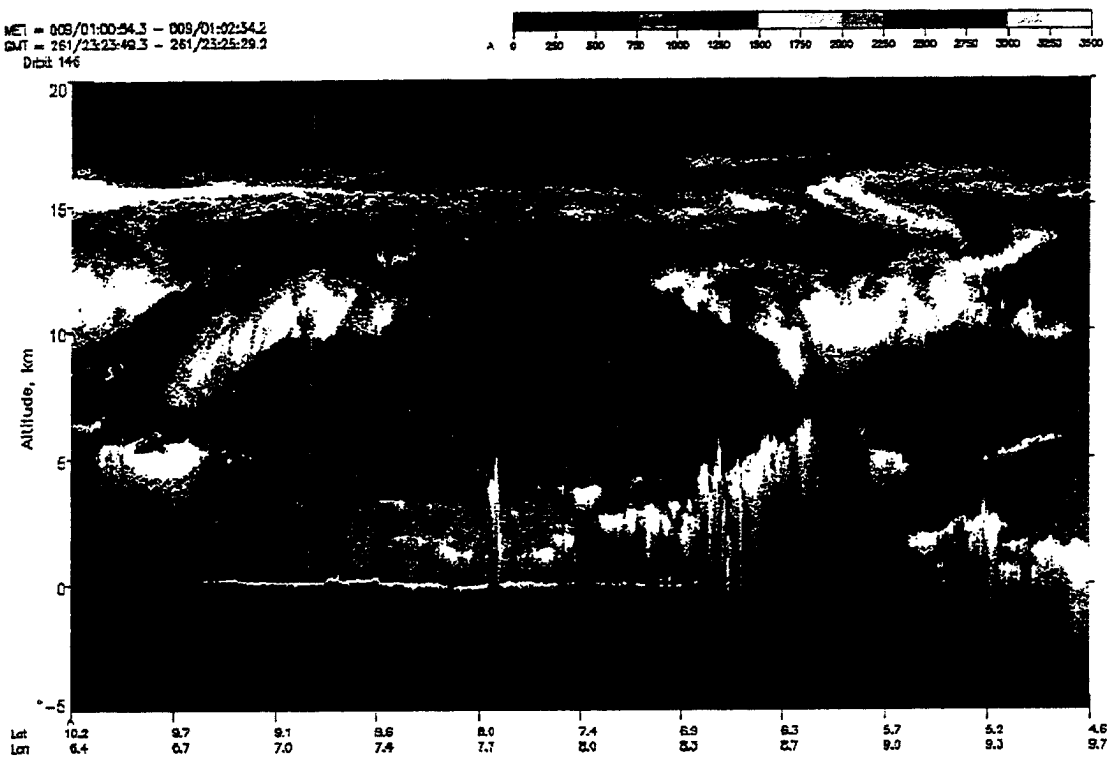

Figure 10.1: An image of LITE data taken on Orbit 149 (McCormick *et al*, 1995)

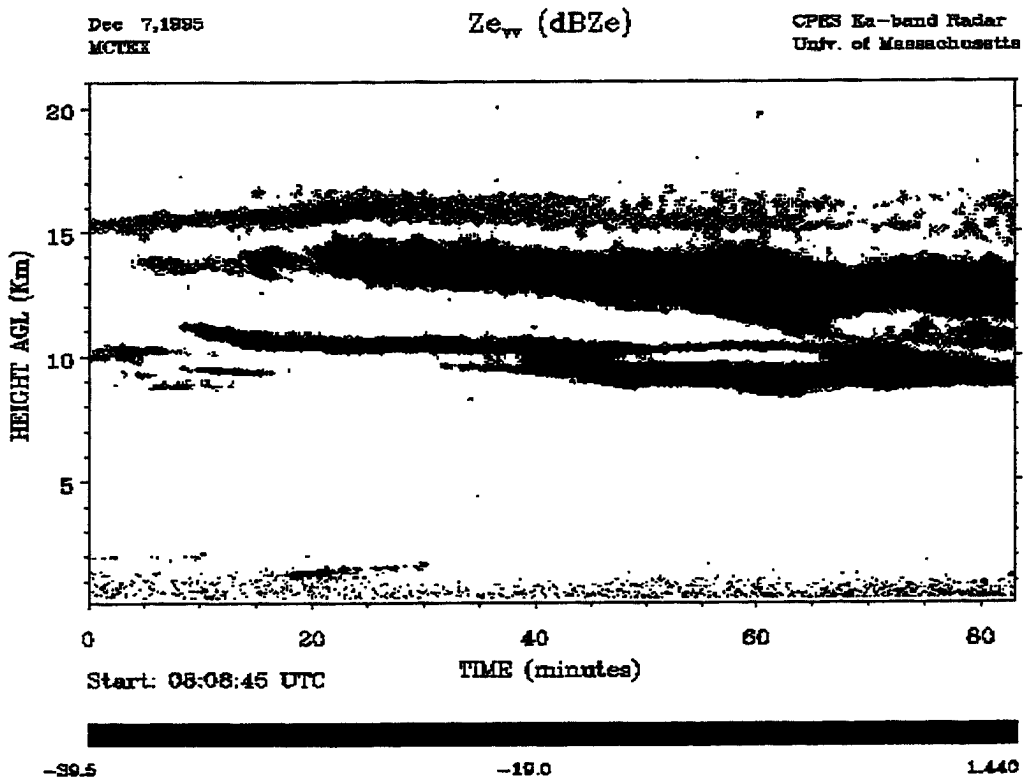

Figure 10.2: Data from the UMASS 35 MHZ RADAR in a zenith pointing mode.

Figures 10.1 and 10.2 illustrate the type of data provided by LIDARs and RADARs. Fig 10.1 shows a segment of data taken along orbit 146 of the LITE mission. As can be seen in Fig 10.1, the LIDAR imagery is able to measure to physical boundaries of cloud and aerosol layers and provides a unique view of the complex structure of cloud systems. The LIDAR signal, however, is unable to penetrate completely into thicker clouds as evidenced by the ragged appearance of the cloud bases for the thicker clouds in Fig 10.1. Unlike LIDAR, RADAR used for cloud remote sensing is able to see through thick clouds and is only significantly attenuated by precipitation. Fig 10.2 shows a plot of radar reflectivity, which is related to returned power, of zenith pointing 33/95 MHz Radar developed by UMASS (http://abyss.ecs.umass.edu/CPRS-http). As with the LIDAR, the RADAR is able to provide direct measurements of cloud positions and cloud structures. The cloud field in Fig 10.2 was a cirrus layer measured during the MCTEX (Maritime Continent Thunderstorm Experiment) during 1995.

10.1 Benefit of Active Data to Single Layer Retrievals

This section explores the benefits of using information provided by active systems in the retrieval of optical properties from single uniform layers of particles as described in Chapters 6,7 and 8. As Figs 11.1 and 11.2 illustrate, LIDARs and RADARs can readily identify the vertical position of scattering layers. One way, therefore, to include information from active systems is to assume that highly accurate *a priori* estimates of p_t and Δp are available. While this retrieval uses only the rudimentary information from the active sensor, the following results show this information to significantly enhance the retrievals.

Figure 10.3 shows result taken from the low cloud retrievals performed in Fig 6.12 which consisted of a low cloud placed between 800-900 mb a reflecting surface with $\alpha_{sfc} = 0.15$. The solid line shows the results from Fig 6.12 with no active information constraining the values of p_t and Δp. The dotted curve in Fig 10.3 is the resulting retrieval performed using the active system constraints. This simulation shows that additional information from the active system greatly enhances the ability to estimate the properties of optically

thin low clouds over a reflecting surface, a situation which presents a difficulty to current passive retrieval methods. Due to the difficulty present in the infrared retrieval of semi-transparent cirrus, the inclusion of LIDAR data in a similar would also greatly benefit to retrieval of cirrus properties from passive infrared techniques, such as the retrievals performed using HIRS, Wylie *et al* (1996).

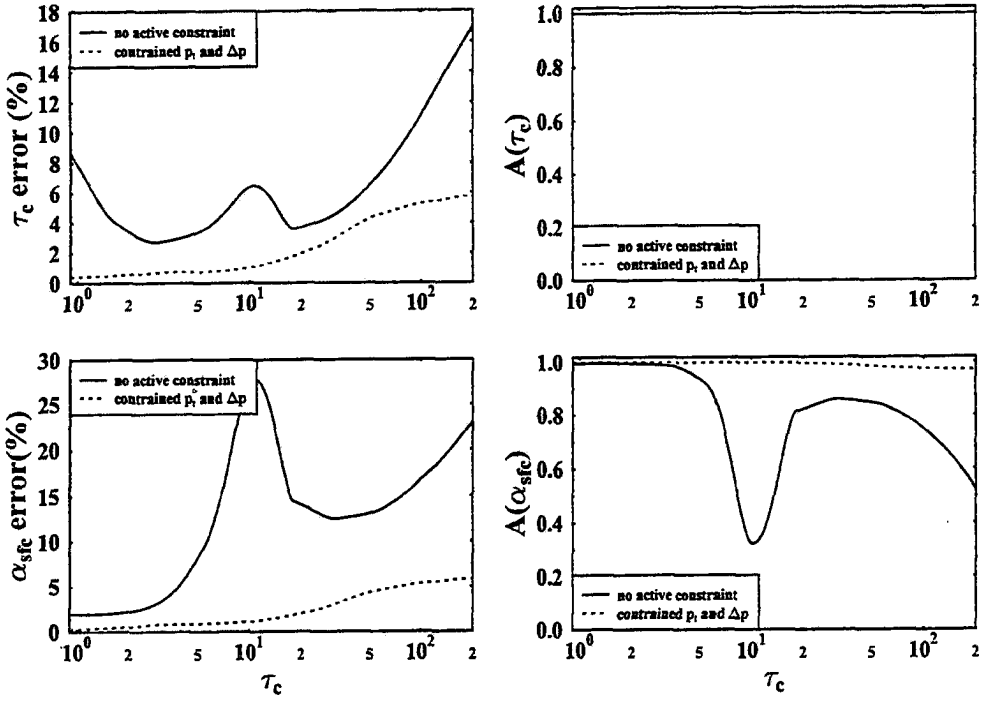

Figure 10.3: Effect of active system constraints to the retrieval results for a single layer low cloud placed 800-900 mb with $\mu_o = 0.8$

The effect of the active system constraints on a simulated cirrus retrieval is shown in Fig. 10.4. The simulated cirrus cloud was placed between 300 -400 mb above a reflecting surface with $\alpha_{sfc} = 0.15$. The results shown in Fig 10.4 computed without the active constraint were taken from Fig 7.13. The results of Fig 10.3 show that the inclusion of the active constraints on p_t and Δp significantly enhances the ability to retrieve both τ_c and g in optically thick cirrus. In addition, results computed for adding an additional constraint of 20% on τ_c are shown. This constraint could be derived by an independent estimate of τ_c based on LIDAR data. As the results show however, this constraint on τ_c, provides little improvement above that provided by the constraints on p_t and Δp.

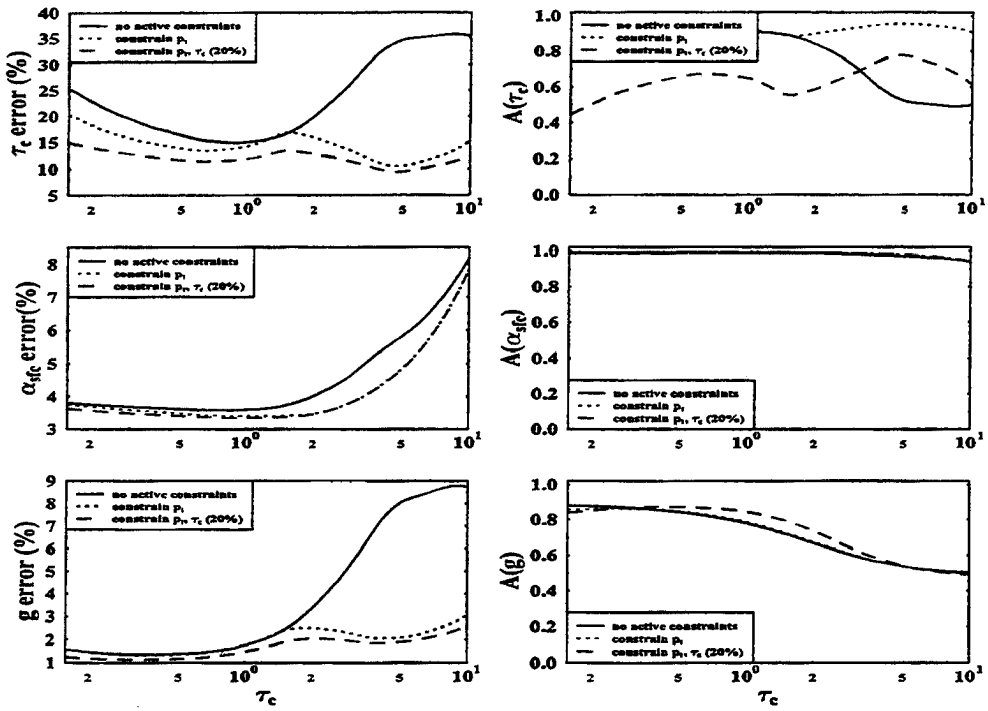

Figure 10.4: Effect of active system constraints to the retrieval results for a single layer cirrus cloud placed 300-400 mb above a surface with $\alpha_{sfc} = 0.15$

10.2 Benefit of Active Data to Multiple Layer Retrievals

In Chapter 9, the vertical information content of A-band spectra was shown to be between 3-5 layers depending on the particular retrieval scenario. Since no *a priori* information on structure was available, the A-band was forced to spread the layers over the entire atmosphere. As a consequence, the retrieved extinction profile captured only grossest features of the true profile. As was exploited in the single layer results above, the pressure boundaries of cloud and aerosol layers are readily provided by LIDARs and radars. In this section, the sample simulated retrieval shown in Section 9.2 is performed assuming an active system is able to correctly locate the clouds in to atmospheric column. The left panel of Fig 10.5 shows the true distribution of extinction assumed in these simulations. The right panel shows the A-band retrieval of the extinction or optical depth in each of the layers identified by the active system. No *a priori* assumption was made concerning the relative extinction between each of the clouds layers. As Fig 10.5 shows, the A-band

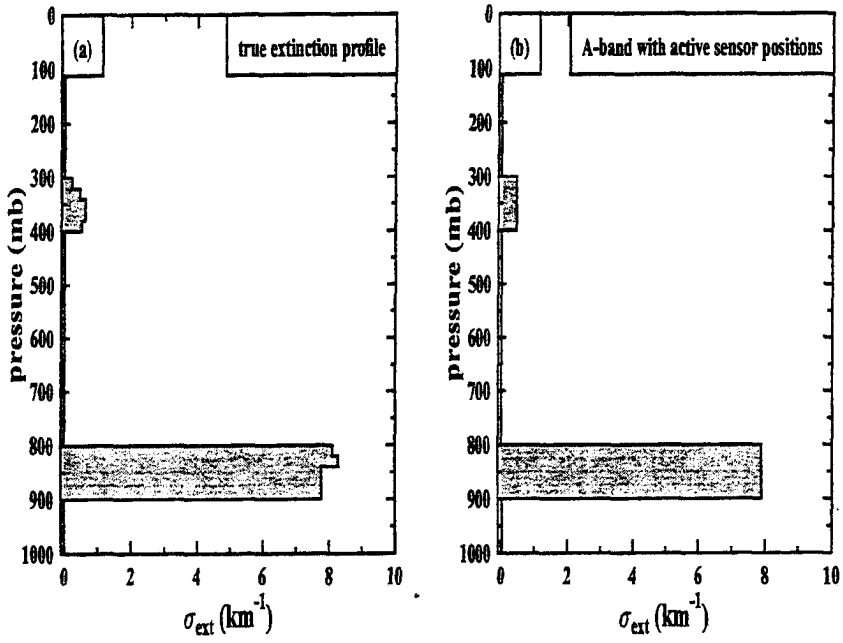

Figure 10.5: Effect of combined LIDAR radiometric data with A-band radiances on the retrieved optical depth of the cirrus cloud,τ_c

retrieval constrained by the cloud positions given by the active sensor is able to reproduce the observed distribution of extinction between the two cloud layers.

10.3 Benefit of LIDAR radiometric data to A-band Retrievals of Cirrus

The above examples use only very rudimentary layer geometry information from the active systems. This section describes how additional information gleaned from these active systems can be used in conjunction with the A-band spectrometer. This information is not only the vertical positions of the cloud layer, but also the radiometric returns from the LIDAR in the active-passive retrieval. This technique can be applied to any coincident visible reflectance and LIDAR measurements.

To illustrate this idea Fig 10.6 was constructed to show the breakdown of the reflectance and the LIDAR return for each order of scatter for a simulated cirrus cloud. The cirrus cloud was placed between 300 and 400 mb with an optical depth of 1.0 and the phase

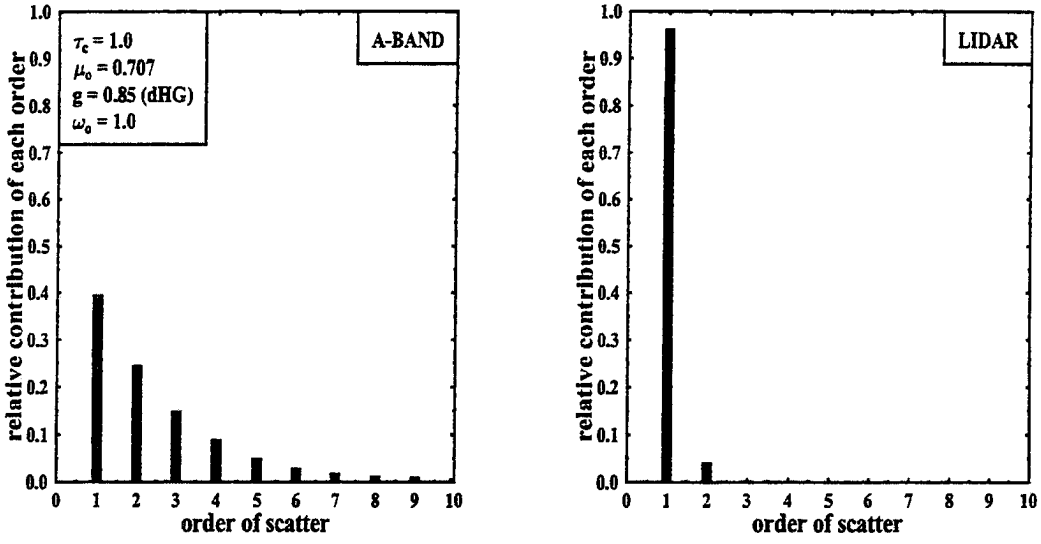

Figure 10.6: Effect of combined LIDAR radiometric data with A-band radiances on the retrieved optical depth of the cirrus cloud,τ_c

function was approximated by the dHG function. The solar zenith angle in this case was 45^o and the lower surface was assumed to be Lambertian with an albedo of 0.15. Due to the differing viewing geometries of each instrument, the contribution of multiple scattering in the passive reflectance exceeds that of LIDAR return. The LIDAR field of view was assumed to be 0.5 μrad which was the field of the LITE LIDAR during daylight operation. Due to this small field of view, photons which do not directly scatter back to the detector quickly leave the field of the detector and it is highly improbable that multiply scattered photons return to the LIDAR detector. The LIDAR simulations were performed using a backward Monte Carlo as described in Appendix B. As a result, 90 %of the LIDAR return is due the first order scatter while only 25 % of the A-band reflectance is from first order scattering.

For Fig 10.6, it is clear that the LIDAR return will be more heavily influenced by the backscattering portion of the particle phase functions than the reflectance value. In addition, the reflectance value is more heavily influenced by the forward peak of the phase function than the LIDAR return. In Chapter 7, the ability of the A-band to simultaneously

estimate both τ_c and the asymmetry parameter of the phase function was illustrated by showing contours of the A-band observables plotted versus τ_c and g. We now apply the same technique to the A-band reflectances and LIDAR returns. Fig 10.7 shows the contours of the continuum reflectance and the LIDAR return as a function of τ_c and g. The left panel shows the values for optical depths less than 1 and the right panel shows the contours for optical depths less than 4. If we approximate the LIDAR return using single scatter theory, the sensitivity of the LIDAR return, I_{lidar} to both τ_c and to g can be expressed as

$$\frac{\partial I}{\partial \tau_c} = F_o e^{-m\tau_c}\left(\frac{\omega_o P_b}{4\pi\mu} - \frac{\alpha_{sfc}}{\pi}m\right)$$

$$\frac{\partial I}{\partial g} = \frac{\omega_o F_o}{4\pi m\mu}(1 - e^{-m\tau_c})\frac{\partial P_b}{\partial g}$$

where P_b is the phase function value for pure back-scatter. As indicated above, I_{lidar} is most sensitive to optical depth for small values of τ_c which is consistent with Fig 10.7 which shows the contours of I_{lidar} to be nearly orthogonal to the τ_c axis. The actual sign of $\frac{\partial I_{lidar}}{\tau_c}$ depends on the relative magnitude of α_{sfc} to p_t. For the simulation presented here with $\alpha_{sfc} = 0.15$, increasing the optical depth decreases I_{lidar} In addition, single scatter theory predicts an increasing sensitivity to g for I_{lidar} as τ_c increases, which is again consistent with Fig 10.9. By contrast multiple scattering, that contributes to the radiance measured by the A-band. forces the radiance to follow follow the contour of $\tau_c(1-g)$, known as the effective optical depth. For very small values of τ_c, the radiance measured by the passive sensor will also be dominated by single scattering which would theoretically allow for the determination of two points of the phase function. Note that the enhanced ability to measure g by using LIDAR measurements would apply to any visible radiance, not just A-band measurements. From these simulations, it appears that determination of phase function information from dual reflectance and LIDAR measurements is more accurate than from A-band measurements alone.

The additional information from the lidar offers the potential to retrieve phase function. In the A-band only retrievals, an estimate of g is governed by the assumed phase function,

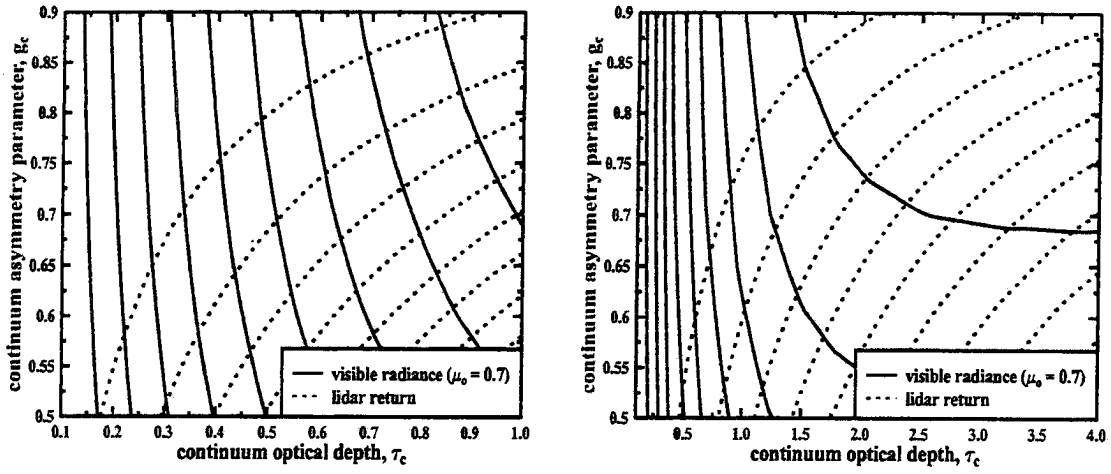

Figure 10.7: Effect of combined LIDAR radiometric data with A-band radiances on the retrieved optical depth of the cirrus cloud,τ_c

in this case the double Henyey Greenstein. The use of LIDAR data allows not only g to be retrieved, but effectively provides two pieces of information about the phase function. Fig. 10.8 shows results of a cirrus retrieval with A-band reflectances together with the LIDAR returns. The results are shown as a comparison of the retrieved phase functions. The true phase used in computing the simulated radiances, shown as the solid line, is the dHG phase function with $g_1 = 0.90, g_2 = -0.60, g = 0.80$. The *a priori* phase function, shown by the dotted line, is a dHG phase function with $g_1 = 0.95, g_2 = -0.60, g = 0.85$. The two remaining curves are the phase functions retrieved with only A-band radiances and with both A-band and LIDAR backscatter data. Alone, the A-band retrieval is forced to retrieve a value of g with the *a priori* values of g_1 and g_2 which best matches the observations. The resulting value of g is 0.82. With the LIDAR data, the retrieval can estimate both g_1 and g of the dHG phase function form. The resulting phase function using both lidar and A-band data is also shown in Fig 10.7. The resulting phase function is virtually identical to the true phase function.

Having shown above that dual reflectance and lidar retrievals can significantly improve on the A-band's ability to retrieve the phase function, the question as to how this additional information effects the errors of cirrus optical depths retrievals is now addressed.

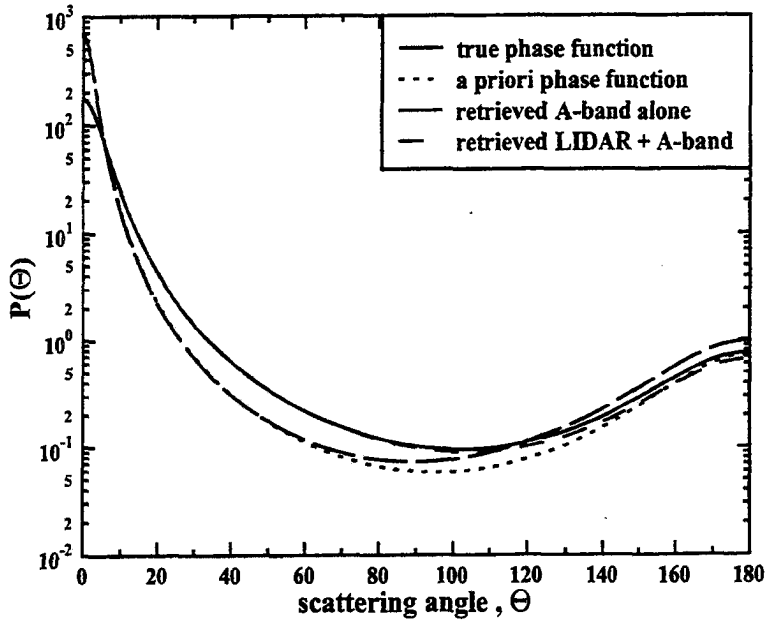

Figure 10.8: Effect of combined LIDAR radiometric data with A-band radiances on the retrieved optical depth of the cirrus cloud,τ_c

To illustrate this point, a simple retrieval was performed on a simulated cirrus cloud with an optical depth of 1.0 and a phase function given by the same dHG parameters used to produce the functions in Fig. 10.6. A AVHRR-like retrieval was performed using only the continuum reflectance assuming a dHG phase function parameters corresponding to the form used in the above simulations. Since this function is an underestimate of the actual backscatter, the cirrus optical depths tend to be overestimated by 60 % when the *a priori* phase function is used. When A-band and lidar data are used together to retrieve two parameters of the phase function, the resulting optical errors are much lower. As Fig 10.7 shows, the optical depth errors are reduced dramatically. This would be expected since the error analysis in Chapter 7 for the A-band alone showed that the phase function errors in the cirrus retrieval are large. Adding LIDAR data to the A-band measurements has a dramatic positive effect.

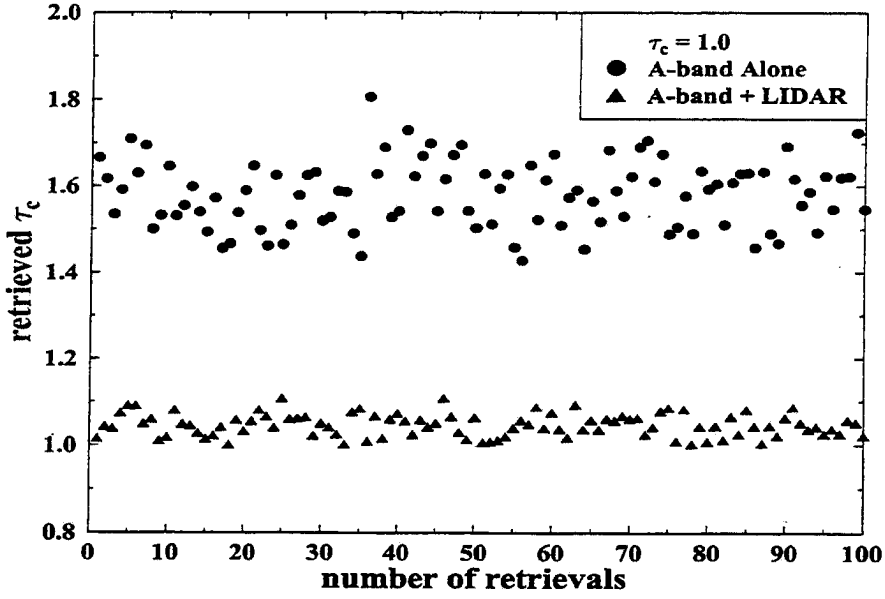

Figure 10.9: Effect of combined LIDAR radiometric data with A-band radiances on the retrieved optical depth of the cirrus cloud,τ_c

10.4 Conclusions

This chapter explores the benefits of incorporating data from active systems, such as RADAR or LIDAR, into A-band retrievals. Use of cloud boundary information from such sensors improves the retrieval of the optical properties from single layers especially in the case of thick cirrus. The *a priori* knowledge of cloud boundaries greatly increases the accuracy of multi-layer retrievals. A significant emerges from to performing simultaneous retrievals of cirrus using both A-band reflectances and lidar returns, as well as the lidar estimates of cloud boundaries. The inclusion of the lidar data leads to improved optical depth estimates through the ability to retrieve more information about the phase function.

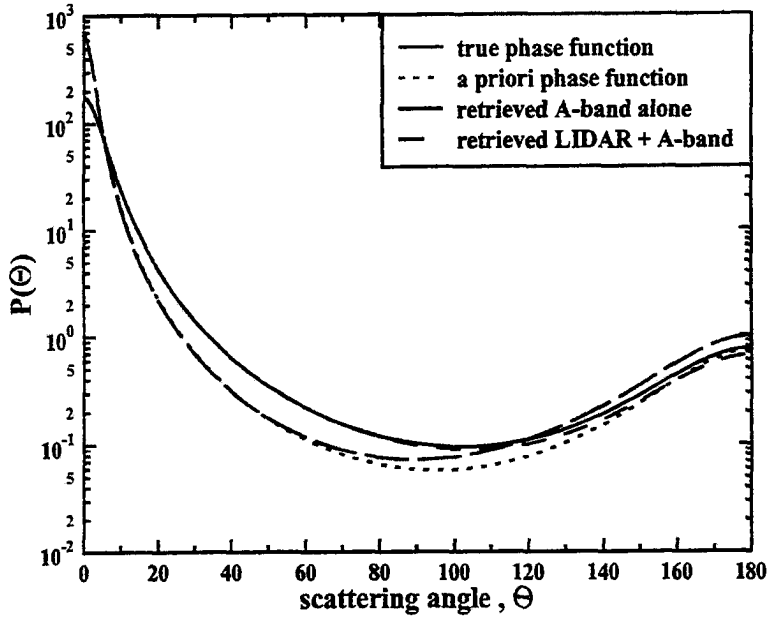

Figure 10.10: Effect of combined LIDAR radiometric data with A-band radiances on the retrieved optical depth of the cirrus cloud,τ_c

Chapter 11

Retrieval of Optical Properties from Spatially Heterogeneous Clouds

This chapter explores the errors incurred in optical property retrievals of clouds with spatial variability or heterogeneity. As mentioned in Chapter 5, the optimal estimator technique used to perform the retrievals in this paper relies on estimates of the errors in the measurements and in the forward model. Since the forward model developed in Chapter 4 assumed no horizontal variability in the cloud and aerosol layers, the errors due cloud heterogeneity need to be quantified and included as forward model errors in order that meaningful retrieval errors can be estimated.

The goal of this chapter is twofold. First the errors in the A-band radiances and radiance ratios due to cloud structure must be quantified. The error estimates will allow more meaningful estimates of the true ability to retrieve optical parameters from A-band measurements. The errors due to cloud structure are alway present to some extent in real-world retrievals but they are rarely quantified. As will be shown, for some conditions, the effects of cloud structure prevent any meaningful retrieval being performed. The second goal of this chapter is to develop methods which allows an A-band retrieval using a standard plane parallel retrieval approach to self-diagnose the effects of heterogeneity on the retrieval. This method is novel in that it is the only method that exists that provides judgments of when retrievals are biased by three dimensional effects.

After briefly reviewing existing research on the retrieval of optical properties in heterogeneous clouds, this chapter will discuss the qualitative effects of cloud heterogeneity on the A-band observable, the radiance and the radiance ratio. Next, sample retrievals will be performed on cloud fields with realistic spatial variability to access the errors in the estimates of optical properties.

11.1 Brief Review of Three Dimensional Radiative Transfer

The radiative effects of cloud spatial variability is an area of much current research in the atmospheric science community. Several methods exist which allow for the rigorous simulation of radiance and fluxes in media with arbitrary spatial heterogeneity. The work of Gabriel *et al* (1993) provides an excellent review of the research performed concerning methods of simulating radiative transfer in heterogeneous media up to 1992. Stephens(1986) developed a method which decomposes the cloud structure into a Fourier series and allows the radiative transfer equation to be solved for each Fourier mode independently in a manner similar to the decoupling of the azimuthal modes in the standard plane parallel formulation. A Fourier-Ricatti technique for three dimensional radiative transfer was developed by Gabriel *et al* (1993). The Fourier Ricatti technique involves a decomposition of the cloud structure into Fourier Series but solves the radiative transfer equation in an iterative manner similar to the invariant imbedding method. The Spherical Harmonics Discrete Ordinate Method (SHDOM) developed by Evans (1997) also solves the radiative transfer equation iteratively by expressing the source functions in term of spherical harmonics and uses discrete ordinate representation of the radiance field. The implementation of the above methods are both computationally and memory intensive because they involve matrix operations which increase in size with both the number of points used to represent the cloud fields and the number of discrete angles and Legdenre' expansion terms used. Until, recently, these methods were capable of only simplistic two and three dimensional simulations. With the continuous increase in computational ability, these techniques are now being applied to more realistic cloud fields, however the simulation of three dimensional radiative transfer is still limited by computational resources.

For example, the work of Chambers and Wielicki (1997) simulated a a cloud field with 64 x 64 x 1 array of cloud extinction and the simulation took 3 days of CPU time on a supercomputer.

The method chosen for his study is the backward Monte Carlo method O'Brien(1992). Monte Carlo models solve the radiative transfer equation by a stochastic approach. This technique involves the direct simulation of the random walk process of photon transport. Unlike the above methods, the Monte Carlo method does not involve matrix operations and therefore can simulate much larger grids of extinction. For example, the LandSat scenes used later in this chapter contain 2048 by 2048 values of column optical depth. The simulation of radiative properties for extinction grids of this size were performed on a desktop personal computer. The computational expense of Monte Carlo models is incurred in the statistical convergence of the solution. The three dimensional Monte Carlo model developed here is discussed in Appnedix B. This model extends the development of O'Brien (1992) by including surface reflection and thermal sources, and using new acceleration techniques for both the radiances and the mean path-length. In addition, Appendix C shows a new application of the equivalence theorem of Irvine (1964) to computation of spectral radiances in three dimensional clouds. This technique involves the use of photon path-length distributions, a product of Monte Carlo models, to compute the effect of gaseous absorption on radiative quantities. This technique allows for the computation of line-by-line resolution spectral from only one set of calculations of the three dimensional radiative transfer code.

Monte Carlo techniques have a long history of application to study of atmospheric radiative transfer. For example, the studies of McKee and Cox (1974) was one of the first to show the effects of cloud structure on reflected and transmitted solar energy. Application of Monte Carlo methods to compute broad-band fluxes has been performed recently by Barker (1996) and others. The above studies all used forward Monte Carlo models. As their name implies, forward and backward Monte Carlo models represent opposite approaches to the solution of the radiative transfer equation. Forward models directly simulate the transfer of photons from the source solar source to all points of

the medium. These models are therefore well suited to investigations that desire radiative properties throughout the medium. If a radiative quantity at a desired point or direction is required, a prohibitive number of photon simulations is needed to be simulated to generate an estimate of the quantity with statistical significance. The backward Monte Carlo technique follows only those photons from the desired point and direction of observation back to the source. The backward Monte Carlo model is therefore more efficient for the type of problems of interest to this research.

11.2 Current Research on the Effect of Cloud Spatial Variability on Satellite Retrievals

With the increasing speed of computers, more and more realistic simulations of spatially variable cloud fields are possible. All forward models used in retrievals, including the one used here, assume spatial uniformity in the cloud fields. Studies using the above techniques to simulate heterogeneous clouds have shown that using plane parallel models to retrieve optical properties in heterogeneous clouds produce significant errors. For example, Duda and Stephens (1995), using the SHDOM method, have demonstrated the effect of cloud structure on the dual channel reflectance technique of Nakajima and King(1989) which estimates both the cloud optical depth and the effective radius of the size distribution. This study used the SHDOM model to simulate radiances reflected from a marine stratocumulus layer which was produced from a cloud resolving model which explicitly produced fields of cloud liquid water and droplet distributions which varied in all dimensions. The results for this specific case indicated that the cloud structure caused errors of about 5% in the optical depth retrieval and about 10% in the effective radius retrieval. These errors in optical properties are much less than those computed later for another specific cloud structure. As pointed out by the authors, these errors were larger than the change in the values due to changes in the initial concentration of condensation nuclei at the onset of cloud formation and the subsequent drop size and concentration changes. It is important to note, however, that these results were performed using a two-dimensional simulation which would reduce the sensitivity to spatial structure compared to the full three dimensional

simulations shown later in the chapter. The work of Gabriel *et al* (1996) used the Fourier-Ricatti approach to study the two dimensional transfer of radiation through a cloud with a repeating Gaussian distribution of extinction. This study demonstrates clearly the role of horizontal transport of photons in spatially variable media and illustrates, at least for the Gaussian geometry, that viewing at nadir is the optimal viewing geometry that minimizes the effects of heterogeneous clouds. Throughout the results of this chapter, the nadir viewing configuration will be used.

11.3 Effect of Cloud Spatial Variability on A-band Observables

To explore the effects of cloud heterogeneity on A-band radiances, the three dimensional radiative transfer model developed in Appendix B was used to simulate the radiances reflected from heterogeneous clouds. The simulated cloud fields were taken from a data-set of cloud fields derived from simple visible optical depth retrievals from LandSat imagery. This dataset is described by Harshvardhan *et al* (1994) and Barker et al (1996) and consists entirely of single layered marine stratocumulus. The spatial resolution of the data is 28.5 meters and each dataset contains data over 58 by 58 km region (2048 by 2048 pixels). Although the retrieval technique used to produce the column optical depths suffers from cloud heterogeneity effects, the cloud data will be taken to represent realistic cloudiness conditions. A stochastic or fractal type model of cloud heterogeneity could have been used to study the effect cloud heterogeneity as a function of the statistical or fractal parameters (Cahalan, 1989). Models of this type are difficult to scale with the instrument resolution which is a crucial issue in satellite remote sensing.

In this study, two LandSat-derived cloud fields were used to represent differing amounts of cloud variability. The results from the simulation of these two cloud fields, although not comprehensive, will be used to define the range of errors due to cloud spatial variability. The errors in most A-band retrievals due to heterogeneity perhaps lie between the values obtained for these two simulations. The horizontal distribution of the total column optical depth along the histogram of occurrence of optical depth for the two chosen datasets are

shown in Fig 11.1 and 11.2. In addition, Table 11.1 summarizes the main statistical properties of the two cloud fields. Cloud field # 1 was chosen to represent a relatively homogeneous cloud field. The mean optical depth is 4.4 and the ratio of the standard deviation to the mean is only 0.80. By contrast, cloud field # 2 is a field of very scattered clouds with a cloud fraction 0.36. The mean optical depth in cloud field # 2 is 2.22 and the ratio of the standard deviation to the mean is about 3.

The simulation of the reflected A-band radiances from the LandSat derived cloud fields will computed assuming an underlying dark surface. Since these simulations are concerned only with relative errors, lack of the inclusion of surface effects should not alter the conclusions of this study. Only the results for nadir radiances with be presented. In addition, only one solar zenith angle, $\mu_o = 0.8$ is used in the simulations. The work of Minnis *et al* (1992) showed that marine stratocumulus cloud had the following relationship between their optical depth τ_c and geometric thickness, Δz

$$\Delta z = 45 \tau_c^{\frac{2}{3}} \tag{11.1}$$

where the units of Δz are in meters. In the simulations presented here, a constant geometrical thickness of 250 meters is assumed which corresponds to a mean optical thickness of 13. This study is concerned solely with horizontal variation of extinction and will ignore the effect of horizontal variation in cloud geometrical thickness. A rigorous study of many cloud fields under many viewing geometries should be performed, but since the motivation of this chapter is merely to estimate the range of errors in A-band radiances, only two vastly different clouds fields with a single viewing configuration will be performed.

In the sections to follow, the backward Monte Carlo model described in Appendix B is used to compute the A-band spectra in the presence of two cloud fields. In Figs 11.1 and 11.2 it was assumed that the clouds were positioned between 850 and 900 mb and that the lower surface was non-reflecting. The cloud droplets were assumed to conservatively scatter and to have an asymmetry parameter of 0.85 which is consistent with the Mie scattering results shown in Chapter 2.

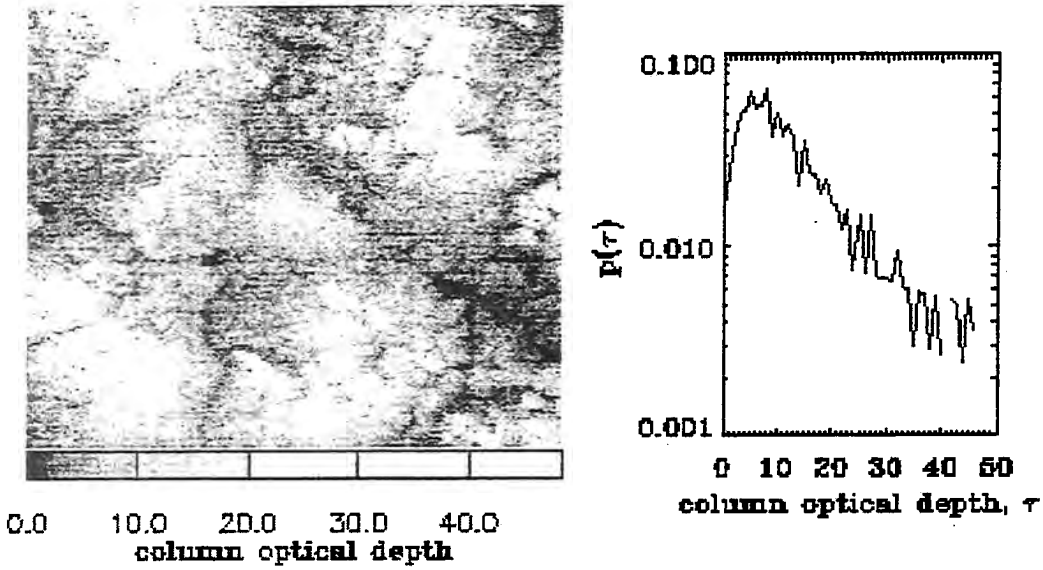

Figure 11.1: Left panel shows horizontal distribution of column optical depth for cloud field #1 and left panel shows the histogram of the column optical depth

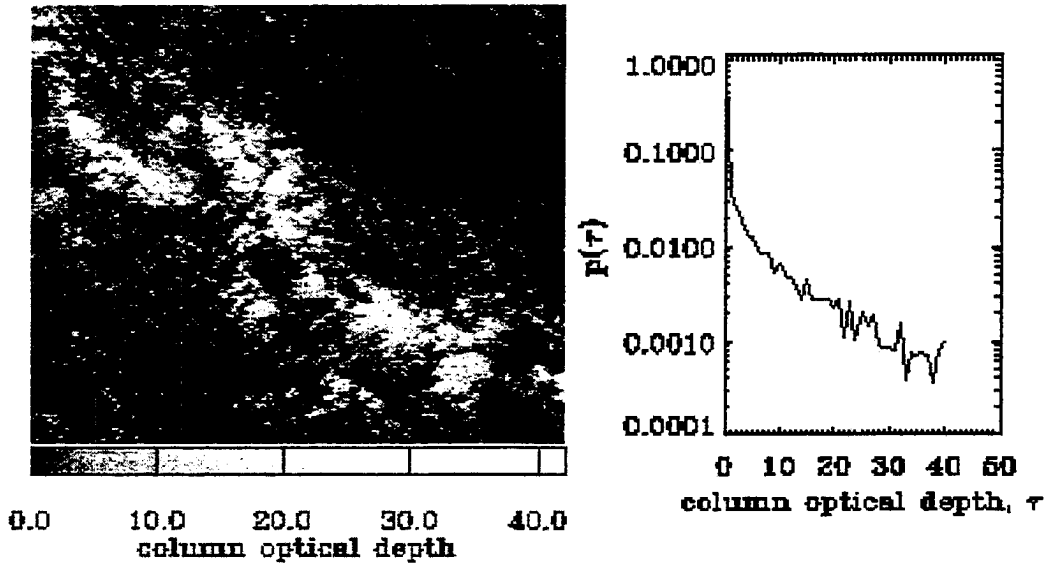

Figure 11.2: Left panel shows horizontal distribution of column optical depth for cloud field #2 and left panel shows the histogram of the column optical depth

quantity	field #1	field #2
N	0.99	0.37
$< \tau_c >$	22.0	2.22
$\frac{\sigma}{<\tau_c>}$	0.80	2.93

Figure 11.3: Properties of cloud fields shown in Fig 11.1 and 11.2

11.4 Effect of Cloud Heterogeneity on A-band Spectra

Three dimensional radiative simulations were carried out to quantify the errors in the A-band radiances due to the cloud spatial variability. The errors in the A-band radiances are computed by comparing the true values, produced by the 3D model, and the values produced from the plane parallel forward model developed in Chapter 5. This error is comprised of two terms. The first term is due to unresolved sub-pixel variability. This error arises from the fixed resolution of the satellite being much larger than the scale of variability of the cloud field. The spatial resolutions of satellite data ranges from 28.5 meter LandSat data to the typical 1 km resolution currently used for GOES and AVHRR retrievals. The spatial resolution of MODIS and CERES are on the order of 200 - 500 meters. A spatial resolution of 100 m is also shown which might be representative of future satellities. As figure 11.2 shows, the 28.5 meter LandSat data shows spatial structure much smaller than the resolution of these operational satellite sensors. Figs 11.4 and 11.5 show the effect of spatially averaging the actual 28.5 meter resolution cloud fields to several representative satellite resolutions. As these figures show, the current resolution of operation satellites needs to be on the order of 100 meters to resolve the structures seen in cloud field #1. In addition, results will be shown later showing the effect of sub-pixel variability on the cloud field #2 is also significant.

The second error source in the plane parallel modeling of A-band radiance is due to the effect of horizontal transport of photons, ignored in one-dimensional forward models. Through horizontal transport, neighboring pixels outside the immediate field-of-view of the sensor can influence the reflectance of those pixels. In plane parallel models, there is no net horizontal transport of photons while in three dimensional clouds, photons tend to escape from denser region of the clouds to more tenuous regions.

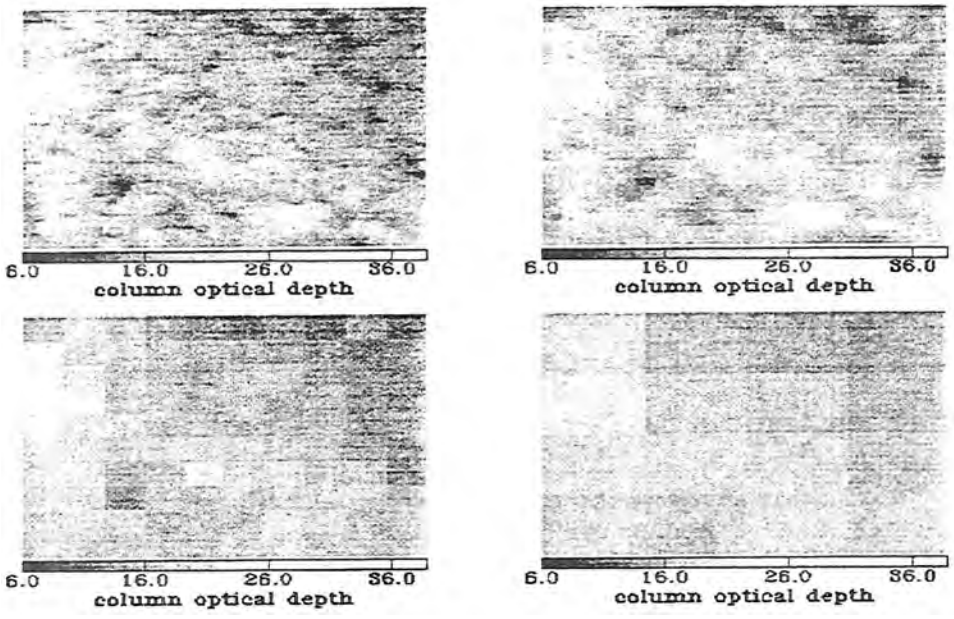

Figure 11.4: Comparison of Satellite Spatial Resolution of the perceived structure of cloud field # 1. The satellite resolutions are 28.5 m (LandSat), 100 m, 300 m(MODIS) and 1000m (AVHRR).

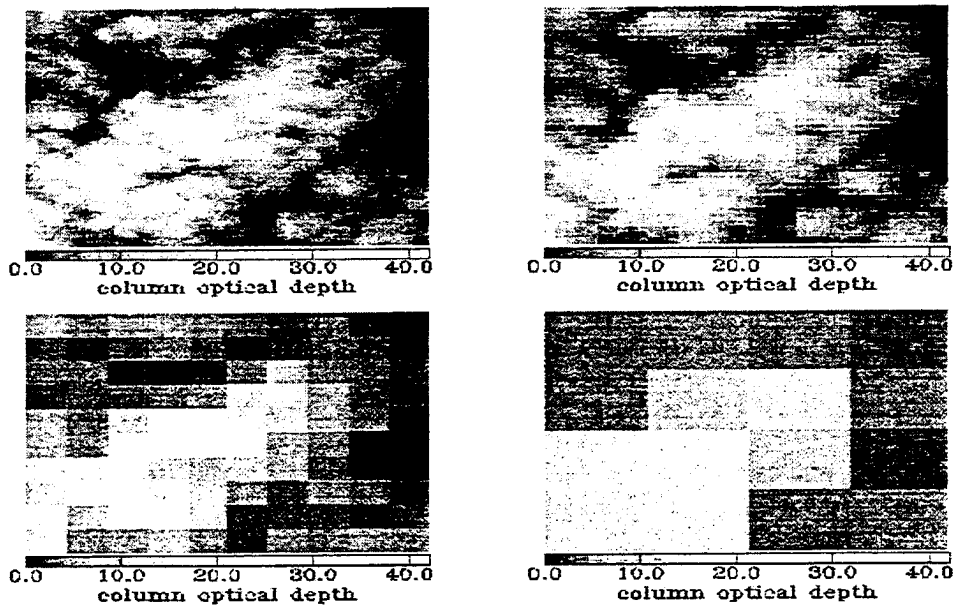

Figure 11.5: Comparison of Satellite Spatial Resolution of the perceived structure of cloud field # 2. The satellite resolutions are 28.5 m (LandSat), 100 m, 300 m(MODIS) and 1000m (AVHRR).

Fig 11.6 illustrates the effect of these two contributions on the spatial variability of A-band radiances. The example shown corresponds to the case of conservative scattering which occurs in the continuum region of the spectrum. The left panel of Fig 11.6 shows the horizontal radiance distribution computed for a small section of cloud field # 1 and averaged to a resolution of 285 meters. The center panel shows the radiances distribution computed assuming using the 285 meter average optical depth in the three dimensional model. The difference in the radiance in the center compared the left panel is due to the effect of sub-pixel averaging. The right panel shows the radiance distribution using the 285 meter averaged optical depth and using a plane parallel model to compute the radiance. This method of using a pane parallel scheme on a pixel by pixel basis is termed the independent pixel approximation(IPA) (Minnis *et al*, 1993). The difference between the left and right panels therefore shows both the errors due to sub-pixel variability and to the horizontal transport of photons. From Fig 11.6 we see that ignoring horizontal transport causes the thick regions of the cloud to appear brighter and the tenuous regions to appear darker relative to the true three dimensional simulation.

11.4.1 Variation in Errors in A-band Spectra due to Cloud Heterogeneity with satellite resolution

As described above, the errors of plane forward model computation of A-band observables, I_ν and s_ν, are comprised of errors due to sub-pixel variability and the horizontal transport of photons. Fig 11.7 shows the variation of these errors as a function of the satellite resolution for three values of the total column optical depth of oxygen $\tau^*_{o_2}$. The left column of panels shows the errors in the nadir reflected radiance, I_ν and the right column shows the errors in the radiance ratio, s_ν. The top line in each plot shows the errors due to both the sub-pixel variability and to horizontal transport. The top line was computed by comparing the true pixel value of the given quantity compared to the IPA estimate for that pixel. The lower curve represents the errors due to sub-pixel averaging and was computed using the 3d model which has horizontal transport but assumed a uniform value of optical depth in the pixel. The shaded region between these two curves represents the errors due to horizontal transport.

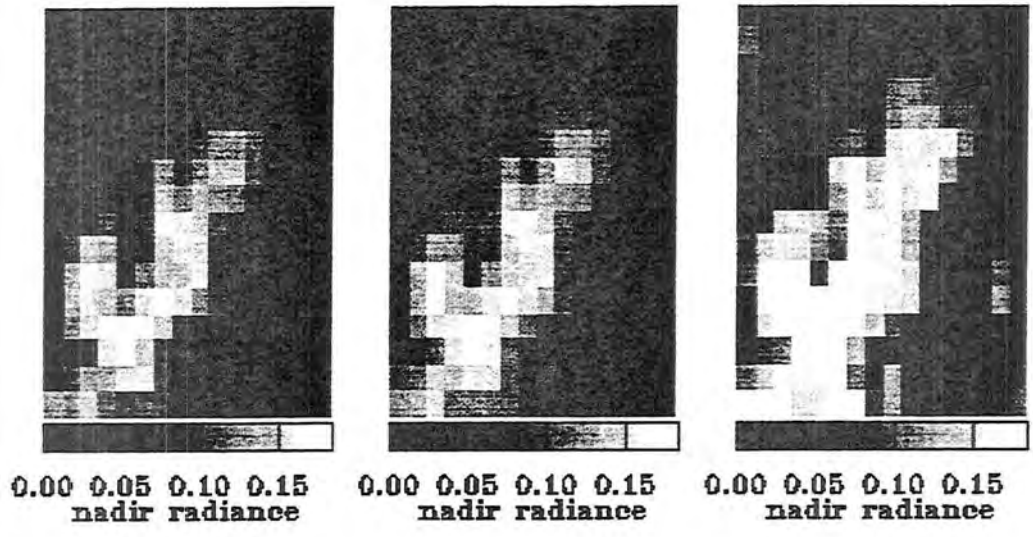

Figure 11.6: Comparison of the continuum nadir radiance fields for cloud field #2. The left panel shows the full simulation, the center panel shows the results with sub-pixel averaging, and the right shows the results with sub-pixel averaging and no horizontal transport

Fig 11.7 shows the errors in the format described above for I_ν and s_ν for cloud field #2. Looking first at the radiance errors, the left column, shows that the sub-pixel averaging error increases almost linearly with the resolution of the satellite. The errors due to sub-pixel averaging range from 7% from 100 meter resolution satellite to over 15 % for a 1 km resolution satellite. In contrast the total errors in the radiances shows much less of a sensitivity to satellite resolution and appears to be about 20 % for the resolution simulated. This is caused by the near balance of the increase in the sub-pixel error and the decrease in the horizontal transport error with increasing satellite resolution. Errors in the radiance are shown for values of $\tau^*_{o_2}$ of 0,1, and 2. These value of $\tau^*_{o_2}$, as shown in Chapter 6, are the range of opacities needed to perform the optical parameter retrievals of low clouds. As the amount of absorption in a cloud layer increases, multiply scattered photons begin to be attenuated. As the absorption increases, the scattering becomes more localized and the influence of neighboring pixels should be minimized. A Fig 11.7 shows, a definite but small decrease in the radiances errors as seen as $\tau^*_{o_2}$ increases. To greatly reduce these

errors would require detecting radiances at those wavelengths with much higher $\tau^*_{o_2}$. For the geometrical thickness of the clouds studied here, only 8 % of the total oxygen optical depth is contained in the cloud layer. Since low clouds are below most of the gas in the atmosphere, the advantage of reducing errors due to horizontal transport is lost by the rapid decrease in the reflectance of the cloud layer as $\tau^*_{o_2}$.

The right panel of Fig 11.7 shows the errors in the spectral radiance ratio s_ν. Since s_ν does involve a ratio of radiances, much of the errors due to spatial variability cancel as they did for in the case of phase function errors. The results are not shown for $\tau^*_{o_2} = 0$ since s_ν is identically unity is all cases and would have no errors. The errors in s_ν appear to be on the order of only 1 - 2 % for the highly spatially variable cloud field #2. As shown in Chapter 6, the sensitivity of s_ν to optical depth of low cloud is much less than the sensitivity of I_ν to optical depth of low cloud. This prohibits an accurate retrieval of low cloud optical depth based on s_ν which is insensitive to cloud heterogeneity. Fig 11.8 shows the variation of I_ν and s_ν with τ_c predicted by plane parallel theory. As Fig 11.8 shows, the relative range of s_ν is much less than the range of I_ν. Therefore, small errors in s_ν can represent as significant of an error in retrieved optical depth as larger errors in I_ν. As will be discussed in the next section, however, the values of s_ν in heterogeneous clouds can be provide key information about the cloud structure.

11.5 Detection of Spatial Variability in A-band Reflectance Spectra

This section introduces a novel technique that diagnoses when estimates of optical parameters retrieved using a conventional forward model are affected by cloud heterogeneity. Again the results are concerned with the retrieval of the optical depth but similar arguments would apply to the other parameters. The retrievals of optical depth shown in this section will not use the full retrieval technique used in Chapter 6. The inclusion of the retrievals of the other parameters such as cloud top pressure and the surface albedo should not alter this conclusions of this section.

The physical mechanism that is the basis for the diagnosis of heterogeneity lies in the differing effect cloud heterogeneity has on each the A-band observables, I_ν and s_ν. To

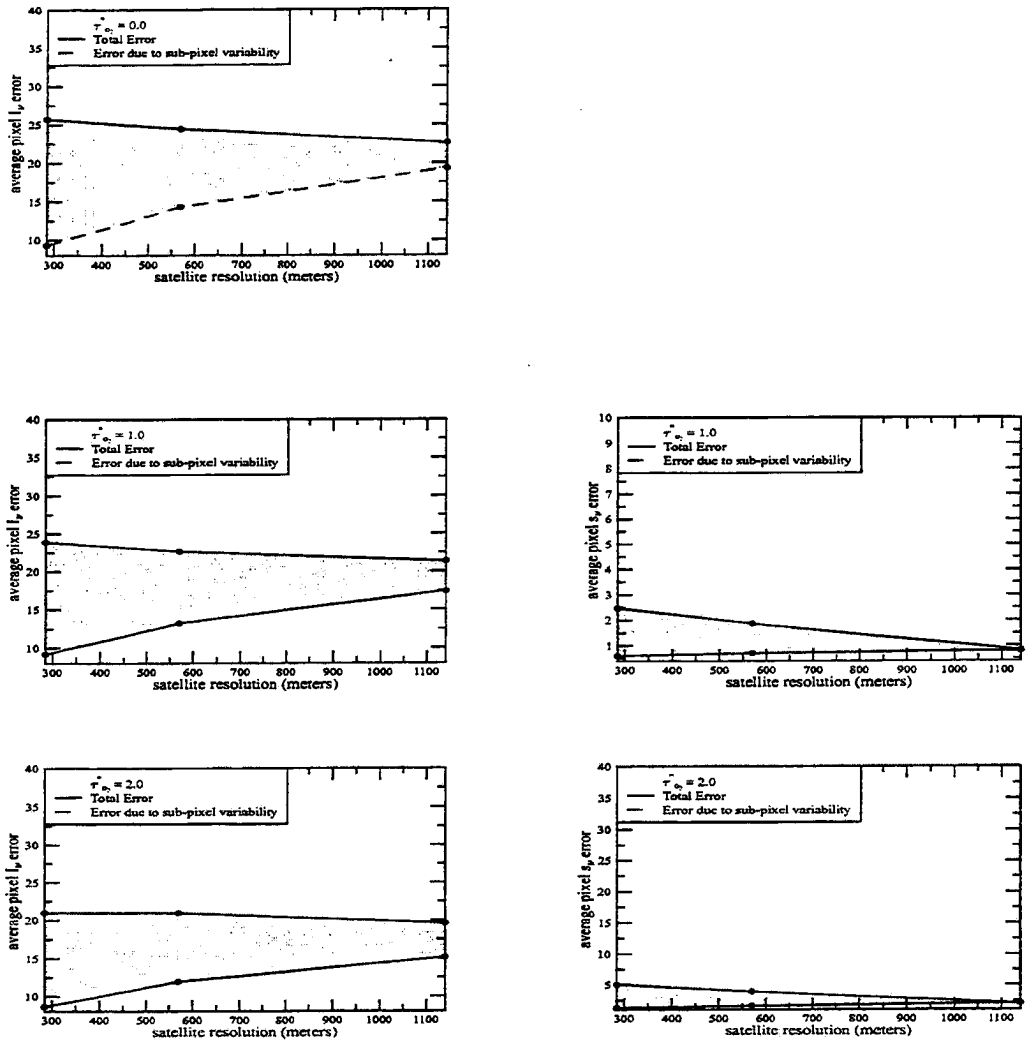

Figure 11.7: Variation with satellite spatial resolution and with column absorption optical depth of oxygen, $\tau^*_{o_2}$ of the average pixel error in A-band observables computed for cloud field #1

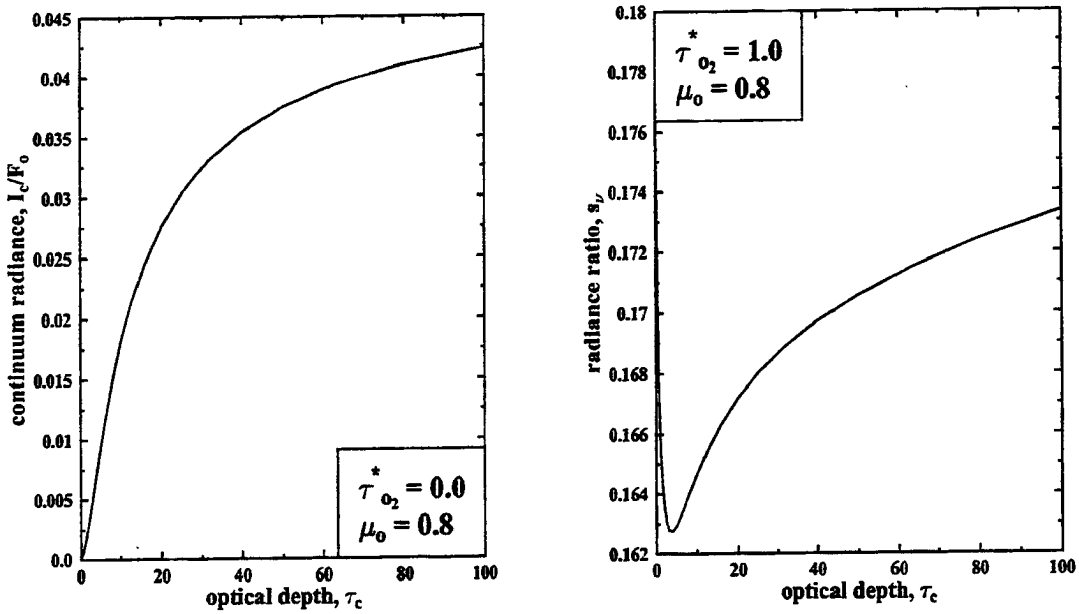

Figure 11.8: The variation of the continuum radiance I_c and radiance ratio, s_ν, predicted by plane parallel theory.

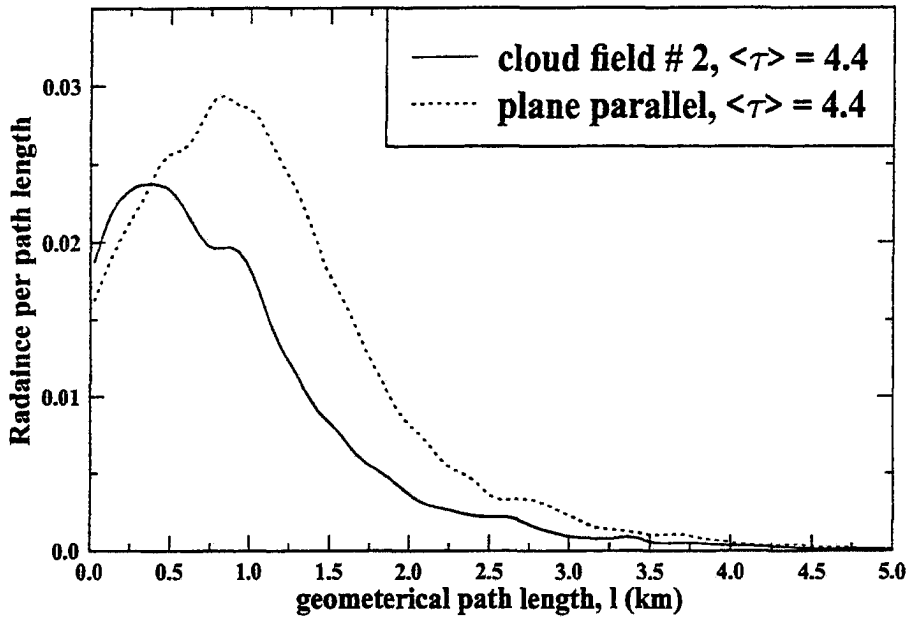

Figure 11.9: Variation with optical depth of I_c and $\frac{l}{\Delta Z}$ predicted by plane parallel theory(solid line). Circles represent three pixels from cloud field # 2.

illustrate these differences, Fig 11.9 shows the distribution of the radiance contribution as a function of path-length. The integral of each curve would give the value of the continuum radiance I_c. The two curves shown in Fig 11.9 correspond to the domain average value for cloud field #2 and to a plane parallel cloud with the same mean optical depth. As Fig 11.9 shows, the domain reflectance of the heterogeneous cloud field is less than the reflectance for the plane parallel cloud. This is consistent both with intuition and with the plane parallel albedo biases reported by Cahalan *et al* (1994). As a consequence, a plane parallel retrieval of optical depth based the domain averaged radiances results in an underestimate of the value of the domain averaged optical depth.

As the results of Figs 11.5 and 11.6 showed, heterogeneity also effects the values of s_ν. To understand the effects of heterogeneity on s_ν it is necessary understand the effect of heterogeneity on photon path-lengths. As the equivalence theorem of Irvine (1964) states,

$$s_\nu = \int_o^\infty p(l) e^{-\sigma_{abs,\nu} l} dl \tag{11.2}$$

where $p(l)$ is the geometric path length distribution, l is geometric path-length and $\sigma_{abs,\nu}$ is the gas volume absorption coefficient. This relationship shows how s_ν and $p(l)$ are inherently related to each other. For a given value of $\sigma_{abs,\nu}$, the greater the contribution from longer path-lengths, the more gas absorption along photon path will occur and the lesser the value of s_ν will be. As the plane parallel calculations of Fig 11.8 showed, the values of s_ν reach a relative minimum at a plane parallel optical depth of around 4 for the parameters used in this simulation. The initial decrease is s_ν with increasing optical depth is due to multiple scattering increasing the geometric distance traveled by the photons comprising the reflected radiance. As the optical depth increases, the photons do not penetrate as far into the cloud layer the photon path-length and the attenuation by gases decreases causing an increase in s_ν.

Fig 11.9 also shows the effect of heterogeneity on the path-length distribution. If each curve in Fig 11.9 where normalized by I_c, the resulting curves would be the geometric photon path-length distributions, $p(l)$. The mean geometric path length for the cloud field #2 was computed to be 0.94 km while in the plane parallel case the mean path length was 1.13 km. From this simulation and others, it can be demonstrated the the effect of cloud heterogeneity acts to decrease the mean geometrical path-length for reflection. In the limiting case where the spatial variability were so great that all of the cloud water in scene #2 were gathered in a single dense optically thick cloud, the geometrical path in reflection would go to zero because the cloud were so optical thick the photons would not penetrate any considerable distance into the cloud.

From Fig 11.9, it is clear that heterogeneity effects both I_ν and s_ν but in different ways. While Fig 11.9 was computed using the domain averaged values from cloud field #2, the ability of the retrieval to exploit these differences on a pixel by pixel basis is now explored. As discussed above, the effect of heterogeneity caused the domain averaged optical depth from a radiance retrieval to be underestimated and the optical depth from a radiance ratio retrieval to overestimated. Fig 11.10 shows the results of applying both radiance and radiance ratio retrievals to pixel level data of cloud fields #1 and #2. The pixels are assumed to be 285 meters wide. The x-axis in Fig 11.10 is the ratio of the

optical depth retrieved using the radiance ratio, s_ν and the optical retrieved using the radiance, I_ν. The y-axis of Fig 11.10 is the ratio of the retrieved optical depth to the true value of optical depth obtained by averaging the LandSat data over the pixel. The y-axis represents the errors incurred by the conventional radiance retrievals performed using the AVHRR and GOES visible channels.

If both cloud fields were plane parallel, with no spatial variability, the radiance and radiance ratio optical depths should be the same as the true optical depth and the all points in Fig 11.10 should be centered closely around the point (1.0,1.0). The spread of the values is a clear indication of the amount of variability in the cloud field. The values for cloud field # 1, being the more uniform of the two cloud fields, cluster around the plane parallel value. The more spatially heterogeneous cloud field #2, shows points deviating significantly from the plane parallel value. Based on these results, it is hypothesized that value of the $\frac{\tau_s^{ipa}}{\tau_I^{ipa}}$ can be used to diagnose when the effect of cloud heterogeneity is too great to allow an accurate retrieval of optical depth using a plane parallel model. It is important to note that this ratio comes entirely from measurement of A-band spectra and does not assume any more *a priori* information about the value of the optical depth than was assumed for the retrievals performed in the low cloud retrievals of Chapter 6. It appears that once this ratio exceeds 2, the retrieved optical depths are in error in excess of 10-20%. Therefore using a plane parallel retrieval model which uses both I and s to estimate optical depth, produces a retrieval which is able to predict when it fails due to cloud spatial variability. This ability is not offered by any current retrieval scheme and would be impossible to implement in retrievals using data from current observing systems based on multiple broad-band channels.

As Fig 11.10 shows, the retrieved optical depth based on the radiance can be less than or greater than the true value. This behavior is evidenced by the two branches in the results in Fig 11.10 for cloud field #2. The physical reason for this behavior is than photons tend to migrate from optically thick regions to optically thin regions. To illustrate this point, Fig 11.11 shows the variation of the ratio of the radiance retrieved optical depth to the true pixel optical depth as function of the pixel optical depth. As this figure shows,

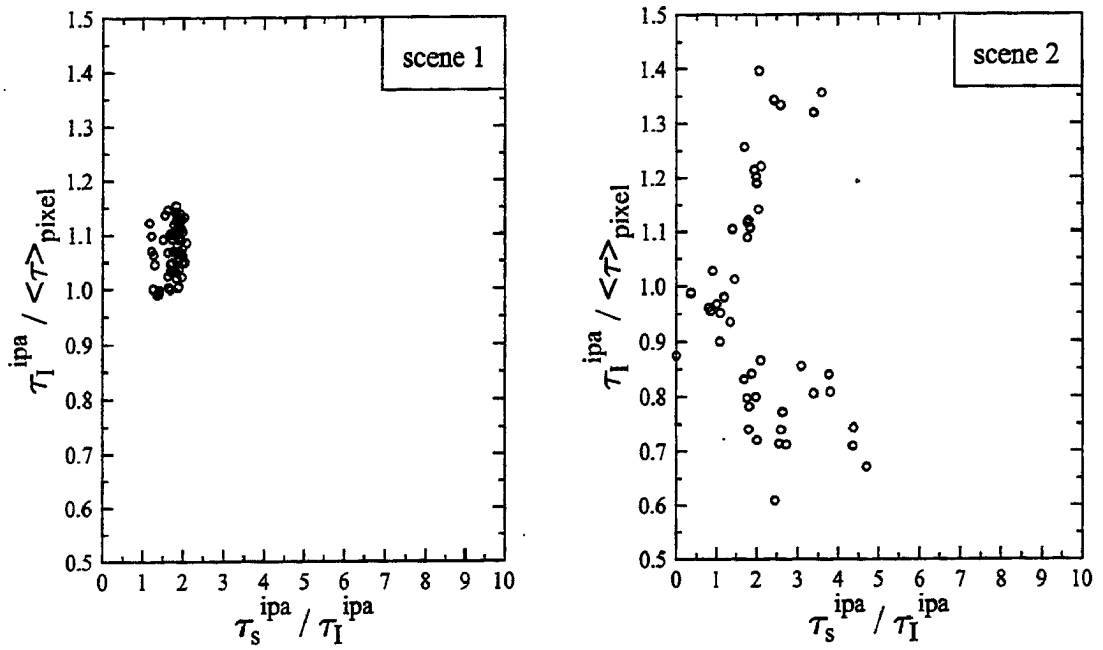

Figure 11.10: Variation of the optical depth retrieval errors using radiance, I, and the radiance ratio, s for cloud fields #1 and #2.

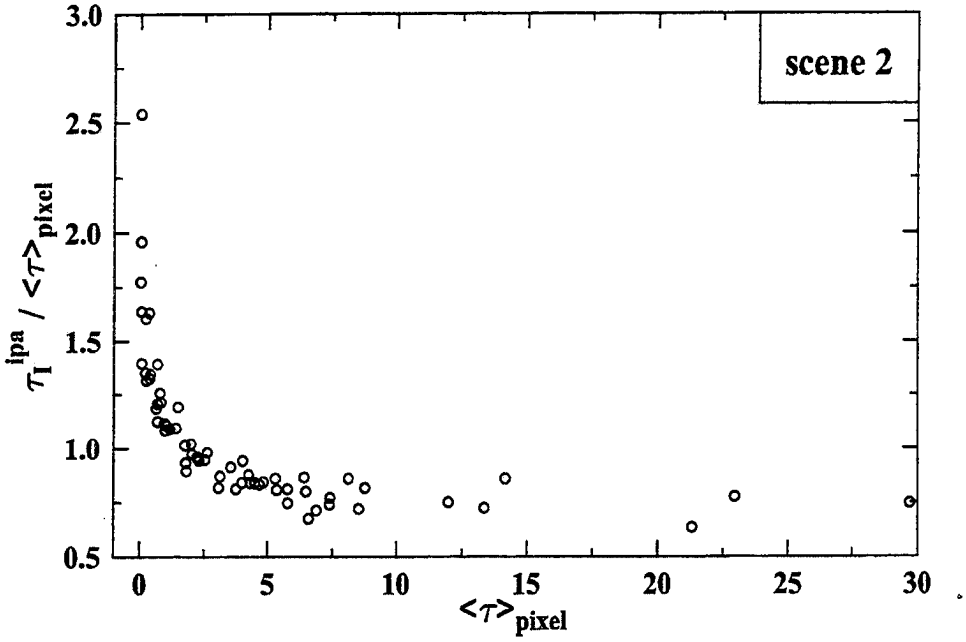

Figure 11.11: Variation of the errors in radiance optical depth with the true value of the optical depth

the optical depths of optically thin pixels tend to be overestimated and the optical depths of optically thick pixel tend to be underestimated.

11.6 Summary and Conclusions

This chapter attempted to use two very different cloud fields to quantify the ranges of the errors in the A-band observables to the cloud spatial structure. As described in Chapter 4, the optimal estimator retrieval approach used here relies on meaningful estimates of the errors in the forward model which includes the errors due to cloud spatial heterogeneity. The results showed that for the marine stratocumulus fields studied, the radiances errors were on the order of 3 - 20% and the radiance ratio errors were on the order of 1-5%. These errors were found to be dominated by the error due to horizontal transport for satellite resolutions less then 200 meters while the error to due sub-pixel variability was dominant for satellite resolutions on the order of 1 km. Using both the radiance and radiance ratios, a technique was developed which allows the plane parallel forward model

developed in Chapter 4 to be able to predict when its retrievals are so influenced by spatial heterogeneity that the results are invalid. This ability would represent a significant step forward in the current abilities of passive retrievals which have no ability to self-diagnose the effect of cloud spatial variability on their retrievals.

Fig 11.11 schematically presents these ideas The left panel of Fig 11.11 shows the plane parallel variation of the continuum radiance, I_c with the optical depth. The left panel of Fig 11.11 shows the plane parallel variation of I_c as a function of τ_c and the right panel presents the ratio of the mean geometrical path length to layer thickness as a function optic optical depth. The retrieval using the one-dimensional forward model will derive optical depths that fall on these curves. Also shown in Fig 11.11 are values from three pixels from cloud field # 2. As the left panel shows, radiance based retrievals tend to bias the retrieved optical depth low though in in thin regions, the bias was slightly positive. By contrast, the radiance ratio or path-length based retrievals bias the optical depth high. As the right panel shows, there are typically two values of optical depth which produce the needed path-length or radiance ratio. Typically, the lower value of optical depth can be ignored since it is inconsistent with the radiance value.

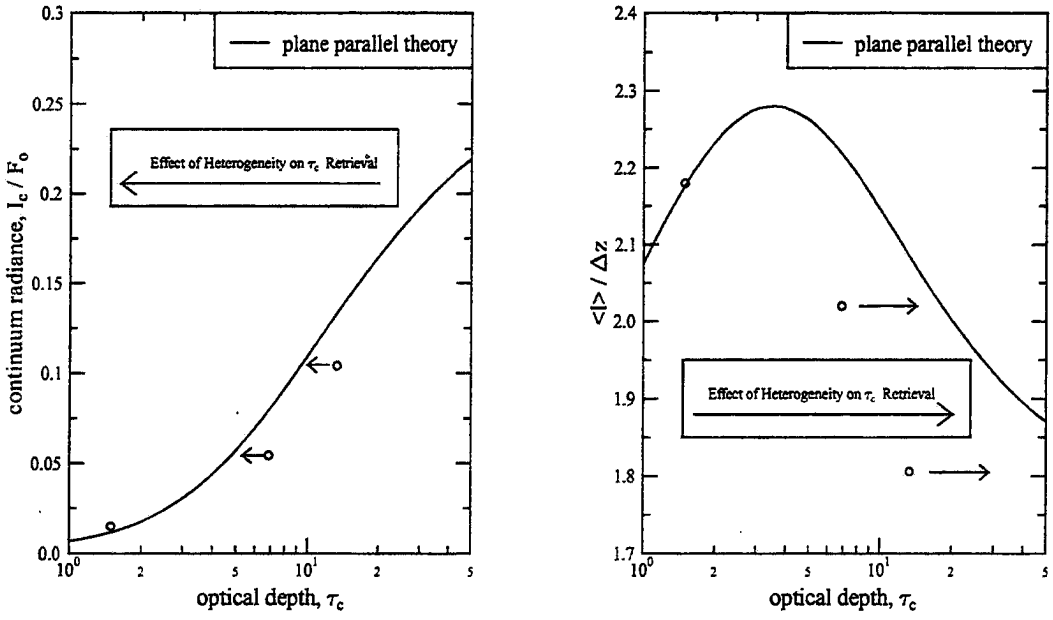
plane parallel theory
Effect of Heterogeneity on τ_c Retrieval
continuum radiance, I_c / F_o
optical depth, τ_c
plane parallel theory
Effect of Heterogeneity on τ_c Retrieval
$\langle I \rangle / \Delta z$
optical depth, τ_c

Figure 11.12:

Chapter 12

Conclusions

This paper explored through theoretical and numerical means, the potential benefits of using nadir reflectance spectra in the oxygen A-band to remotely sense cloud and aerosol properties. Better estimates of cloud and aerosol properties is a critical need for advancing atmospheric and climate sciences. Currently, the national funding agencies involved in atmospheric science research have committed vast resources to development and launching of observing systems to remotely sense cloud and aerosol layers. As discussed in Chapter 1, these observing systems consist mainly of multiple broad-band channels. The bulk of the techniques used to estimate cloud properties involve the use of channels that measure reflected solar radiation and channels that measure emission by the atmosphere. The use of the A-band of oxygen as a basis for an observing system is a different approach in that it uses a combination of absorption by gases and scattering by particles. As described in detail in Chapter 2, the A-band consists of a narrow spectral region where oxygen is the only absorbing gas. An instrument of sufficient resolution can view the atmosphere through channels which are virtually transparent or opaque to oxygen absorption. It is the ability to measure at many differing values of oxygen absorption which allows for the independent retrieval of the various optical parameters.

To judge the utility of using A-band measurements as an observing system, the optimal estimator technique of Rodgers (1976), developed originally for the use in the retrieval of temperature and water vapor profiles, was used. This retrieval approach constrains the solution through *a priori* estimates of the estimated parameters. The strength of this technique lies in its ability to estimate directly the errors in the retrieved parameters and

to estimate how much the retrieval relied on *a priori* data sources. The cost of using this approach was the necessity to make meaningful estimates of the uncertainties in both the measurements and the ability to model those measurements with the forward model. Throughout this paper, realistic estimates of both the measurement and forward model errors were used. The two main error sources include both phase function and the effects of cloud spatial variability - errors that are rarely quantified in the remote sensing of cloud and aerosol layers.

Coupled with the forward model of A-band reflectance, developed in Chapter 4, the simulated A-band observing system was applied to representative retrieval scenarios including low clouds, cirrus clouds and aerosol layers. The results of the retrieval computed with realistic estimates of the errors due the phase function and spatial heterogeneity uncertainties are summarized below.

- For low clouds with $\tau_c > 5$, the retrieval could estimate τ_c to within 10 %, p_t to within 3 % and Δp s within 20 %. When optically thin low clouds were present, the retrieval could estimate α_{sfc} to within 5 %.

- Even with a realistic accounting of the large uncertainties in cirrus phase function, the retrieval could estimate τ_c of cirrus to within 20 % for τ_c ranging from 0.2 to 4 and could estimate p_t to within 10 %. The retrieval demonstrated the ability to estimate g to within 3 % for may cirrus conditions.

- With currently achievable measurement and forward model errors, estimates of aerosol optical depth accurate to about 10 % are possible over a dark surface. In addition, meaningful estimates of ω_o are possible for thick layers of aerosol $\tau_c > 0.5$. A 1 % measurement requirement is needed to estimate properties of aerosol over bright surfaces

- Use of active sensor information to constrain p_t and Δp was shown to greatly enhance the retrieval accuracy of thin low clouds. The additional constraints were also shown to allow for better estimation of g for cirrus clouds.

- A combined A-band - LIDAR retrieval was shown to offer the possibility of accurately estimating both the phase function and optical depth of cirrus to a degree surpassing the abilities of the separate instruments.

The current arsenal of remote sensing methods has several weakness in their ability to estimate cloud and aerosol properties. The specific areas where the A-band observing system was shown to improve upon the current capabilities are listed here.

- The ability to detect and estimate the properties of thin low clouds positioned near a reflecting surface
- The ability to detect and estimate the properties of thin cirrus over any surface
- The ability to estimate cloud top pressure of optically thin cirrus
- The ability to estimate cloud pressure thickness
- The ability to estimate extinction in multiple layers
- The ability to independently retrieve both optical depth and some measure of the phase function in cirrus clouds
- The ability to estimate the optical depth, location and surface albedo for aerosol layers of moderate thickness over land.
- The ability to estimate the single scatter albedo for thick aerosol layers in addition to other optical properties.
- The ability to self-diagnose when cloud heterogeneity prevents a meaningful retrieval

The above list of capabilities were shown to be possible a space-borne A-band radiometer with a spectral resolution of $0.5cm^{-1}$ and realistic levels of noise and calibration. The above list of capabilities is not put forth to say that the A-band observing system supersedes the abilities of the multi-channel broadband observing systems discussed in Chapter 1. For example, since the A-band occurs in spectral region where cloud particles do not absorb, the A-band is incapable of making estimates of particle size, an important

micro-physical parameter Also, A-band spectra contain no information about the spectral variation of cloud properties which is crucial for the proper treatment of clouds and aerosols in climate models.

While passive observing systems, such as AVHRR and MODIS, will continue to play a main role in the remote sensing of cloud and aerosol properties, it is clear from the recent LITE and planned TRMM missions that active sensors will join with current passive systems in estimating cloud and aerosol properties. The results of Chapter 11 clearly showed the potential benefits of combining passive A-band measurements with those from an active system to enhance to ability to estimate cloud and aerosol parameters. For example, the results showed that, an A-band and LIDAR system in conjunction could make meaningful estimates of the phase function in cirrus clouds. This combination was shown to greatly enhance the phase function information deducible from A-band or LIDAR measurements alone. The shape of cirrus phase function is currently an area of much research the capabilities offered by these measurements would be a significant advancement.

12.1 Future Work

Though attempts were made to incorporate realistic estimates of measurement and forward model error, the validation through measurements of the merits of basing a cloud and aerosol observing system on nadir A-band reflectances needs to be performed. Under a project headed by Prof. J. Anderson at Harvard University, a spectrometer which measures in the A-band with the resolution simulated in this study will fly on-board the NASA ER-2 high altitude aircraft. The goal of this mission is to test techniques for the remote sensing of clouds and water vapor and offers an ideal platform to test the retrieval techniques put forth in this paper. Engineering test flights have already taken place with the instrument payload and research flights are scheduled for next year. While the use of surface based measurements can not validate a space-borne nadir reflectance retrieval method, it can demonstrate the ability of a forward model to match observed A-band radiances. The use a surface based LIDAR and A-band radiometer should be able to demonstrate the ability of the combined measurements to retrieve phase function information.

References

Ardanuy, P. E., L. Stowe, A. Gruber, M. Weiss, and C. Long, 1989: Longwave cloud radiative forcing as determined from Nimbus-7 observations. *J. Climate*, **2**,766-799.

Arking, A. and J. Childs, 1985: Retrieval of cloud cover parameters from multispectral satellite images. *J. Clim. App. Met.*, **24**,322-333.

Bakan and Quenzel, 1976: Path length distributions of photons scattered in turbid atmospheres. *Contr. Atmos. Phys.*, **49** 272-284.

Barker, H. W., B. W. Wielicki and L. Parker, 1996: A parameterization for computing grid-averaged solar fluxes for inhomogenous marine boundary layer clouds. Part II: Validation using satellite data. *J. Atmos. Sci.*, **53**, 2304-2316.

Bernstein, L. S., A. Berk, P. K. Acharya, D.C. Robertson, G. P. Anderson, J. H. Chetwynd and L. M. Kimball, 1996: Very narrow band model calculations of atmospheric fluxes and cooling rates, *J. Atmos. Sci.*, **53**,2887-2904.

Bohren, C. and D. R. Huffman, 1983: *Absorption and Scattering of Light by Small Particles.* Wiley, New York, 520 pp.

Cahalan, R.F., 1989: Overview of Fractal Clouds, in *Remote Sensing Retrieval Methods*, Deepak Ed, 371-389

Cahalan, R. F., W. Ridgway, W. Wiscombe, T.L. Bell and J.B. Snider, 1994; The albedo of fractal stratocumulus clouds, *J. Atmos. Sci.*, **51** 2434-2455.

Cahalan, R. F., D. Silberstein and J.B. Snider, 1995:Liquid water path and plane-parallel albedo bias during ASTEX. *J. Atmos. Sci.*, **52**,3002-3012.

Chamberlain, J.W and D. M. Hunten, 1987: Theory of Planetary Atmospheres, (second Edition), Academic Press, Orlando Florida, 481pp.

Chambers L. H., 1997: Computation of the effects of inhomogenous clouds on retrieval of remotely sensed properties. Preprints, *Ninth Conf. on Atmospheric Radiation*, Long Beach, CA, Amer. Meteor. Soc., 378-382.

Chandrashekar, S., 1960: *Radiative Transfer*, Dover, 393 pp.

Chou, M. D., and A. Arking, 1980: Computation of infrared cooling rates in the water vapor bands, *J. Atmos. Sci.*, **37**, 855-867.

Curran, R. J., H. L. Kylie, L. R. Blaine, J. Smoth and T. Clem, 1981: Multichannel scanning radiometer for remote sensing cloud physical parameters. *Rev. Sci. Instrum.*,53, 1546-1555. Dianov-Klokov, V. and L. Krasnokutskaya, 1972: Comparison of observed and calculated effective photon path length in clouds,*Izvestia*,8,843-852.

Duda, D. P. and G. L. Stephens, 1994: *Macrophysical and microphysical influences on radiative transfer in two dimensional marine stratus.* Ph.D. dissertation, Colo. State. Univ., Dept. of Atmos. Sci., Fort Collins, 202pp.

Elasser, W. M., 1942: Heat Transfer by Infrared Radiation in the Atmosphere, *Harvard Meterol. Stud.*, **6**, Harvard University Press, Cambridge, Mass.

Fishbein, E.F., R. Cofield, L. Froidevaux, R. Jarnot, T. Lungu, W. Read, Z. Shippony, W. Waters, I. McDermid, T. McGee, U. Singh, M. Gross, A. Hauchecorne, P. Keckhut, M. Gelamn, R. Nagatani, 1996: Validation of UARS Microwave Limb Sounder temperature and pressure measurements. *J. Geophys. Res.*, 101, 9983-10016.

Fischer, J., and H. Grassl, 1991: Detection of cloud–top height from backscattered radiances within the oxygen–A band. Part I: theoretical study. *J. Appl. Met.*, **30**, 1245–1259.

Fischer, J., W. Cordes, A. Schmitz-Peoffer, W. Renger, and P. Mörl, 1991: Detection of cloud-top height from backscattered radiances within the oxygen A band. Part 2: Measurements. *J. Appl. Meteor*, **30**, 1260-1267.

Gabriel, P. M., S.-C. Tsay, G. L. Stephens, 1993: A Fourier-Ricatti approach to radiative transfer. Part I: Foundations. *J. Atmos. Sci.*,**50**,3125-3147.

Gao,B.-C., A. Goetz, and W. Wiscombe, 1993: Cirrus cloud detection from airborne imaging spectrometer data using the 1.38 μm water vapor band. *Geophys. Res. Let.*,**20**,301-304.

Gerber, H. E., 1984: Variability of some optical coefficients of north atlantic maritime aerosols. *Aerosols and Their Climatic Effects*, H. E. Gerber and A. Deepak (Eds.), A. Deepak Pub.,63-81.

Grechko Ye.I., V. I. Dianov-Klokov, and I. P. Malkov, 1973: Aircraft measurements of photon paths in reflection and transmission of light by clouds in the 0.76 μm oxygen A-band. *Atmos. Ocean. Phys.*,**9**,262-269.

Grechko, Ye.I., V. I. Dianov-Klokov and I. P. Malkov, 1975: Measurement of photon effective paths in natural cloud systems. *Atmos. Ocean. Phys.*,**11**,125-138.

Goody, R. M., and Y. L. Yung, 1989: *Atmospheric Radiation: Theoretical Basis*, Oxford University Press, New York, 519 pp.

Guenther, B. W. Barnes, E. Knight, J. Barker, J. Harnden, R. Weber, M. Roberto, G. Godden, H. Montgomery, and P. Abel, 1995: MODIS calibration: A brief review of the strategy for the at-launch calibration approach. *J. Atmos. Ocean Tech.*, **13**, 274-285.

Han, Y., Rossow and A. Lacis, 1994: Near-global survey of effective droplet radii in liquid water clouds using ISCCP data, *J. Clim.*, **7**,465-491.

Hansen, J. E. and L. D. Travis, 1974: Light scattering in planetary atmospheres. *Space Science Reviews*, **16**, 527-610.

Harrison, E. F, P. Minnis, B. Barkstrom, V. Ramanathan, R. Cess, and G. Gibson, 1990: Seasonal variation of cloud radiative forcing derived from the earth radiation budget experiment. *J. Geophys. Res.*, **95**, 18687-18703.

Harshvardhan, B. A. Wielicki, K. M. Ginger, 1994: The interpretation of remotely senssed cloud properties from a model parameterization perspective. *J. Climate*, **7**, 1987-1998.

Heidinger, A. K. and S. K. Cox, 1995: Finite cloud effects in longwave radiative transfer. *J. Atmos. Sci.*, **53**, 953-963.

Hofstafter, K. and A. Heidinger, 1997: Infrared low cloud detection. *Proceedings of the Optical Society of America Topical Meeting on Remote Sensing of the Atmosphere*, Santa Fe, New Mexico, USA.

Irvine, W. M., 1964: The formation of absorption bands and the distribution of photon optical paths in a scattering atmosphere. *B.A.N.*, **17**, 266-279.

Irvine, W. M. 1967: Absorption bands and photon optical paths in a nonconservative scattering atmosphere. *Astrophys. J.*, **147**, 1193–1197.

Koepke, P., and H. Quenzel, 1981: Turbidity of th atmosphere determined from satellite: Calculation of optimal wavelength, *J. Geophys. Res.*,**86**, 9801-9805.

Kratz, D. P., 1995: The correlated-k technique applied to the AVHRR channels. *J.Q.R.S.T*, **53**, 501-517.

Lacis, A. A., and V. Oinas, 1991: A description of the correlated k distribution method for modeling nongray gaseous absorption, thermal emission, and multiple scattering in vertically inhomogeneous atmosphere. *J. Geophys. Res.*, **5**, 9027-9063.

Macke, A., P. N. Francis, G. M. McFarquhar, and S. Kinne, 1997: The role of ice particel shapes and size distributions in cirrus cloud radiative transfer. *submitted to J. Atmos. Sci.*

Marks, C. J., C.D. Rodgers, 1993: A Retrieval Method for Atmospheric Composition from Limb Emission Measurements, *J. Geophys. Res.*,98,14939-14953.

McKee, T. B., and S. K. Cox, 1974: Scattering of visible radiation by finite clouds, *J. Atmos. Sci.*, **31**,1885-1892.

Menke, W.,1989: *Geophysical Data Analysis: Discrete Inverse Theory.* Rev. ed., Academic Press, 285pp.

Michaels, H. H., 1963: Abscissas and weight coefficients for Lobatto quadrature. *Math, Comput.*, **17**, 237-244.

Minnis, P., P.W.Heck, D.F.Young, and B.J. Snider, 1993: Stratocumulus cloud properties derived from simultaneous satellite and island-based instrumentation during *FIRE. J. Atmos. Sci.*, **54**,1525-1532. Mitchell, R. M., and D. M. O'Brien, 1987: Error estimate for passive satellite measurements of surface pressure using absorption in the A band of oxygen. *J. Atmos. Sci.*, **44**, 1981–1991.

Nakajima, T, and M. D. King, 1990: Determination of the Optical Thickness and Effective Particle Radius of Clouds from Reflected Solar Radiation Measurements. Part I: Theory. *F. Atmos. Sci.*,47, 1878-1893.

O'Brien, D. M., and R. M. Mitchell, 1991: Error estimates for retrieval of cloud top pressure using absorption in the A-band of oxygen. *J. Appl. Met.*, **31**, 1179–1192.

O'Brien, D. M., 1992: Accelerated quasi Monte Carlo integration of the radiative transfer equation. *J. Quant. Spectrosc. Radiat. Transfer*, **48**, 41-59.

O'Brien, D.M., 1997: Detection of atmospheric turbidity from observations in the O_2 A-band. *submitted J. Ocean. Atm. Tech.*

Platt, C.M.R. and D.M. Winker, 1994: Vertical distribution and optical depths of clouds LITE observations. *Lidar Techniques for Remote Sensing, Proc., SPIE*, **2310**, 106-115.

Prabhakara, C., R. S. Fraser, G. Dalu, M.L.C. Wu, R.J. Curran, and T. Styles, 1988: Thin cirrus clouds: seasonal distribution over oceans deduced from Nimbus-4 IRIS. *J. Appl. Meteorol.*, **27**, 379-399.

Rodgers, C. D., 1976: Retrieval of atmospheric temperature and composition from remote measurements of thermal radiation, *Rev. Geophys. Space. Phys.*, **14**, 609-624.

Romanova, L. M., 1965: Limiting cases of the path distribution function of photons emerging from a thick light-scattering layer. *Atmos. Ocean. Phys.*, **1**, 348-351.

Rothman, L. S., R. R. Gamache, R.H. Tipping, C. P. Rinsland, M.A.H. Smith, D. Chris Benner, V. Malathy Devi, J.–M. Flaud, C. Camy–Peyret, A. Perrin, A. Goldman, S.T. Massie, L. R. Brown, and Barbe, N. Husson, and R. A. Toth, 1987: The HITRAN molecular database: editions of 1991 and 1992, *J. Quant Spectrosc. Radiat. Transfer,* , **48**, 469–507.

Saiedy, F., H. Jacobowitz and D. Wark, 1966: On Cloud-Top Determination from Gemini-5. *J. Atmos. Sci.*,24,63-69.

Smith, W. L., and R. Frey, 1990: On cloud altitude determination from high resolution interferometer sounder (HIS) observations, *J. Appl. Met.*,**29**, 658-662.

Stackhouse ,P.W., G. L. Stephens, 1991: A Theorectical and observational study of the radiative properties of cirrus: Results from FIRE 1986. *J. Atmos. Sci.*,**48**,2044-2059.

Stephens, G. L., 1979: Optical properties of eight water cloud types. *CSIRO Aust. Div. Atmos. Phys. Tech. Pap.*, **36**,1-35.

Stephens, G. L., 1988: Radiative transfer through arbitrarily shaped optical media. Part I: A general method of Solution. *J. Atmos. Sci.*, **45**, 1818-1836.

Stowe, L. L., 1991: Cloud and aerosol products at NOAA/NESDIS. *Palaeogeogr. Paleoclimatol. Paleoecol.*,**90**,25-32.

Takano, Y., and K.N. Liou, 1989: Solar radiative transfer in cirrus clouds. Part I: Single-scattering and optical properties of hexagonal ice crystals. *J. Atmos. Sci.*, **46**, 3-19.

Twomey, S., 1966: *Introduction to the mathmatics of inversion in remote sensing and indirect measurements*, Dover, 256pp.

Twomey, S. , H. Jacobowitz and H. B. Howell, 1966: Matrix methods for multiple-scattering problems. *J. Atmos. Sci.*, **23**, 289-296.

van de Hulst, H. C., and K. Grossman, 1968: Multiple light scattering in planetary atmospheres., *The Atmospheres of Venus and Mars*, New York, Gordon and Breach, 288 pp.

van de Hulst, H. C., 1980: *Multiple Light Scattering, Tables, Formulas and Applications* (Vol. II), Academic, New York, 303-739.

Vonder Haar, T. H. and D. W. Reynolds, 1974: A bispectral method for inferring cloud amount and cloud top temperature using satellite data, *Sixth Conf. on Aerospace and Aeronautical Meteorology,*. Amer. Meteor. Soc., 190 pp.

Waggoner, A. P., R. Weiss, N. Ahlquist, D. Covert, S. Will, R. Charlson, 1981: Optical Characteristics of atmospheric aerosols. *Atmos. Env.*, **15**, 1891-1909.

Wiscombe, W., 1976: On initialization, error and flux conservation in the doubling method. *J. Quant. Spectrosc. Radiat. Transfer*, **16**, 637-658.

Wiscombe, W., 1976: Extension of the doubling method to inhomogenous sources. *J. Quant. Spectrosc. Radiat. Transfer*, **16**, 477-489.

Wiscombe, W. J., 1977: The delta-M method: rapid yet accurate radiative flux calculations for strongly asymmetric phase functions. *J. Atmos. Sci.*, **34**, 1408-1422.

Wiscombe, W. J. and S. G. Warren, 1980: A model for the spectral albedo of snow, I. Pure snow. *J. Atmos. Sci.*,**38**,2712-2733.

Wylie, D. P., W. Menzel, H. Woolf and K. Strabala, 1994: Four Years of Global Cirrus Statistics Using HIRS. *J. Climate*, 7,1972-1986.

Wu, M–L.C., 1985: Remote sensing of cloud–top pressure using reflected solar radiation in the oxygen A–band. *J. Clim. Appl. Meteorol.*, **24**, 539–546.

Yamamoto, G. A., and D. Q. Wark, 1961: Discussion of the letter by R. A. Hanel, "Determination of cloud altitude from a satellite." *J. Geophys. Res.*, **66**, 3596.

Appendix A

Extinction Profile Retrievals from a Limb-Viewing O_2 A-band Radiometer

A.1 Introduction

This paper explores the feasibility of using a limb viewing O_2 A-band radiometer to retrieve upper tropospheric aerosol extinction values. The motivation fro this study is the need for in situ methods for extinction measurements to validate the retrieved extinction profiles from SAGE III, to be launched in 1998. As will be discussed later, the ability to measure at different strengths of gaseous absorption offered by O_2 A-band radiometers provides the ability to provide accurate retrievals of the local values of extinction. The theoretical description of the growth of absorption lines in a scattering media was described more fully in Stephens and Heidinger (1997).

One of the main goals of SAGE III is to produce estimations of upper tropospheric - lower stratospheric aerosol extinction profiles to within 20%. A typical aerosol extinction profile at 0.65 $/mum$ is shown in Fig. A.1. From Fig. A.1 , typical values of the aerosol extinction coefficient range from 10^{-2} to 10^{-4} km^{-1} in the region from, 100 to 400 mb, the region of interest for SAGE III retrievals. The following retrievals and radiative transfer calculations will all be based on the extinction profile shown in Fig. A.1 unless stated otherwise. In addition the optical properties of aerosol will be assumed to be i vertically uniform and well approximated by a single scatter albedo, $\omega_o = 0.95$ and a Henyey-Greenstein phase function with an asymmetry parameter of $g = 0.75$.

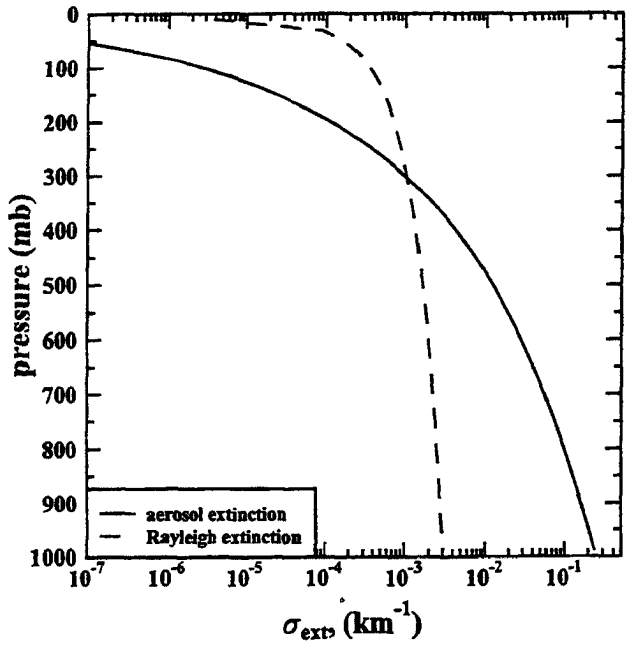

Figure A.1: Sample atmospheric profile of visible aerosol extinction

A.2 The O_2 A-band

The O_2 A-band refers to the spectral region of 0.765-0.785 μm where oxygen is the only significantly absorbing atmospheric gas. The main application of O_2 A-band measurements to remote sensing has been in the estimation of cloud top pressure (Saiedy and Jacobowitz, 1966). The applicability of O_2 A-band measurements to lower atmospheric aerosol retrievals has been explored by (O'Brien, 1996) and Heidinger and Stephens (1997). Throughout this paper, the spectral dependence of the gas absorption in the A-band will be ignored and the total column optical depth due to O_2, $\tau^*_{O_2}$, will used as proxy for frequency. As Fig. 2 shows, the range of $\tau^*_{O_2}$ available to an instrument is a function of the instrument resolution. Currently, the proposed instrument design is for an A-band spectrometer with a resolution of 0.05 cm^{-1}. Stephens and Heidinger(1997) discuss the necessity of a wide range of channel opacities in the retrieval of cloud and aerosol optical properties.

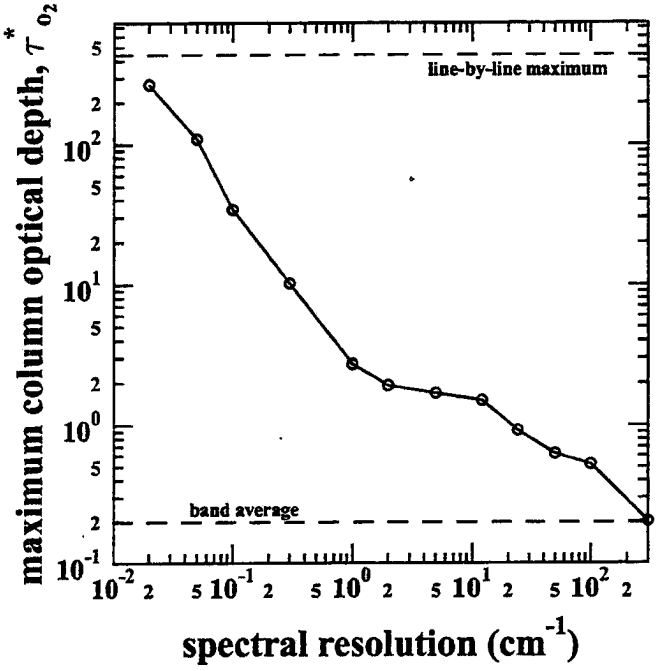

Figure A.2: Variation of the maximum channel O_2 optical depth as a function of instrument resolution

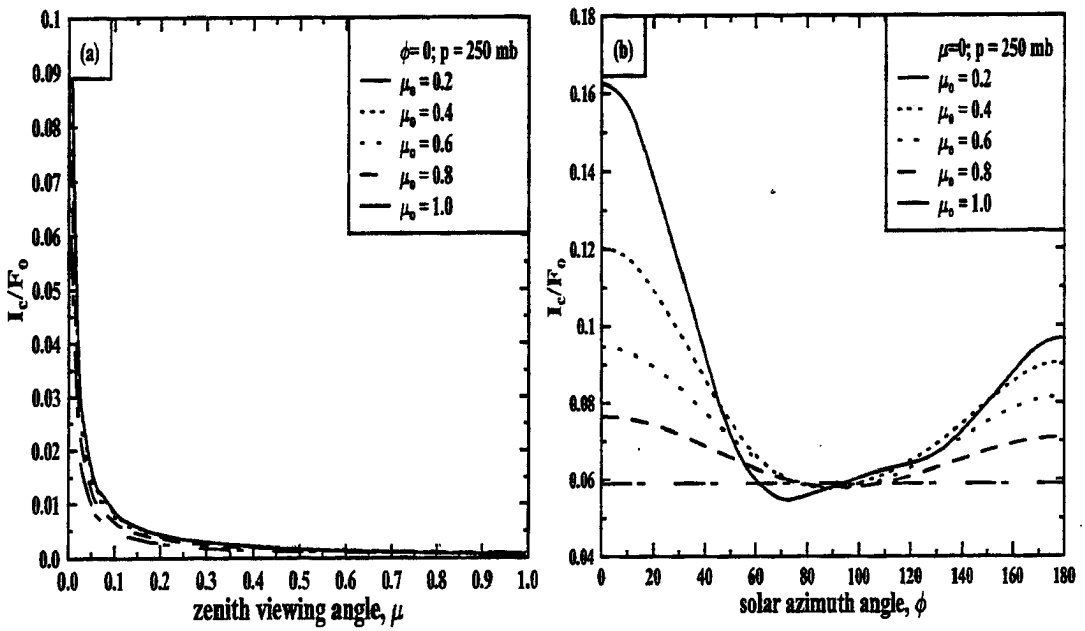

Figure A.3: Variation of the continuum radiance, I_c as a function of viewing angle in the principle plane of the sun(a). Variation of the continuum limb radiance as a function of azimuth angle (b).

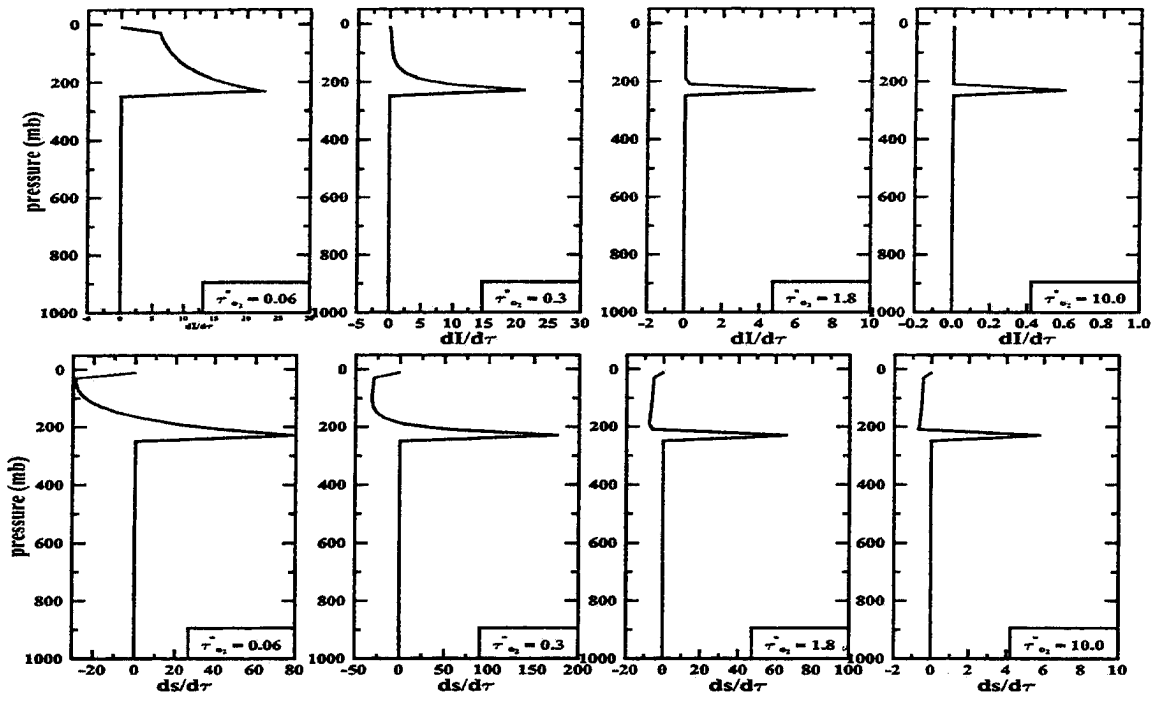

Figure A.4: Sensitivity of the limb radiance (top) and limb radiance ratio (bottom) at 250 mb to changes in the aerosol extinction at each level as function of the total column oxygen optical depth, $\tau^*_{O_2}$

A.3 Information Content in A-band spectra

Unlike the previous remote sensing studies based on nadir viewing A-band measurements, the retrieval methodologies in this paper are based on limb viewing measurements. One reason for viewing the limb, is the rapid increase in the magnitude of the radiance as the viewing angle increases. This limb brightening is illustrated in Fig. A.3a which shows the radiance measurements in the A-band continuum for an instrument at 250 mb as a function of the viewing angle. The sun in this case is directly overhead and ,as Fig. A.3a shows, the limb radiance is roughly an order of magnitude greater than radiances measured at nadir. As will be discussed later, current estimates of signal to noise for proposed instruments make accurate retrievals of upper tropospheric - stratospheric aerosol layers impossible for non-limb-viewing scenarios in the range of extinctions needed for SAGE validation. Fig. A.3b shows the variation in the limb radiance as function of solar relative azimuth angle

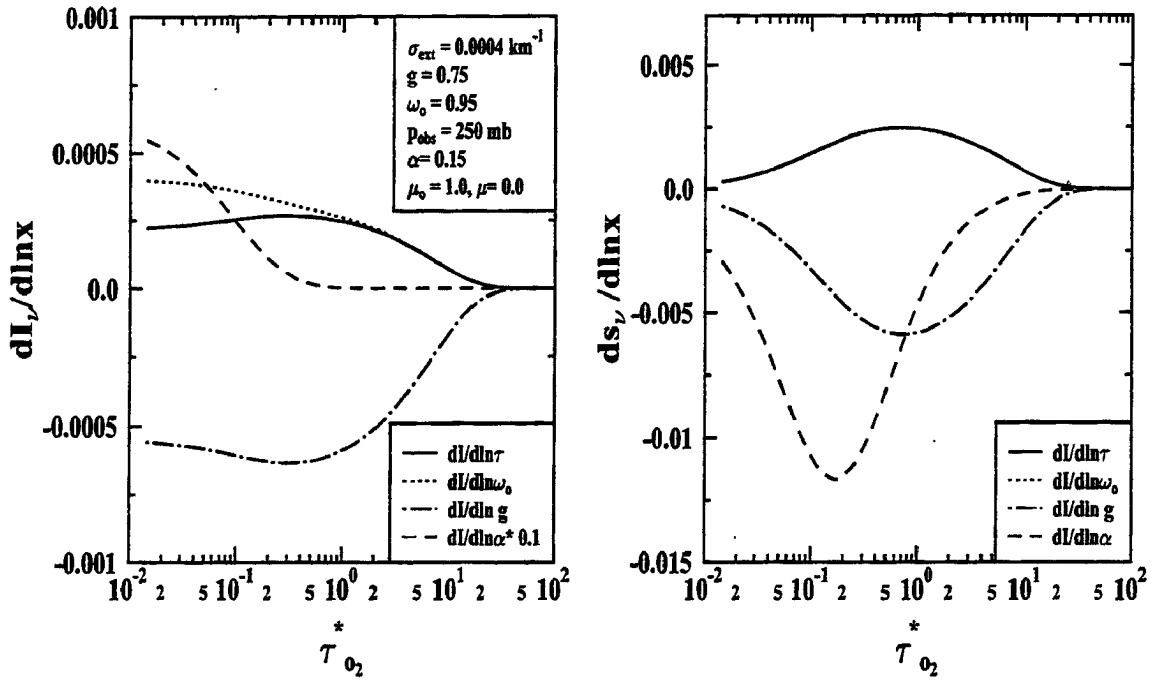

Figure A.5: Sensitivity of limb radiance , I_{nu} to changes in the optical properties as a function of column oxygen optical depth(a). Same as (a) except for s_ν (b).

and solar zenith angle. The actual shape of the these curves is a function of the particle phase functions. Due to the significant peak in the radiances in the principal plane of the sun, all retrievals shown in this work are based on limb-viewing radiances measured in the principal plane of the sun.

Another reason for preferring limb viewing measurements is shown in Fig. A.4. Fig. A.4 shows the the sensitivity of the radiance at 250 mb to changes in the extinction at each level in the atmosphere. Unlike solar photometers which are sensitive to the total extinction above the observation level, limb viewing measurements have the highest sensitivity to changes in the extinction near the level of observation. The sensitivities in Fig. A.4 are shown for 4 different values of $\tau^*_{O_2}$. As Fig. A.4 shows, radiances measured at larger and larger values of $\tau^*_{O_2}$ are less and less sensitive to changes in extinction at other levels. Therefore, multiple A-band measurements at differing values of $\tau^*_{O_2}$ allow for the retrieval of the local values of extinction with minimal errors due to uncertainties in the entire extinction profile. Physically this dependence solely on the local extinction values is due to dominance of single scatter radiance as the amount of gaseous absorption increases.

While the retrieval of the extinction is the main goal of this study, the information content of A-band spectra allows for the retrieval other optical and surface properties. Fig. A.5 shows a sensitivity analysis similar to those shown in Stephens and Heidinger (1997). Fig A.5 shows the sensitivity in each A-band observable, I_ν an s_ν to changes in the vector of retrievable $(\sigma_{ext}, \omega_o, g, \alpha_{sfc})$ where α_{sfc} is the surface albedo. As Fig. A.5 shows, measurements of limb radiances over a range of $\tau^*_{O_2}$ allow for the separation of the effect of each of these quantities. The exception is the inability of limb measurements of s_ν to allow for the separation of the effects of σ_{ext} and ω_o. This is consistent with the nadir viewing aerosol sensitivities shown in Chapter 9 where in the single scatter limit, the effect of τ_c and $\omega_{o,c}$ could not be differentiated.

A.4 Forward Model

The forward model used to perform the retrievals is a multi-stream multi-layer radiative transfer model based on the eigenmatrix method as described in Flatau and Stephens(1988).

The model incorporates a lower reflecting surface and includes the radiative effects of cloud, aerosol and Rayleigh scattering. The δ-M phase function re-normalization was used to produce accurate treatment of highly forward peaked phase functions, as are are typical for cloud and aerosol particles at visible wavelengths. The double-Gaussian quadrature scheme was used for the zenith angle expansion of the radiance field. Using a 32 stream quadrature scheme gave a limb viewing zenith angle of 0.05, which will be assumed to be representative of the true limb radiance. To produce realistic perturbations of the extinction profile, the atmosphere was divided into 50 mb thick layers except at the observation pressure. The level of observation was surrounded by two 1 mb thick layers. All perturbation of extinction were confined to these thin layers surrounding the observation level.

A.5 Retrieval Theory

The retrieval method adapted in this study is based on the work of Rogers(1976). This method seeks to minimize a cost function , Φ

$$\Phi = (\hat{x} - x_a)^T S_a^{-1}(\hat{x} - x_a) + (y - f(\hat{x}))^T S_y^{-1}(y - f(\hat{x})$$

where the first term represents constraints introduced by the appearance of a priori data as characterized by the error covariance matrix S_a. The second term is the contribution by the simulated radiances, $f(\tilde{x})$, relative to the measurements, y . The error covariance matrix, S_y characterizes the errors of the measurements, both actual and simulated. A Newton iteration method is applied to minimize the above cost function, Φ so that the retrieved parameter vector, $\tilde{x}$, is updated at each iteration using the following expression

$$x^{i+1} = x^i + \frac{K^T S_y^{-1}(y - f^i) + S_a^{-1}(x_a - x^i)}{S_x^{-1}} \tag{A.1}$$

where K is the kernel containing the sensitivities of each simulated measurement to each retrieved parameter

$$K = \frac{df(\tilde{x})}{d\tilde{x}}$$

and S_x is the error covariance of the vector x which can be expressed as

$$S_x = (S_a^{-1} + K^T S_y^{-1} K)^{-1} \tag{A.2}$$

Note in the absence of any a priori data($S_a = \infty$), (A.1) simplifies to the standard linear least squares estimate.

The error covariance matrix of measurements, $S_{\tilde{y}}$ is composed of two terms(e.g. Marks and Rodgers, 1993), the first being the error in the measurements,S_y, the second being the error in the forward model,S_f.

$$S_{\tilde{y}} = S_y + S_f$$

The measurement error matrix, S_y, represents the uncertainty in the measurements can be represented in terms of the error due to absolute or shot noise, ϵ_{shot} and the error due calibration errors, ϵ_{cal}.

$$S_y = (\epsilon_{shot}^2 + \epsilon_{cal}^2)$$

In the simulated retrievals in the next section, the shot noise is assumed to vary randomly for each measurement with in a magnitude governed by the signal-to-noise ratio (snr) referenced to some absolute radiance value. Unless stated otherwise, this absolute radiance value used for computing ϵ_y will taken to be the radiance reflected from a 5% Lambertian surface. The calibration error will assumed to constant for all channels as in the case of an A-band spectrometer using a single detector. The error matrix for the forward model is defined as

$$S_f = < (\tilde{y} - \tilde{f})^2 >$$

which represents the squared difference between the measurements and the forward model averaged over all possible measurement scenarios. The various components of S_y are described in Chapter 5. Since aerosols are much more isotropic than cloud particles and much more evenly distributed, no forward model or three dimensional error is assumed.

A.6 Results

To test the ability of a limb-viewing instrument to retrieve aerosol extinction profiles, a sample set of retrievals is performed on an atmosphere with an aerosol extinction profile given by Fig. 1. In addition, the following retrievals have assumed a surface albedo of 0.15 and a solar zenith angle cosine of 0.6. The results are presented for differing signal to noise (snr) values. In this study, the noise of a radiance measurement will be given relative to the reflection from a surface with a 0.05 albedo. The noise is applied randomly to each simulated measurement. The snr value of 100:1 is representative of the noise characteristics of individual spectra. Temporal and spatial averaging is typically necessary to produce higher values of snr however due to the large spatial coverage of limb-viewing instruments, this averaging in no way reduces the quality of the retrieval.

Shown in Fig. A.6a are the estimated errors the extinction retrievals for two value of snr, 100:1 and 1000:1. The retrievals were conducted over the pressure range necessary for SAGE validation. As these results indicate, measurements with a snr above 1000:1 have no difficulty in exceeding the 20% accuracy requirement necessary for SAGE validation. An instrument with a snr of 100:1, meets this criterion only for the lower range of validation where the extinction is above $10^{-3}km^{-1}$. Fig. A.6b shows the reliance of these retrievals on the a priori data. In these retrievals, the a priori estimates of the extinction profiles were assumed to be accurate to within 100%. As discussed earlier, deviation of the A from 1.0 indicate some reliance of the solution on the a priori estimate. It appears from these retrievals the the a priori estimate is affecting the solution only when the extinction falls below $10^{-5}km^{-1}$ which outside the stated range necessary for SAGE validation.

A.7 Conclusions

Accurate estimates of aerosol extinction profiles are possible from currently available A-band radiometers. Using realistic estimates of instrument noise, a limb viewing A-band radiometer was shown to be able to estimate the vertical profile of upper-tropospheric aerosol. The simulated errors were less than 20 % in the range from 100 to 400 mb, the stated goal for SAGE III validation.

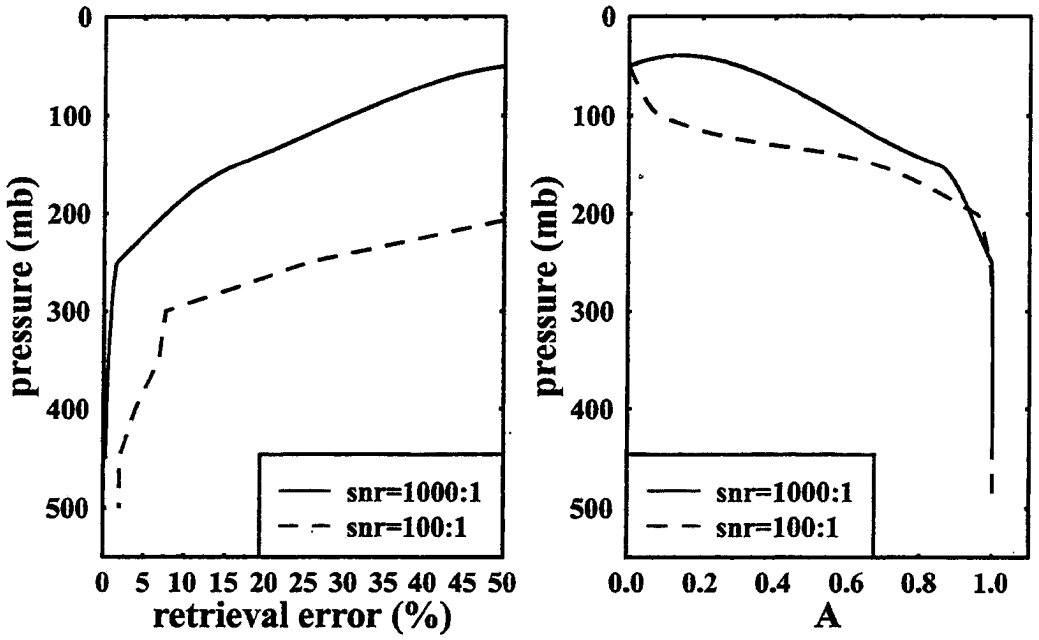

Figure A.6: Effect of noise on the retrieval of extinction from a limb viewing A-band spectrometer.

Appendix B

A Three Dimensional Backward Monte Carlo Model

In this section, a three-dimensional radiative transfer model is developed. The type of solution used is the backward Monte Carlo technique(O'Brien, 1994). Monte Carlo solutions to radiative transfer have been used widely in the study radiative transfer in heterogeneous media dating back to the work of McKee and Cox(1974). While computationally intensive, Monte Carlo techniques allows for the simulation of complex cloud structures and directly computes the photon path length distribution, which are fundamental to understanding of cloud heterogeneity on radiative transfer and retrieval methods.

In its most general form, where the only assumptions include local thermodynamic equilibrium and coherent scattering, the radiative transfer equation can be written as

$$\frac{dI(\vec{s},\xi)}{\xi \cdot d\vec{s}} = -\sigma_{ext} I(\vec{s},\xi) + \sigma_{ext}\left(\omega_o \Im(s) + (1-\omega_o)\mathcal{B}(s)\right) \tag{B.1}$$

where I is the radiance at position s along direction ξ, σ_{ext} is the total extinction coefficient and ω_o is the single scatter albedo. In the above equation, the first term on the right hand side accounts for the attenuation of radiation due to absorption and scattering out of the line of sight. The second term is the source due to thermal emission and is a function only of the local temperature. The third term is the source due to the scattering of radiation and can be expressed formally as

$$\Im(s,\xi) = \int_\Omega p(\xi,\xi') I(s,\xi') d\Omega \tag{B.2}$$

where $p(\xi, \xi')$ is the scattering phase function which represents the probability of $I(\xi')$ being scattered into the direction ξ. As is traditionally assumed in atmospheric radiative transfer, the phase function will be assumed to vary only with the scattering angle ψ defined by $cos\psi' = \xi \cdot \xi'$. The integral form of the radiative transfer equation, (B.2), can be derived by integrating (B.1) from the media boundary, defined by position $\vec{u}$ along a line defined by ξ to the observation position, $\vec{s}$.

$$I(s,\xi) = I(u,\xi)e^{-\tau(s,u)} + \int_u^s \left((1-\omega_o)\mathcal{B}(s') + \omega_o \Im(s')\right) e^{-\tau(s,s')} \sigma_{ext} \xi \cdot d\vec{s}' \qquad \text{(B.3)}$$

For Monte Carlo solutions, it is more convenient to replace the above integral over s, the geometrical distance, to an integral over transmission, $\mathcal{T}$. Assuming that transmission varies exponentially with optical depth , τ, an incremental change in transmission can be express as

$$d\mathcal{T} = -e^{-\tau} d\tau = \mathcal{T} \sigma_{ext} \xi \cdot d\vec{s}$$

$$I(s,\xi) = I(u,\xi)\mathcal{T}(s,u) + \int_{\mathcal{T}(s,u)}^1 \left((1-\omega_o)\mathcal{B}(s') + \omega_o \Im(s')\right) d\mathcal{T}(s') \qquad \text{(B.4)}$$

B.1 The Monte Carlo Solution to Radiative Transfer Equation

The Monte Carlo solution to the radiative transfer equation is essentially a stochastic implementation of the traditional successive orders of scatter solution which is described in van de Hulst(1977). Using this approach the radiance, I can be decomposed into component from each order of scatter.

$$I = \sum_{k=0}^{\infty} I_k$$

For example, the direct or zero order scatter radiance can be written as

$$I_0(\vec{s},\xi) = I(\vec{u},\xi)\mathcal{T}(\vec{s},\vec{u}) + \int_{\mathcal{T}(\vec{s},\vec{u})}^1 (1-\omega_o)\mathcal{B}(\vec{s}')d\mathcal{T}(\vec{s}') \qquad \text{(B.5)}$$

where the first term represents the transmission of radiance at the boundary and the second term represents the source due due to thermal emission which shall be subsequently

referred to as I_{ems}. In a similar fashion, the first order radiance can be expressed as

$$I_1(s,\xi) = \int_{\mathcal{T}(s,u)}^{1} \omega_o \left(\mathcal{T}(\vec{s},\vec{u}_\odot p(\xi,\xi_\odot) F_\odot + \int_\Omega p(\psi') I_0(s',\xi') d\Omega \right) d\mathcal{T}(s') \tag{B.6}$$

where the first term is the source of radiance due to the single scattering of the solar source defined by its intensity, $F_\odot$ and direction, $\xi_\odot$. Note in the above equation, only zero order radiance appears on the right hand and in general for the k^{th} order radiance, only term involving radiation scattering $k-1$ and fewer times will be on the right hand side. For plane parallel radiative transfer, techniques are available to to compute each order of scatter directly from the previously computed lower orders of scatter allowing the total radiance to be computed. In the presence of heterogeneous media, the Monte Carlo method solves these equations by a stochastic integration. As is common to all Monte Carlo techniques, this is accomplished by allowing randomly sampling over the entire dimensional space and averaging the results to obtain a final solution.

As done in O'Brien(1994), it is convenient to transform the angular integrals to integrals which vary between 0 and 1. The angular integral appearing in the scattering source term which can be rewritten as

$$\Im(s,\xi) = \int_0^{2\pi} d\phi' \int_0^{pi} p(\xi,\xi') I(s,\xi') sin\theta' d\theta' \tag{B.7}$$

where θ' and ϕ^prime are the zenith and azimuth angles measured relative to ξ. Introduction of the two following variables,

$$\zeta' = \frac{\phi'}{2\pi}$$

and

$$\eta' = \frac{1}{2} sin\psi' p(\psi^prime)$$

allows (B.7) to be written as

$$\Im(s,\xi) = \int_0^1 d\zeta' \int_0^1 I(s,\xi') d\eta'$$

The inclusion of the phase function in the above angular transformation automatically ensures the correct accounting of the angular pattern of the particle scattering. Note that

this transformation is not needed for the integral over transmission since $\mathcal{T}$ is bounded between 0 and 1. With this angular transformation, I_1 can be rewritten as

$$I_1(s,\xi) = \int_0^1 \int_0^1 \int_0^1 \omega_o \int_\Omega p(\psi') I_0(s',\xi') d\eta' d\zeta' d\mathcal{T}(s') \tag{B.8}$$

which is evaluated as follows

$$I_1(s,\xi) = \frac{1}{N} \sum_{n=1,N} \omega_o I_0(s'_n, \xi'_n) \tag{B.9}$$

where s'_n is the scattering position of the n^{th} estimate chosen randomly depending on the value of $\mathcal{T}'$ and ξ' is the direction of the incoming radiation determined by the values of η' an ζ'.

Note that in (B.8), if $\mathcal{T}'$ is chosen so that its value is below the transmission to boundary of the media, $\mathcal{T}(s,u)$ the photon has exited the media. In thin media most photons will exit after only a few scattering and accurate estimates of higher order scattering contribution require many photon trajectories. This problem can be avoided by forcing a scattering event to occur before the photon exits the media. This can be accomplished by the introduction of the new variable, ϵ defined as

$$\epsilon = \frac{\mathcal{T}(s,s') - \mathcal{T}(s,u)}{1 - \mathcal{T}(s,u)}$$

Replacing the integral over $\mathcal{T}$ to an integral over ϵ allows I_1 to be written as

$$I_1(s,\xi) = \frac{1}{N} \sum_{n=1,N} \omega_o (1 - \mathcal{T}'_n) I_0(s'_n, \xi'_n)$$

In general, an expression for the kth order radiance can now be written as

$$I_k(s,\xi) = \frac{1}{N} \sum_{k=1,N} I_{k-1}(s'_n, \xi'_n) \tag{B.10}$$

Recursively applying (B.10) allows the k^{th} order radiance to be expressed as

$$I_k(s,\xi) = \mathcal{R}_k \left(\mathcal{T}(s_k,u_k) I(s_k,u_k) + I_{ems}(s_k,u_k) + \mathcal{T}(s_k,u_\odot) \frac{p(\xi,\xi_\odot}{4\pi} F_\odot \right) \tag{B.11}$$

where $\mathcal{R}_k$ is the weight of the k^{th} photon trajectory as is defined as

$$\mathcal{R}_k = \prod_1^k \omega_o(s_k) \prod_0^{k-1} (1 - \mathcal{T}_k) \tag{B.12}$$

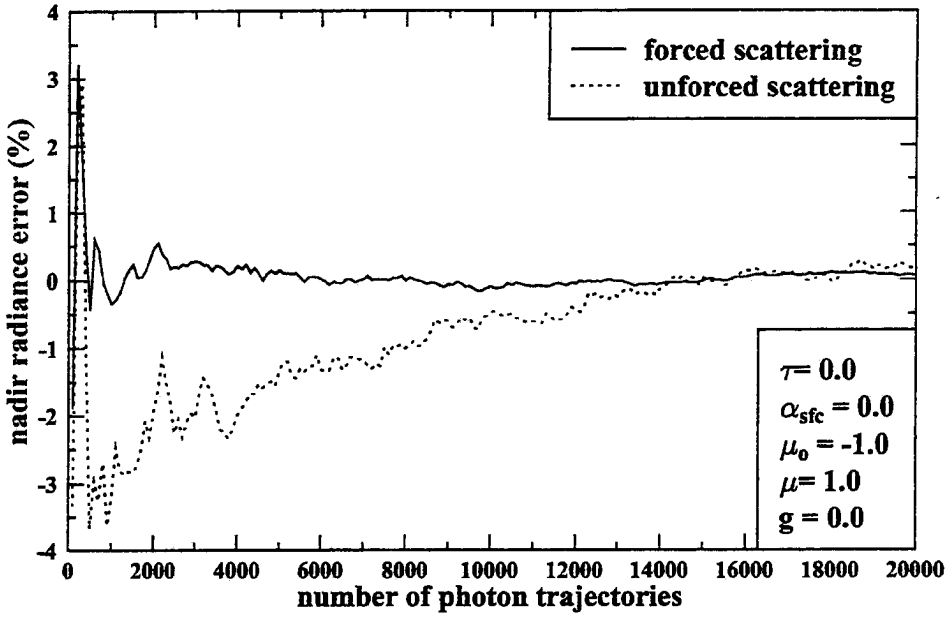

Figure B.1: Comparison of convergence of nadir radiance using forced and unforced scattering events. The errors are relative to van de Hulst (1977)

As a validation of this technique, Fig. B.1 shows the convergence of the total radiance for a conservatively isotropic scatter layer with an optical depth of unity illuminated by a direct beam with normal incidence. The total radiance here is comprised of the first 30 orders of scatter. In Fig. B.1, the convergence for forced and unforced collisions is shown and as expected the forced collision solution convergences to the correct answer more quickly than the unforced. In addition, even for this simple case, 10,000 photon trajectory simulations are needed to reduce the error to under 1%.

B.2 Estimation of total radiance from finite orders of scatter

In the previous section, the method for estimating the contribution to the total radiance, I, from each order of scatter was developed. As the scattering medium becomes optically thick, the number of order of scatter needed to estimate I becomes prohibitively large. In

this section, a method is developed which allows I to estimated from a finite number of scattering orders.

After k orders of scattering have been simulated, the error in the total radiance, E_k, can be expressed as:

$$E_k = I - S_k \tag{B.13}$$

where I is the true radiance integrated over all orders of scatter and S_k is the estimate of I after k orders of scatter.

$$S_k = \sum_{0}^{k} I_k \tag{B.14}$$

For sufficiently large values of k, Irvine(1964) shows:

$$\lim_{k\to\infty} \frac{I_k}{I_{k-1}} = \eta \tag{B.15}$$

which allows us to express E_k as:

$$E_k = I_k \sum_{m=1}^{\infty} \eta^m \approx CI_k \tag{B.16}$$

Let us define our accelerated estimate of I as Q where:

$$Q_k = S_k + CI_k \tag{B.17}$$

If one assumes that for large k

$$Q_k \approx Q_{k-1} \tag{B.18}$$

then we can eliminate C above and write for the k_{th} estimate of the accelerated radiance,

$$Q_k = S_k + R_k \frac{S_k - S_{k-1}}{R_{k-1} - Rk} \tag{B.19}$$

B.3 Estimation of the mean path-length from finite orders of scatter

In addition, the radiance or flux, another radiative quantity desired from a Monte Carlo model is the mean path-length, $< \lambda >$.

$$< \lambda >= \int_o^{\infty} \lambda p(\lambda) d\lambda \tag{B.20}$$

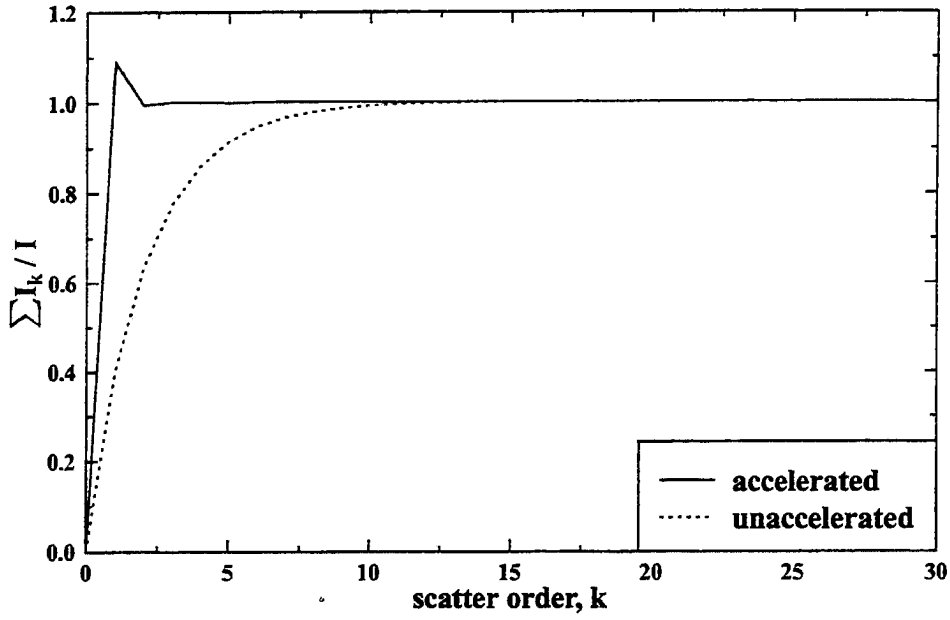

Figure B.2: Comparison of convergence with orders of scatter of nadir radiance using acceleration method given by (B.9). Optical properties are identical to those in Fig. B.1

$$< \lambda >= \sum_{o}^{\infty} \frac{I_k \lambda_k}{Q} \tag{B.21}$$

For a summation over the first k orders of scatter, the error in the estimate of the mean path-length is given by

$$E_{\lambda,k} = < \lambda > - \sum_{o}^{\infty} \frac{I_k \lambda_k}{Q} \tag{B.22}$$

It is desired to make an accurate estimate of $< \lambda >$ after only k scatter orders has been simulated. Let the accelerated estimate of $< \lambda >$ after k scatters be denoted L_k. As done in the acceleration of the radiance, after a sufficient number of scatters one would expect

$$L_k \approx L_k - 1 \tag{B.23}$$

To be able to compute L_k, the approximation is made the change in the mean path-length between two orders of scatter is proportional to the weight of the scattering order.

$$< \lambda >_k - < \lambda >_{k-1} = CR_k \tag{B.24}$$

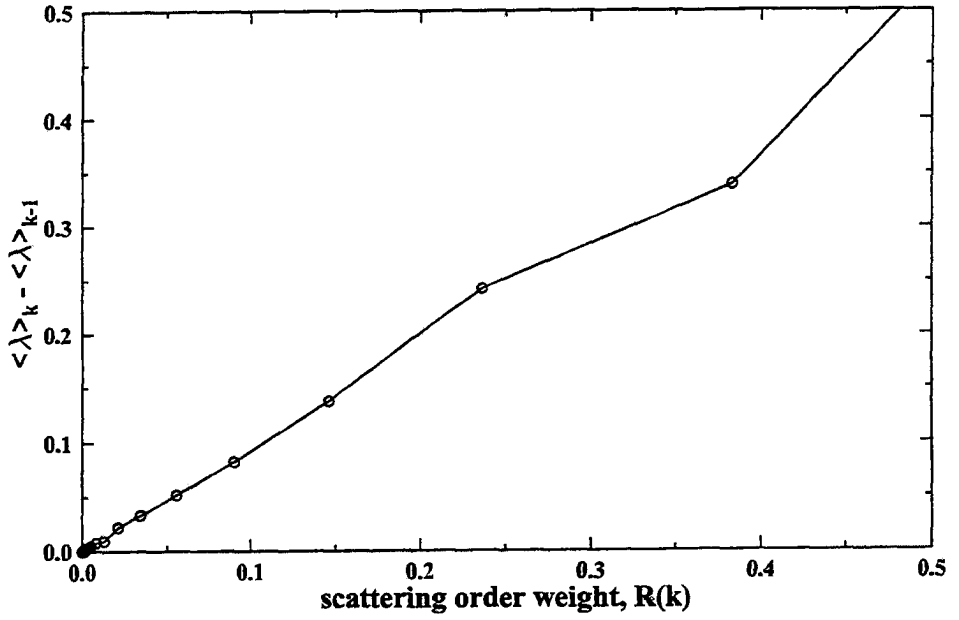

Figure B.3: Test of (B.12) which states the difference in mean path-length between two orders of scatter is proportional to scatter weight

With these two approximations, the following acceleration technique for mean path-lengths is produced.

$$L_k = < \lambda >_k + \frac{I_k \lambda_k R_k}{Q(R_{k-1} - R_k)} \tag{B.25}$$

B.4 Conclusions

This backwards Monte Carlo model will be used to simulate the effect of cloud spatial variability on A-band retrievals shown in Chapter 12. In Appendix C, photon path-length distributions, a product of the Monte Carlo model, are used to generate the radiances at any spectral location in the A-band based on only one running of the Monte Carlo model. Even though Monte Carlo models are known for their slow convergence and computational expense, the ability to simulate high spectral resolution radiances, as needed for A-band retrievals, makes the Monte Carlo approach the most feasible.

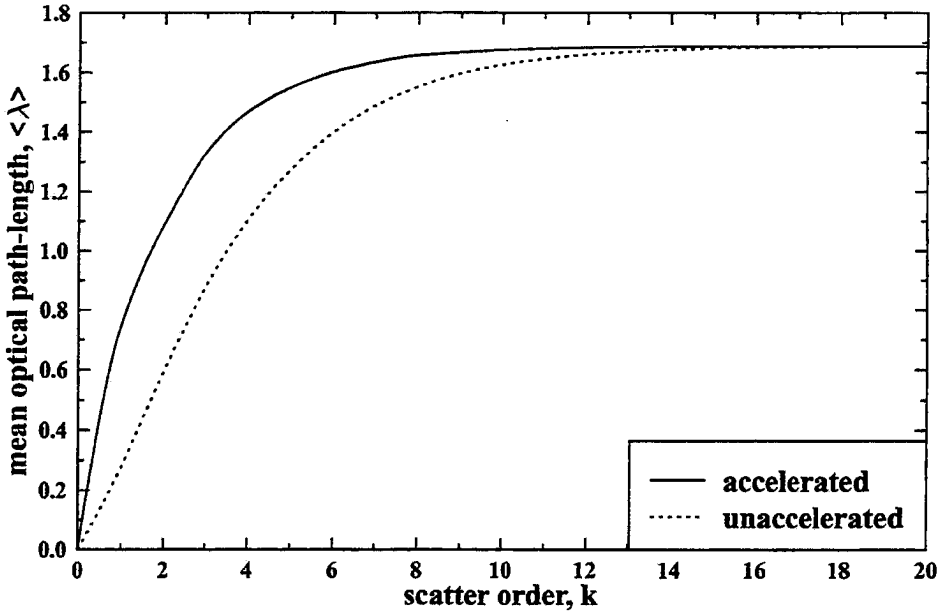

Figure B.4: Comparison of convergence with orders of scatter of mean optical path-length using acceleration method given by (B.13). Optical properties are identical to those in Fig. B.1

Appendix C

Use of Photon Path-lengths to perform High Spectral Resolution Radiative Transfer in Three Dimensional Media

C.1 Introduction

This appendix explores the potential application of the equivalence theorem developed by Irvine (1964) to the computation of gaseous absorption in three dimensional radiative transfer models. The typical approach to the computation of gaseous absorption in radiative transfer models is to run the radiative transfer model separately for each value of gaseous absorption and combine the results to generate to spectral quantity of interest. Even though plane parallel radiative transfer schemes are efficient and computationally quick enough to run in climate models, the ability to simulate line-by-line radiances using this method is a very computationally expensive process. For example, the simulate one lbl spectra of the A-band of oxygen which spans 300 cm^{-1} requires approximately 300,000 solutions of the radiative transfer equation. This high number is necessitated due to half-widths of the absorption lines in the A-band being on the order of 0.005 cm^{-1}. In the presence of any three dimensional variation, where the efficient plane parallel schemes can not be used, the computation of lbl spectra is a challenge.

While the equivalence theorem is used exclusively for the simulation of high resolution A-band spectra, the theorem can also be used to generate broad-band radiances and fluxes.

The most popular method for computing broad-band fluxes currently is the correlated-k method described in Goody *et al* (1989) and Lacis and Oinas(1990). The correlated-k method involves multiple solution of the radiative transfer equation at varying strengths of the absorbing gas. To generate broad-band fluxes, the correlated-k approach is typically applied separately to several bands where the optical properties of the cloud or aerosol particles can be considered uniform. For example, the correlated-k parameterization of gaseous absorption for channel 1 on NOAA's Advanced Very High Resolution Radiometer (AVHRR) (Kratz, 1994) requires 29 separate radiative transfer computations to commutate the channel values of any radiative quantities. Even though the speed of three dimensional radiative transfer models is increasing constantly, the accurate estimate of broad-band radiative quantities is still a difficult process.

Use of the equivalence theorem greatly speeds the computation of the variation of radiances and fluxes with varying gaseous absorption since it reduces the number of times the radiative transfer equation needs to be solved. As put forth in Irvine(1964), the equivalence theorem states that knowledge of the photon path length distribution in the conservative scattering case allows for the direct computation of the flux or radiance at a frequency with any amount of gaseous absorption.

$$\frac{F(r \neq 0)}{F(r = 0)} = \int_0^\infty \exp(-r\lambda) p(\lambda) d\lambda \tag{C.1}$$

where λ is the optical photon path length and r is the ratio of gaseous to scattering extinction. The optical path length, λ, differs from the geometric path length, l, only the factor the extinction coefficient, σ_e expressed as inverse length. Physically, the equivalence theorem is based on the principle that gaseous constituents do not effect the scattering behavior of the particles. The effect of gas in a scattering medium is to add attenuation as the photon traverses between the scatters. The equivalence was developed in the field of astrophysics to allow for the measurement of $p(\lambda)$ by observations of absorption lines through the inverse Laplace transform of (C.1). As will be shown, later the inclusion of particle absorption in the above formulation is straightforward.

Since the equivalence theorem allows for gaseous and particle absorption, the radiative transfer equation only needs to solved once to generate the conservative scattering flux,

$F(r=0)$ and the optical path length distribution, $p(\lambda)$. Once these quantities are known, the spectral variation of gaseous and particle absorption can be accounted for without additional solutions of the radiative transfer equation. The only limitation on the spectral range of the equivalence theorem is that the $p(\lambda)$ must be remain constant which implies that the single scattering phase function and single scatter albedo do not change appreciably over the spectral range of interest.

This appendix will first demonstrate the utility of the equivalence theorem to computation of radiative quantities from a single layer. The section will numerically validate the use of the equivalence theorem by by comparing its results with results using an explicit treatment of gaseous absorption. In addition, the equivalence theorem is extended to include variable particle absorption, which greatly extends its spectral range of validity. The next section will demonstrate the utility of using the equivalence theorem to compute spectral radiances in spatially varying media, as was done to generate the results of Chapter 11. The last section will discuss the extension of the equivalence theorem to the case of vertically varying gaseous absorption.

C.2 Photon Path-length distributions

Since the photon path-length distribution governs gaseous absorption through (C.1), it is beneficial to review the variation of path-length distributions with differing optical properties of the medium. Fig C.1 shows three photon path-length distributions for three conservatively scattering plane parallel clouds with optical depths of 1,4 and 16. The cloud with an optical of 1 is isotropically scattering and has a mean path-length of 1.698 which is same as the results obtained theoretically in Table 2 of Irvine(1964). The thick clouds have single Henyey-Greenstein phase function with $g = 0.85$. The reflection at the lower surface is ignored and the solar zenith angle cosine is 0.8. Both the optical and geometrical path-length distributions are shown in Fig C.1 for values of the continuum optical depth τ_c = 1,4 and 16.

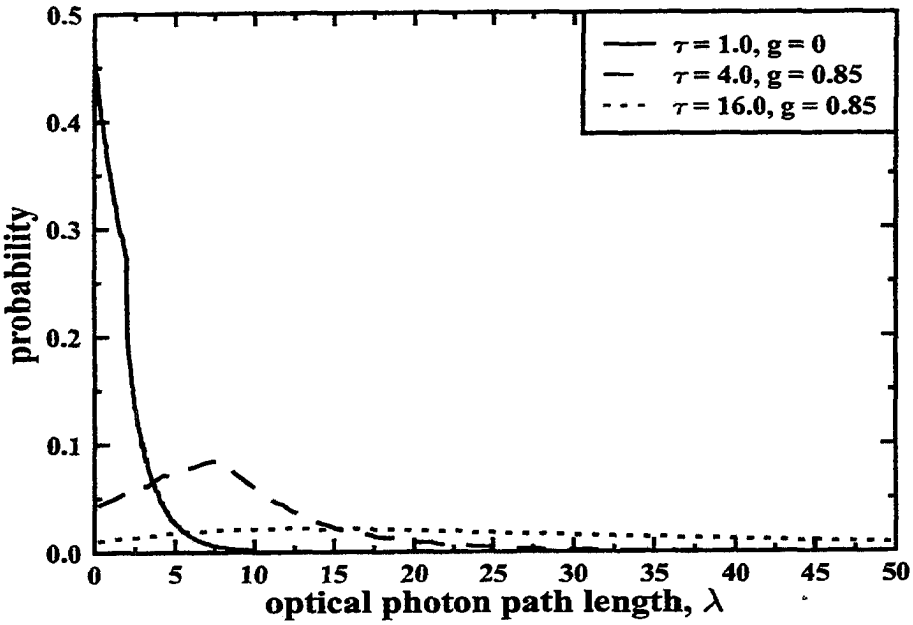

Figure C.1: Photon path length distributions from a Monte Carlo Model

C.2.1 The mean photon path-length

In addition to the actual photon path-length distribution, $p(\lambda)$, another quantity of interest is the mean photon path-length, $< \lambda >$. In terms of $p(\lambda)$, the mean photon path length is defined as

$$< \lambda >= \int_0^\infty \lambda p(\lambda) d\lambda \tag{C.2}$$

Using this definition and the equivalence theorem given by (C.1) gives an expression for the mean path-length as:

$$< \lambda >= \frac{d \ln F}{d\tau} \tag{C.3}$$

The above expression is valid for measurements taken at differing spectral location in an absorption line. Since the continuum optical depth, τ_c remains constant inside and outside the absorption line ($\omega_{o,\nu}\tau_\nu = \omega_{o,c}\tau_c$), we can write

$$< \lambda >= \frac{d \ln F}{dln\omega_o} - \frac{d \ln F}{dln\tau} \tag{C.4}$$

As done described in Chapter 6, the nadir radiance at the top of the atmosphere can be described as

$$I_{ss} = \frac{\omega_o F_o}{m\mu} \frac{P}{4\pi} (1 - e^{-m\tau})$$

where τ is optical depth of the scattering layer, ω_o is the single scatter albedo of the scattering particles and P is the value of the phase function in the single scatter direction defined by the solar geometry and F_o is the strength of the solar beam. The quantity m is the air mass factor which is defined as $\frac{1}{\mu} + \frac{1}{\mu_\odot}$ where mu is the viewing angle cosine, here taken to be 1.0, and μ_o is the solar zenith angle cosine also assumed 1.0. Using (A.3), the mean path-length predict by single scatter theory is given by

$$< \lambda >_{ss} = 1 - \frac{m\tau e^{-m\tau}}{1 - e^{-m\tau}}. \tag{C.5}$$

As τ goes to zero, the single scattering dominates so that the value of $< \lambda >$ in the optically thin limit becomes

$$< \lambda >_{\tau \to 0} = \frac{m}{2}$$

As shown by van de Hulst, in the semi-infinite limit the mean path-length for nadir radiance with overhead sun is given by

$$< \lambda > = \mu + \mu_o \tag{C.6}$$

To test these asymptotic behaviors, Fig C.3 was made. Fig C.3 shows the results of numeric computation of $< \lambda >$ for both radiance and flux for nadir viewing and an overhead sun. Results for isotropic and an anisotropic phase function(g=0.85) were shown. Looking at the radiance, the effect of the phase function has no effect on the asymptotic behavior of $< \lambda >$. The forward scattering phase function does exceed the asymptotic over a significant range in optical depth however. The values of $< \lambda >$ for the flux also approach the same asymptotic value regardless of the phase function. This thick limit value is the same as the diffusivity factor of Elasser(1942). This is an interesting validation of pervasive assumption in atmospheric radiative transfer. It appears that in the thin limit, the phase function does effect the values of $< \lambda >$ for flux.

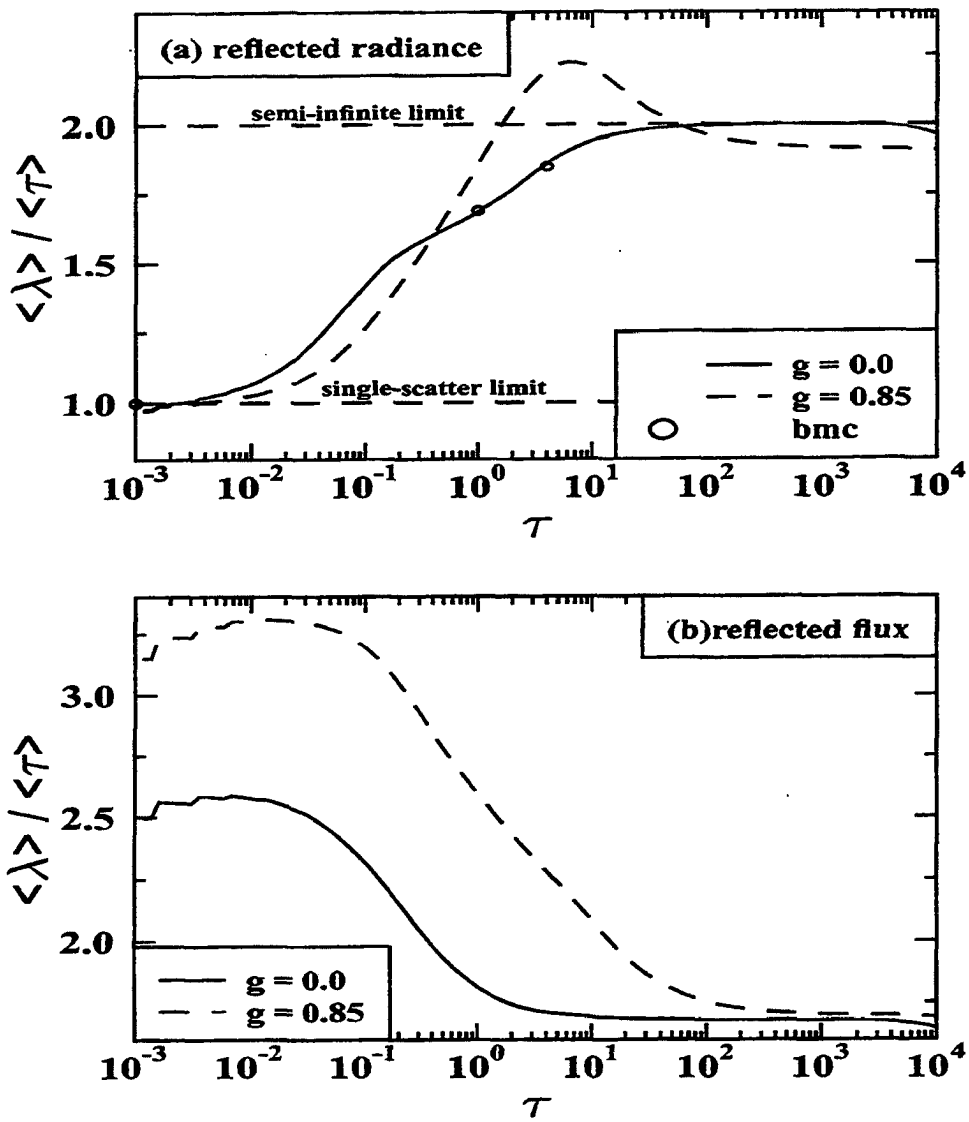

Figure C.2: Variation of the ratio of mean path-length $< \lambda >$ to optical depth τ with τ for reflected nadir radiance and flux for different asymmetry parameters, g

C.3 The Single layer

In this section, we apply the equivalence theorem to the computation of fluxes in a single scattering layer. In the first part of this section, the equivalence will applied to compute the spectral variation of radiances or fluxes due to spectrally varying gaseous absorption. The section ends with an approximate equivalence theorem for particle absorption is developed.

C.3.1 Gaseous Absorption

In order to confirm the ability of the equivalence theorem to account for gaseous absorption, a backward Monte Carlo model was used to compute explicitly the optical photon path-length distributions. The isotropic scattering simulation with $\tau_c = 0$ is identical to the optical photon path-length distribution for identical optical properties published by Irvine(1964). In the following simulations, the scattering layer was assumed to be suspended in a transparent atmosphere above a reflecting surface with Lambertian properties. In addition, the vertical distribution of gas was assumed uniform. Results for four different single layer comparisons are shown in Fig. C.3. The continuum optical depth, τ_c, was varied from 1, 4 and 16 in the plane parallel simulations. The photon path-length distribution for these simulations are shown in Fig C.1. The direct computations shown in Fig. C.3 represent traditional radiative transfer computations where both the effects of scattering and gaseous absorption were included. The equivalence theorem results where computed using (C.1) with the $p(\lambda)$ and $F(r = 0)$ being computed with the Monte Carlo model. As Fig. C.3 shows, the equivalence theorem accurately predicts the spectral variation of flux due to gaseous absorption.

C.3.2 Particle Absorption

The equivalence theorem assumes that the particle scattering properties are uniform. As the Mie computations in Chapter 3 showed, this approximately holds in the visible region for the asymmetry parameter but there are significant spectral variations in the single albedo of cloud particles between 0.2 and 2.0 microns. Absorption by particles is fundamentally different than absorption by gas. The former depends only on the photon

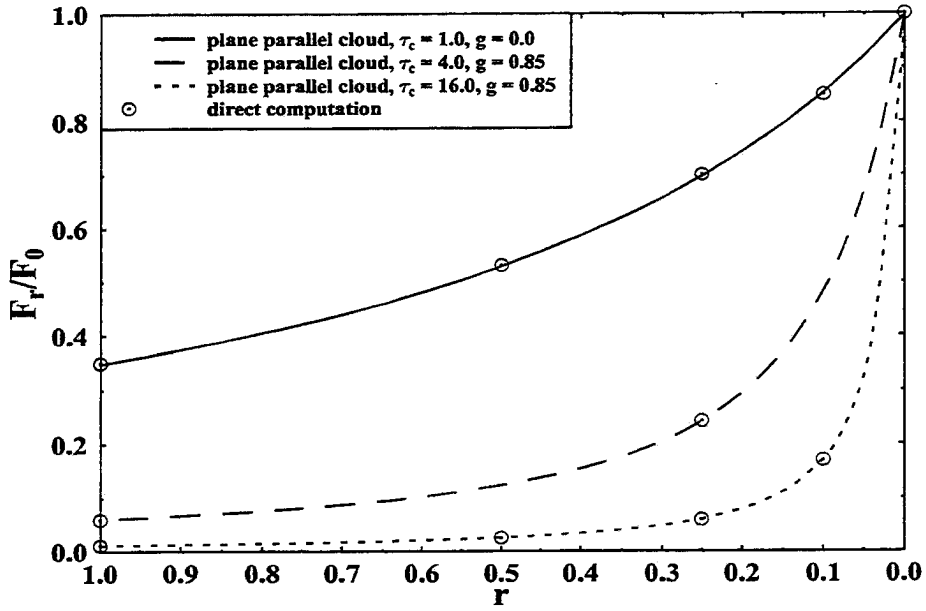

Figure C.3: Variation in albedo for plane parallel clouds with gaseous absorption. The lines represent the results from (C.1) while the points are direct radiative transfer simulations.

path length but the latter depends on the number particle/radiation interactions. As described by van de Hulst (1980), the flux or radiance from a non-conservative scattering layer with no gaseous absorption is identical to the flux or radiance from conservatively scattering layer with gaseous absorption if the following conditions are met:

$$\begin{aligned} \tau_c^{'} &= \omega_{o,c}\tau_c \\ \tau_g^{'} &= (1-\omega_{o,c})\tau_c \\ \omega_{o,p}^{'} &= 1.0 \end{aligned}$$

Therefore, to simulate particle absorption with the equivalence theorem, we attempt to use the above equivalence between gaseous and particle absorption to reformulate the (C.1), which accounts only for gaseous absorption, to account for particle absorption. If the absorbing fraction of the particle optical depth is considered to be a gas, the effect of particle absorption can be included in the (C.1) as follows.

$$F(\tau_c, \omega_{o,c} \neq 1) = F(\tau_c^{'}, \omega_{o,c}^{'} = 1) \int_0^{\infty} \exp -(r^{'}\lambda^{'}) p(\lambda^{'}) d\lambda^{'}$$

where

$$\begin{aligned} \lambda^{'} &= \omega_{o,c}\lambda \\ r^{'} &= \frac{1-\omega_{o,c}}{\omega_{o,c}} \end{aligned}$$

While the above formulation is accurate, it requires the computation of $p(\lambda^{'})$ which is the continuum photon path length for a layer of optical thickness $\tau_c^{'}$. To account for a spectrally varying $\omega_{o,c}$ therefore requires the computation of many distributions of $p(\lambda^{'})$. Thus computational gains of employing the equivalence theorem are lost. It would be advantageous then to include particle absorption in a equivalence theorem based on $p(\lambda)$, the continuum photon path length with the true continuum optical depth which is needed to account for gaseous absorption.

In an attempt to include particle absorption, we can make the following assumption.

$$F_c(\tau_c)p(\lambda) \approx F_c(\tau_c^{'})p(\lambda^{'}) \qquad \text{(C.7)}$$

To justify this assumption, an example of its application is shown in Fig. C.4. In this example, the cloud is assumed to have an optical depth, τ_c of 4 and a single scatter albedo, $\omega_{o,c}$, of 0.9. To apply to equivalence theorem of (C.1), the photon path-length distribution for a conservatively scattering cloud with on optical depth of $\omega_{o,c}\tau_c$ is needed. As described before, it is computationally efficient to compute the path-length distribution for conservatively scattering layer with optical depth of τ_c and use this in all equivalence theorem calculations. Fig. C.4 shows the path-length distribution for each of the above cases. Note that the difference in the continuum optical depths causes a significant change in the photon path-length distributions. In the right panel of Fig C.4, the approximation of (C.5) is applied to the path-length distribution for the $\tau = \tau_c$ case and plotted with the same axes as the $\tau = \omega_{o,c}\tau_c$ simulation. The agreement between these two path-length distributions shows that the pdf for the case of no particle absorption can be used to account absorption thus eliminating the need to recompute the photon path-lengths as a function of $\omega_{o,c}$.

With this assumption, an equivalence theorem for particle absorption based on $p(\lambda)$ can be written as:

$$F_{(\tau_c,\omega_{o,c}\neq 1)} = F_c(\tau_c)\omega_{o,c}\int_0^\infty \exp\left(-(1-\omega_{o,c})\lambda\right)p(\lambda)d\lambda \tag{C.8}$$

In Fig 5, this equivalence theorem for particle absorption is compared against direct radiative transfer computations. As these results illustrate, the equivalence theorem seems to be to account for particle absorption over a wide range of both τ_c and $\omega_{o,c}$. Therefore, particle and gaseous absorption can be included in an equivalence theorem of the form

$$F_\nu = F_c\omega_{o,c}^\nu\int_0^\infty \exp\left((1-\omega_{o,c})+\tau_\nu\right)\lambda p(\lambda)d\lambda \tag{C.9}$$

where τ_ν defines the amount gaseous absorption and a frequency, ν and $p(\lambda)$ is the photon path-length distribution computed without any absorption, either particle or gaseous.

C.4 The Use of the Equivalence Theorem in Spatially Inhomogeneous Media

The equivalence makes no assumption about the spatial structure of the cloud layer. Up to this point, the photon path length distribution has been expressed in terms of the optical

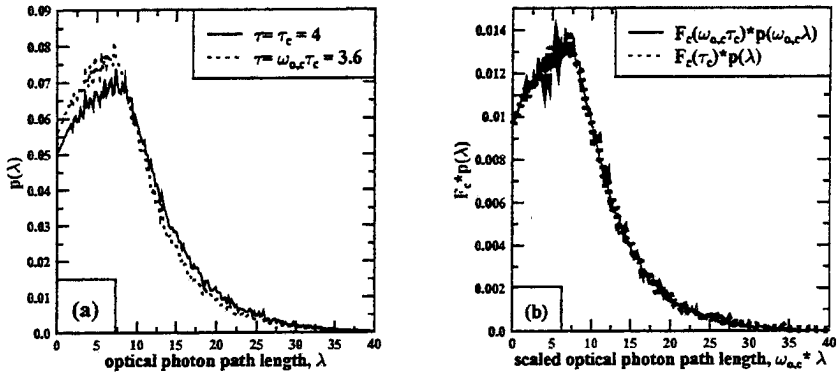

Figure C.4: (a) Comparison of conservatively scattering up-welling flux photon pdf's for true and scaled continuum optical depths. (b) Comparison of pdf's after applying scaling of (C.5).

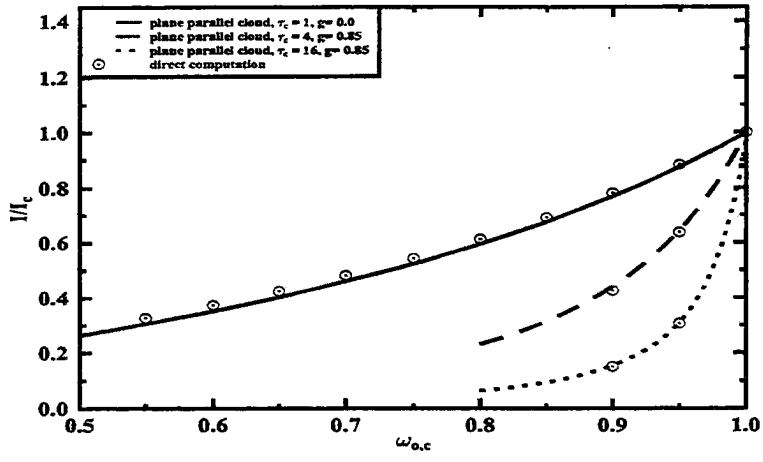

Figure C.5: Comparison of effect particle absorption on the albedo of plane parallel cloud computed from the equivalence theorem of (C.7) and direct numerical simulation.

path-length. In the presence of spatial heterogeneity however, the geometrical and optical path-lengths diverge from each other and are no longer related by the mean extinction coefficient. It is also the geometric path not the optical path which the amount of gaseous absorption along a path. Based on the geometrical path-length, the equivalence theorem can be written as

$$I_\nu = I_c \int_0^\infty p(l) e^{-\sigma_\nu l} dl \tag{C.10}$$

where l is the geometrical path expressed as a geometrical length and σ_ν is the spectral gaseous volume absorption coefficient. It is important to note the above expression, still assumes spatially uniformity in the gaseous absorption. To explore the utility of the equivalence theorem in spatially variable clouds, Fig A.6 was made. The upper left panel shows the horizontal variation for an 80 by 80 array of column optical depth measured with a resolution of 28.5 meters from LandSat data(see Chapter 11). The cloud is placed between 850 and 900 mb and column optical depth of oxygen is 2. The upper right panel shows the results using the equivalence theorem based on the geometrical path-lengths averaged over a coarser 8 by 8 grid. The backward Monte Carlo model described in Appendix B and Chapter 11 was used to generate the photon path pdf's as the continuum radiance, I_c. The Monte Carlo model was developed with the option of explicitly treating gaseous absorption by including the effect gas along each photon trajectory directly. The results using the explicit representation of gaseous absorption is shown in the lower left panel of Fig a.6. The lower right panel shows the difference between the two treatments. The average pixel error is less than 2% which is approximately the error of radiance in each pixel. The error in the domain averaged radiance between the two methods is only 0.2 %. Once the path-lengths and continuum radiances have been computed, the radiance at any gaseous absorption strength can be readily computed. Therefore, once the initial computation cost of performing the Monte Carlo is occurred, the ability to the do line by line spectra in three dimensional media is readily available. This type of approach can then be used to test the application of broad-band gaseous absorption such as k-distribution (Chou and Arking, 1988) and the correlated-k distribution (Goody et al , 1989) to spatially inhomogeneous media.

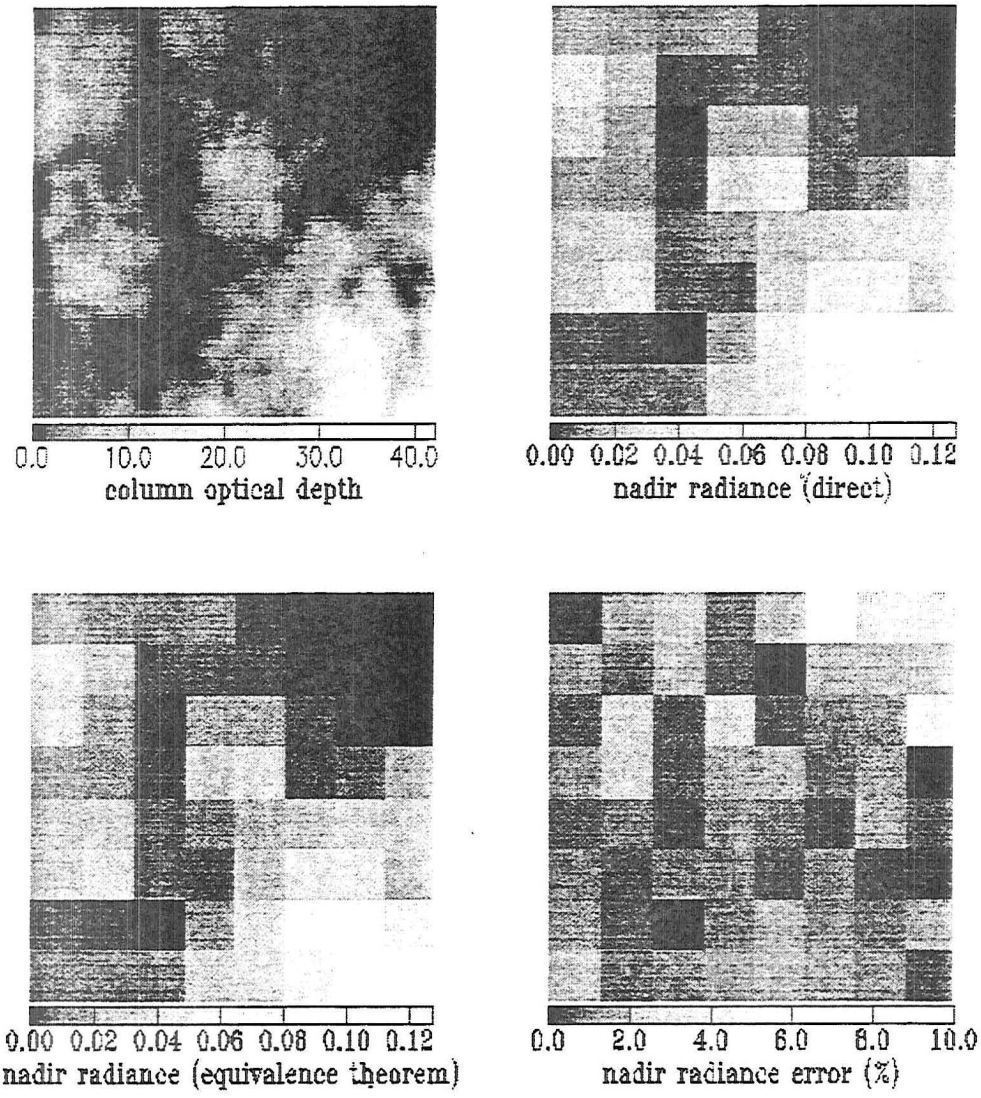

Figure C.6: Comparison of nadir radiance computed for a heterogeneous stratus cloud (upper left) placed between 800 and 850 mb above a dark surface. Nadir radiance computed directly for a backward Monte Carlo model with $\tau^*_{o_2} = 2$ (upper right) is compared with equivalence theorem result (lower left). Relative Errors are shown in lower right. Error in domain averaged quantity is less than 0.5 %

C.5 Vertical Inhomogeneity

While the photon path-length distribution is sufficient for the application of (C.1) to the problem of vertically uniform gaseous absorption, (C.1) must be modified to account for realistic vertical variation in gaseous absorption. Alone, the photon path-length distribution contains no information on the distribution of the gaseous absorber along the path. In the most general case, (C.1) can be modified to account for a an arbitrary distribution of gaseous absorption by incorporating this additional information which is readily obtainable from a Monte Carlo simulation. In a more general form, (C.5) can be written as:

$$F_\nu = F_c \int_0^\infty p(l)\mathcal{T}_{gas}(l)dl \tag{C.11}$$

where $\mathcal{T}_{gas}$ is gaseous transmission along the photon path of length l.

$$\mathcal{T}_{gas}(l) = e^{-(\int_0^\infty p(P|l)\sigma_{gas}(P)dP)l} \tag{C.12}$$

where $p(P|l)$ is the probability distribution of pressure ,P, along path l. The function $p(P|l)$ therefore contains the information concerning the pressure and therefore the absorber amount along the path of the photons. While the above expression is valid for gases with no horizontal gradient in distribution, such as o_2 and co_2, gases such as water vapor which exhibit strong horizontal gradients require information on the horizontal travel of the photon paths. For example, strong horizontal gradients in water vapor can exist in cumulus fields with active up-drafts surrounded by general subsidence. Equation (C.5) could be modified to include the information on the horizontal positions of the photon paths. However, this information can be incorporated by computing the probability of gas optical mass and path-length as follows

$$\mathcal{T}_{gas}(l) = e^{-(\int_0^\infty p(u_{eff}|l)k_{gas}u_{eff}du_{eff})l} \tag{C.13}$$

where

$$u_{eff} = u\left(\frac{T_o}{T}\right)^m\left(\frac{P}{P_o}\right)^n \tag{C.14}$$

The transmission would then be computed using the k-distribution method.

While the above formulations are rigorous, they do require additional computations. The following two approximations to the above rigorous methods which do not require two dimensional probability distributions to be computed. The first approximation, valid for horizontally uniform gas assumes that knowledge of the mean pressure on the path is sufficient to compute the transmission.

$$\mathcal{T}_{gas}(l) = e^{-\left(\sigma_{gas}(P_{eff}(l))\right)l} \tag{C.15}$$

where $P_{eff}(l)$ is the effective or mean pressure along a photon path of length l. In a similar vain, the mean optical mass along a path can be computed and the transmission along a path can be computed as:

$$\mathcal{T}_{gas}(l) = e^{-\left(k_{gas}(u_{eff}(l))\right)l} \tag{C.16}$$

C.6 Conclusions

The chapter dealt with a new application of an old theorem to compute gaseous absorption quickly in any type of scattering media. The method was extended to include particle absorption which greatly increases the spectral range to which the equivalence theorem can be applied. The power of this approach was demonstrated by comparing the results from a fully 3d simulation using an explicit incorporation of gaseous effects and the equivalence theorem. The equivalence theorem results were shown to accurately reproduce the effect of gaseous absorption in the three dimensional cloud field. This method appears to be the only way to compute the line by line spectra in the presence of three dimensional varying scattering media.